Mechanism of Hydrolysis-Activation of the Cardioprotective Antioxidant Dexrazoxane and Identification of More Effective Analogs by Development of a Quantitative Structure-Activity Relationship Describing Imide Hydrolysis

by

Joan L. Buss

A Thesis
Submitted to the Faculty of Graduate Studies
in Partial Fulfilment of the Requirements
for the Degree of

DOCTOR OF PHILOSOPHY

Department of Chemistry
University of Manitoba
Winnipeg, Manitoba

0-612-31967-9

THE UNIVERSITY OF MANITOBA

FACULTY OF GRADUATE STUDIES

*****

COPYRIGHT PERMISSION PAGE

MECHANISM OF HYDROLYSIS-ACTIVATION OF THE CARDIOPROTECTIVE ANTIOXIDANT DEXRAZOXANE AND IDENTIFICATION OF MORE EFFECTIVE ANALOGS BY DEVELOPMENT OF A QUANTITATIVE STRUCTURE-ACTIVITY RELATIONSHIP DESCRIBING IMIDE HYDROLYSIS

BY

JOAN L. BUSS

A Thesis/Practicum submitted to the Faculty of Graduate Studies of The University

of Manitoba in partial fulfillment of the requirements of the degree

of

DOCTOR OF PHILOSOPHY

Abstract

Dexrazoxane reduces the cardiotoxicity of anthracyclines, without affecting its antitumor activity. Doxorubicin-induced cardiomyopathy is thought to be due to iron-based oxidative stress. Dexrazoxane is thought to act by hydrolyzing *in vivo* to ADR-925, a metal ion chelator, which displaces Fe^{3+} from doxorubicin. It was demonstrated that ADR-925 and the one-ring open hydrolysis intermediates of dexrazoxane, **B** and **C**, are effective chelators, which are able to completely displace Fe^{3+} from anthracyclines. Thus, **B** and **C** may be pharmacologically active. Titrations of Fe^{3+}-**B** with N_3^- and daunorubicin demonstrated the existence of ternary complexes, and models of Fe^{3+}-(**B**)-$(H_2O)_2$ and Fe^{3+}-(**B**)-(daunorubicin) complexes were proposed. Fe^{2+} and Fe^{3+} promoted the hydrolysis of **B** and **C** to ADR-925 by factors of up to 6000 and 8, respectively. The pH dependence of these hydrolysis reactions were consistent with hydroxide ion catalysis. Mn^{2+}, Co^{2+}, Ni^{2+}, Cu^{2+}, and Zn^{2+} were also found to promote the hydrolysis of **B** and **C**, by factors of 25 to >50,000. Physiological concentrations of Mg^{2+} and Ca^{2+} also promoted the hydrolysis of **B** and **C**; these ions may mediate the formation of **D**, the most effective chelator, *in vivo*. In addition to promoting the hydrolysis of **B** and **C**, Zn^{2+} promoted the hydrolysis of dexrazoxane itself. The kinetics of base-catalyzed hydrolysis of a series of imides was characterized. Data from molecular mechanics and semi-empirical calculations were regressed against the kinetic parameters to yield a quantitative structure-activity relationship between imide hydrolysis rates and molecular modelling parameters, which was used to predict the hydrolysis rates of a series of analogs of dexrazoxane. Analogs which were predicted to hydrolyze 2-5 times faster than dexrazoxane, and may therefore be more active, were identified as target molecules.

Acknowledgments

I have had the excellent fortune of working among intelligent and productive scientists, many of whom were directly involved in my program of studies. I hope that I have learned enough from these people to justify their efforts on my behalf.

My graduate advisor, Dr. Brian Hasinoff, taught me what I know about experimental design, and the evaluation of both my own work and that of others. His enthusiasm for and dedication to his research reminded me, when I forgot, that we should enjoy our work. My advisory committee consisted of Dr. R. Bird, Dr. H. Duckworth, Dr. N. Hunter, and Dr. A. Queen, who examined my work with fresh eyes, and always offered me new perspectives. Between the Faculty of Pharmacy and the Chemistry Department, there was a faculty member or fellow student with expertise in every area in which I needed advice. Although there were many who offered their assistance during my program, the advice and support of two were outstanding. Our laboratory technician, Mukhtiar Singh, has an apparently encyclopedic knowledge of the methods used in our laboratory, and always made time to discuss them with me. Our research associate, Yangzhi Ling, was an excellent resource. In the very short time he was with our group, he patiently taught me aspects of synthetic organic chemistry which I had until then believed impenetrable.

Throughout my program, I have been supported by studentships from the Manitoba Health Research Council, the Natural Sciences and Engineering Research Council, and the Pharmaceutical Manufacturers' Association of Canada/Medical Research Council.

Table of Contents

List of Figures

List of Tables

List of Abbreviations

ADP	adenosine diphosphate
AM1	Austin Model 1
DHPase	dihydropyrimidine amidohydrolase
DMSO	dimethylsulfoxide
DNA	deoxyribonucleic acid
DOX	doxorubicin
DTPA	diethylenetriaminepentaacetic acid
EDTA	ethylenediaminetetraacetic acid
EPR	electron paramagnetic resonance
$FADH_2$	flavin adenine dinucleotide (reduced form)
HOMO	highest occupied molecular orbital
HPLC	high performance liquid chromatography
LUMO	lowest unoccupied molecular orbital
m. p.	melting point
NADH	nicotinamide adenine dinucleotide (reduced form)
NADPH	nicotinamide adenine dinucleotide phosphate (reduced form)
NMR	muclear magnetic resonance
PRESS	predicted residual error sum of squares
RMS	root-mean-square
SEM	standard error of the mean

TLC	thin layer chromatography
Tris	tris(hydroxymethyl)aminomethane
UV	ultraviolet

Chapter 1 Introduction

1.1 Clinical use of doxorubicin

The antitumor anthracycline, doxorubicin, was first isolated from a strain of *Streptomyces peucetius*, and was found to have a wider spectrum of activity and a larger therapeutic index than daunorubicin [1] (Figure 1.1), the first anthracycline discovered. Doxorubicin, marketed by Pharmacia & Upjohn as Adriamycin®, is the most successful of the anthracyclines, and is used against a wide variety of cancers, including leukemias, lymphomas, and sarcomas. It is the most-used agent against breast cancer.

Doxorubicin causes side effects common to antitumor agents, including myelosuppression, nausea, and alopecia [2]. Anthracyclines likely cause these effects by affecting bone marrow stem cells, gastro-intestinal mucosal cells, and hair follicles specifically due to their rapid proliferation relative to other tissues. These are common responses to antitumor agents, and, in the case of doxorubicin, are thought to be due to DNA damage and interference with DNA replication through topoisomerase II. Anthracyclines also cause a dose-limiting, cumulative cardiotoxicity [3], which results in irreversible, potentially fatal congestive heart failure [4], symptoms of which include reduced cardiac output, edema, cardiomegaly, and venous congestion. As a result, the maximum recommended cumulative dose of doxorubicin for the 21-day schedule is 550 mg/m^2 [5], although many patients might benefit from larger doses. Since heart cells grow very slowly, the mechanism of cardiac toxicity is not likely due to DNA damage. Evidence has accumulated to suggest that this toxicity, unique to anthracyclines, is caused by iron-based oxidative stress.

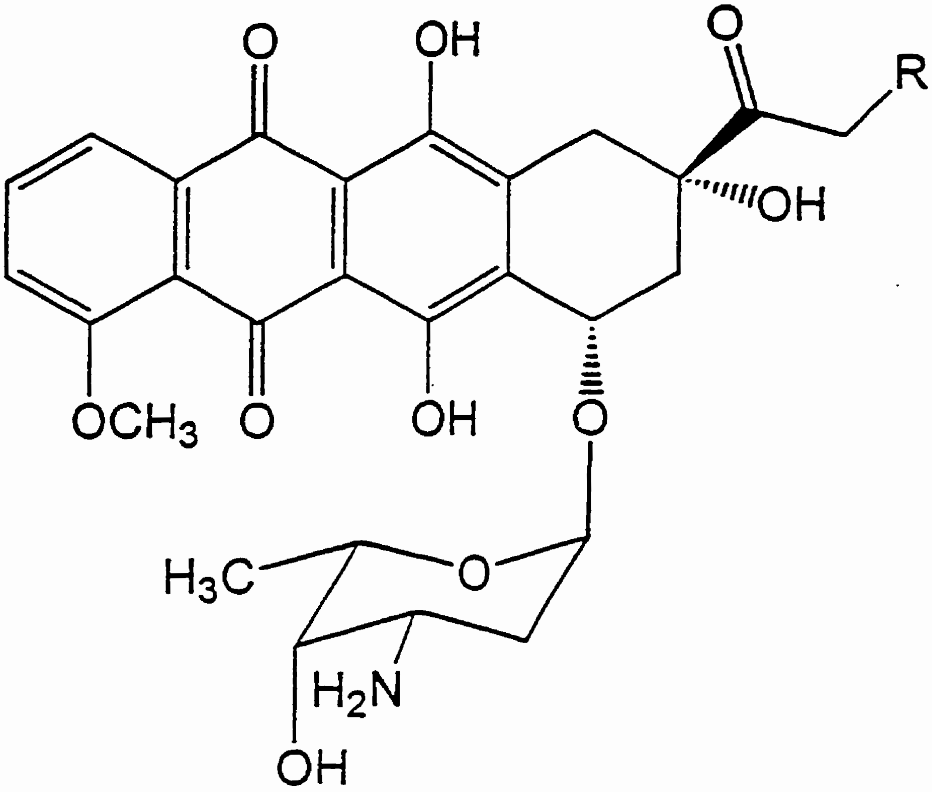

Figure 1.1. Structures of doxorubicin and daunorubicin. Doxorubicin, R = OH. Daunorubicin, R = H.

1.2 Oxidative stress in biological systems

Oxidative stress involves oxidation of cellular components beyond that which can be prevented or repaired by cellular antioxidant mechanisms. Membranes, nucleic acids, and proteins may be the targets of this damage. Oxidative stress is initiated by generation of the reduced oxygen species, superoxide ion and hydrogen peroxide. Superoxide ion is the product of single electron reduction of molecular oxygen:

$$e^- + O_2 \rightarrow O_2^- \quad (1.1)$$

Many biological processes are capable of producing superoxide ion by this reaction [6], including the electron transport chain in the mitochondria, by which electrons are transferred from NADH and $FADH_2$ to O_2, producing water. O_2 bound to the Fe^{2+} ion in hemoglobin may be released as O_2^-, with concomitant oxidation of the metal ion. Oxidative enzymes, such as xanthine oxidase, indoleamine dioxygenase, tryptophan dioxygenase, and aldehyde oxidase also release superoxide ion.

Superoxide ion reduces biological Fe^{3+}, including cytochrome *c* [6]. Superoxide ion also dismutates, both chemically and catalyzed by superoxide dismutase, to hydrogen peroxide:

$$2O_2^- + 2H^+ \rightarrow H_2O_2 + O_2 \quad (1.2)$$

Hydrogen peroxide oxidizes thiols, thereby inactivating enzymes, including glyceraldehyde-3-phosphate dehydrogenase [6]. In the presence of Fe^{2+}, hydrogen peroxide is reduced in the Fenton reaction:

$$Fe^{2+} + H_2O_2 \rightarrow Fe^{3+} + OH^- + OH^{\cdot} \quad (1.3)$$

Hydroxyl radical is highly reactive; its rate of reaction with cellular components is diffusion-controlled. It is this species which is primarily responsible for lipid peroxidation. A scheme by which hydroxyl radical may initiate the peroxidation of lipids (LH), forming lipid radicals ($L^{\cdot}$), lipid peroxy radicals ($LOO^{\cdot}$), and lipid peroxides (LOOH) as intermediates, is as follows:

$$LH + OH^{\cdot} \rightarrow L^{\cdot} + H_2O \quad (1.4)$$

$$L^{\cdot} + O_2 \rightarrow LOO^{\cdot} \quad (1.5)$$

$$LOO^{\cdot} + LH \rightarrow LOOH + L^{\cdot} \quad (1.6)$$

Lipid peroxidation is a chain reaction by which unsaturated membrane lipids are oxidized and degraded.

1.3 Biochemistry of the anthracyclines

In the presence of either chemical or enzymatic reducing agents, doxorubicin damages DNA [7] and membrane lipids [8]. The redox chemistry associated with anthracyclines requires single electron reduction, producing a semiquinone radical. Several enzymes are capable of transferring an electron to doxorubicin (DOX), including xanthine oxidase, cytochrome *c* reductase, glutathione reductase, and NADPH cytochrome P-450 reductase [9, 10]. In the presence of O_2 the doxorubicin semiquinone ($DOX^{\cdot-}$) transfers its electron producing superoxide ion [10]:

$$DOX^{\cdot -} + O_2 \rightarrow DOX + O_2^{\cdot -} \quad (1.7)$$

thereby initiating oxidative damage mediated by reactions 1.2 and 1.3.

The Fe^{3+}-doxorubicin complex has more extensive redox chemistry than free doxorubicin. Fe^{3+}-doxorubicin may be reduced to the Fe^{2+} complex by superoxide ion, or by the doxorubicin semiquinone radical [11]:

$$Fe^{3+}\text{-}(DOX)_3 + O_2^{\cdot -} \rightarrow Fe^{2+}\text{-}(DOX)_3 + O_2 \quad (1.8)$$

$$Fe^{3+}\text{-}(DOX)_3 + DOX^{\cdot -} \rightarrow Fe^{2+}\text{-}(DOX)_3 + DOX \quad (1.9)$$

The Fe^{2+} complex reduces hydrogen peroxide in the Fenton reaction [12, 13]:

$$Fe^{2+}\text{-}(DOX)_3 + H_2O_2 \rightarrow Fe^{3+}\text{-}(DOX)_3 + OH^- + OH^{\cdot} \quad (1.10)$$

Fe^{3+}-doxorubicin self-reduces to a Fe^{2+} species, with the concomitant oxidation of one of the doxorubicin molecules [14]:

$$Fe^{3+}\text{-}(DOX)_3 \rightarrow Fe^{2+}\text{-}(DOX)_2(DOX^{\cdot +}) \quad (1.11)$$

On addition of O_2 the complex is regenerated with the production of hydrogen peroxide. The self-reduced complex produces a radical species which may be hydroxyl radical, thereby causing lipid peroxidation [15]. It may be due to its ability to self-reduce that the Fe^{3+}-doxorubicin complex is a much better promoter of oxidative damage than doxorubicin. A scheme of the reactions 1.2, 1.3, and 1.7-1.11 is shown in Figure 1.2.

Doxorubicin was observed to produce twice as much superoxide radical as daunorubicin when incubated with submitochondrial particles [13]. Although their affinities for Fe^{3+} are similar [16], doxorubicin exceeded daunorubicin in oxygen consumption, self-reduction, reduction of electron transport chain components, and hydroxyl radical production in the presence of submitochondrial particles. Since they differ in structure by one hydroxyl group (Figure 1.1), all observed differences in activity must be due to this small structural change. When the experiments for daunorubicin were repeated in the presence of acetol, the

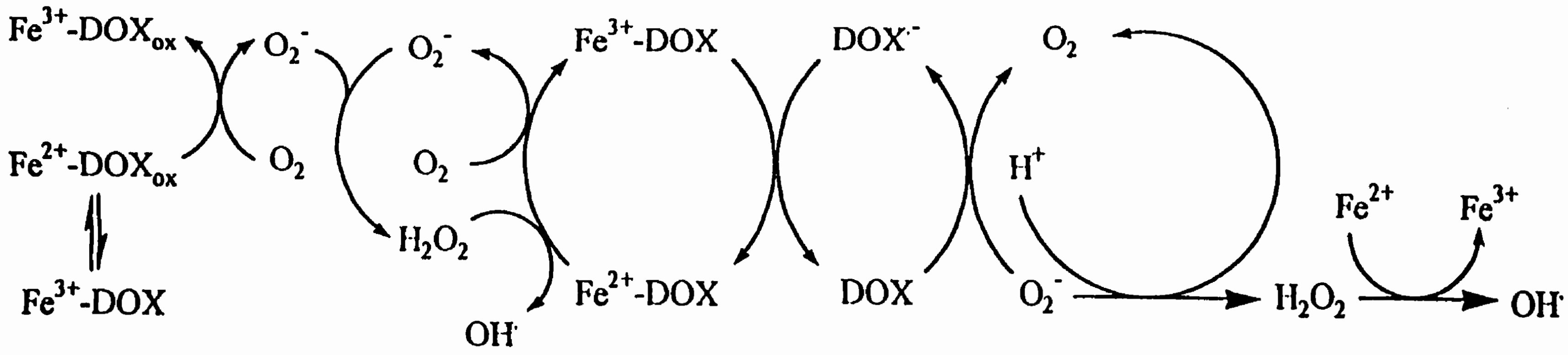

Figure 1.2. Redox reactions of doxorubicin. DOX is doxorubicin, Fe^{3+}-DOX and Fe^{2+}-DOX are the iron complexes of doxorubicin, Fe^{2+}-DOX_{ox} is the self-reduced iron-doxorubicin complex, and DOX_{ox} is DOX which has been oxidized on its ketol side chain.

rates of hydroxyl radical production and reduction of ferricytochrome *c* were significantly increased [17]. Thus, it was concluded that the presence of an α-ketol group, such as that of doxorubicin, was responsible for the high levels of redox cycling observed. Since the presence of an α-ketol group has been correlated with the capacity of anthracyclines for self-reduction [18], it may be through self-reduction that these effects are mediated.

1.4 Role of Fe^{3+} in doxorubicin cardiotoxicity

Doxorubicin strongly binds Fe^{3+} in a 3:1 ratio [19], presumably through its quinone-hydroquinone oxygen atoms [20, 21]. The stepwise formation constants for this complex are 10^{18}, 10^{11}, and $10^{4.4}$ M^{-1} [19]. Although intracellular levels of loosely bound iron are low [6], it is likely that the Fe^{3+} has access to doxorubicin *in vivo*. In dogs [22, 23], rabbits [24], and miniature swine [25], but not in rats [26, 27], doses of 1 to 3.2 mg/kg doxorubicin caused 15 to 18 μM reductions in serum iron levels, which corresponds to a 30-40% decrease, possibly due to mobilization of Fe^{3+} from ferritin. Doxorubicin removes iron from ferritin [28], the major iron storage protein [29, 30], possibly by reducing the Fe^{3+} in ferritin to Fe^{2+}, as does O_2^- [31]. It may be through the production of O_2^- that doxorubicin releases Fe^{3+} from ferritin. Because ferritin is specific for Fe^{3+}, it has much lower affinity for Fe^{2+}. Due to the likelihood of appreciable formation of Fe^{3+}-doxorubicin complexes, mechanisms of damage involving this species must be considered.

The oxidative damage which doxorubicin causes in biological systems is enhanced by its affinity for cellular components. Doxorubicin [32] and its Fe^{3+} complex [33] strongly bind negatively charged phospholipids, and have particular affinity for cardiolipin, which is a major constituent of the mitochondrial inner membrane [34], where much of the observed cardiac damage takes place [35]. Cardiolipin consists of two diacyl glycerol phosphates, linked through the phosphate moieties by a third molecule of glycerol. Because cardiolipin is doubly negatively charged, it is able to bind two molecules of doxorubicin [32], and the affinity of doxorubicin for cardiolipin is 100-fold higher than for phosphatidic acid and phosphatidylserine, both of which have one phosphate group [36]. Since *N*-acetyldoxorubicin does not bind cardiolipin [32], it is likely that the positively charged amino group of doxorubicin is closely associated with the phosphate groups. A correlation has been observed between the toxicity of anthracyclines and their affinities for cardiolipin [37].

The major site of damage by doxorubicin is apparently the cell membrane. Doxorubicin conjugated to membrane-impermeable polymers is more cytotoxic than free drug [38, 39], indicating that although doxorubicin accumulates up to 100-fold within cells [40], at least some of its toxic effects occur extracellularly. The Fe^{3+}-doxorubicin complex initiates the lipid peroxidation of erythrocyte ghost membranes [8], while free doxorubicin does not. In this study, the Fe^{3+} complex of acetohydroxamic acid produced oxy radicals at similar rates, but did not cause lipid peroxidation. It was concluded that the strong affinity of Fe^{3+}-doxorubicin for membranes caused a greater fraction of the Fe^{3+} to be in close proximity to the membranes when complexed with doxorubicin than with acetohydroxamic acid. Thus, production of highly reactive hydroxyl radicals by Fe^{3+}-doxorubicin would occur site-specifically at the membranes, resulting in the observed capacity of Fe^{3+}-doxorubicin to damage membranes, relative to Fe^{3+}-acetohydroxamic acid, despite their similar abilities to produce hydroxyl radicals. Another study demonstrated that EDTA reduced the lipid peroxidation of submitochondrial particles, demonstrating the significant role of Fe^{3+} in the mechanism of generation of oxy radicals [41], even in the presence of cellular reducing agents.

Many electron transport chain enzymes, which are associated with the mitochondrial membrane, are inactivated by doxorubicin and its Fe^{3+} complexes, including NADPH-cytochrome P-450 reductase, NADH cytochrome *c* reductase, and cytochrome *c* oxidase [42, 43]. Following doxorubicin administration in mice, reduced activity of NADH cytochrome *c* reductase and oxidase has been measured [44]. Since neither *N*-acetyldoxorubicin, which does not specifically bind membranes, nor 5-iminodaunorubicin, which does not redox cycle, caused similar damage, it was concluded that both of these activities are necessary for inactivation of respiratory enzymes [44]. Fe^{3+} may play a significant role in causing this damage *in vivo*, since inactivation of electron transport chain enzymes by doxorubicin in submitochondrial particles occurs much more quickly in the presence of Fe^{3+} [43], and EDTA prevents the inactivation of NADH cytochrome *c* reductase *in vitro* [45]. Some respiratory enzymes require cardiolipin for activity, such as cytochrome *c* oxidase [46]. Cardiolipin may attract doxorubicin to this enzyme, which is then inhibited and inactivated by the Fe^{3+}-doxorubicin complex [47]. Cholate solubilization, which disrupts the membranes of submitochondrial particles, restores cytochrome *c* oxidase activity [48]. It may be that the cardiolipin is damaged or removed from the enzyme during inactivation.

Free anthracyclines are intercalators [49], and anthracyclines [50], and their Fe^{3+} complexes [20], bind DNA. The ternary Fe^{3+}-(DOX)(DNA) complex damages DNA in the presence of the reducing agent, glutathione, and is so tightly bound that it is not dissociated from DNA in the presence of the very strong chelator, EDTA [20].

Doxorubicin, therefore, has the ability to produce free radicals site-specifically, causing DNA damage, lipid peroxidation, and inactivation of electron transport chain enzymes. These effects damage cellular systems which are critical for cell survival.

1.5 Cardiac selectivity of anthracycline toxicity

It has been demonstrated that doxorubicin accumulates in the heart to a lesser extent than in other organs [51, 52]. However, heart tissue is rich in mitochondria [53], which are targets of damage by anthracyclines [35]. Cardiolipin, for which doxorubicin has particular affinity [32], is a major constituent of the mitochondrial inner membrane [34]. Thus, doxorubicin has high affinity for mitochondrial membranes, where the enzymes of the electron transport chain are located. Doxorubicin specifically damages mitochondria, which could result in impaired cardiac function.

The heart may be the specific target of oxidative damage due to its lack of protection against the reactive oxygen species which initiate free radical reactions. The levels of superoxide dismutase, which decomposes superoxide ion (Reaction 1.2), and catalase, which dismutates hydrogen peroxide:

$$H_2O_2 \rightarrow H_2O + \frac{1}{2}O_2 \quad (1.12)$$

are significantly lower in the heart than in other organs [54-58]. Mice subjected to exercise training had higher blood levels of superoxide dismutase, catalase, and glutathione peroxidase than untrained animals, and, on administration of doxorubicin, had reduced cardiotoxicity

[59]. However, since rats with 1% the normal levels of glutathione peroxidase were equally sensitive to doxorubicin as were rats with normal levels [60], this enzyme may not be as important a defense against doxorubicin-induced toxicity as superoxide dismutase and catalase.

1.6 Synthesis and antitumor activity of dexrazoxane

Dexrazoxane (Figure 1.3) and its analogs were originally designed as antitumor agents [61]. It was postulated that since many antitumor agents were chelators, an antitumor agent with the abilities to penetrate the cell membrane and to chelate metal ions might be effective [62]. ICRF-154, the first compound in the series, is the bis-imide of EDTA, a powerful chelator of divalent and trivalent metal ions.

Dexrazoxane and its analogs are synthesized from their respective tetracarboxylic acids by condensation with formamide [61]. The products are bis-cyclic imides (Figure 1.3). Imides may be similarly synthesized by condensation of dicarboxylic acids with other nitrogen-containing species, including ammonia [63] and urea [64]. Ammonia may also serve as the nitrogen donor for such compounds as acid halides [65] and diesters [66]. While diamides cyclize to imides upon heating [67], the half-amide half-ester will do so only in the presence of a base [68].

ICRF-159, the racemate of dexrazoxane, and ICRF-154, the bis-imide derivative of EDTA, were both active against experimental tumors in mice [62]. In this study, these compounds demonstrated both antitumor and antimetastatic properties. ICRF-159 was also active in combination with cisplatin or daunorubicin against murine L1210 leukemia [69].

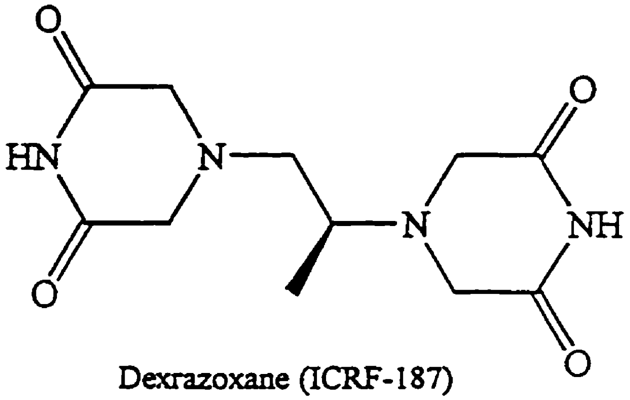

Dexrazoxane (ICRF-187)
Racemate = ICRF-159

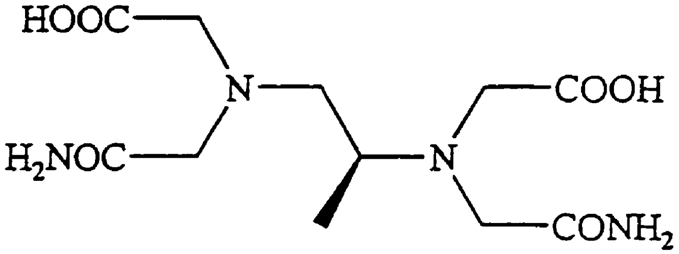

ADR-925
Racemate = ICRF-198

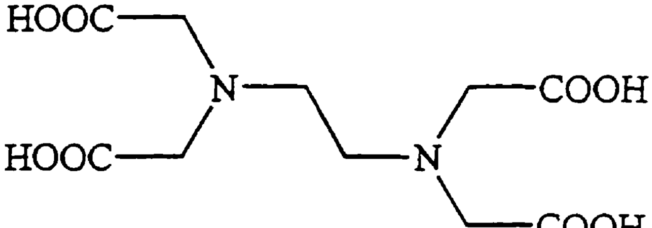

EDTA

Figure 1.3. Structures of dexrazoxane, ADR-925, and EDTA.

Early clinical studies of the biological activity of ICRF-159 also demonstrated antitumor activity, either alone [70], or as adjuvant therapy with surgery [71] against metastatic colorectal carcinoma, or against Hodgkin's and non-Hodgkin's lymphoma [72]. Due to its low water solubility [73], ICRF-159 was administered orally. Oral delivery of this drug is inefficient, as a large fraction of each dose may not be absorbed, depending on the dose [74]. The discovery that the enantiomers of ICRF-159, ICRF-186 and dexrazoxane (ICRF-187), are approximately five times more water-soluble than the racemate allowed the administration of dexrazoxane by an intravenous route [73]. The maximum tolerated daily dose of intravenous dexrazoxane was found to be 1250 mg/m^2 [75] which is similar to the oral doses of ICRF-159 in previous clinical trials discussed above. Although the preliminary results in small trials were encouraging, no studies were able to demonstrate that dexrazoxane was a sufficiently effective antitumor agent to be accepted for this use.

The side effects of dexrazoxane include myelosuppression, gastro-intestinal toxicity, and alopecia [70, 76]. Effects such as these are thought to be due to general toxicity toward rapidly proliferating cells, and are common to antitumor agents. The severity of these effects increases with dose and exposure time, and the overall toxicity toward cultured cells is attenuated as the drug decomposes, presumably through hydrolysis [77]. These observations suggest the unexpected possibility that the toxic species is the parent compound, and not its hydrolysis product.

The first observation of the cellular effects of ICRF-154 and ICRF-159 was inhibition of DNA synthesis [78], which was correlated to observed antitumor activity [62]. Since, in the former study, these drugs had no effect on RNA and protein synthesis, the observed toxicity appears to be mediated directly through DNA synthesis. If DNA synthesis is the actual target of dexrazoxane and its analogs, their observed toxicity toward tumor and other rapidly proliferating cells is expected.

The cytotoxicity of ICRF-159 is cell-cycle-dependent; the strongest inhibition of cell growth occurs when it is administered to cultured cells during the G2/M transition [79]. Although the rate of DNA synthesis is unaffected, cell division is irregular [80]. After 24 h exposure to 10 μg/mL ICRF-159, 95% of the surviving cells were tetraploid, indicating that chromosome replication may have occurred without cell division [80]. A similar study with dexrazoxane demonstrated that, at equal concentrations, it has the same effect as ICRF-159 on cell division [81]. Accumulation of tetraploid cells, which is reversible after 48 h [77], has been observed in the bone marrow of patients receiving dexrazoxane. Thus, these effects, which may be the mechanism by which dexrazoxane is toxic, are observed clinically.

Cell cycle studies indicated that dexrazoxane affects the progress of cells through mitosis. Cultured epithelial cells entered mitosis at a normal rate, and normal mitotic proteins were detected [82]. During anaphase, however, it was observed that the chromatids did not separate, and consequently, all the DNA was frequently found in one daughter cell [82]. *In vitro* inhibition of topoisomerase II, an enzyme required for mitosis, was demonstrated, and it was postulated that inhibition of this enzyme was the mechanism by which dexrazoxane exerts its cytotoxicity [83, 84]. ICRF-193, a more cytotoxic analog of dexrazoxane, inhibited topoisomerase II at much lower levels than dexrazoxane [84], and a structure-activity study of dexrazoxane and its analogs demonstrated a linear relationship between topoisomerase II inhibition and cytotoxicity toward Chinese hamster ovary cells [85]. Thus, it is likely that this is the main mechanism of cytotoxicity of this series of compounds.

Topoisomerases are responsible for the relaxation, unknotting, and decatenation of double-stranded DNA, which is necessary for DNA synthesis and cell division. Type II topoisomerases cleave double-stranded DNA, pass another strand of DNA through the gap, and religate the DNA. This activity is required for separation of sister chromatids. Thus, the absence of chromosome separation during anaphase, and the correlated cytotoxicity [82], may be solely due to inhibition of topoisomerase II. The cellular effects of dexrazoxane are very similar to those observed in yeast with a mutant topoisomerase II [86]. Thus, inhibition of this enzyme is sufficient to cause the effects observed in the studies described above.

1.7 Protection against anthracycline cardiotoxicity by dexrazoxane

Dexrazoxane (Figure 1.3) is the only drug which has been unequivocally shown to reduce doxorubicin-induced cardiotoxicity in animal studies. Doses of doxorubicin can be safely administered with dexrazoxane, which alone would cause potentially fatal cardiomyopathy in mice [87], rats [27], dogs [22], and miniature swine [25]. When it was also demonstrated in clinical trials that the co-administration of dexrazoxane permits significantly higher cumulative doses of doxorubicin without an associated increase in cardiotoxicity [88, 89], it was approved for use by the Food and Drug Administration in the U. S. A. and the Health Protection Branch in Canada.

In animal studies, it was demonstrated that dexrazoxane is most effective when administered three hours before or after daunorubicin [90], an anthracycline which differs from doxorubicin only by the absence of a hydroxyl group (Figure 1.1). A similar schedule dependence was also observed for dexrazoxane and doxorubicin [23]. Clinically, dexrazoxane is administered by a 15-minute intravenous dose, started 30 minutes prior to administration of doxorubicin, and the recommended ratio of the two doses, measured in mg/m^2, is 10:1, respectively [5].

Although vitamin E protected mice from cardiac damage in an acute toxicity study [91], it was later determined that the sixty-day death rate is the same for animals receiving α-tocopherol as for the doxorubicin control group [92]. It has been shown that dexrazoxane prevents, rather than delays, anthracycline toxicity. When doses of daunorubicin which killed 90% of a group of hamsters within three weeks were administered with dexrazoxane, half the animals survived longer than four months [93]. Ten weeks after treatment, the hearts of dexrazoxane-pretreated animals were morphologically identical to animals which had received no daunorubicin. Similar results were obtained with rabbits [94]. Cardiac damage in rats continued to worsen over 20 weeks after drug administration, regardless of whether they had received dexrazoxane, although dexrazoxane reduced the extent of the damage [95].

Clinical trials have clearly demonstrated the protective effect of dexrazoxane against doxorubicin-induced cardiotoxicity when administered as therapy for metastatic breast cancer [88]. However, these trials were too small to determine whether administration of dexrazoxane affects the antitumor activity of doxorubicin. A recent retrospective trial of breast cancer patients demonstrated a significant increase in survival time for the patients receiving dexrazoxane [96]. Thus, co-administration of doxorubicin and dexrazoxane prevents the cardiomyopathy associated with doxorubicin, without affecting its antitumor activity.

Patients who have received radiation therapy to the heart, or who have a history of heart disease, are at greater risk for developing doxorubicin-induced congestive heart failure [97]. Reduction of doxorubicin-associated cardiotoxicity by dexrazoxane may allow patients to receive doxorubicin-containing chemotherapy who were previously refused the drug due to cardiac risk factors. Long-term protection is also of great importance in the clinical use of anthracyclines. Many patients treated with doxorubicin suffer congestive heart failure long after their chemotherapy is discontinued [98]. There is concern that if doxorubicin is administered to pediatric patients, they may develop cardiotoxicity years later [89]. If dexrazoxane is proven to offer long-lasting protection in humans, as appears to be the case in animals, patients who suffer relapses may be treated with additional courses of anthracycline with a reduced risk of cardiotoxicity.

1.8 Mechanism of cardioprotection by dexrazoxane

Since the role of Fe^{3+} in the redox chemistry of doxorubicin has been established, the possibility that dexrazoxane acts by hydrolyzing to its metal ion chelating form, ADR-925 (Figure 1.3), thus preventing it from interacting with doxorubicin, has been investigated. Since it is known that the levels of loosely bound Fe^{3+} *in vivo* are extremely low [6], the possibility that ADR-925 removes Fe^{3+} bound to other biological species is of interest. The hydrolysis product of dexrazoxane, ADR-925 (Figure 1.3), does not remove Fe^{3+} from transferrin, the Fe^{3+} transport protein, at pH 7.4, and it does so from ferritin [99], but at a rate much slower than its elimination *in vivo* [100]. Since dexrazoxane has no effect on serum iron levels [22-25], it may not act by depleting the body's iron stores, but rather by removing Fe^{3+} from its complex with doxorubicin [101].

Although dexrazoxane is optimally active when administered to dogs three hours before or after anthracyclines [90], it retains some of its cardioprotective ability when it is administered 24 hours before daunorubicin [90, 102]. It has been demonstrated that at least 90% of a dose of dexrazoxane is eliminated unchanged from rats [103] and mice [104] by the end of the elimination phase of its pharmacokinetics. If this is also the case for dogs, 24 hours after administration of an intravenous dose, dexrazoxane and its hydrolysis products have been eliminated from dogs [105]. Protection in this model, therefore, is not likely due to direct displacement of Fe^{3+} from anthracyclines, since dexrazoxane does not have to be present at the same time as anthracyclines to be protective.

Dexrazoxane passively diffuses across the cell membrane [106]. Thus, chelation of Fe^{3+} and Cu^{2+} by its hydrolysis product, ADR-925, which has been demonstrated *in vitro* [101] may occur both intra- and extracellularly. Fe^{3+}-(ICRF-198) produces hydroxyl radicals at approximately the same rate as Fe^{3+}-EDTA [107] (structures of these ligands are shown in Figure 1.3). Thus, the greater protective ability of ICRF-198 [108] as compared to EDTA is not due to any difference in the production of hydroxyl radicals. It is more likely that since dexrazoxane readily enters cells [106], it has access to intracellular metal ions, which EDTA does not.

In vitro reduction of the Fe^{3+} chelate of ADP and ferritin-bound Fe^{3+} by doxorubicin was inhibited 10% by dexrazoxane and 77% by ICRF-198, the hydrolysis product of razoxane (ICRF-159) [109]. Dexrazoxane likely acts by removing Fe^{3+} from doxorubicin, thereby reducing its potential to redox cycle. In this study, it was also determined that while reduction of Fe^{3+}-(ICRF-198) by rabbit heart microsomes and doxorubicin was 20% of that of free Fe^{3+}, the complex caused only 6% as much lipid peroxidation in the same system. Thus, some of the protective effect of ICRF-198 is due to a slower rate of reduction, since Fe^{3+}-(ICRF-198) was reduced more slowly than was Fe^{3+} when it was added to the system without ICRF-198. Since the rate of lipid peroxidation was decreased by an even larger factor, it was concluded that protection was also due to its decreased affinity for membranes, relative to Fe^{3+} which was added to the system without a ligand. ICRF-198 was maximally effective in preventing iron-based hydroxyl radical production and lipid peroxidation *in vitro* at a concentration equal to that of Fe^{3+} [109], which corresponds to the expected 1:1 chelation of Fe^{3+} by a hexadentate ligand. Lipid peroxidation by anthracyclines was attenuated by Fe^{2+} and Fe^{3+} chelators, confirming the role of iron in the reductive damage caused by anthracyclines [110]. Hydroxyl radical production by doxorubicin, and its inhibition by dexrazoxane, was observed in perfused rat hearts [111].

Dexrazoxane and the Fe^{3+} chelator desferrioxamine protected against a doxorubicin-induced decrease in mouse atrial contractile force *in vitro* [112], indicating a common mechanism of action. Thus, it is hypothesized that both *in vitro* and *ex vivo*, the hydrolysis product of dexrazoxane chelates Fe^{3+}, decreasing the production of reactive oxygen species, thereby preventing anthracycline-induced cardiotoxicity.

N-acetylcysteine did not protect against doxorubicin cardiotoxicity in dogs [113, 114]. In both studies, more animals receiving doxorubicin plus *N*-acetylcysteine died than those receiving only doxorubicin. Although *N*-acetylcysteine is a free radical scavenger, it is also a reducing agent which donates electrons to the Fe^{3+}-doxorubicin complex [8]. Since *N*-

acetylcysteine worsened doxorubicin toxicity, rather than preventing it, it may have served as a reducing agent *in vivo*.

1.9 Hydrolysis-activation of dexrazoxane

Since chelation is implicated as a significant mechanism by which dexrazoxane protects against doxorubicin toxicity, the location and rate of hydrolysis of dexrazoxane *in vivo* is of interest. Dexrazoxane passively diffuses across the cell membrane [106]. Thus, hydrolysis may occur intracellularly, extracellularly, or both. The hydrolysis product of dexrazoxane may therefore have access to metal ions which other chelators, such as EDTA, do not, since they are too polar to cross the cell membrane. ADR-925 (Figure 1.3), the product of complete hydrolysis of dexrazoxane, is a metal ion chelator [115]. The formation constants of ICRF-198, the racemate of ADR-925, with Ca^{2+}, Mg^{2+}, Fe^{2+}, and Zn^{2+} are $10^{6.9}$, $10^{5.1}$, 10^{10}, and $10^{9.5}$ M^{-1}, respectively [115]. ADR-925 is able to remove Fe^{3+} from its complexes with doxorubicin [116]. Although it is a weaker chelator than EDTA [115], it may chelate an equal amount of transition metal ions in plasma. Since ADR-925 has much lower affinity for Ca^{2+} and Mg^{2+} than does EDTA [115], which are abundant in plasma, a larger fraction of the former ligand may therefore be available to bind transition metal ions, whose plasma concentrations are much lower.

Dexrazoxane undergoes base-catalyzed, first-order hydrolysis to the diacid diamide, ADR-925, *via* one of two one-ring open intermediates, **B** or **C** (Figure 1.4) [117]. Imide hydrolysis occurs *via* a two-step mechanism, as shown in Figure 1.5, which is analogous to that of esters [118]. Imides hydrolyze under much milder conditions than do amides [119],

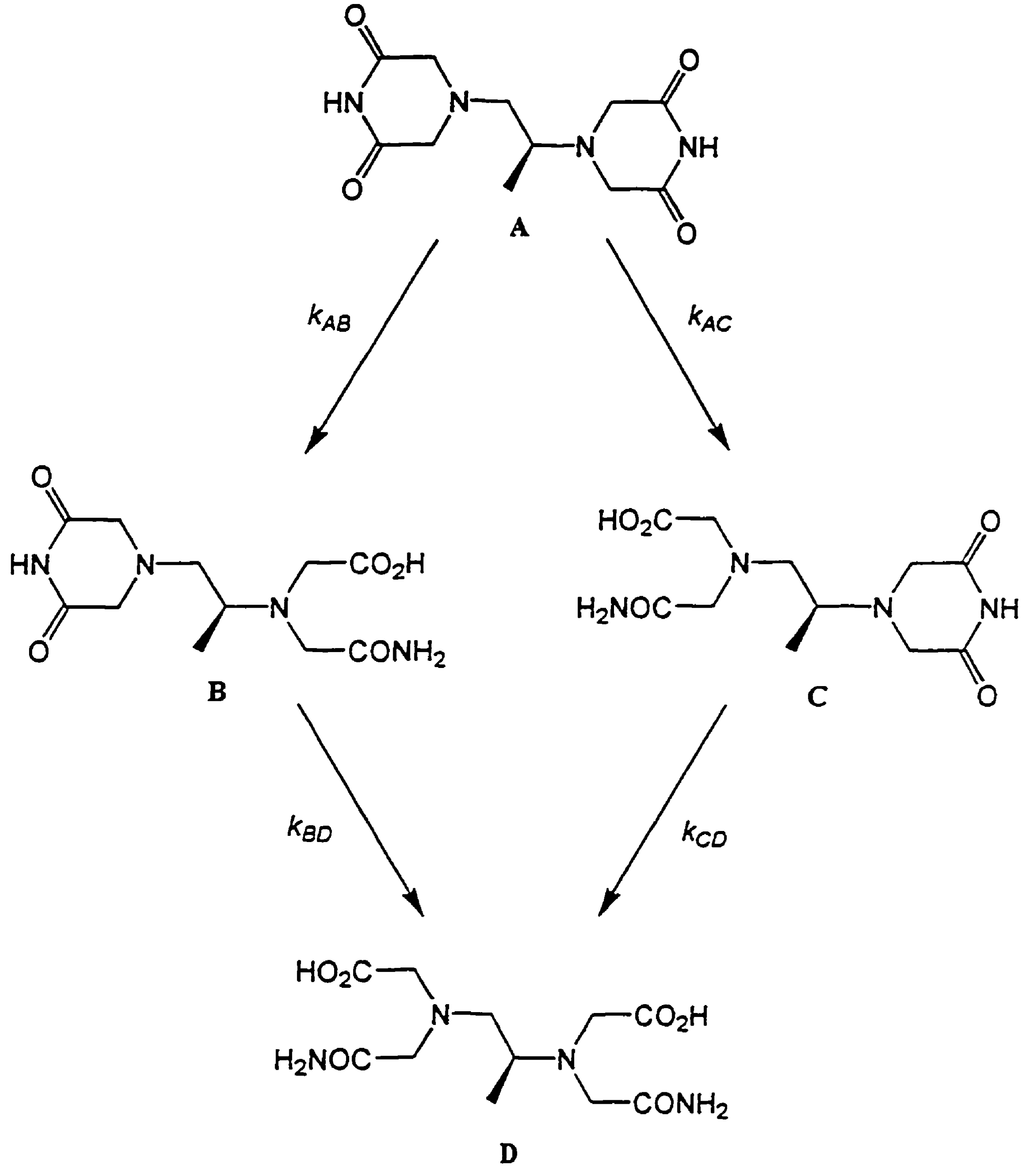

Figure 1.4. Hydrolysis scheme of dexrazoxane. Dexrazoxane (ICRF-187, A) hydrolyzes to ADR-925 (D) *via* one of two one-ring open intermediates, B or C. The rate constants, k_{AB}, k_{AC}, k_{BD}, and k_{CD} describe the pseudo-first-order, hydroxide ion catalyzed hydrolysis reactions.

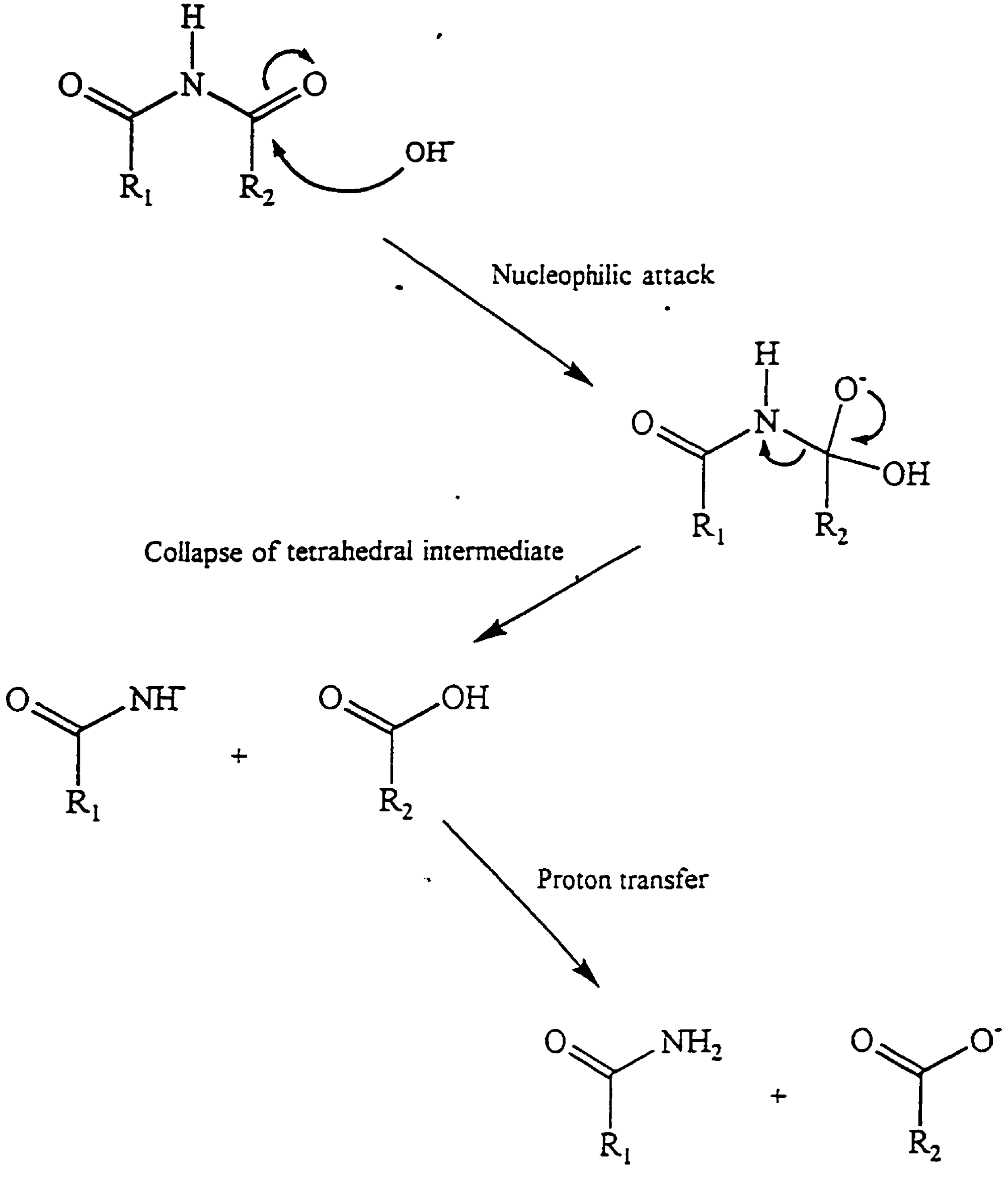

Figure 1.5. Mechanism of hydrolysis of imides.

presumably due to the distribution of the electron density of the nitrogen atom between two carbonyl groups, rather than one.

Each of the four hydrolysis reactions described in Figure 1.4 is hydroxide-ion-catalyzed [117]. At pH 7.4 and 37 °C, dexrazoxane disappears with a half-time of 9.3 h, and ADR-925 accumulates with a half-time of 28 h [117].

The pseudo-first-order rate constant of dexrazoxane hydrolysis increases sigmoidally with pH, and reaches a maximum at approximately pH 11 [117]. The inflection point of the sigmoidal curve occurs at approximately pH 9.6, corresponding to the pK_a of dexrazoxane, at which pH the protons are simultaneously lost from the two imide nitrogen atoms [117, 120]. The imide anion is much less reactive toward hydroxide ion, and may be considered unreactive below pH 13 [120]. Thus, the rate constant describing imide hydrolysis reaches a limiting value above its pK_a; as the concentration of one reactant, hydroxide ion, increases with pH, that of the other, the neutral imide, decreases. Both water and hydroxide ion are nucleophiles for the hydrolysis of dexrazoxane over the pH range of 7-13 [117, 120]. The resistance of the deprotonated species to nucleophilic attack is in agreement with kinetic studies of the hydrolysis of other imides, including maleimide [121] and succinimides [122, 123]. At pH 7.4 and 37 °C, k_{AB} is approximately twice k_{AC} [117]. Thus, two thirds of the hydrolysis of dexrazoxane proceeds *via* the intermediate **B**.

The enzyme, dihydropyrimidine amidohydrolase (DHPase, EC 3.5.2.2), catalyzes the hydrolysis of dexrazoxane to **B** and **C** (*i. e.* the reactions characterized by k_{AB} and k_{AC} in Figure 1.4) [124]. This enzyme is found in the liver and kidney, but not in the heart [125]. It has been shown that radioactivity from a dose of ^{14}C-dexrazoxane accumulates in the liver and kidney of dogs [126], which suggests that DHPase hydrolyzes dexrazoxane to **B** and **C**, which are trapped in these tissues due to their polarity. However, it may also be that these species, or others, accumulate in the extraction organs during elimination.

DHPase hydrolyzes dexrazoxane four times more quickly than its (*R*) enantiomer, ICRF-186 [124]. From these results, it may be predicted that dexrazoxane has a lower cardioprotective ability than ICRF-186, since its rate of activation *in vivo* may be lower. It may also be predicted to be more active, since hydrolysis in the liver and kidney would presumably limit the ability of the drug to reach the heart, its putative site of action. A study of the relative effects of dexrazoxane and ICRF-186 against doxorubicin cardiotoxicity in Syrian golden hamsters [127] demonstrated that these two drugs have approximately equal cardioprotective effects. A similar study with spontaneously hypertensive rats, however, demonstrated that, at doses approximately twice those recommended for clinical use, dexrazoxane was slightly more effective that ICRF-186. Thus, at present, whether the effect of enzymatic metabolism is significant *in vivo* is unknown.

Previous studies of the ability of dexrazoxane to remove Fe^{3+} from its complexes with doxorubicin demonstrated that displacement of the metal ion occurred much faster than expected [116]. From these studies, it was apparent that either complete hydrolysis of dexrazoxane to ADR-925 was not necessary for Fe^{3+} displacement, or that the Fe^{3+}-doxorubicin complex promoted the hydrolysis reactions, or both. In either case, the production of chelating species may be significantly faster *in vivo* than estimated. Until these studies were done, it was assumed that the half-time of hydrolysis-activation of dexrazoxane *in vivo* was equal to that measured at pH 7.4 and 37 °C; approximately 30 h [120, 128]. If the activation of dexrazoxane *in vivo* is significantly faster than that measured *in vitro*, the production of chelating species would be sufficient to make the hypothesis of cardioprotection by chelation more reasonable. Since the half-time of elimination of dexrazoxane from humans is 4.2 h [88], the previous estimate of the half-time for *in vivo* activation of 30 h would lead to the conclusion that a very small fraction of a dose of dexrazoxane is hydrolyzed before it is excreted. Thus, the importance of determining the *in vivo* activation rate is clearly important to the understanding of the mechanism of action of dexrazoxane.

1.10 Pharmacokinetic studies of dexrazoxane

Dexrazoxane undergoes base-promoted, first-order hydrolysis to the diacid diamide, ADR-925 (**D**), *via* one of two one-ring open hydrolysis intermediates, **B** or C (Figure 1.4) [117]. Each of the four hydrolysis reactions is catalyzed by hydroxide ion [117]. At pH 7.4 and 37 °C, dexrazoxane disappears with a half-time of approximately 10 h, and **D** accumulates with a half-time of approximately 30 h (Section 4.3) [128].

Hydrolysis of ICRF-159 and dexrazoxane occur at similar rates in the absence [128] and presence of BHK-21S [106] and HEp/2 [79] cells. It has been demonstrated, however, that liver and kidney homogenates contain an enzyme, dihydropyrimidine amidohydrolase (DHPase, EC 3.5.2.2), which catalyzes the first ring-opening reactions of dexrazoxane, producing **B** and **C** [125]. It has not been determined whether hydrolysis of dexrazoxane by DHPase occurs to a significant extent *in vivo*.

Direct observation of the hydrolysis products of dexrazoxane, **B**, **C**, and **D** in biological samples has proven difficult. They have low UV absorption, and are resistant to derivatization. Recently, the one-ring open hydrolysis intermediates, **B** and C, have been quantified in plasma by HPLC [129]. Studies using radioactive ICRF-159 and dexrazoxane have allowed the indirect quantitation of metabolites of dexrazoxane *in vivo*, which are likely to be its hydrolysis products, and they have been qualitatively observed by TLC [106].

The pharmacokinetics of ICRF-159 and dexrazoxane are similar in all species studied, including mice [130], rats [131], rabbits [132], dogs [130], monkeys [133], and humans [74, 100, 134-136]. In all cases, elimination from the bloodstream is described by a two-compartment open model, which describes biphasic kinetics:

$$[Dexrazoxane]_{plasma} = Ae^{-\alpha t} + Be^{-\beta t} \qquad (1.13)$$

in which α and β are the first-order rate constants describing the fast distribution of dexrazoxane from the blood into the tissues [74, 131, 132], and the slower elimination of dexrazoxane from the body [132], respectively. β, the rate constant describing the elimination phase, ranges from 0.16 to 0.5 h^{-1} in humans [100, 134, 136-138].

If it is assumed that dexrazoxane hydrolysis due to non-enzymatic processes is similar among all animals studied (*i. e.* the pH and available levels of relevant metal ions are similar), any observed differences in metabolism must reflect differences in the contributions of enzyme-catalyzed hydrolysis to the total elimination rate. The much larger values of β observed for small animals such as mice [139] and rats [132], must be due to enzymatic hydrolysis, possibly by DHPase. A pharmacokinetic study in rats [129] demonstrated a significant difference in the distribution phase between dexrazoxane and its enantiomer, ICRF-

186, which paralleled their relative hydrolysis rates by DHPase. Thus, it was concluded that DHPase-catalyzed hydrolysis affects the distribution rate of dexrazoxane in rats.

Since it is the hydrolysis product of dexrazoxane, ADR-925, which is thought to be the active species, the relative rates of these processes are critical in determining the fraction of a dose which is hydrolyzed before its elimination. Since 90% of an intravenous dose is recovered in the urine of rats [103] and mice [104], recovery of dexrazoxane in the urine can be used to determine its relative rates of metabolism and excretion. Human pharmacokinetic studies have determined that approximately 50% of a dose of dexrazoxane is excreted unchanged in the urine [134, 136]. Thus, half the dose is hydrolyzed, or otherwise metabolized, before its excretion, and the other half is excreted unchanged.

In four human pharmacokinetic studies [100, 134-136], values ranging from 0.17 to 0.36 h^{-1} were reported for the kinetic parameter, β. This parameter describes the disappearance of dexrazoxane from plasma, which may be due to excretion, hydrolysis, and other metabolism. It is possible that *in vivo* hydrolysis occurs at a faster rate than at pH 7.4 and 37 °C, under which conditions dexrazoxane is hydrolyzed to its one-ring open intermediates with a first-order rate constant of 0.074 h^{-1} [128]. Even so, it has been determined that half of a dose of dexrazoxane is excreted unchanged [74, 134-136]. Thus, an analog of dexrazoxane with a faster hydrolysis rate may be more active, since a larger fraction of the drug may be hydrolyzed to its active forms before excretion.

1.11 Protection against doxorubicin-induced cardiotoxicity by other agents

It is believed that the cardiotoxicity associated with the administration of doxorubicin is due to oxidative stress. A number of antioxidants have been investigated to evaluate their potential use as protective agents, as they may reduce the production of free radical species, or prevent them from irreversibly damaging the heart tissue.

The free radical scavenger, vitamin E, has been studied in animal [25, 92, 114] and clinical [140] models of doxorubicin-induced cardiotoxicity. An early study of the effects of tocopherol on doxorubicin toxicity in mice demonstrated that, when administered with tocopherol, the acute toxicity due to a single large dose of doxorubicin was attenuated [91]. However, studies of chronic cardiotoxicity due to repeated doses of doxorubicin, similar to those received clinically, demonstrated that vitamin E did not offer protection in mice [92], miniature swine [25, 114], rabbits [141], or humans [140]. In a number of these studies [25, 92, 114], cardiotoxicity was measured by mortality and histological screening.

N-acetylcysteine was also examined for the ability to reduce doxorubicin-induced toxicity. Like vitamin E, it is a free radical scavenger, and undergoes single-electron oxidation, to a relatively stable sulfur radical, and dimerization, which produces a disulfide bond. Chronic doxorubicin toxicity studies in dogs measured histologically detected abnormalities in the heart tissue, as well as hematological effects, including myelosuppression [113, 114]. Both studies revealed the protective effect of dexrazoxane, which was administered 30 min prior to doxorubicin in a 14:1 ratio. Similar administration of *N*-acetylcysteine in a 120:1 ratio, however, had no significant effect. It may be that the latter drug did not reach the site of damage, or that it was ineffective as a scavenger.

Probucol, a drug with lipid-lowering and antioxidant activities, was effective in preventing doxorubicin-induced congestive heart failure in rats [142]. Since doxorubicin causes increases in cholesterol, low- and high-density lipoproteins, and triglycerides in blood [143], the effects of probucol on lipid levels, as well as its antioxidant properties, may be responsible for the observed protection. Lovastatin, a lipid-lowering drug with no known antioxidant activity, protected against doxorubicin toxicity in rats, although not as well as probucol [143]; lovastatin had a smaller, but significant protective effect on heart function, myocardial lipid peroxidation, and plasma and cardiac lipids, but not on myocardial glutathione peroxidase levels. Thus, it was concluded that both the antioxidant and lipid-lowering activities of probucol are important in its mechanism of reduction of doxorubicin-induced cardiac damage, and that clinical trials of probucol are warranted, to determine whether the protection observed in the rat also occurs in humans.

Since dexrazoxane, which is thought to be the prodrug of a metal ion chelator, was an effective protective agent, other chelators have been studied. The abilities of desferrioxamine, EDTA, dexrazoxane, and three hydroxypyridones (bidentate Fe^{3+} chelators) to prevent acute doxorubicin toxicity were measured [144]. In this study, a decrease in contractile force of isolated mouse atria was observed on perfusion with 30 μM doxorubicin. Of the chelators investigated, only desferrioxamine and dexrazoxane attenuated this effect. In a rat model of acute doxorubicin toxicity, desferrioxamine, which is clinically used to reduce iron overload, reduced the damage detected by clinical chemistry tests and histological screens [145]. It cannot be assumed from this experiment that desferrioxamine will also have an effect on chronic toxicity, since the protection studies of vitamin E described above have demonstrated that acute and chronic toxicity are dependent on different factors.

1.12 Questions addressed in this work

It has been demonstrated that the product of complete hydrolysis of dexrazoxane, ADR-925, is able to remove Fe^{3+} from its complexes with doxorubicin. However, the possibility that the one-ring open hydrolysis intermediates, **B** and **C**, may act as chelators has not been investigated. A study of the Fe^{3+}-chelating abilities of these species, relative to the anthracyclines, doxorubicin, daunorubicin, epirubicin, and idarubicin, was undertaken in Chapter 2.

Although dexrazoxane has been accepted for use in Europe, Canada, and the United States as a protective agent against doxorubicin cardiotoxicity, little is known about either its mechanism of action or activation. Pharmacokinetic studies on human subjects [134, 136-139] followed only the disappearance of the parent drug, since the hydrolysis products are difficult to detect. Thus, the fates of the latter species in biological systems are unknown, including the rate of production of the final product, ADR-925, and the possible chelating ability of the one-ring open intermediates, **B** and **C**. In Chapters 3 and 4, studies of the hydrolysis-activation of dexrazoxane *in vitro* was undertaken, in the presence of metal ions which may accelerate its hydrolysis in biological systems.

It is hypothesized that dexrazoxane protects against doxorubicin-induced oxidative damage by hydrolyzing to the strong chelator, ADR-925. Thus, the relative rates of hydrolysis and elimination from the body are important in understanding the observed offects of dexrazoxane *in vivo*. The large doses of dexrazoxane administered in clinical trials [88] are consistent with the finding that much of the drug is excreted before it is hydrolyzed [134, 136-139]. If the effective dose can be reduced, the likelihood of adverse drug effects such as myelosuppression [100, 137] may be reduced also. If an analog hydrolyzes moderately faster than dexrazoxane, such that the rate of its activation allows a greater fraction to be hydrolysis-activated before it is eliminated, it may be more active, and it may be active at lower doses. A structure-activity study of analogs of dexrazoxane was undertaken in Chapter 5, with the objective of designing an analog of dexrazoxane with a faster hydrolysis rate.

Chapter 2 Chelating ability of the hydrolysis intermediates of dexrazoxane

2.1 Introduction

Clinical use of anthracyclines such as doxorubicin and daunorubicin results in irreversible cardiomyopathy, which limits the cumulative dose which can be administered [3]. This cardiac damage is thought to be due to production of oxygen radicals *via* iron-based Fenton chemistry [3, 8, 15, 43, 146]. Dexrazoxane has been shown to protect against doxorubicin-induced cardiotoxicity in a breast cancer clinical trial [88]. Dexrazoxane undergoes hydrolysis to **D**, which has both imide rings open, *via* one of two one-ring open intermediates, **B** or **C** (Figure 1.4) [128]. It is believed that protection by dexrazoxane is achieved through its hydrolysis to ADR-925 (**D**), which is a strong chelator [115], and has a structure similar to that of EDTA.

When displacement of Fe^{3+} from its anthracycline complexes by dexrazoxane was found to be faster than its hydrolysis to **D**, it was concluded that a direct reaction occurs between dexrazoxane and the Fe^{3+}-doxorubicin complex [101, 116]. Such a reaction may involve the direct displacement of doxorubicin from Fe^{3+} by dexrazoxane, or the acceleration of hydrolysis of dexrazoxane to **D**, which is a strong chelator. The ability of the three hydrolysis products of dexrazoxane, **B** and **C**, to remove Fe^{3+} from its anthracycline complexes has not previously been determined. It may be that these species are involved in the mechanism of displacement of Fe^{3+}. This study examines the reactions of dexrazoxane, **B**, **C**, and **D** with the Fe^{3+} complexes of doxorubicin, daunorubicin, epirubucin, and idarubicin (Figure 2.1). These anthracyclines were chosen for study due to their clinical relevance.

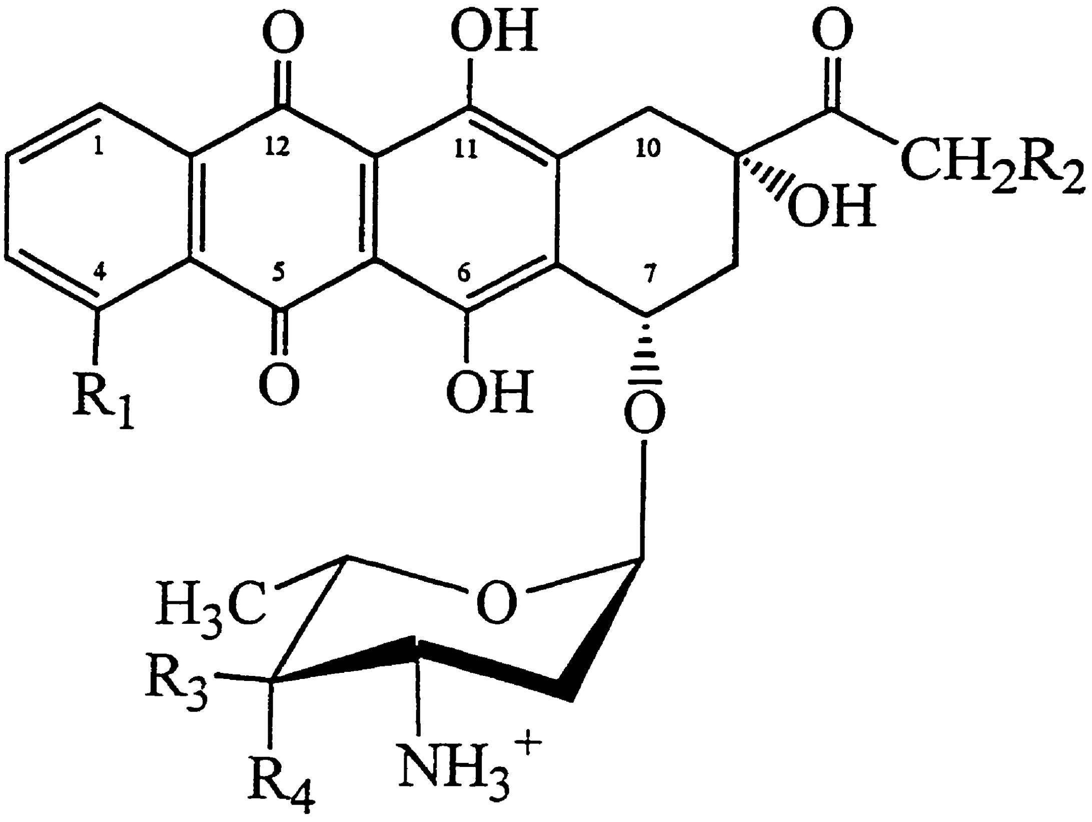

Anthracycline	R_1	R_2	R_3	R_4
Doxorubicin	$-OCH_3$	-OH	-H	-OH
Daunorubicin	$-OCH_3$	-H	-H	-OH
Epirubicin	$-OCH_3$	-OH	-OH	-H
Idarubicin	-H	-H	-H	-OH

Figure 2.1. Structures of the antitumor anthracyclines. Atom numbers are labelled.

2.2 Materials and methods

Dexrazoxane (ICRF-187), **D** (ADR-925), doxorubicin, epirubicin, and idarubicin were gifts from Adria Laboratories (Columbus, OH). Daunorubicin was a gift from Rhône-Poulenc Pharma (Montreal, Canada). $FeCl_3{\cdot}H_2O$ was from J. T. Baker Chemical Co. (Phillipsburg, NJ). Tris-HCl was from Sigma (St. Louis, MO). All other chemicals were of the highest grade available.

Concentrations of stock solutions of doxorubicin, daunorubicin, and epirubicin were determined spectrophotometrically. Their molar absorptivities in methanol are 12200, 12100, and 12200 M^{-1} cm^{-1}, at 480, 478, and 480 nm, respectively [147]. The stock solutions of idarubicin were prepared by weight. Fe^{3+}-anthracycline complexes were formed in a 1:3 ratio [3] by adding $FeCl_3$ in 1.5 mM HCl (to prevent precipitation of ferric hydroxides) to the anthracycline. Sodium azide solutions were titrated to pH 7.0 with HCl to prevent pH changes from affecting the equilibria among Fe^{3+} and the ligands. Stock solutions of dexrazoxane in water were prepared immediately before use, and were stored on ice until used. The concentration of Fe^{3+}-anthracycline was 15 μM in Fe^{3+} and 45 μM in anthracycline in all experiments, as in previous studies [101, 116], unless otherwise indicated. Since the ratio of Fe^{3+} to anthracycline is constant at 3:1, the concentration of this complex is described in the text by the concentration of Fe^{3+}.

The HPLC procedure for isolation of **B** and **C** was essentially as described by Burke *et al.* [148], using a Waters μBondapack C18 10 μm 3.9 x 300 mm reversed phase HPLC column with a Varian 9010 solvent delivery system, a Varian 9050 variable wavelength detector with a 8 mm path length cell, Varian Star Integrator software, and a Rheodyne injector with a 10 µL sample loop. A solution of partially hydrolyzed dexrazoxane was prepared by adding 40 µL of 1 M NaOH to 500 µL 5 mg/mL dexrazoxane, incubating it at 25 °C for 40 minutes, and quenching with 40 µL of 1 M HCl. This sample was stored at 4 °C until it was injected onto the HPLC column. Fractions of the one-ring open hydrolysis intermediates were separated with a 0-10 % linear methanol gradient over eight minutes [149] with 100 µM HCl in the aqueous mobile phase, collected in 600 µL aliquots, and pooled in 0.1 M HCl, to prevent further hydrolysis. As monitored spectrophotometrically, approximately the center 70% of each peak was collected. The purity of the collected fractions was high as determined by HPLC. Neither dexrazoxane nor **D** was identified in fractions of either **B** or **C**. Fractions of intermediate **B** contained 0.2 % **C**, while the fractions of **C** contained 1.1 % **B**. **B** and **C** were determined spectrophotometrically in 47 mM NaOH at 227 nm. Since **B** and **C** each have one intact imide ring, whereas dexrazoxane has two, their absorptions at 207 nm due to the imide functional group are expected to be half that of dexrazoxane. The molar absorptivities of **B** and **C** were therefore estimated to be half of 35,900 M^{-1} cm^{-1}, that of dexrazoxane under these conditions [117].

Spectrophotometric measurements were made on a Varian Cary 1 spectrophotometer at 25 °C, in cells of 1 cm path length. Polystyrene cells were used for all experiments involving anthracyclines, to minimize adsorption of the Fe^{3+}-anthracycline complexes to the cell walls. Reactions of the Fe^{3+}-anthracycline complexes were initiated by the addition of the complex to the reaction mixture. All experiments were carried out using a buffer of 50 mM Tris and 150 mM KCl (pH 7.40), except the titration of the Fe^{3+}-**B** complex with daunorubicin, which was done in 40 mM Tris (pH 7.40). Titration experiments were carried out by successive addition of aliquots of titrant. Absorbance data were corrected for volume changes. Determinations of k_{obs} for spectrophotometric data were made using Cary release 3 software from Varian (Mulgrave, Australia), and non-linear least squares curve fitting was done using Sigmaplot 5.0 from Jandel Scientific (San Rafael, CA).

Molecular modelling of the Fe^{3+} complexes of **B** and **C** was carried out using PCModel version 4.0 from Serena Software (Bloomington, IN) on a 486 IBM PC-compatible computer. This software uses the MMX force field, which is derived from the MM2 force field [150].

2.3 Displacement of Fe^{3+} from anthracyclines by dexrazoxane and its hydrolysis products

Previous experiments demonstrated that dexrazoxane can displace Fe^{3+} from its complex with doxorubicin [101, 116]. It is not known whether the reaction occurs through direct displacement, or through partial or complete hydrolysis followed by displacement. The final hydrolysis product, **D**, may not be the only species capable of removing Fe^{3+} from anthracycline complexes. At concentrations of dexrazoxane below 400 μM, the rates of displacement of 15 μM Fe^{3+} from its 3:1 complex with doxorubicin [116] exceed the rates at which dexrazoxane hydrolyzes to **D** under physiological conditions [128]. Since, at these concentrations, the rate of Fe^{3+} displacement is much faster than the rate of hydrolysis, either Fe^{3+} must accelerate the production of **D**, or complete hydrolysis is not necessary for effective Fe^{3+} displacement, or both. The displacement of Fe^{3+} from its anthracycline complexes by dexrazoxane and its hydrolysis products was studied.

Anthracyclines form complexes with Fe^{3+} in a ratio of 3:1 [19]. The formation and dissociation of these complexes can be observed spectrophotometrically, as there is a change in the absorbance spectra of the anthracyclines when they bind Fe^{3+}. Spectra of 45 µM daunorubicin and 15 µM Fe^{3+}-daunorubicin are shown in Figure 2.2. From similar spectra, the changes in molar absorptivity at 600 nm for the binding of anthracyclines to Fe^{3+} were determined (Table 2.1).

Table 2.1. Change in molar absorptivity of anthracyclines on binding Fe^{3+}.

Anthracycline	A_{600} 15 µM Fe^{3+} + 45 µM anthracycline	A_{600} 45 µM anthracycline	ΔA_{600}	$\Delta \varepsilon_{600}$ (M^{-1} cm^{-1})
Doxorubicin	0.1383	0.0034	0.1349	3000
Daunorubicin	0.1454	0.0043	0.1411	3140
Epirubicin	0.1422	0.0061	0.1361	3020
Idarubicin	0.1582	0.0029	0.1553	3450

The displacement of Fe^{3+} from anthracyclines by dexrazoxane was followed by recording spectra every six h for 60 h following the addition of dexrazoxane to the reaction mixture. These repeat spectra showed differences in the rates of displacement of Fe^{3+} from each anthracycline. Data for daunorubicin are shown in Figure 2.3a. The total absorbance changes observed at 600 nm were consistent with those observed for nearly complete displacement of Fe^{3+} from anthracyclines (Table 2.1). Absorbance spectra of this solution with

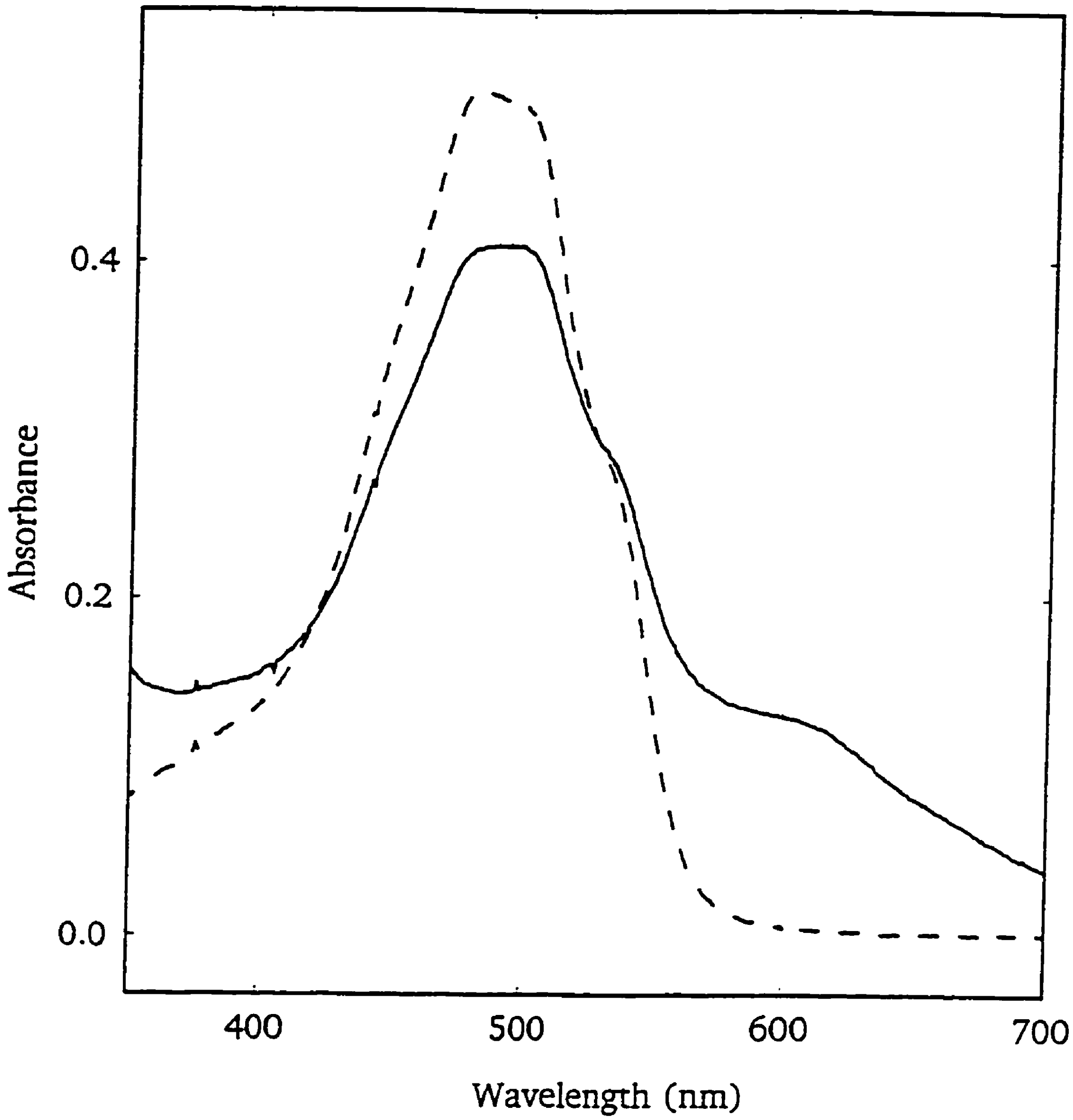

Figure 2.2. Spectra of daunorubicin and Fe^{3+}-daunorubicin. Spectra were recorded in 50 mM Tris (pH 7.40) and 150 mM KCl, at 37 °C. The curves represent the absorbance spectra of 45 μM daunorubicin (solid line) and 15/45 μM Fe^{3+}-daunorubicin (dashed line).

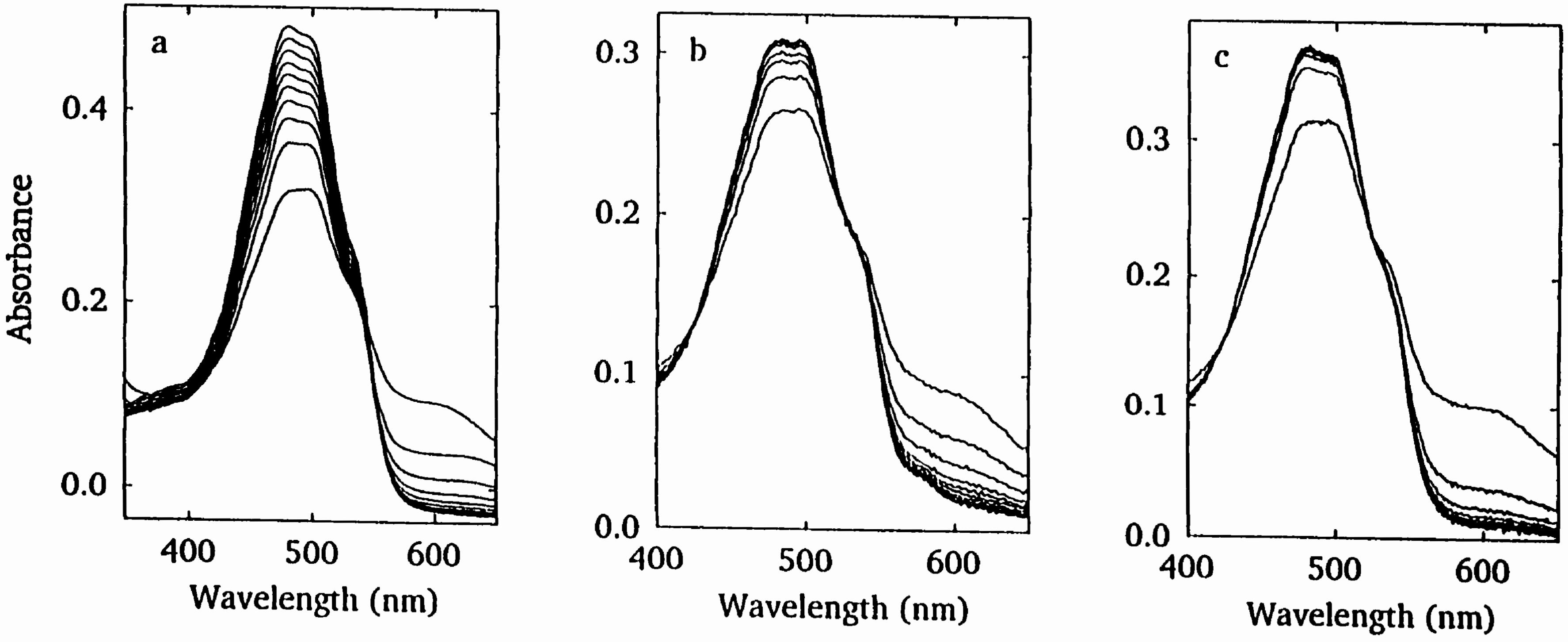

Figure 2.3. Spectral scans demonstrating the decrease in absorbance at 600 nm, corresponding to displacement of Fe^{3+} from its daunorubicin complexes at 37 °C were recorded in 50 mM Tris (pH 7.40), 150 mM KCl by dexrazoxane and its hydrolysis products. (a) Addition of 100 μM dexrazoxane to 15 μM Fe^{3+}-(daunorubicin)$_3$. Spectra were recorded every 6 h for 60 h. (b) Addition of 45 μM **B** to 10 μM Fe^{3+}-(daunorubicin)$_3$. Spectra were recorded every 2.8 min for 30 min. (c) Addition of 100 μM **D** to 15 μM Fe^{3+}-(daunorubicin)$_3$. Spectra were recorded every 1.6 min for 15 min.

daunorubicin, recorded at fixed time intervals, exhibit two clearly defined isosbestic points at 418 and 528 nm. This may indicate that there are no reaction intermediates present which contribute to the total absorbance. It is also possible, however, that there are intermediates which absorb in this range with spectra similar to those of daunorubicin or Fe^{3+}-(daunorubicin)$_3$. Fe^{3+} with one or two anthracyclines bound are likely intermediates, and may have spectra which are similar to those of Fe^{3+}-(anthracycline)$_3$. Reactions of dexrazoxane with Fe^{3+} complexes of doxorubicin, epirubicin, and idarubicin produced similar spectral changes. Spectral changes were recorded every 2.8 minutes for 30 minutes of the displacement of Fe^{3+} from its anthracycline complexes by **B** (Figure 2.3b) and every 1.6 minutes for 15 minutes of the same displacement reaction by **D** (Figure 2.3c). These spectra were similar to those of dexrazoxane, with isosbestic points at similar wavelengths. **B**, **C**, and **D** displaced Fe^{3+} from its anthracycline complexes much faster than dexrazoxane. Thus, all the hydrolysis products of dexrazoxane are effective chelators, since they rapidly displace Fe^{3+} from anthracyclines.

Dexrazoxane and its hydrolysis products displaced nearly all the Fe^{3+} from its anthracycline complexes; at the end of the reactions, the spectra resembled those of the free anthracyclines (Figure 2.3 for daunorubicin). The observed decreases in absorbance at 600 nm for dexrazoxane, **C**, and **D** (Figure 2.4a,b,c, respectively) were fitted to a non-linear least squares three-parameter exponential decay equation:

$$A = A_\infty + (A_0 - A_\infty)\, e^{-k_{obs} t} \qquad (2.1)$$

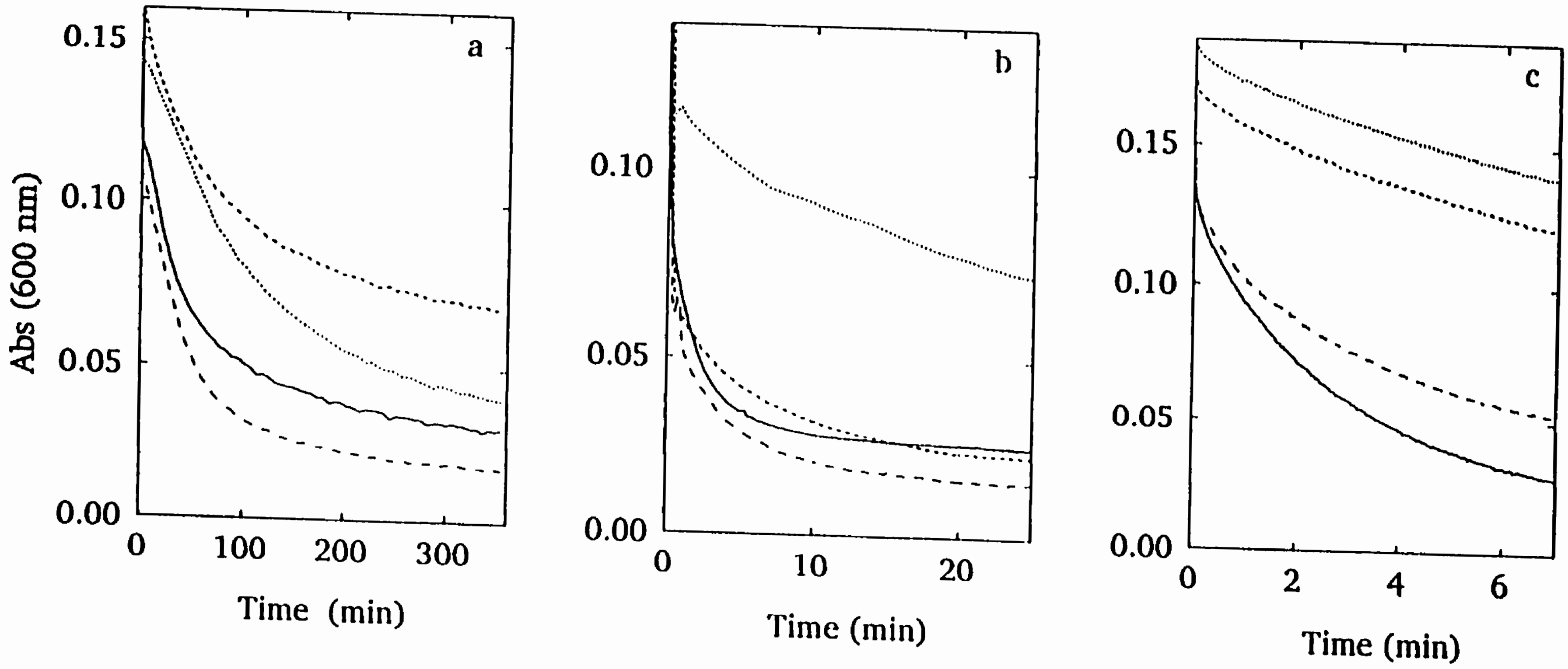

Figure 2.4. Absorbance changes for the reactions of dexrazoxane and its hydrolysis products with Fe^{3+}-anthracycline complexes. Absorbance data were recorded at 600 nm as a function of time. (a) 15 μM Fe^{3+}-(anthracycline)$_3$ with 500 μM dexrazoxane. (b) 10 μM Fe^{3+}-(anthracycline)$_3$ with 71 μM C. (c) 15 μM Fe^{3+}-(anthracycline)$_3$ with 50 μM D. Legend: daunorubicin (—), doxorubicin (---); epirubicin (- - -); idarubicin (……).

in which t is the time in minutes, k_{obs} is the observed pseudo-first-order rate constant, and A_0 and A_∞ are the absorbances at time zero and infinity, respectively. The first 10% of the reaction of dexrazoxane was ignored as it was not first order. This may be due to the presence of small amounts of **B** and C, which react much more quickly, or to adsorption of anthracycline to the cell walls. Absorbance-time data for the reaction of 500 μM dexrazoxane and 15 μM Fe^{3+}-daunorubicin are shown in Figure 2.5a, along with its fitted curve. The residual plot for these data is shown in Figure 2.5b.

To determine the extent of these displacement reactions by dexrazoxane and its hydrolysis products, 100 μM diethylenetriaminetetraacetic acid (DTPA), a strong chelator of Fe^{3+}, was added to the reaction mixtures once the absorbances of the solutions had levelled off, indicated by the absence of any further absorbance changes. DTPA has a formation constant of $10^{28.6}$ M^{-1} for Fe^{3+} [151] ; being a much stronger chelator than **B**, **C**, or **D**, should displace any anthracycline which remained bound to Fe^{3+}. Absorbance of the solutions following addition of DTPA therefore corresponded to 100% displacement of the anthracycline from Fe^{3+}. These measurements were made after incubation of the solutions with DTPA for 60 min for daunorubicin and doxorubicin, and 120 min for epirubicin and idarubicin, which were displaced more slowly than daunorubicin and doxorubicin (Figure 2.4). The displacement of Fe^{3+} by dexrazoxane, **B**, **C**, and **D** was similar, regardless of the anthracycline ligand. The average extents of the displacement of Fe^{3+} by dexrazoxane and its hydrolysis products from all four anthracycline complexes are listed in Table 2.2.

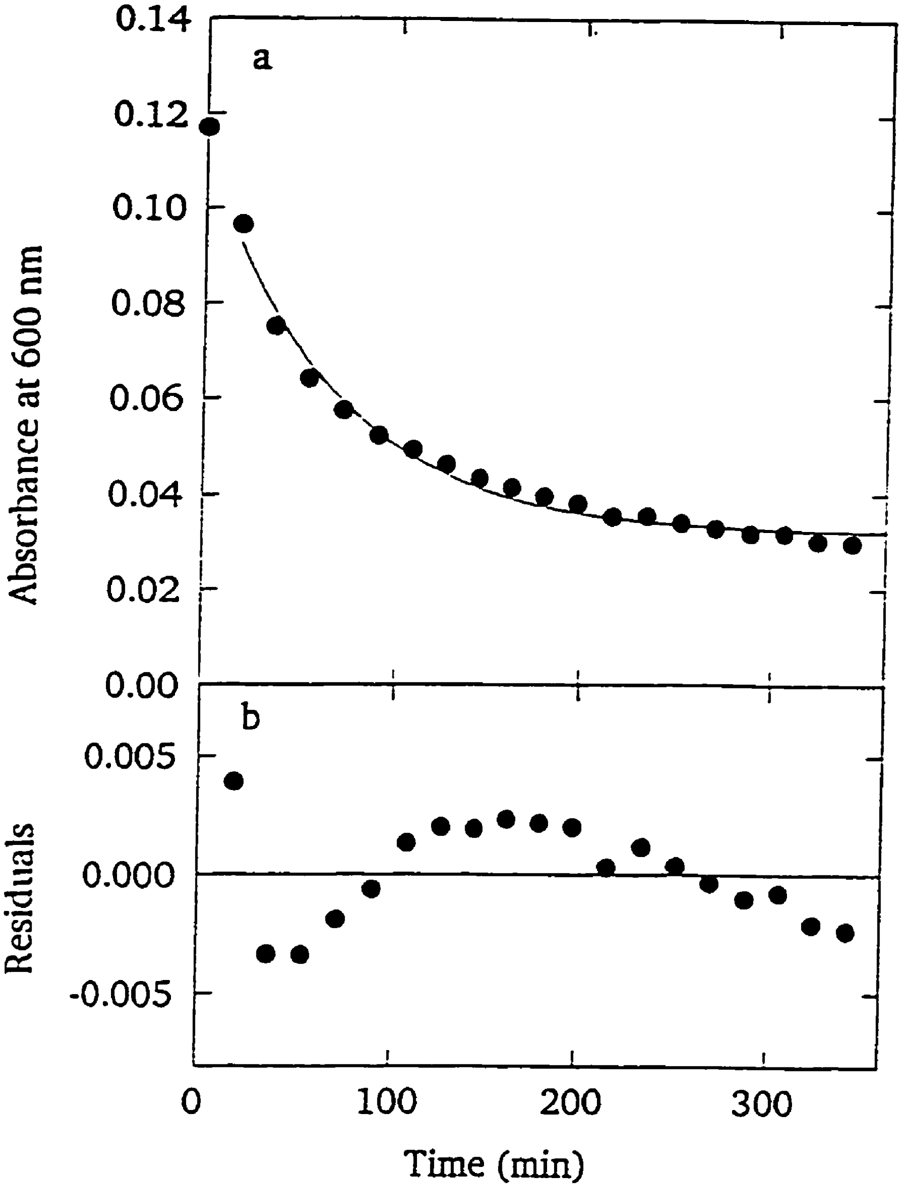

Figure 2.5. First order curve fits to absorbance data of the reaction of dexrazoxane with Fe^{3+}-(daunorubicin)$_3$. (a) Absorbance change at 600 nm, relative to the absorbance of free anthracycline, of 15 μM Fe^{3+}-(daunorubicin)$_3$ and 500 μM dexrazoxane (solid circles) and curve fit to Equation 2.1 (solid line). (b) Residual plot of this data.

Table 2.2. Extent of displacement of Fe^{3+} from anthracycline complexes by dexrazoxane and its hydrolysis products

Species	% Fe^{3+} Displacement[a]	n[b]	Range (%)
Dexrazoxane	97.6 ± 1.6	8	93-105
B	89.7 ± 1.1	8	83-95
C	92.0 ± 0.7	8	89-95
D	96.4 ± 0.5	7	95-98

[a] Errors cited are standard errors of the mean.
[b] Number of observations.

Reactions of Fe^{3+}-anthracycline complexes with **B** and **C** did not proceed to the same extent as did the reactions with dexrazoxane (Table 2.2). This may indicate weaker affinity of **B** and **C** for Fe^{3+}, or perhaps, since the reaction was followed over a much shorter time, the reaction may not have achieved equilibrium.

The pseudo-first-order rate constant, k_{obs}, of the displacement of Fe^{3+} from its anthracycline complexes by dexrazoxane increased with the dexrazoxane concentration (Figure 2.6a), and approached limiting values at high dexrazoxane concentration. For descriptive purposes only, these data were fitted, by a non-linear least squares method, to an equation of the form

$$k_{obs} = \frac{k_{lim}\,[L]}{K + [L]} \qquad (2.2)$$

in which k_{lim} is the rate constant at an infinite dexrazoxane concentration, [L] is the dexrazoxane concentration, and K is the concentration of dexrazoxane which yields a pseudo-

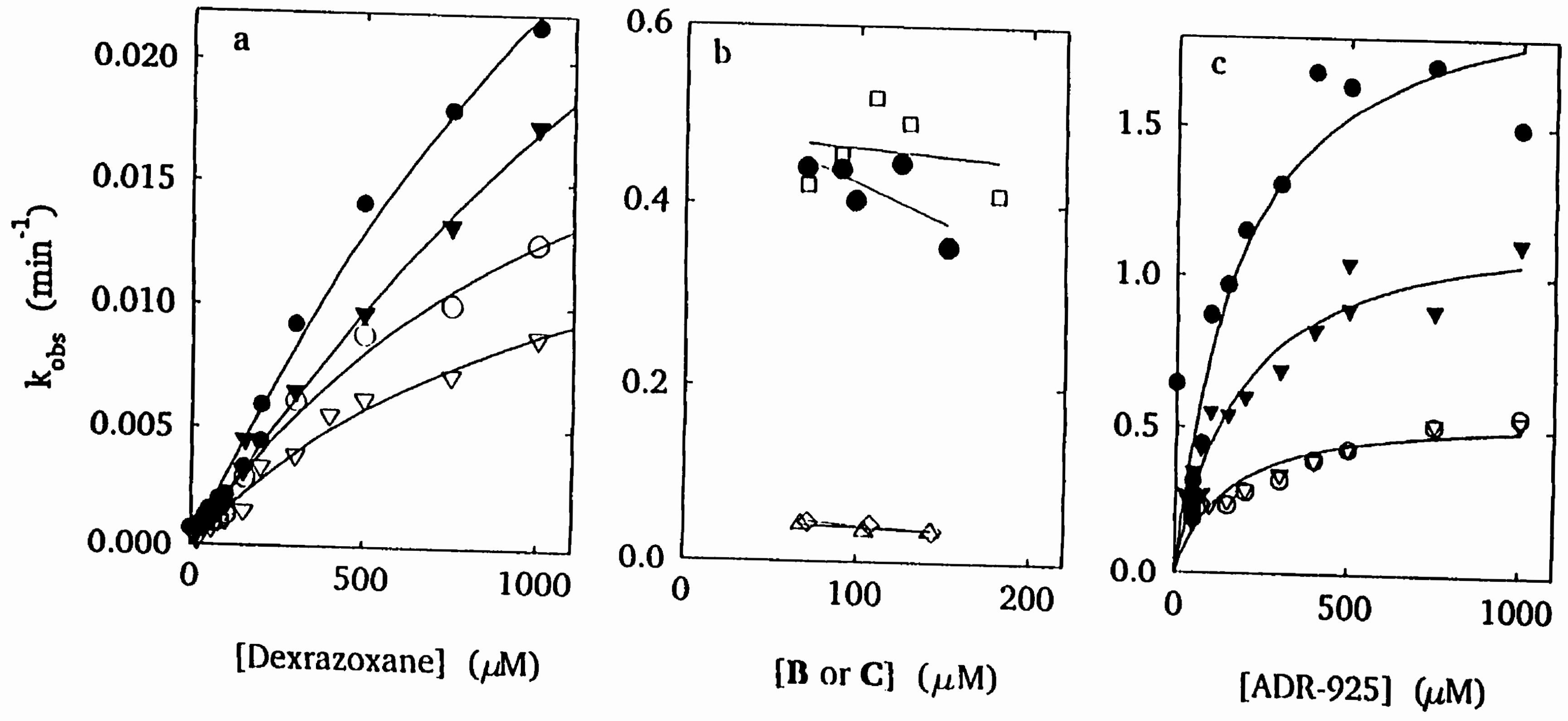

Figure 2.6. Dependence of k_{obs} for the displacement of anthracyclines from their Fe^{3+} complexes on the concentration of dexrazoxane and its hydrolysis products, **B**, **C**, and **D**. (a & c) Solid lines are the curve fits from Equation 2.2. Legend: daunorubicin (●); doxorubicin (▼); epirubicin (○); idarubicin (▽). (b) Solid lines are least squares linear fits. Legend: daunorubicin + **B** (●); daunorubicin + **C** (□); idarubicin + **B** (△); idarubicin + **C** (◇). Data for doxorubicin and epirubicin are not shown.

first-order rate constant of half its maximum value. The rate constants describing the reactions of **D** also demonstrated saturation behaviour at high concentrations (Figure 2.6c). Although the data are described by a saturation equation, it can not be concluded that the mechanism of this reaction involves a rapid pre-equilibrium, followed by displacement of Fe^{3+}, since it is unknown whether the reactions involve contributions from more than one mechanism. The values of k_{obs} and K obtained from Equation 2.2 are listed in Table 2.3.

Table 2.3. Kinetic parameters for the reactions of dexrazoxane and its hydrolysis products with Fe^{3+}-anthracyclines.

Reaction System		K (μM)	k_{lim} [a] (min^{-1})	k_{lim}/K (M^{-1} min^{-1})	$t_{1/2}$ [b] (min)
Dexrazoxane	Daunorubicin	3020	0.069	22.8	230
	Doxorubicin	2340	0.074	31.4	315
	Epirubicin	1200	0.028	22.9	327
	Idarubicin	1140	0.019	16.7	453
B	Daunorubicin	--	0.416	--	1.7
	Doxorubicin	--	0.319	--	2.2
	Epirubicin	--	0.211	--	3.3
	Idarubicin	--	0.039	--	17.8
C	Daunorubicin	--	0.459	--	1.5
	Doxorubicin	--	0.278	--	2.5
	Epirubicin	--	0.177	--	3.9
	Idarubicin	--	0.042	--	16.7
D	Daunorubicin	181	2.09	11 500	0.9
	Doxorubicin	178	1.23	6 900	1.6
	Epirubicin	147	0.57	3 900	3.0
	Idarubicin	142	0.56	4 000	3.0

[a] Reactions of **B** and **C** were not concentration dependent; k_{lim} are averages of two measurements.

[b] Calculated from Equation 2.2 at 100 μM.

The reactions of the one-ring open hydrolysis intermediates, **B** and **C**, with Fe^{3+}-anthracycline complexes were not concentration dependent over the experimentally accessible range (Figure 2.6b). The maximum concentration of the stock solutions of **B** and **C**, which were obtained by HPLC, was approximately 250 μM.

Displacement of Fe^{3+} from its anthracycline complexes was also dependent on the anthracycline. In the presence of dexrazoxane and its hydrolysis products, the rate constants for Fe^{3+} displacement by dexrazoxane and its hydrolysis products followed a general trend: idarubicin < epirubicin < doxorubicin < daunorubicin (Figure 2.6, Table 2.3). The anthracycline molecules investigated are sterically and electronically similar (Figure 2.1), and the differences in their rates of reaction, especially at the low concentrations of interest for biological systems, are not large. The fact that the anthracyclines react at different rates indicates that there is some contribution to the overall reaction by one or more steps in which anthracyclines dissociate from Fe^{3+}. Idarubicin is electronically different from the other anthracyclines examined due to the absence of the methoxy group (Figure 2.1). That it reacted significantly more slowly than the other anthracyclines was unexpected, as the methoxy group is expected to conjugatively release electron density into the aromatic ring system. The decrease in overall electron density due to its absence should decrease the electron density on the quinone-hydroquinone oxygen atoms, which are involved in chelation of the metal ion. Thus, idarubicin is expected to have a reduced ability to chelate, and, therefore, may be displaced faster by competing ligands. A small difference in structure may easily shift the equilibrium of an initial binding step, causing the observed differences in reaction rate.

The stepwise formation constants of Fe^{3+}-(doxorubicin)$_3$ are 10^{18}, 10^{11}, and $10^{4.4}$ M^{-1} [19]. At the low total concentrations used in these experiments, both Fe^{3+}-(doxorubicin)$_2$ and Fe^{3+}-(doxorubicin)$_3$ are present in significant amounts. If dexrazoxane and its hydrolysis products react preferentially with Fe^{3+}-(anthracycline)$_2$, as expected from steric and electronic factors, the overall reaction rate may be affected by the concentration of this species. Once an initial complex is formed between Fe^{3+}-doxorubicin and the incoming ligand, the remaining anthracyclines may be rapidly displaced. Since the values of k_{lim} are different for each anthracycline (Table 2.3), the dissociation of anthracycline from the complex affects the overall rate of Fe^{3+} displacement by dexrazoxane and its hydrolysis products.

That the displacement of Fe^{3+} from anthracyclines by **B** and **C** is not concentration-dependent over the experimentally accessible range can not be explained by stronger binding of Fe^{3+}. The lack of concentration dependence of these reactions over the range studied may be due to a strongly bound initial complex which is quickly formed, followed by one or more rate-determining steps to displace all three anthracyclines. The displacement reaction could begin with an outer sphere association between the positively charged Fe^{3+}-anthracycline complex and a negatively charged one-ring open intermediate, followed by a rate-determining step involving the dissociation of one anthracycline.

Although it has been demonstrated that dexrazoxane and all of its hydrolysis products displace Fe^{3+} from anthracyclines, it is not known whether they do so by direct displacement or by hydrolysis followed by displacement. The final hydrolysis product, **D**, may not be the only species capable of removing Fe^{3+} from anthracycline complexes. The half-time for the displacement of 15 μM Fe^{3+}-doxorubicin by 100 μM dexrazoxane is 5.25 h (Table 2.3). The half-time for the production of **D** under physiological conditions is 28 h [128]. Since Fe^{3+} displacement by dexrazoxane is much faster than its hydrolysis, either Fe^{3+} must accelerate the production of **D**, or complete hydrolysis is not necessary for effective Fe^{3+} displacement, or both. The data from the preceding experiments are consistent with either of these possibilities.

The chelating ability of the one-ring open intermediates does not account for the rate of Fe^{3+} displacement from doxorubicin by dexrazoxane. The half-time for displacement of Fe^{3+} from doxorubicin by **B** or **C** is approximately 2.4 min (Table 2.3), much faster than hydrolysis of these species to **D** (17 and 8 h for **B** and **C**, respectively [128]). This may be due either to direct displacement, or to acceleration of the hydrolysis of the one-ring open intermediates to **D**, which then chelate Fe^{3+}. Since the half-time for production of **B** and **C** is 9.3 h [128], the minimum half-time for displacement of Fe^{3+} from doxorubicin is also 9.3 h. Thus, either dexrazoxane directly displaces Fe^{3+} from doxorubicin, or its hydrolysis to **B** and **C** is accelerated in the presence of Fe^{3+}-doxorubicin, or both. The possibility of metal ion catalysis of dexrazoxane hydrolysis is investigated in the following two chapters.

Previous studies [101, 116] have also demonstrated that dexrazoxane removes Fe^{3+} faster than it hydrolyzes to **D**. In both these studies, a direct reaction between dexrazoxane and Fe^{3+}-doxorubicin was proposed.

2.4 Direct reaction between dexrazoxane and Fe^{3+}-daunorubicin

An experiment was designed to determine whether dexrazoxane interacts directly with Fe^{3+}-anthracycline complexes. Daunorubicin was chosen for this reaction as it self-reduces far more slowly than does doxorubicin [17]; redox behaviour complicates the absorbance data, due to absorbance changes due to the products of self-reduction. In the control cell, dexrazoxane and Fe^{3+}-daunorubicin were incubated. In the experimental cell, dexrazoxane was incubated alone. After two hours, the contents of the experimental cell were mixed with Fe^{3+}-daunorubicin, and both reactions were allowed to proceed for another hour. The absorbance of both cells at 600 nm was recorded throughout.

As expected, there was a direct reaction between dexrazoxane and Fe^{3+}-daunorubicin, and more daunorubicin was displaced in the control cell than in the experimental cell after three hours total incubation time, and the absorbance of the control cell was lower than that of the experimental cell (Figure 2.7). The absorbance of the control cell decreased gradually, corresponding to displacement of Fe^{3+}. The absorbance of the experimental cell is constant until the addition of the partially hydrolyzed dexrazoxane solution at two hours. The drop in absorbance corresponds to the rapid displacement of daunorubicin by the **B** and **C** produced during the pre-incubation phase. The reaction in the experimental cell had reached to 21 ± 1% (n = 3) displacement, while that of the control cell had reached 55 ± 1% (n = 3) displacement of the total Fe^{3+}. Errors cited are standard errors of the mean. Thus, approximately two thirds of the reaction proceeded by a direct interaction between dexrazoxane and Fe^{3+}-daunorubicin. Whether the interaction is direct displacement of daunorubicin or acceleration of hydrolysis of dexrazoxane by the complex is unknown, although a similar reaction is known to occur with Cu^{2+}, presumably through a metal ion bound hydroxide ion nucleophile [152, 153]. Thus, the k_{lim} and K for dexrazoxane (Table 2.3) are composite quantities, representing the

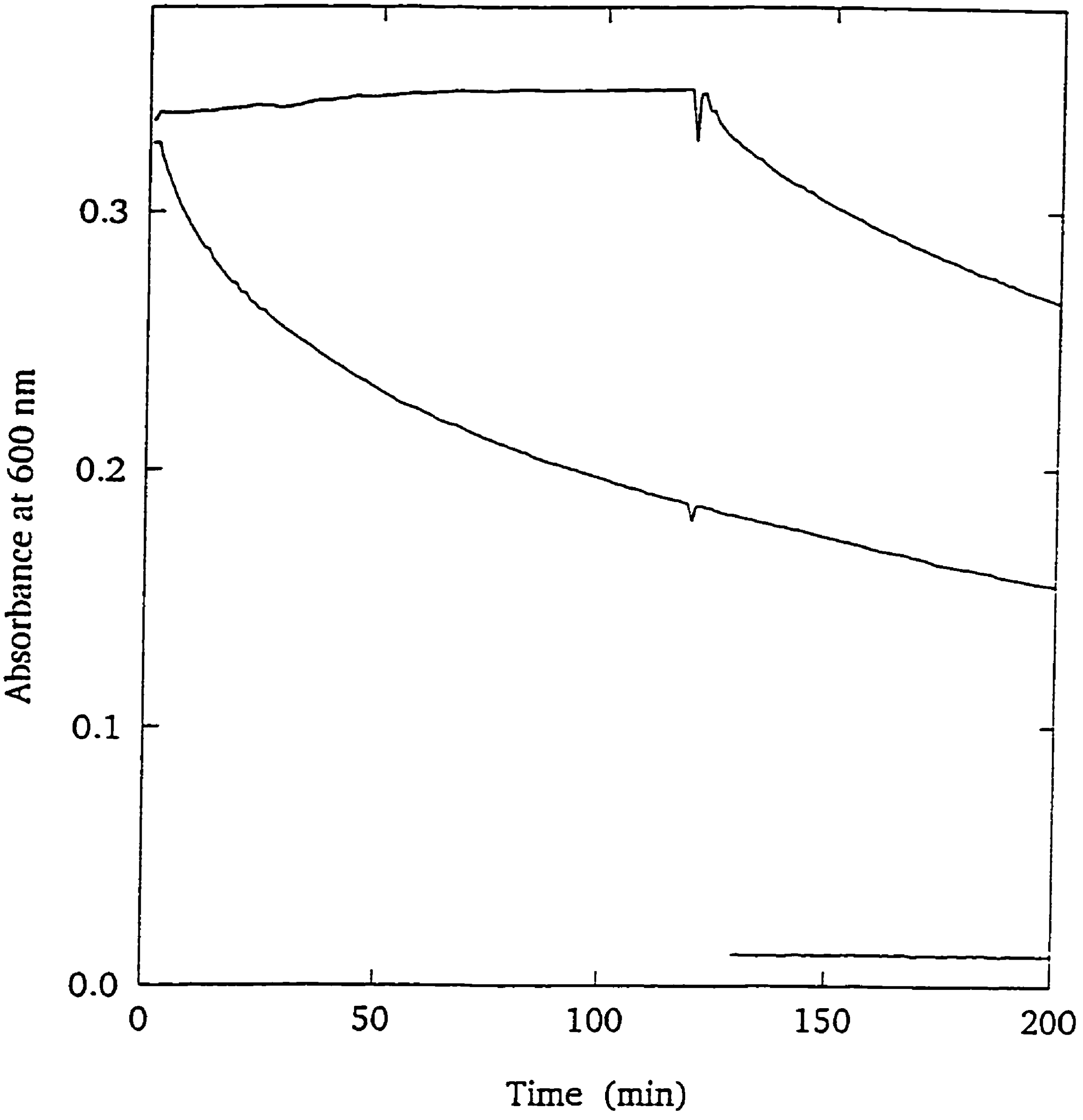

Figure 2.7. Direct reaction of dexrazoxane with Fe^{3+}-daunorubicin. Data were collected at 600 nm. Control (middle trace): 200 μM dexrazoxane incubated with 30 μM Fe^{3+}-daunorubicin$_3$ for 180 min. Experiment (upper trace): 30 μM Fe^{3+}-daunorubicin$_3$. At 120 min, 200 μM dexrazoxane which had been pre-incubated under identical conditions was added. The reaction was followed for an additional 60 min. The bottom trace corresponds to 90 μM free daunorubicin (*i. e.* complete reaction).

contributions of at least two pathways of iron displacement. Three possible pathways of displacement of Fe^{3+} by dexrazoxane are shown in Figure 2.8.

2.5 The complex between Fe^{3+} and the one-ring open hydrolysis intermediates of dexrazoxane

2.5.1 Azide titration of Fe^{3+}-B

The ability of Fe^{3+} complexes to produce hydroxyl radicals is correlated to the presence of free or loosely bound binding sites on these complexes to N_3^- ion [154]. It is assumed that if azide ion competitively displaces chelator functional groups, water may do so also. In the presence of reducing agents, the complex may redox cycle. Titrations of Fe^{3+}-**B** and Fe^{3+}-**D** with sodium azide will indicate whether these complexes have binding sites which are able to produce hydroxyl radicals *via* the Fenton reaction (Reaction 1.3).

An absorbance change between 300 and 450 nm is observed as free azide ion binds Fe^{3+}-EDTA [154]. Titration of the Fe^{3+}-**B** and Fe^{3+}-**D** complexes with azide likewise produced spectral changes consistent with the formation of a ternary complex with azide ion. These results demonstrate co-ordination positions available to monodentate ligands. The spectra of Figure 2.9a&b were corrected for the absorbance of free azide ion and volume changes, and adjusted to an absorbance at 900 nm of zero, a wavelength at which none of the species produced absorbs. Data at 453 nm (Figure 2.9c) were extracted from the spectral data.

These data can not be interpreted quantitatively, due to the changes in ionic strength over the azide concentration range used (0 - 1.9 M), and there is little evidence of saturation of the available binding sites for either the **B** or the **D** complex. The isosbestic point observed

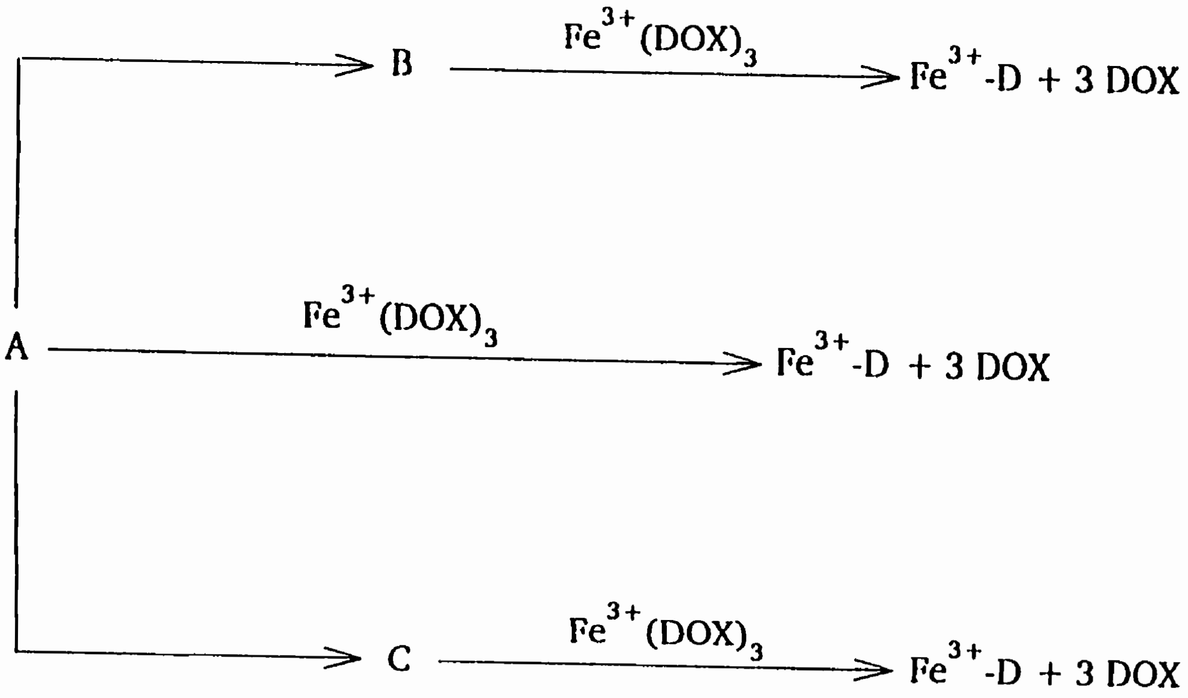

Figure 2.8. Proposed reaction scheme for the displacement of Fe^{3+} from its doxorubicin complex by dexrazoxane. Displacement occurs through a direct reaction with dexrazoxane (A), or through the hydrolysis of dexrazoxane to its one-ring open hydrolysis intermediates, B and C. The reactions of all these species with Fe^{3+}-doxorubicin$_3$ are complex, and likely proceed *via* several intermediates before the final products are obtained.

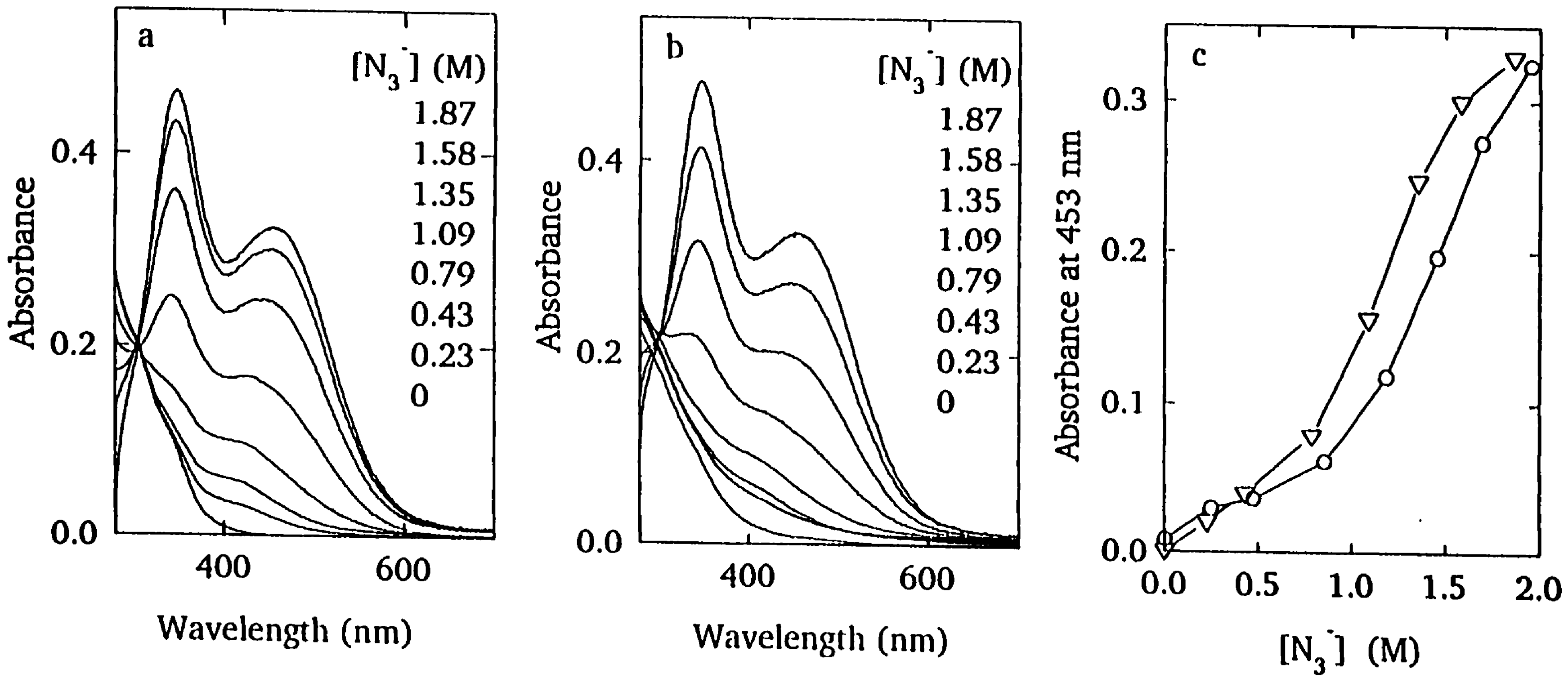

Figure 2.9. Formation of an N_3^- ternary complex with Fe^{3+}-**B** and Fe^{3+}-**D**. (a) Spectra showing the decrease in absorbance observed on addition of NaN_3 to 60 μM preformed Fe^{3+}-**D** at 25 °C in 50 mM Tris (pH 7.40) and 150 mM KCl. (b) Spectra showing the decrease in absorbance observed on addition of NaN_3 to 60 μM preformed Fe^{3+}-**B**. (c) Absorbance changes at 453 nm. Legend: Fe^{3+}-**D** (▽); Fe^{3+}-**B** (○). All data have been corrected for absorbance due to NaN_3.

near 300 nm indicates that there may be only two absorbing species (*i. e.* the Fe^{3+} complex and the N_3^--bound complex). However, this is not distinguishable from a case with many absorbing species which have similar spectra. It is possible that more than one azide ion binds the complex, since it is likely that the spectra of complexes with one and two N_3^- bound are similar.

The binding sites available to azide ion may ordinarily be occupied by water or atoms of the polydentate ligands. The Fe^{3+}-**D** complex may therefore be hexacoordinate, as is Cu^{2+}-ICRF-198 [155], or heptacoordinate, as is Fe^{3+}-EDTA [156].

Since the presence of binding sites available to N_3^- indicates hydroxyl radical producing ability [154], both Fe^{3+}-**B** and Fe^{3+}-**D** are expected to produce hydroxyl radicals. This is consistent with EPR spin-trapping results obtained with Fe^{2+}-**D** [157]. In these experiments, similar quantities of hydroxyl radical were trapped by 5,5-dimethyl-1-pyrroline-*N*-oxide when either Fe^{3+}-EDTA or Fe^{3+}-**D** was added to Tris buffer at 37 °C, in the presence and absence of hydrogen peroxide.

2.5.2 Molecular modelling of Fe^{3+}-C

ICRF-198, the racemate of **D**, is a hexadentate ligand, capable of chelating Cu^{2+} in an octahedral conformation through its carboxylate oxygen atoms, amide oxygen atoms, and main chain nitrogen atoms [155]. The x-ray structure of this complex was used as a starting point for the modelling of the Fe^{3+}-**D** complex. The radius of the Fe^{3+} ion was set at 1.53 Å, which resulted in Fe^{3+}-N and Fe^{3+}-O bond distances comparable to those found in Fe^{3+}-EDTA [156]. Covalent bonding was used to model the coordination of **D** to Fe^{3+}. The structure was minimized using PCModel (Figure 2.10). To model Fe^{3+}-**B**, bonds between Fe^{3+} and **D** were broken to close one of the imide rings, atoms of the imide functional group were designated as pi atoms, and the resulting tetradentate structure was minimized. To investigate the possibility that the model was strained, a tridentate model was produced by breaking the bond between Fe^{3+} and the piperazine ring nitrogen atom. Since the bond lengths and angles of the remaining atoms were not significantly altered by this change, it is unlikely that the association of this atom causes steric strain on the others. It was not possible to form any further Fe^{3+}-ligand bonds without disrupting the planarity of the imide functional group. Thus, only tetradentate models were further considered. Since Fe^{3+} prefers octahedral co-ordination, the two remaining positions were occupied by water.

The energies of various conformations of Fe^{3+}-**B** were compared. Conformations with the imide ring oriented such that the bond between the main chain nitrogen atom and Fe^{3+} was pseudoaxial were more stable than those with a pseudoequatorial conformation. Conformations in which the amide and carboxylate oxygen were *cis* were more stable than the corresponding *trans* conformations. The most stable conformation is shown in Figure 2.11. Fe^{3+}-**C** is similarly capable of chelating iron.

2.5.3 Titration of Fe^{3+}-B with daunorubicin

The tetradentate model of Fe^{3+}-**B** proposed above leaves two co-ordination positions which may be available for binding to water or anthracyclines. Fe^{3+}-**B** was titrated with daunorubicin to determine whether a ternary complex Fe^{3+}-**B**-daunorubicin could be formed.

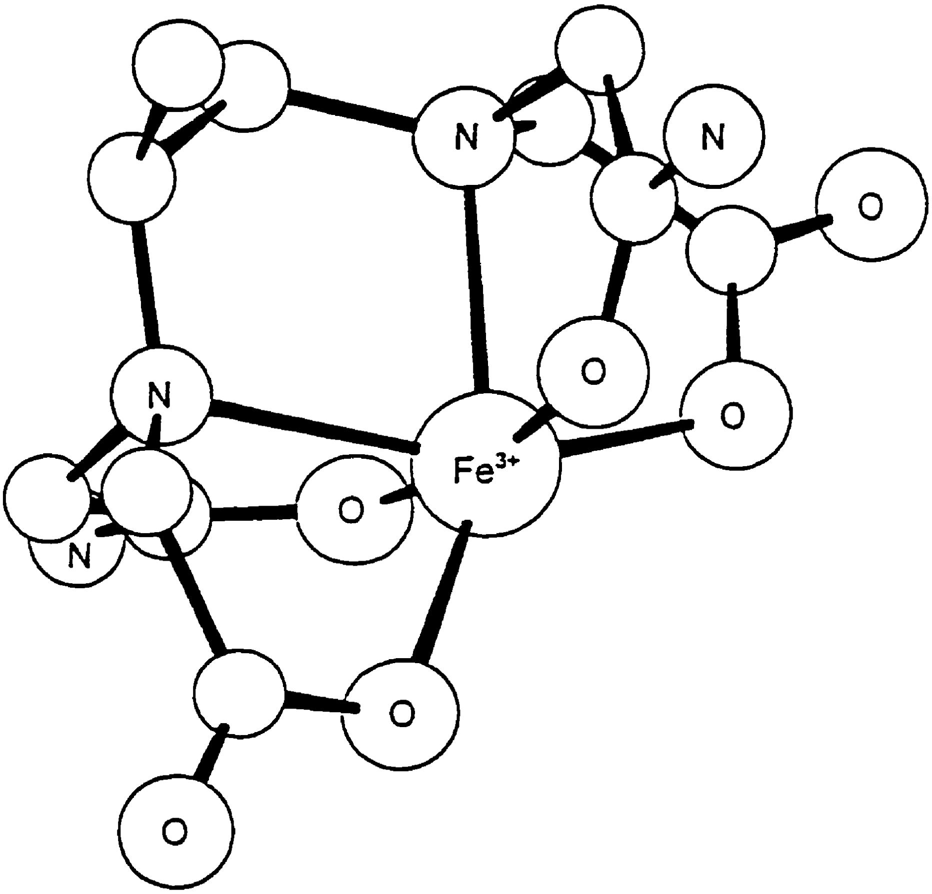

Figure 2.10. Structure of the proposed Fe^{3+}-**D** complex. The energy-minimized structure was obtained by molecular modelling. Heteroatoms are labelled. Hydrogen atoms were modelled, but are not shown.

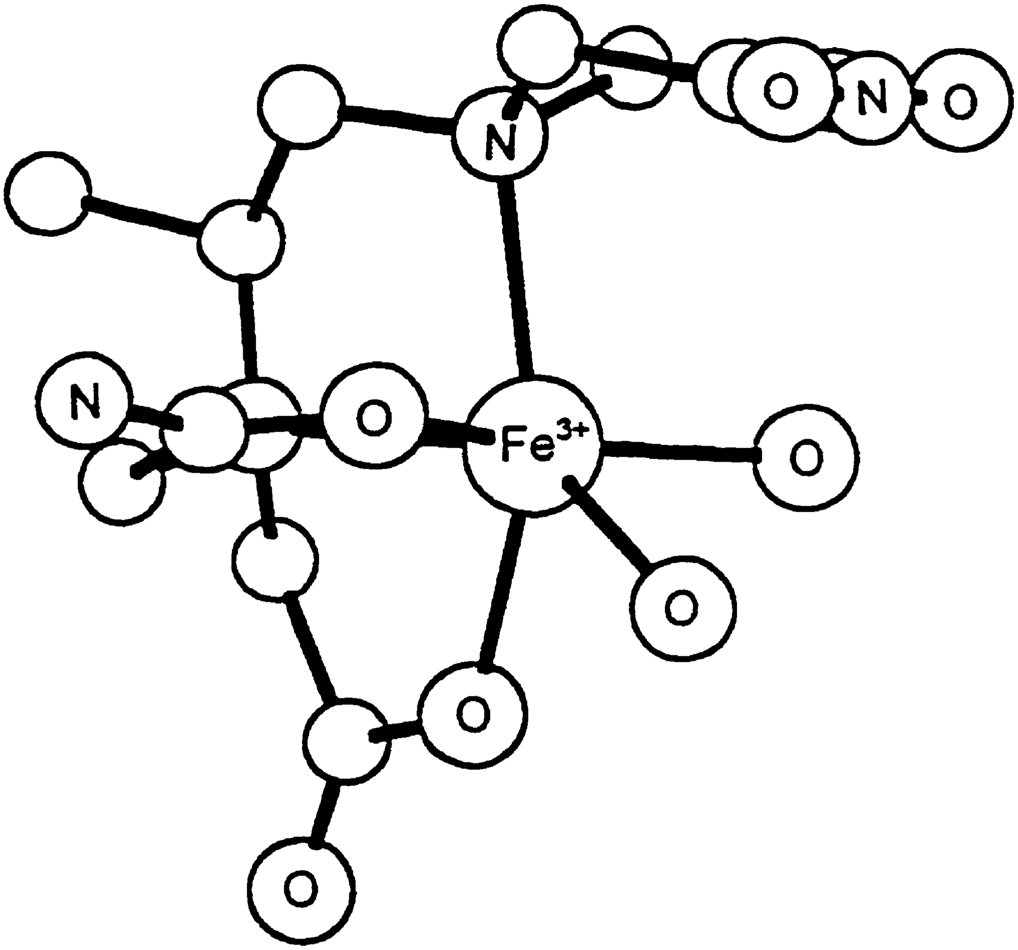

Figure 2.11. Structure of the proposed Fe^{3+}-**B** complex. The energy-minimized structure was obtained by molecular modelling. Heteroatoms are labelled. **B** is a tetradentate ligand, and the remaining two co-ordination positions are occupied by water molecules.Hydrogen atoms were modelled, but are not shown.

Anthracyclines self-associate in aqueous solution, and they adsorb to the sides of the spectrophotometer cell. Beer's law plots of daunorubicin at 600 nm in 50 mM Tris buffer with 150 mM KCl, and 50 mM Tris with 150 mM KCl in methanol, were not linear over a sufficient range to be useful. Since a Beer's law plot of daunorubicin in 40 mM Tris, pH 7.4 yielded a straight line over a sufficient concentration range, these conditions were chosen for further experiments. Addition of aliquots of daunorubicin to Fe^{3+} complexes of **B** and daunorubicin produced increases in absorbance at 600 nm (Figure 2.12). There was a small, rapid decrease in absorbance immediately following each addition, perhaps corresponding to some daunorubicin adhering to the cell walls. Absorbance measurements were made once the absorbance reached equilibrium (approximately 15 min).

The titration curves for daunorubicin, Fe^{3+}-daunorubicin, and Fe^{3+}-**B**-daunorubicin shown in Figure 2.12 were fitted to a linear, unweighted, least squares equation, and are the averages of three, three, and two determinations, respectively. The slope of the daunorubicin calibration curve was significantly different from those of the other curves ($p < 0.001$). The slopes of the Fe^{3+}-**B** and Fe^{3+}-daunorubicin curves were not significantly different ($p > 0.2$). If daunorubicin were not binding with Fe^{3+}, the Fe^{3+}-**B** titration curve (■) would parallel the daunorubicin curve. If daunorubicin completely displaced **B**, the Fe^{3+}-**B** titration curve would be identical with the Fe^{3+}-daunorubicin curve (▼). Thus, a ternary Fe^{3+}-**B**-daunorubicin complex is formed. Since the slopes of the two titration curves were similar, it is likely that the binding constants and molar absorptivities for daunorubicin are similar for the two complexes. It is possible that these ternary complexes are responsible for the residual

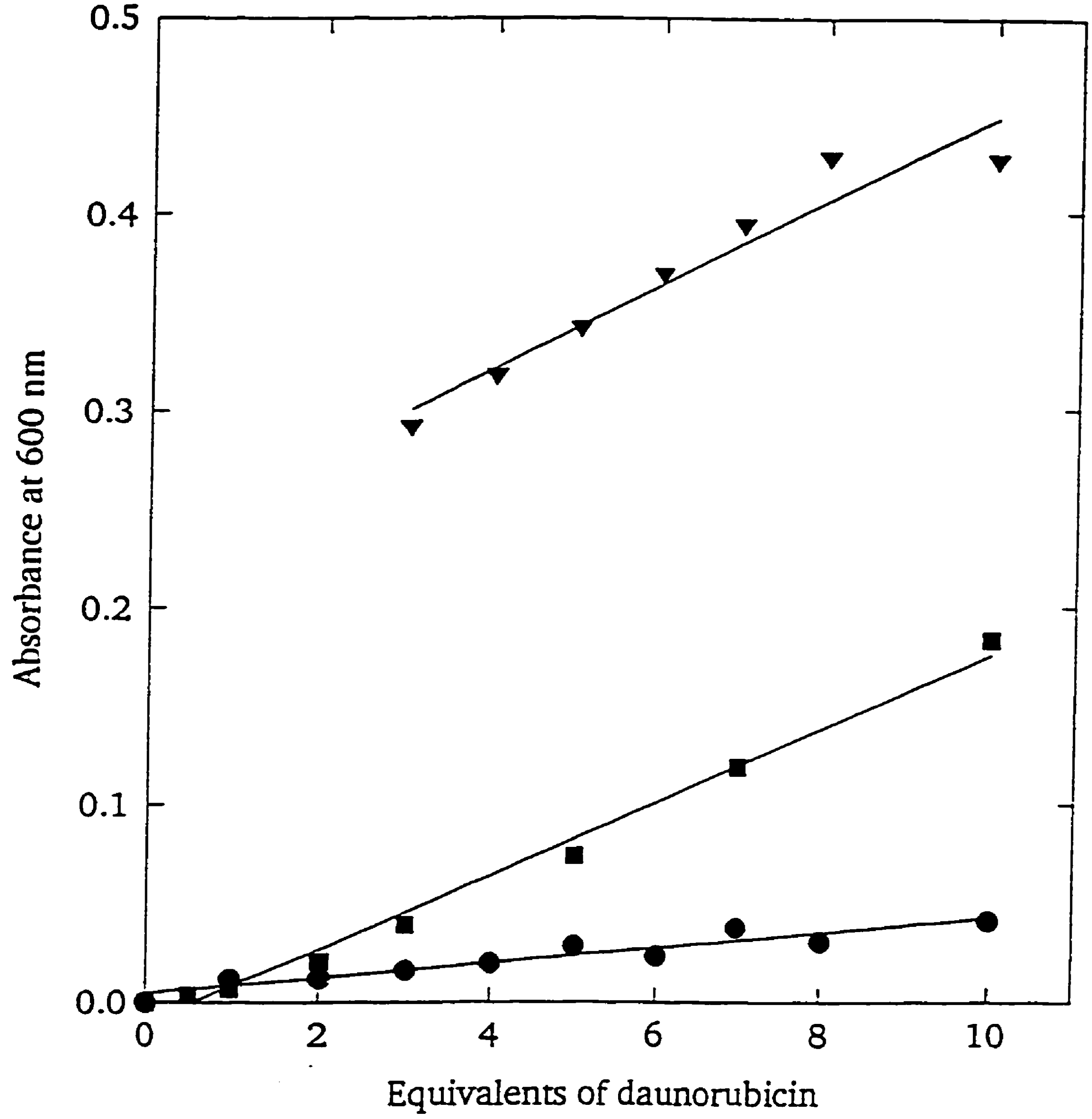

Figure 2.12. Formation of a daunorubicin ternary complex with Fe^{3+}-**B**. Absorbance data were collected at 600 nm. Experiments were done in 40 mM Tris (pH 7.40) at 25 °C. Legend: Beer's law curve of daunorubicin (●); titration of Fe^{3+}-(daunorubicin)$_3$ (▼); titration of Fe^{3+}-**B** (■). Solid lines are unweighted least squares linear fits. One equivalent of daunorubicin equals 30 nmol.

absorbance observed in the experiments in which **B** and **C** displace Fe^{3+} from anthracyclines (Figure 2.3b, 2.4b).

2.5.4 Molecular modelling of the ternary complex, Fe^{3+}-(C)-(daunorubicin)

The lowest-energy configuration of Fe^{3+}-**B** found by molecular modelling is shown in Figure 2.11. The results of titration of this complex with daunorubicin indicates that the two remaining co-ordination positions can be occupied by an anthracycline, acting as a bidentate ligand. Molecular modelling of the proposed ternary complex yielded many possible orientations for both **B** and daunorubicin. **B** may prefer a conformation in which the main chain is pseudoaxial or pseudoequatorial. The preferred conformation of Fe^{3+}-(**B**)-(daunorubicin) may differ from that of Fe^{3+}-**B** due to additional steric constraints due to the binding of daunorubicin. The anthracycline may be bound through the quinone and hydroquinone oxygen atoms at carbons 5 and 6, or 11 and 12, and it may be oriented face up or face down. Conformations involving co-ordination through the α-ketol side chain were not considered. Three variables were considered; orientation of the imide ring, atoms involved in co-ordination of the daunorubicin, and orientation of the daunorubicin, for which there are two possibilities each. Thus, eight conformations were modelled. The lowest-energy configuration is shown in Figure 2.13. Two of the seven remaining conformations had energies within one kcal/mole of this structure. Thus, more than one conformation likely exists.

Both the azide and daunorubicin titrations of Fe^{3+}-**B** demonstrate available co-ordination positions on the complex, supporting the existence of the tetradentate complex

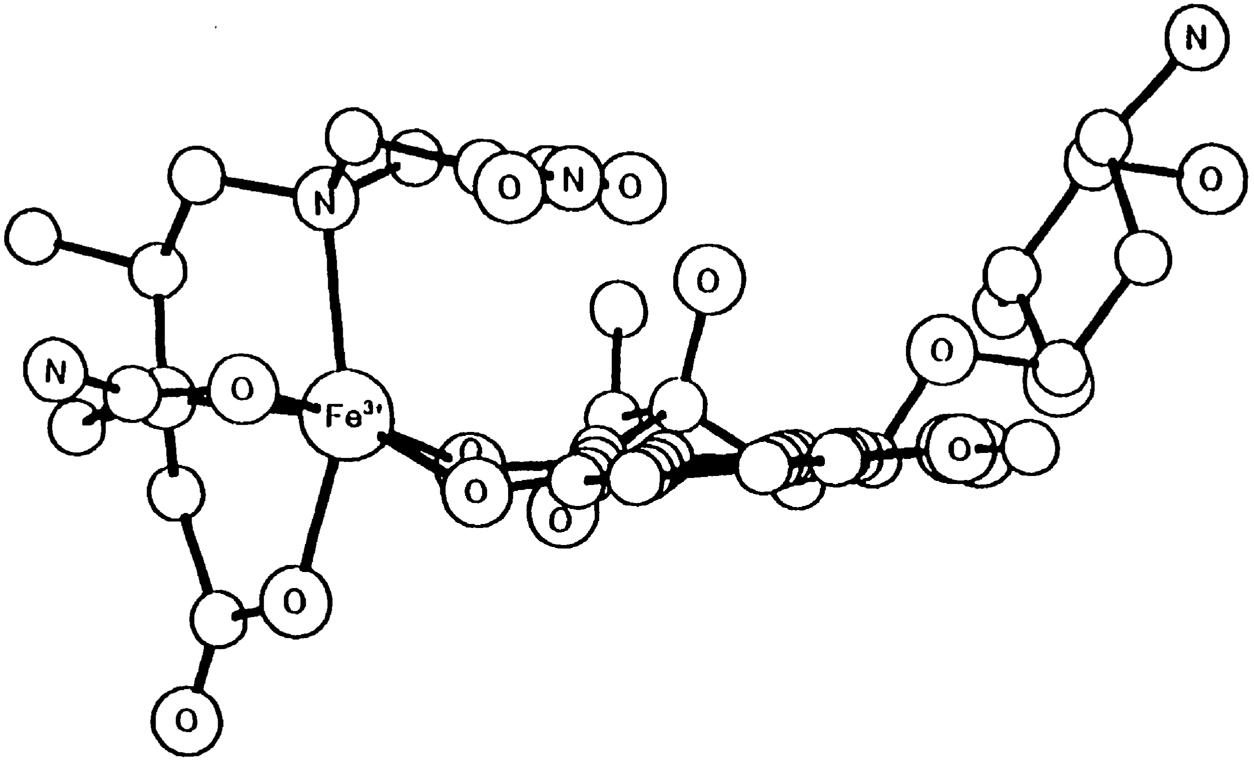

Figure 2.13. Structure of the proposed ternary Fe^{3+}-(**B**)-(daunorubicin) complex. The energy-minimized structure was obtained by molecular modelling. Heteroatoms are labelled as space permits. **B** is a tetradentate ligand, and the remaining positions are occupied by the quinone and hydroquinone oxygen atoms of daunorubicin. Hydrogen atoms were modelled, but are not shown.

proposed in Figure 2.11. Molecular modelling and the daunorubicin titrations indicate the existence of a ternary Fe^{3+}-**B**-daunorubicin complex. It may be possible for anthracyclines to reduce Fe^{3+} in this complex by a self-reduction mechanism, as in the Fe^{3+}-anthracycline complex [17].

2.6 Estimation of the rate of hydrolysis-activation of dexrazoxane *in vivo*

Both **B** and **C** quickly and effectively displace Fe^{3+} from its anthracycline complexes. By this activity, they should be able to reduce oxygen radical production by Fe^{3+}-anthracycline complexes as does ICRF-198 [109], and they likely are effective species in protecting against anthracycline-induced cardiotoxicity. Thus, the time required for hydrolysis of dexrazoxane to active species *in vivo* may be 9.3 h, the half-time for production of **B** and **C** [128]. This is significantly less than previously estimated, as complete hydrolysis to **D**, the half-time for which is 28 h [128], may not be required in order to produce a chelating form of the drug. Further increases in the activation rate of dexrazoxane are possible *in vivo*. *In vitro* studies have shown that the enzyme dihydropyrimidine amidohydrolase (DHPase) catalyzes the hydrolysis reactions of dexrazoxane to **B** and **C** [124, 158]. This enzyme is present in liver and kidney, but not the heart [125]. Increased hydrolysis may deplete physiological iron stores, reducing the iron available to bind anthracyclines, thereby protecting the heart. Alternatively, hydrolysis, which renders the drug impermeable to the cell membrane [106], may trap the drug at a site distant from the site of protection, thereby preventing it from acting.

Chapter 3 Acceleration of the hydrolysis of dexrazoxane by iron

3.1 Introduction

Although doxorubicin is an effective antitumor agent, its clinical use is limited by its cardiotoxicity, which is correlated with the cumulative dose received [3]. It has been demonstrated that the Fe^{3+}-anthracycline complex initiates oxidative damage *in vitro* [7, 8]. It is believed that the observed cardiotoxicity *in vivo* is due to iron-dependent oxidative stress on the cardiac muscle, which has relatively low levels of the enzymes which detoxify reactive oxygen species [58]. Dexrazoxane, which has been shown in clinical trials [88] to reduce this toxicity, presumably does so by hydrolyzing to its chelating forms, which bind redox cycling metal ions, thereby reducing their interaction with anthracyclines.

Dexrazoxane undergoes hydroxide-ion-catalyzed hydrolysis to its final product, **D**, *via* one of two one-ring open intermediates, **B** or **C** (Figure 3.1) [117]. The half-times for the production of the open-ring open intermediates and **D**, respectively, are approximately 9 and 28 h [128]. It has been shown that, in addition to **D** [101, 115], the one-ring open hydrolysis intermediates of dexrazoxane, **B** and **C**, are effective chelators (Chapter 2). Thus, the hydrolysis reactions of dexrazoxane in the presence of Fe^{2+} and Fe^{3+} are of interest. The results of previous studies of the interaction between dexrazoxane and the Fe^{3+} complexes of doxorubicin suggested that Fe^{3+} may accelerate the hydrolysis reactions of dexrazoxane (Chapter 2) [101, 116, 159].

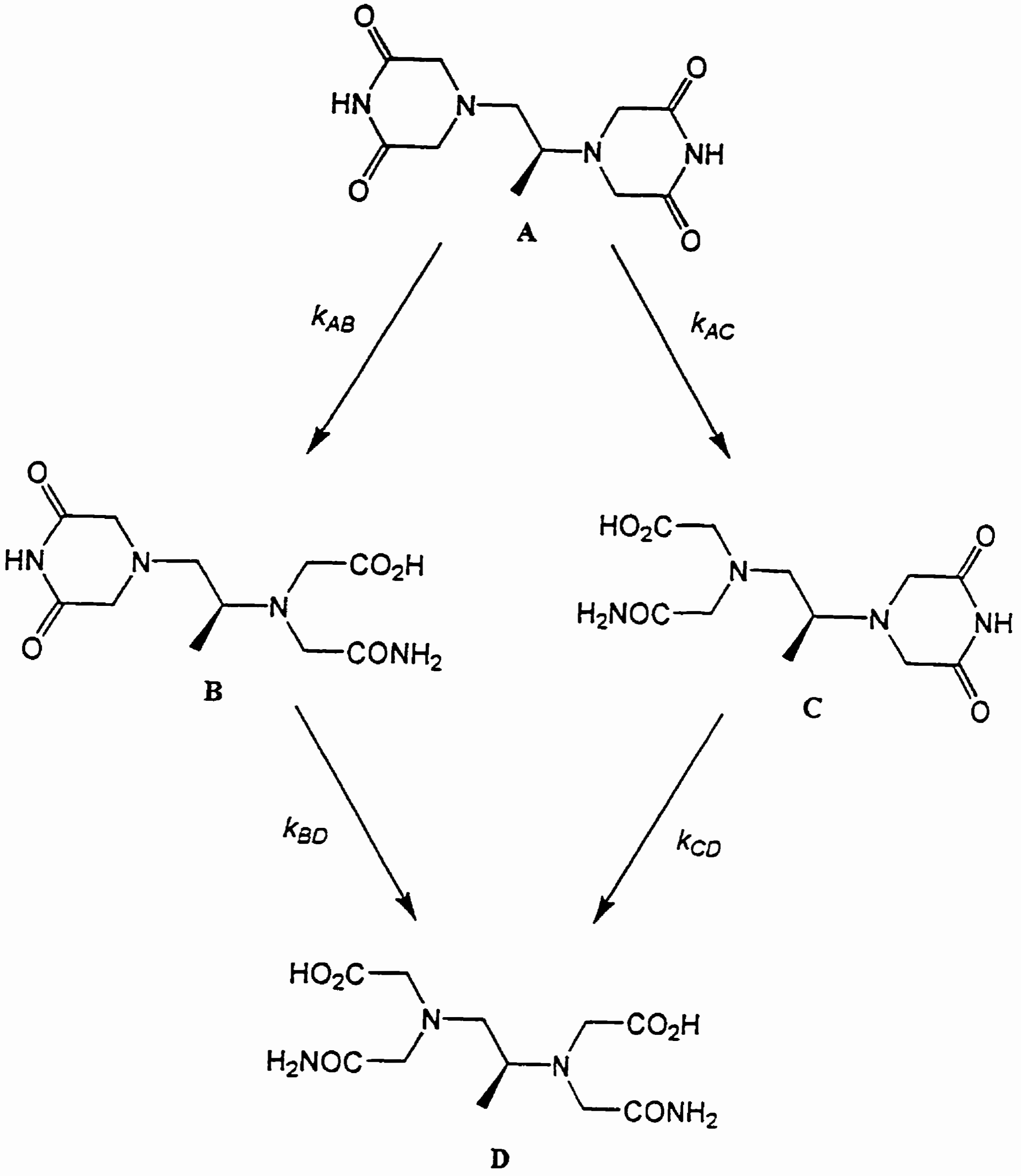

Figure 3.1. Reaction scheme for the hydrolysis of dexrazoxane (ICRF-187, **A**) to its one-ring open hydrolysis intermediates (**B** and **C**), and its final product, ADR-925 (**D**). At constant pH, the reactions shown are pseudo-first-order, described by the rate constants k_{AB}, k_{AC}, k_{BD}, and k_{CD}.

3.2 Materials and methods

$FeCl_3 \cdot 6H_2O$ was from J. T. Baker Chemical Co. (Phillipsburg, NJ). $Fe(NH_4)_2(SO_4)_2 \cdot 6H_2O$ was from Fisher Scientific (Fair Lawn, NJ). Tris was from Sigma (St. Louis, MO). All other chemicals were of the highest grade available. Dexrazoxane (ICRF-187, ADR-529) and **D** (ADR-925) were gifts from Adria Laboratories (Columbus, OH). The ring-open intermediates **B** and **C** were prepared as described in Section 2.2.

Spectrophotometric measurements were made in 1 cm silica cells on a Varian Cary 1 spectrophotometer (Mulgrave, Australia) with thermostatted cell compartments. Reactions with Fe^{2+} were initiated by adding a stock solution of 6 mM Fe^{2+} in 100 mM HCl into buffer in the cell, to which either **B** or **C** had just been added. For reactions involving the Fe^{3+} complex of either **B** or **C**, the complex was preformed by adding the ligand to Fe^{3+} at final concentrations of 2 to 4 mM Fe^{3+}-ligand and 200 mM HCl to prevent formation of insoluble iron hydroxides, and then added to the buffer to start the reaction. Unless otherwise stated, the reactions were carried out in Tris-HCl/KCl buffer (50 mM Tris, 150 mM KCl, pH 7.4). Appropriate volumes of 1 M KOH were added to the buffered solutions to neutralize the HCl in the stock solutions of Fe^{2+} and Fe^{3+}. Solutions for reactions observed under anaerobic conditions were sparged with argon for 5 minutes. The buffer was sparged in the spectrophotometer cell. The sparged stock Fe^{2+} solution was delivered by syringe through the septum which sealed the cell.

The HPLC separations and quantitations were done by Mukhtiar Singh in our laboratory, using a Varian LC Star System (Walnut Creek, CA) using a Waters μBondapak 10 μm 3.9 x 300 mm reversed phase C_{18} column and spectrophotometric detection at 205 nm as previously described (Chapter 2) [149, 159], with the following modifications. For the experiments in which dexrazoxane was incubated with Fe^{2+}, the aqueous eluent contained 2 mM of the ion pair reagent sodium 1-heptanesulfonate (Sigma, St. Louis, MO) to increase the retention time of **D** to 4.6 min. Samples were treated with a two-fold molar excess of EDTA to preferentially displace iron before injection onto the column. For the experiment carried out to identify the product of the reaction of **B** and Fe^{2+}, isocratic elution was used, with 20% 4 mM sodium 1-octanesulfonate and 80% 500 µM EDTA (pH 3), which gave a retention time of 6.4 min for **D**. Data were analyzed using Cary 1/3 E software (Varian, Mulgrave, Australia) and Sigmaplot, version 5.00 for DOS (Jandel Scientific, San Rafael, CA).

3.3 Hydrolysis of B and C, the one-ring open hydrolysis intermediates of dexrazoxane

To further characterize the ring-opening hydrolysis of **B** and **C** to **D**, the reactions of these intermediates were followed spectrophotometrically at 37 °C in Tris buffer, by recording complete spectra at fixed intervals (Figure 3.2a). Spectra of both **B** and **C** were characteristic of imides, with a single peak at approximately 207 nm. The decrease in magnitude of this peak observed over the 195 to 250 nm range was consistent with imide hydrolysis [117]. The slow exponential decreases in absorbance at 207 nm (Figure 3.2b) were fitted to the three-parameter exponential decay equation:

$$A = Amp \cdot e^{-k_{obs}t} + A_{\infty} \qquad (3.1)$$

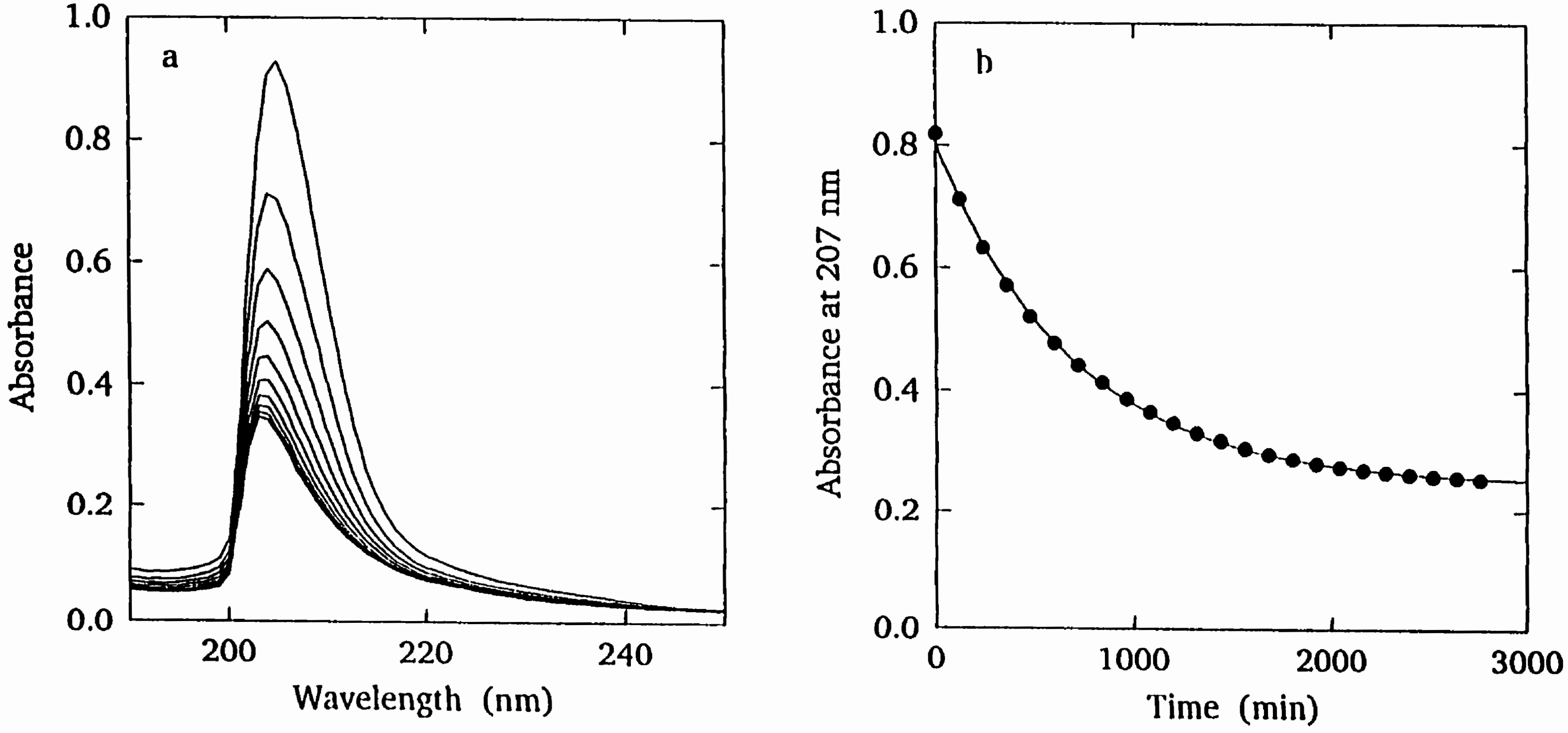

Figure 3.2. Hydrolysis of the one-ring open hydrolysis intermediate of dexrazoxane, C. The reaction was carried out in Tris/KCl buffer, pH 7.4, at 37 °C. a) Spectral changes characteristic of imide hydrolysis observed for 50 μM C. Spectra were recorded at 30 min intervals. For clarity, spectra recorded every 3 hours are shown. b) Absorbance data at 207 nm for the hydrolysis of C (symbols), and their fit to Equation 3.1.

in which k_{obs} is the pseudo-first-order rate constant, A and A_∞ are the absorbances at times t and infinity, respectively, and Amp is the amplitude of the absorbance change. The measured values of k_{obs} for **B** and **C** of 0.00077 and 0.0015 min^{-1} (Table 3.1), respectively, compare very well to 0.00067 and 0.0014, the values of k_{BD} and k_{CD} (defined in Figure 3.1) previously obtained by HPLC [149] for **B** and **C**. The pseudo-first-order hydrolysis reaction of **B** is:

$$\mathbf{B} + H_2O \rightarrow \mathbf{D} \quad (3.2)$$

Table 3.1. First order rate constants for the hydrolysis of **B** and **C** at pH 7.4 and 37°C.

Reaction	k_{obs} (min^{-1})	$t_{1/2}$ (min)	relative rate[a]	Reaction	k_{obs} (min^{-1})	$t_{1/2}$ (min)	relative rate[a]
B→**D**	0.00077[b]	900	1	**C**→**D**	0.0015[b]	470	1
Fe^{3+}-**B**→Fe^{3+}-**D**	0.0042[b]	170	5.4	Fe^{3+}-**C**→Fe^{3+}-**D**	0.0054[b]	130	3.6
Fe^{2+}-**B**→Fe^{2+}-**D**	1.6[c]	0.43	2100	Fe^{2+}-**C**→Fe^{2+}-**D**	8.9[c]	0.07	6000
Fe^{2+}-**B**→Fe^{2+}-**D**	1.3[b,d]	0.53	-	Fe^{2+}-**C**→Fe^{2+}-**D**	4.4[b,d]	0.16	-
Fe^{2+}-**B**→Fe^{2+}-**D**	0.69[b,e]	1.0	-	Fe^{2+}-**C**→Fe^{2+}-**D**	1.1[b,e]	0.60	-

[a] Relative rate calculated from the ratio of k_{obs} to the k_{obs} measured in the absence of added iron.

[b] These measurements are the results of single measurements.

[c] These measurements are the averages of two measurements. The average deviations for the reactions with **B** and **C** are 0.3 and 0.2, respectively.

[d] At 25°C.

[e] At 15°C.

3.4 Hydrolysis of B and C in the presence of Fe^{3+}

The spectral changes observed on hydrolysis of the Fe^{3+}-**B** and Fe^{3+}-**C** complexes were similar to those of **B** and **C** alone, although the hydrolysis reactions in the presence of Fe^{3+} were five- and eight-fold faster, respectively, than in its absence (Figure 3.3). Exponential fits of the absorbance data, using Equation 3.1, were obtained to give k_{obs} of 0.0042 and 0.0054

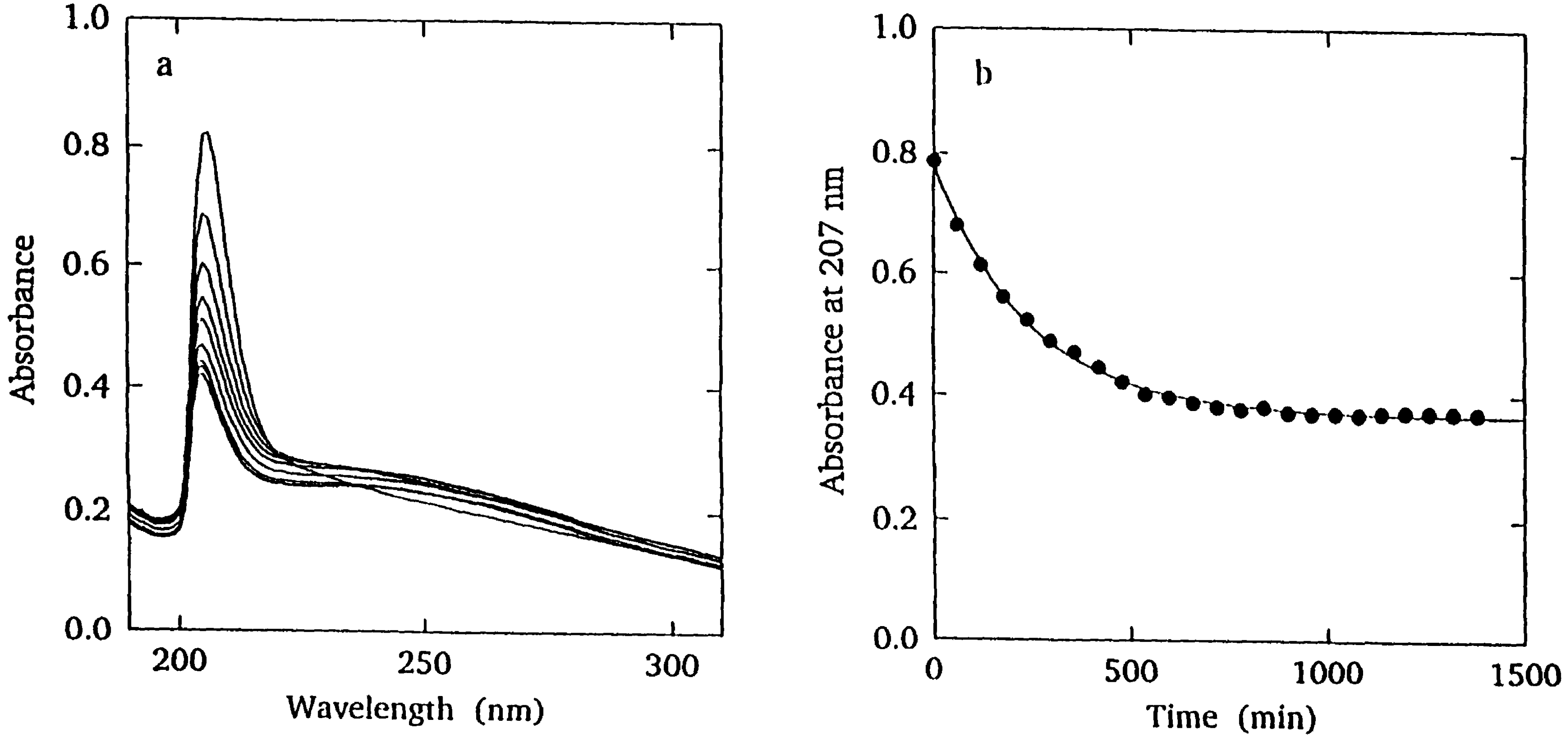

Figure 3.3. Hydrolysis of the Fe^{3+} complex of the one-ring open hydrolysis intermediate of dexrazoxane, **B**. Reactions were carried out in Tris/KCl buffer, pH 7.4, at 37 °C. a) Spectral changes characteristic of imide hydrolysis observed for Fe^{3+}-**B**. Spectra were recorded every 30 minutes. For clarity, spectra recorded every 90 minutes are shown. The concentrations of Fe^{3+} and **B** were 60 and 50 μM, respectively. b) Absorbance data at 207 nm for the hydrolysis of Fe^{3+}-**B** (symbols) and their fit to Equation 3.1.

min^{-1} for Fe^{3+}-**B** and Fe^{3+}-**C**, respectively, describing the reactions (Table 3.1). The hydrolysis reaction in the presence of Fe^{3+} is, in the case of **B**:

$$Fe^{3+}\text{-}\mathbf{B} + H_2O \rightarrow Fe^{3+}\text{-}\mathbf{D} \qquad (3.3)$$

Fe^{3+} enhances the rates of hydrolysis of **B** and **C** by factors of 5.4 and 3.6, respectively, at pH 7.4 and 37 °C.

The hydrolysis of dexrazoxane [117] and its one-ring open intermediates [128] are both base-catalyzed. As shown in Figure 3.4a, the rate constant describing the pseudo-first-order hydrolysis of Fe^{3+}-**C**, k_{obs}, increases with pH. A plot of log k_{obs} *vs.* pH (Figure 3.4b) was linear below pH 7.6, with a slope of 0.64 ± 0.07, indicating that in this pH range, the reaction was approximately first order in hydroxide ion. The observed results could not be described by a mechanism involving only one pK_a. The reaction scheme described in Figure 3.5 was the simplest that satisfactorily fit the data. A mechanism involving only one pK_a yielded a worse fit, for which the square root of the sum of the squares of the residuals was 75% larger than for the fit shown in Figure 3.4a. The fitted curve was obtained from a weighted non-linear least squares fit to the following equation, derived from the reaction scheme shown in Figure 3.5 (Appendix):

$$k_{obs} = \frac{k_2 K_{a1} K_w + [H^+](k_1 K_w + k_3 K_{a1})}{[H^+]^2 + K_{a1}[H^+] + K_{a1} K_{a2}} \qquad (3.4)$$

in which k_1 and k_2 are second order rate constants for the bimolecular reaction of free hydroxide ion with $Fe^{3+}(ImH)(H_2O)$ and $Fe^{3+}(ImH)(OH^-)$, respectively. The parameter k_3 is a first order rate constant for intramolecular hydrolysis, in which the nucleophile is a

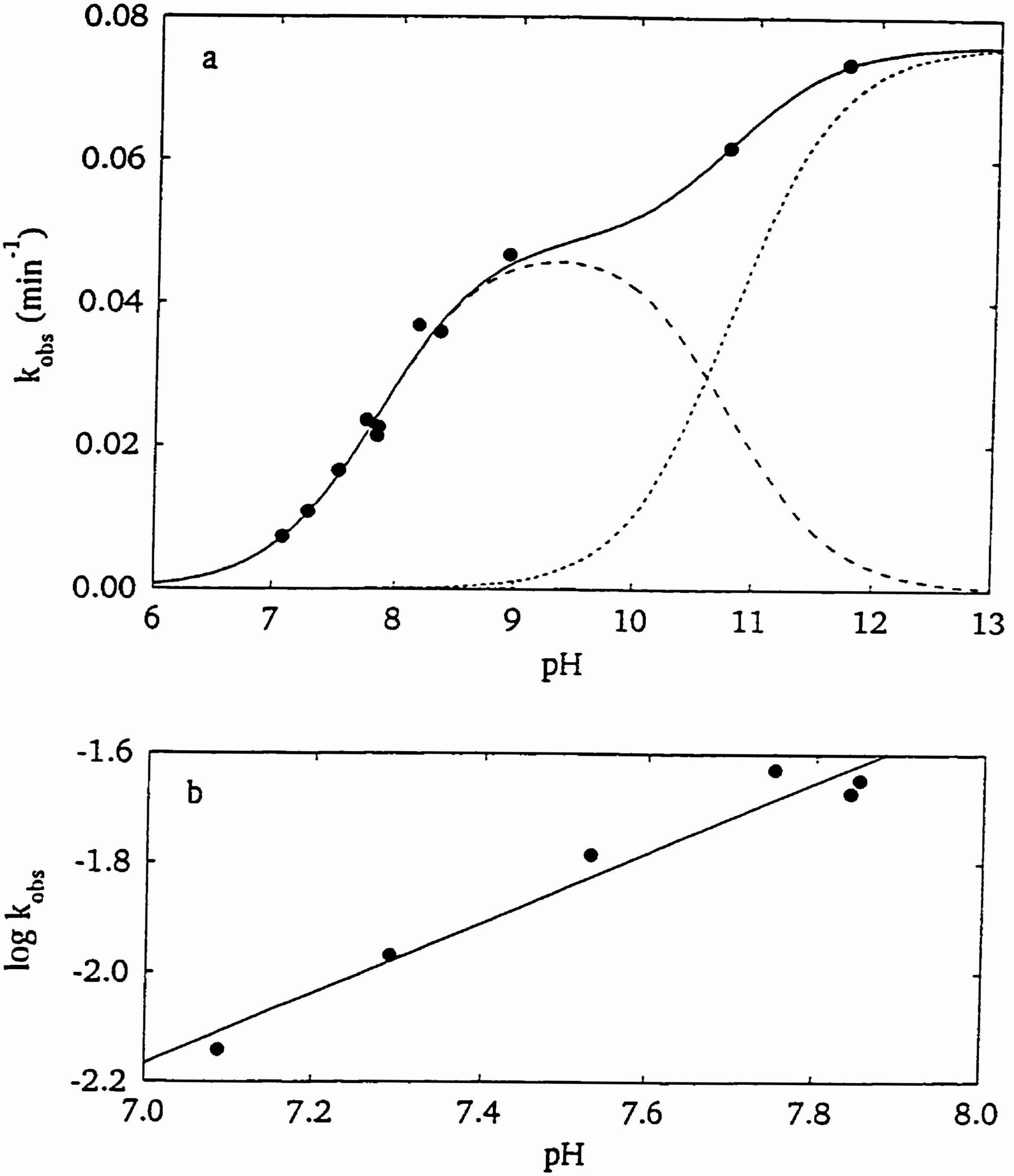

Figure 3.4. pH dependence of the hydrolysis of Fe^{3+}-C. Reactions were carried out at 24 μM in Tris/KCl buffer, titrated with NaOH, at 37 °C. a) Experimental data (symbols) and fit to Equation 3.4 (solid line). Broken lines represent the contributions of the k_2 (—), and the combined k_1 and k_3 (·····) terms. b) Log-log plot of the data below pH 7.6 (symbols), and the least squares calculated line.

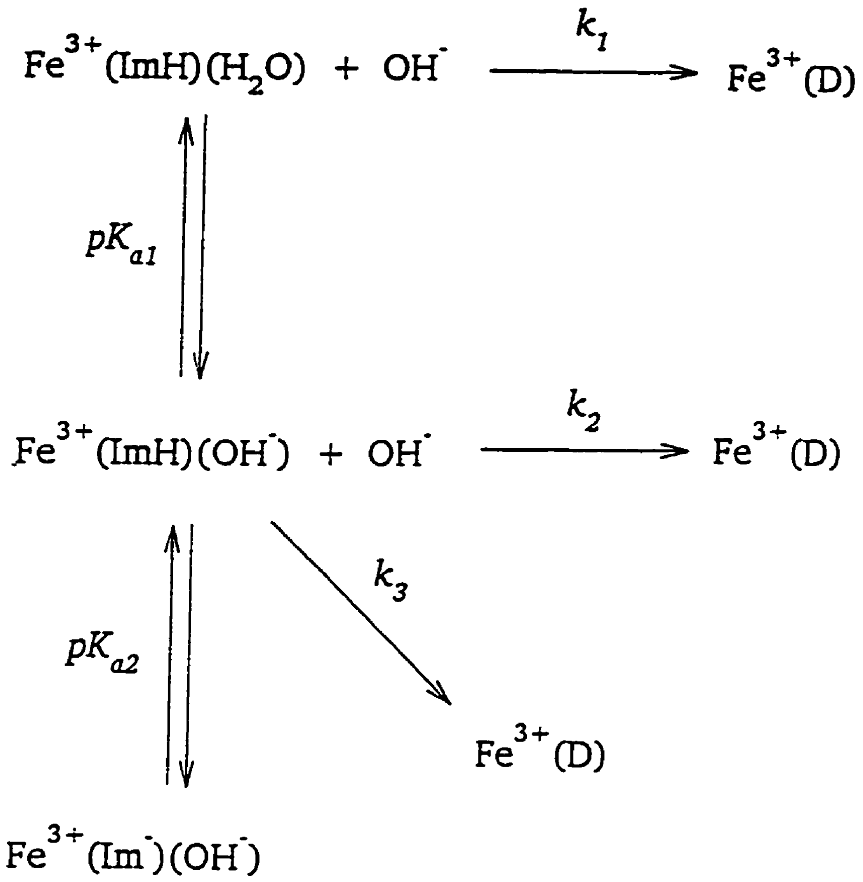

Figure 3.5. Reaction scheme describing the hydrolysis of Fe^{2+}-C. The protonated and deprotonated forms of C are represented as (ImH) and (Im$^-$), respectively. The parameters pK_{a1}, pK_{a2}, k_1, k_2, and k_3 correspond to those in Equation 3.4. The pathway described by k_3 involves intramolecular nucleophilic attack by coordinated hydroxide ion.

hydroxide ion coordinated to Fe^{3+}. K_{a1} and K_{a2} are acid dissociation constants, and K_w is the ionization constant of water. In the scheme shown in Figure 3.5, the imide ring reacts with hydroxide ion, while the imide anion does not do so significantly in this pH range, as has been shown previously in the absence of Fe^{3+} [117]. The reaction pathways described by k_1 and k_3 have the same dependence on pH (Figure 3.4), since both pathways involve nucleophilic attack on the Fe^{3+}-bound imide by a hydroxide ion. Due to this proton ambiguity, these two pathways cannot be distinguished from each other by a kinetic experiment. Weighted nonlinear least squares curve fitting to Equation 3.4 gave pK_{a1} and pK_{a2} of 7.8 ± 0.05 and 10.8 ± 0.5, respectively, and k_2 of 50 ± 5 $M^{-1}\ min^{-1}$. The value of the composite parameter $(k_1K_w + k_3K_{a1})$ was 6.8 ± 0.4 x 10^{-10} M min^{-1}.

In addition to the observed pH-dependent changes in the hydrolysis rate constant of Fe^{3+}-C, the amplitude of the absorbance change for the hydrolysis of Fe^{3+}-C also varied with pH (Figure 3.6). In the upper range of pH values, a peak with an absorbance maximum at 227 nm was observed. Since C was previously observed to have an absorbance maximum at 227 nm due to imide deprotonation [128, 149], it was concluded that the Fe^{3+}-bound imide is also deprotonated at high pH. Since this absorbance change is caused by deprotonation, a static determination of pK_{a2} can be made. A two-parameter nonlinear least squares fit of the absorbance change (A) at 227 nm to an equation derived from a scheme in which the deprotonated species absorbs, but the protonated species does not (Appendix):

$$A = \frac{\epsilon[Im]_T}{1 + \frac{[H^+]}{K_{a2}}} \qquad (3.5)$$

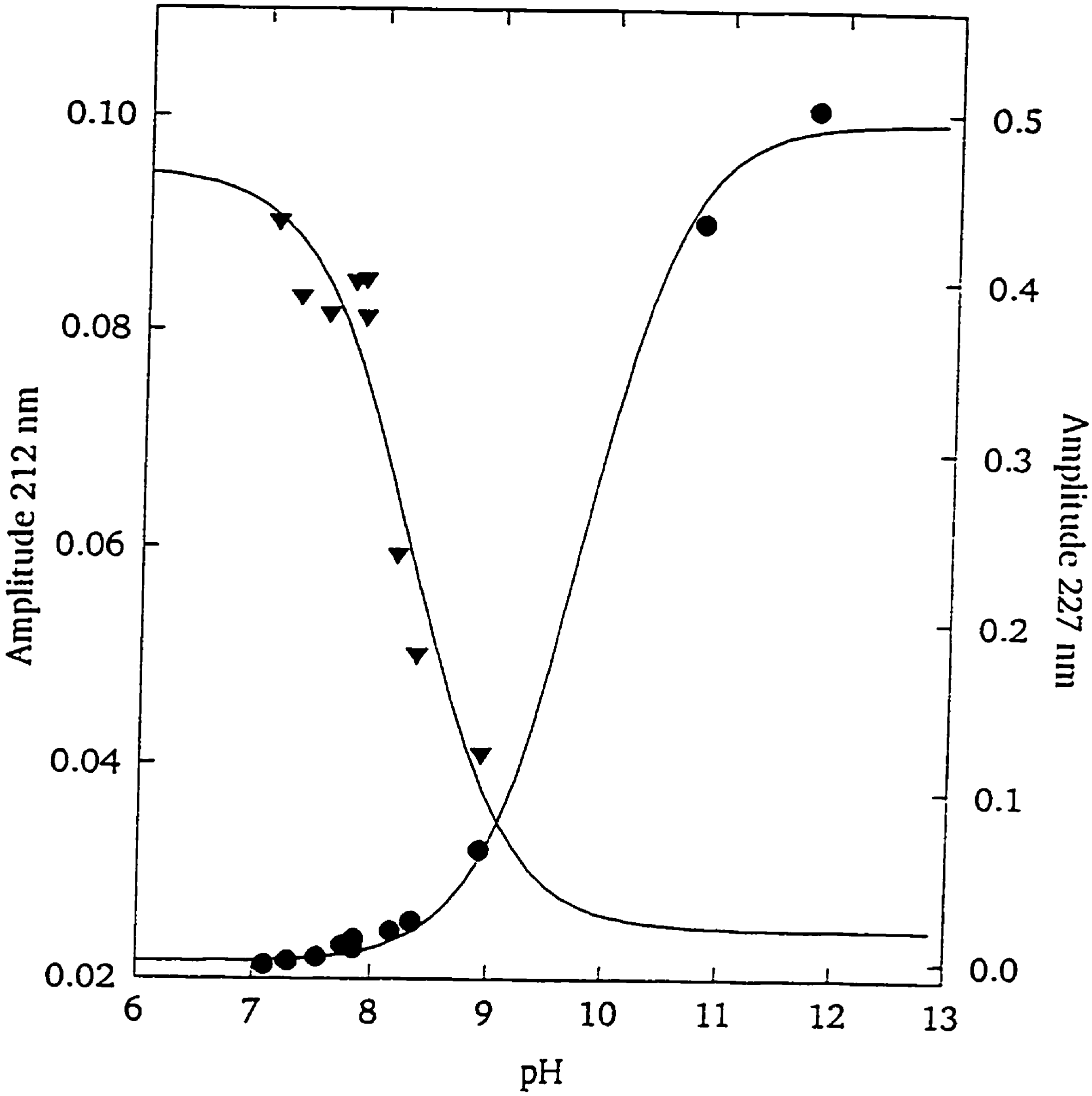

Figure 3.6. Static determinations of pK_{a1} and pK_{a2} of Fe^{3+}-C. Data at 212 nm (▼) and 227 nm (●) were fitted to equations 3.6 and 3.5, respectively (lines). Reactions were carried out at 24 μM in Tris/KCl buffer, titrated with NaOH, at 37 °C.

in which ϵ is the difference in molar absorptivity between the reactants and the products of the hydrolysis reaction, and $[\mathrm{Im}]_T$ is the concentration of imide, gave a pK_a of 9.8 ● 0.06. The kinetic and static determinations of pK_{a2}, 10.8 and 9.8, respectively, can be compared to spectrophotometric determinations of the pK_a of dexrazoxane of 9.6 at 37 °C [149], which correspond to the simultaneous deprotonation of both imide functional groups.

Another change in the amplitude of the absorbance change due to Fe^{3+}-C hydrolysis, due to deprotonation of Fe^{3+}-C, was observed at 212 nm, at lower pH (Figure 3.6). In this wavelength range, the absorption of the Fe^{3+} ion may be altered by changes, *i.e.* deprotonation, in the ligand, C. To obtain a static measurement of pK_{a1}, these data were fitted to a three-parameter equation derived from a scheme in which the protonated species has a greater absorbance than the deprotonated species (Appendix):

$$A = \frac{\epsilon[Im]_T}{1 + \frac{K_{a1}}{[H^+]}} + A_l \qquad (3.6)$$

in which A_l is the limiting absorbance at high pH, gave a pK_{a1} of 8.3 ± 0.3. This pK_a value is also in reasonable agreement with the kinetically determined value of 7.8 ± 0.05. The smaller absorbance changes occurring at 212 nm are likely due to changes in the charge transfer spectrum of the complex as bound water is deprotonated.

3.5 Hydrolysis of B and C in the presence of Fe^{2+}

The hydrolysis of 1 mM dexrazoxane was followed under argon (to prevent aerobic oxidation of Fe^{2+}) by HPLC in the presence of 2 mM Fe^{2+} (Figure 3.7, ● and ○). The solid lines were calculated from the rate constants previously measured [149] substituted in the

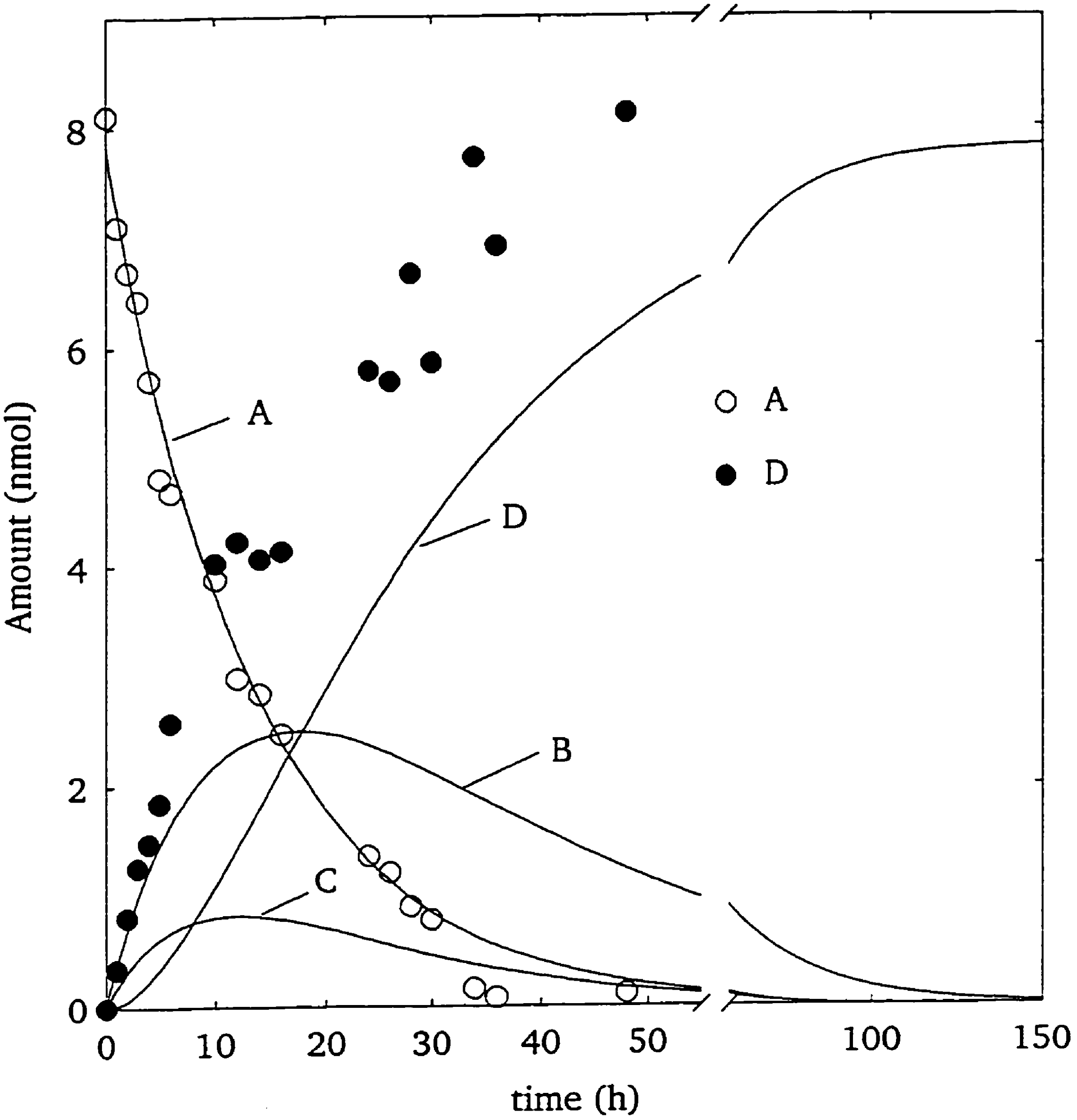

Figure 3.7. Hydrolysis of dexrazoxane (**A**, ○) and formation of **D** (●) at 37 °C (pH 7.4) in the presence of Fe^{2+} in argon-saturated solutions, determined by HPLC. For comparison, curve fits to Equations 4.1-4.4 of data collected in the absence of Fe^{2+} from a previous study are shown (scaled to the same starting amount of dexrazoxane) [149].

integrated rate equations for the reaction scheme of Figure 3.1 (Equations 4.1-4.4). In contrast to these observations in the absence of Fe^{2+}, neither **B** nor **C** was detected in the reaction mixture. In addition to the lack of a lag period in the production of **D**, the half-time for the formation of **D** decreased from 26.5 h [149] to 8.9 h. As determined from non-linear least squares curve fitting to Equation 3.1, the amount of dexrazoxane decreased with a pseudo-first-order rate constant, k_{obs}, of 0.00130 ● 0.00005 min^{-1}. This agrees with the previous determination of 0.0012 min^{-1}, obtained in the absence of Fe^{2+} [149]. Since k_{obs} is unchanged, Fe^{2+} does not promote the hydrolysis of dexrazoxane itself. However, the fact that neither **B** nor **C** was detected in the reaction mixture indicated that Fe^{2+} strongly promotes the hydrolysis of both **B** and **C** to **D**, such that they do not measurably accumulate in the reaction mixture.

The hydrolyses of **B** and **C** in the presence of Fe^{2+} in 50 mM Tris-HCl and 150 mM KCl buffer (pH 7.4) were followed at 207 nm (data for Fe^{2+}-**B** are shown in Figure 3.8). Under aerobic conditions, these hydrolysis reactions displayed multiphasic kinetics at 37 °C, with a fast ($t_{1/2}$ of 0.4 min) initial non-exponential drop in absorbance, followed by a slower ($t_{1/2}$ of 130 min) rise in absorbance. The fast process was also observed for an identical solution, observed under argon to prevent aerobic oxidation of Fe^{2+} (Figure 3.8). The initial decrease in absorbance, shown on the first time-scale in Figure 3.8, is characteristic of imide hydrolysis (compare to Figure 3.2b), while the absorbance changes associated with the second, slow phase were consistent with oxidation of Fe^{2+} to Fe^{3+}. Since the concentration of Fe^{2+}-**B** was 24 μM, the presence of very small amounts of oxygen are sufficient to permit significant oxidation. Thus, under argon, the second, slow process occurred, likely due to

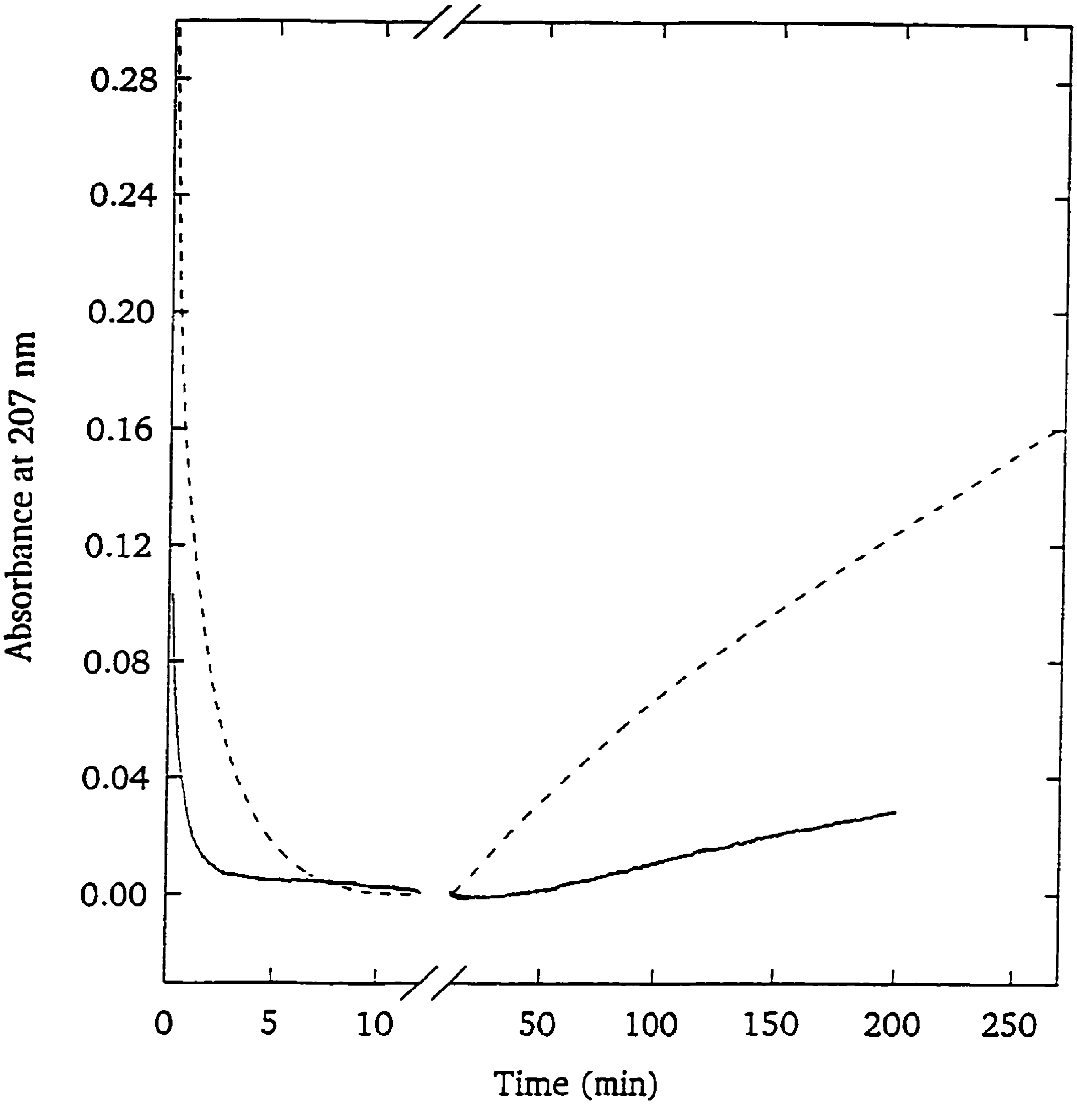

Figure 3.8. Absorbance changes due to hydrolysis and oxidation of 24 μM Fe^{2+}-B complex. The reactions were carried out in Tris/KCl buffer, pH 7.4, at 37 °C, in air (dashed line) or under argon (solid line).

trace amounts of O_2, but it did so much more slowly. Preliminary experiments, in which spectra were recorded at fixed time intervals, were used to identify the reactions which caused these absorbance changes. The first, fast process was observed as a sharp peak over 195-225 nm, consistent with imide hydrolysis [117]. The absorbance changes due to the second, slow process occurred over 210-310 nm, and were similar to those observed for oxidation of the Fe^{2+}-EDTA complex. Fe^{2+}-**B** in 5 mM Tris buffer, pH 7.4, was allowed to react for 24 h. After treatment with a twofold excess of EDTA, the solution was concentrated by freeze drying. As determined by HPLC, **D** was obtained in over 80% yield. Thus, **B** is not irreversibly reduced as Fe^{2+} oxidizes. Thus, the first process was imide hydrolysis, and was followed by oxidation of Fe^{2+}.

Although the hydrolysis reactions of Fe^{2+}-**B** and -**C** (Figure 3.8) were not exponential, these data were fitted to Equation 3.1 to yield pseudo-first-order rate constants of 1.6 and 8.9 min^{-1}, respectively, for comparison with those of the analogous reactions of **B** and **C**, and their Fe^{3+} complexes (Table 3.1). Fe^{2+} enhances the rates of hydrolysis of **B** and **C** by factors of 2100 and 6000, respectively, at pH 7.4 and 37 °C.

The dependence of Fe^{2+}-**B** hydrolysis on Fe^{2+} was determined at 15 °C. k_{obs} reached a limiting value with respect to Fe^{2+} (Figure 3.9), which is consistent with rapid, reversible complex formation of Fe^{2+} with **B** or **C**. Data were fitted to a saturation equation:

$$k_{obs} = \frac{k_{max} \cdot [Fe^{2+}]}{K + [Fe^{2+}]} \qquad (3.7)$$

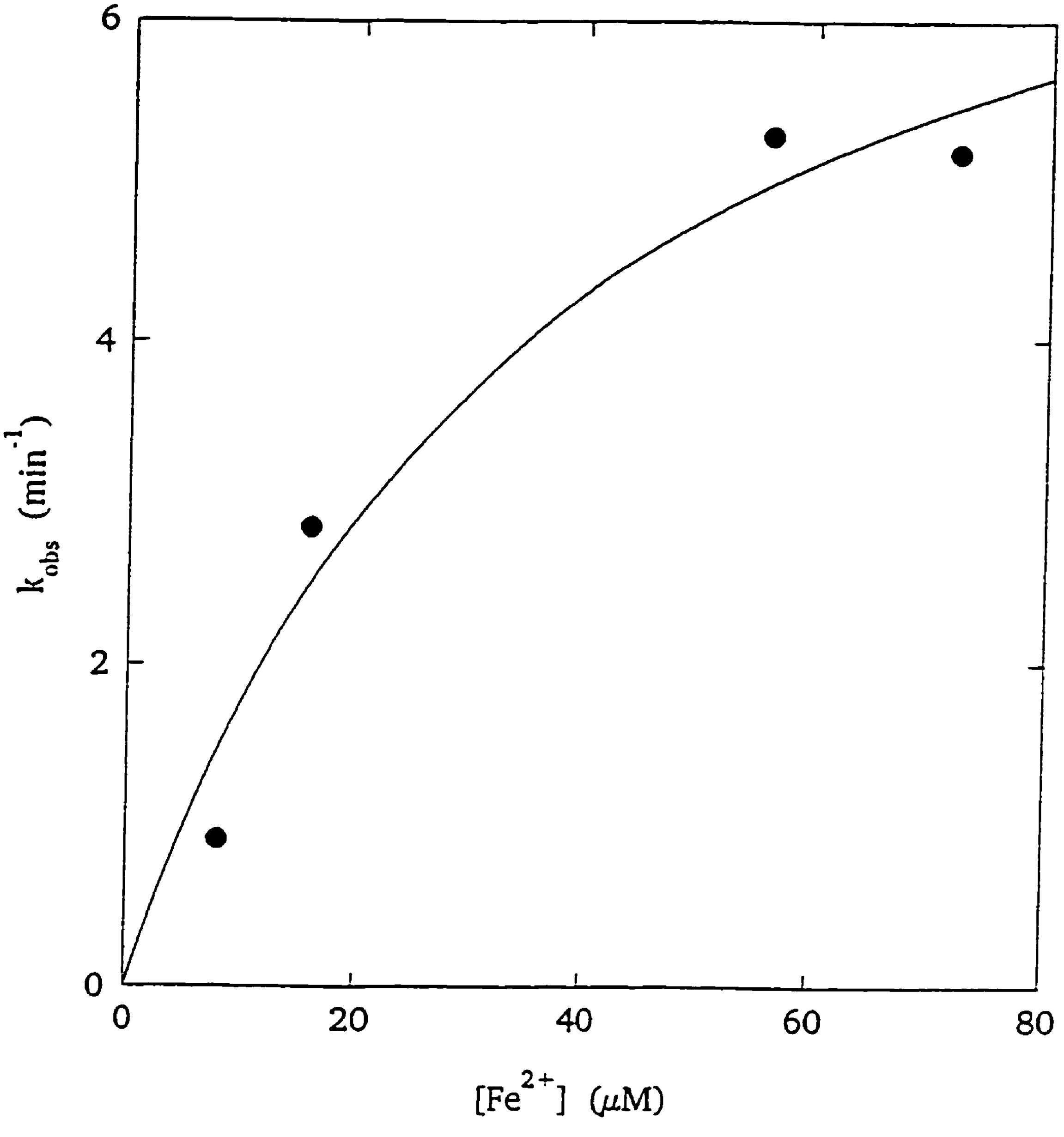

Figure 3.9. Dependence of the Fe^{2+}-B hydrolysis rate on Fe^{2+}. Reactions were carried out at 8 μM dexrazoxane, in Tris/KCl buffer, pH 7.4, at 15 °C. Experimental data (symbols) were fitted to Equation 3.7 (line) to yield parameters of 8.2 min^{-1} and 37 μM for k_{max} and K, respectively.

in which k_{max} is the limiting value of k_{obs}, and K is the concentration of Fe^{2+} at which $k_{obs} = \frac{1}{2} k_{max}$, and, because it is the rate-determining species, [Fe^{2+}-**B**] is half the total concentration of **B**. The values obtained for these parameters are 8.2 min^{-1} and 37 μM, respectively.

The proposed reactions describing the kinetics and absorbance changes observed are, in the case of **B**:

$$Fe^{2+} + \mathbf{B} \rightleftharpoons Fe^{2+}\text{-}\mathbf{B} \qquad \text{(fast complex formation)} \qquad (3.8)$$

$$Fe^{2+}\text{-}\mathbf{B} + H_2O \rightarrow Fe^{2+}\text{-}\mathbf{D} \qquad \text{(fast } Fe^{2+}\text{-promoted hydrolysis)} \qquad (3.9)$$

$$Fe^{2+}\text{-}\mathbf{D} \xrightarrow{O_2} Fe^{3+}\text{-}\mathbf{D} \qquad \text{(slow aerobic oxidation)} \qquad (3.10)$$

The Fe^{2+} promoted hydrolysis of **C** is strongly pH dependent (Figure 3.10a). Above pH 7.6, hydrolysis was too fast to measure spectrophotometrically. The pseudo-first-order kinetic data were fitted to an equation describing a first order dependence on hydroxide ion:

$$k_{obs} = k_2 [OH^-] \qquad (3.11)$$

in which k_2 is a second order rate constant. From a linear least squares analysis, k_2 was found to be 1.13 ± 0.05 x 10^7 $M^{-1}min^{-1}$. If the reaction is first order in hydroxide ion, and is not influenced by any pK_a of Fe^{2+}-**C**, the log-log plot of this data, shown in Figure 3.10b, should be linear, since the logarithm of Equation 3.11 is:

$$\log k_{obs} = \log k_2 + m \cdot \log [OH^-] \qquad (3.12)$$

in which m, the order of the reaction in terms of hydroxide ion, should equal one. A plot of log k_{obs} *vs.* pH was linear, with a slope of 1.29 ± 0.07, consistent with first order dependence on hydroxide ion over this pH range. Since the Fe^{2+} promoted reaction displays a simple pH

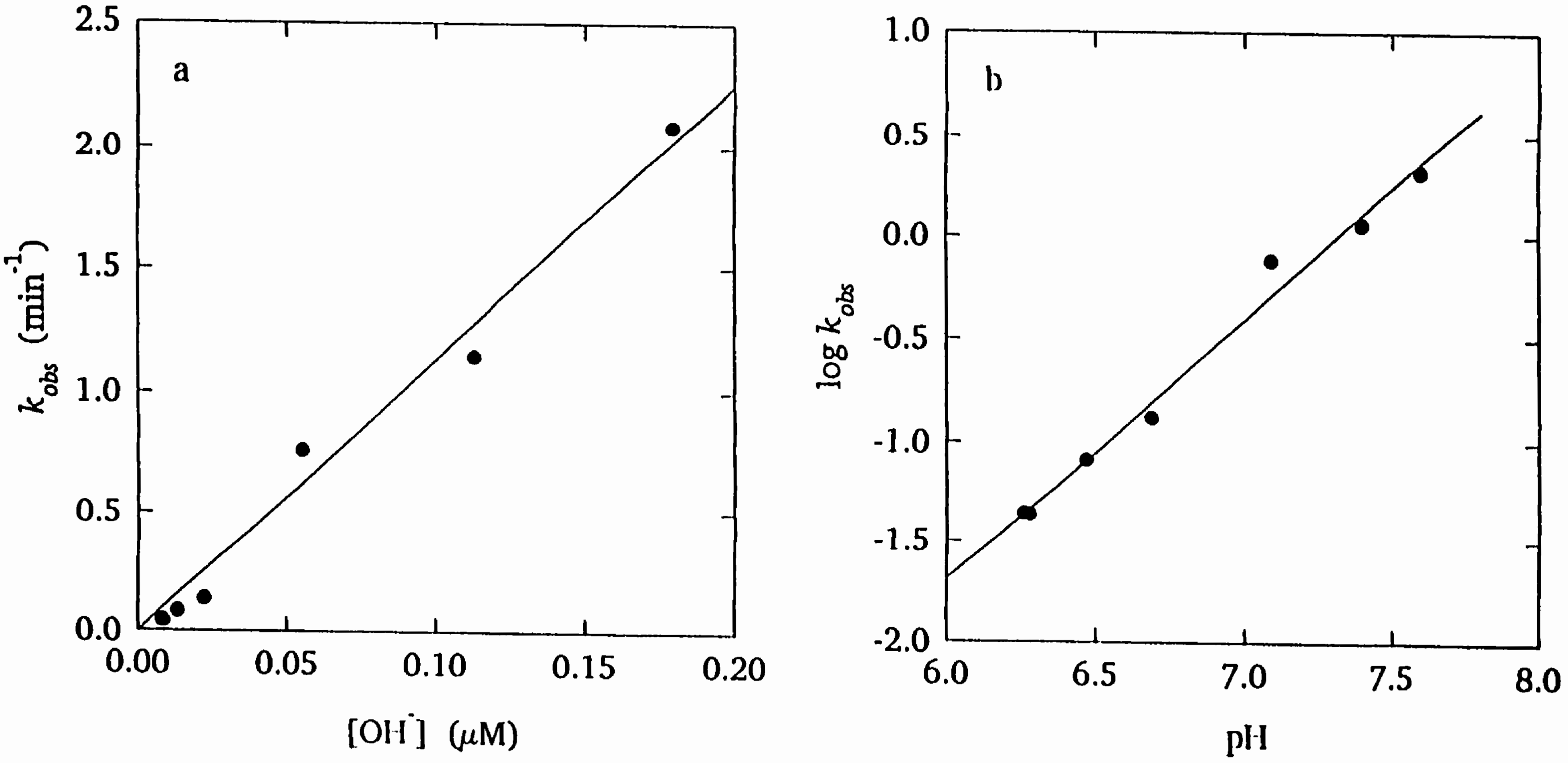

Figure 3.10. pH dependence of the hydrolysis of Fe^{2+}-C. Reactions were carried out at 24 μM in Tris/KCl buffer, titrated with NaOH, at 15 °C. a) Experimental data (●) and their least squares calculated line. b) Log-log plot of the data.

dependence over the accessible pH range, the mechanism to explain this dependence is simple. Because the log-log plot is linear (Figure 3.10b), any pK_a affecting hydrolysis kinetics must lie far outside this range. Thus, a simplification of Equation 3.4 for Fe^{2+}-promoted hydrolysis, with $K_{a2} = k_2 = 0$ and pH << pK_{a1}, yields the equation:

$$k_{obs} = (k_1 + \frac{k_3K_{a1}}{K_w})[OH^-] \qquad (3.13)$$

in which the composite term corresponds to k_2 in Equation 3.11. As with the Fe^{3+}-promoted reaction (Section 3.4), there is the problem of proton ambiguity with the reaction pathways, with rate constants k_1 and k_3 kinetically equivalent. Hence in this case as well, the second order bimolecular reaction with external hydroxide ion as the nucleophile can not be distinguished from the first order intramolecular reaction of hydroxide ion bound to Fe^{2+}.

3.6 Discussion of the mechanism of Fe^{3+}- and Fe^{2+}-promoted hydrolysis of B and C

The metal ion promoted hydrolyses of amides by divalent metal ions such as Cu^{2+}, Ni^{2+}, Co^{2+} and Zn^{2+} have been well studied [160-162] as models for metalloenzyme proteases and hydrolases. Metal ion promoted hydrolysis of amides occurs when a coordinated water (or hydroxide ion) acts as a nucleophile towards the carbonyl carbon atom of the amide. Particularly large rate enhancements (up to 10^9) [160, 162] can occur when the amide undergoing hydrolysis forms a complex with the metal ion, placing the bound water close to the carbonyl carbon atom.

The kinetics of divalent metal ion (Zn^{2+}, Co^{2+}, Ni^{2+}, and Cu^{2+}) promoted hydrolysis of the amide bond in *N*-acylimidazoles [160] showed a strong dependence on hydroxide ion. In this case, due to the very large rate enhancements observed, the possibility of a bimolecular attack of external hydroxide ion was eliminated, as it exceeded the diffusion-controlled rate limit. Thus, it was certain that the nucleophile was coordinated hydroxide ion. Similarly, Zn^{2+}-promoted hydrolysis of a metal ion binding bicyclic azalactam also sharply increased with pH [161]. In this case, the intramolecular reaction was proposed on the assumption that Zn^{2+}-bound hydroxide ion was 10 times more reactive than Zn^{2+}-bound water. However, for the reactions studied here, if it is assumed that $k_1 \gg k_3K_{a1}/K_w$ for Equation 3.4, the second order rate constant k_1 is 1.8×10^5 $M^{-1}sec^{-1}$ (estimated from the slope of the line in Figure 3.10a), well below the diffusion-controlled rate limit of 10^9 - 10^{10} $M^{-1}sec^{-1}$ [163]; no distinction between the two processes can be made on the basis of the present data. Other possible mechanisms of rate enhancement include polarization of the imide carbonyl group, either by induction or through a hydrogen bond with one of the metal-bound water molecules. It has been demonstrated that **B** and **C** are strong enough chelating agents to displace Fe^{3+} from its complexes with anthracyclines (Section 2.3). Using molecular modelling based on the x-ray structure of Cu^{2+}-ICRF-198 [152], a structure for Fe^{3+}-**B**$(H_2O)_2$ was proposed (Section 2.5.2). In this structure, the oxygens of both the bound water molecules were positioned close to the carbonyl carbon atoms of the ring-closed imide (3.0 and 3.2 Å). The geometry of the proposed Fe^{3+}-**C** complex is consistent with the latter possibility. However, since the static and kinetic determinations of pK_a (10.8 and 9.8, respectively) for deprotonation of the imide functional group of **C** described in Section 3.4 are similar to the value of 9.6 determined for dexrazoxane [128], it appears that binding of **C** to Fe^{3+} does not significantly withdraw electrons from the imide group, which would result in a decrease in pK_a, due to reduced electron density on the imide nitrogen atom. Thus, the most likely mechanism by which Fe^{3+} accelerates hydrolysis of the one-ring open intermediates is through polarization of coordinated water molecules. Although Fe^{3+}-bound hydroxide ion is certainly a weaker nucleophile than the free species, it will be present in higher concentrations in the pH range of this study. Coordinated hydroxide ion is also localized; it is ideally situated to serve as a nucleophile. An alternate mechanism to explain the acceleration of hydrolysis of **B** and **C** by Fe^{2+} and Fe^{3+} involves intramolecular hydrogen bonding by the coordinated water molecules. Both of the coordinated water molecules of Figure 2.11 are well positioned to form hydrogen bonds with the imide carbonyl oxygen atoms. This could result in polarization of the imide bond, facilitating its hydrolysis.

At neutral pH, a fraction of the Fe^{2+}- and Fe^{3+}-bound water is likely ionized, and may be expected to be a good nucleophile [160]. The fact that Fe^{3+} is much less effective than Fe^{2+} in promoting the hydrolysis of **B** and **C** may be due to its stronger polarization of the bound hydroxide ion, which would reduce its nucleophilicity. Another possible explanation of the faster hydrolysis of **B** and **C** in the presence of Fe^{2+} may be the ability of bound water (or hydroxide ion) to dissociate more quickly from the less positively charged Fe^{2+} and substitute on the carbonyl carbon atom.

3.7 Implications of faster hydrolysis activation for *in vivo* dexrazoxane activity

The formation of **D** through the hydrolysis of dexrazoxane takes place under physiological conditions of pH 7.4 and 37 °C with a half-time of approximately 30 h [149, 164]. Given the slow hydrolysis of dexrazoxane, and its relatively rapid *in vivo* elimination (half-time of 4.2 h) [100], it is unclear how sufficient quantities of the active form of the drug could be present in heart tissue to chelate loosely bound iron, or to displace iron from its complex with doxorubicin. In the presence of 2 mM Fe^{2+}, **D** was produced with a half-time of 9 h (Figure 3.7), *i. e.* the same rate at which dexrazoxane hydrolyzes to its one-ring open intermediates, **B** and **C**. **B** and **C** are not observed; they are hydrolyzed as soon as they are produced, which is in agreement with the rapid hydrolysis rates of the Fe^{2+} complexes of **B** and **C** reported in Section 3.5.

It is proposed that the protective action of dexrazoxane may involve either the enzymatic (dihydropyrimidine amidohydrolase) [124] or non-enzymatic [117, 149] formation of the one-ring open intermediates, **B** and **C**. These intermediates could chelate free iron or displace iron from its anthracycline complexes (Chapter 2). The Fe^{2+} complexes of **B** and **C**, so formed, would then undergo a rapid conversion to Fe^{2+}-**D**. Displacement of iron from its complexes with anthracyclines would decrease the oxygen-radical-induced lipid peroxidation caused by redox cycling of the membrane-bound Fe^{3+}-doxorubicin complex [45]. The Fe^{3+} complexes of **B** and **C** would also undergo a slower metal ion promoted hydrolysis. However, biological reducing agents, such as ascorbate, or reducing enzymes, such as NADPH-cytochrome-P450-reductase, may reduce the Fe^{3+} complexes of **B** and **C** to their Fe^{2+} states, which would then undergo rapid conversion to Fe^{2+}-**D**. Since available cellular iron concentrations are estimated to be very low, it is uncertain whether iron-accelerated hydrolysis is significant *in vivo*. However, the hydrolysis products of dexrazoxane are stronger chelators than anthracyclines; since the latter species are able to chelate iron *in vivo* [22, 24, 25], so must the former.

It is Fe^{2+} which reduces H_2O_2 to the extremely reactive and damaging hydroxyl radical [54, 55]. It is also in the presence of the potentially damaging Fe^{2+} that **B** and **C** are most rapidly hydrolyzed to a strong chelator. In this way dexrazoxane may reduce the ability of the Fe^{2+} to participate in site-specific hydroxyl radical damage. EPR spin trapping studies have shown that while the Fe^{3+}-**D** complex is able to produce hydroxyl radicals in a NADPH-cytochrome-P450-reductase system, it does so only at a very low rate [165].

Chapter 4 Metal ion promoted hydrolysis of dexrazoxane

4.1 Introduction

Since it has been demonstrated that the Fe^{3+}-anthracycline complex initiates oxidative stress *in vitro* [7, 8], it is believed that this is the mechanism of their cardiotoxicity. Dexrazoxane presumably protects against anthracycline-induced cardiac damage by hydrolyzing to its chelating forms, which bind redox cycling metal ions, thereby reducing their interaction with anthracyclines (Section 2.3).

Dexrazoxane hydrolyzes to its final product, **D**, *via* one of two one-ring open intermediates, **B** or **C** (Figure 4.1) [117]. Since it was shown that Fe^{2+} and Fe^{3+} accelerate the hydrolysis of **B** and **C** (Chapter 3), the effects of other biologically relevant metal ions on these reactions should also be examined, to determine their relative activities and to probe the mechanism of catalysis. Since hydrolysis of dexrazoxane produces the active chelating species, the rates of reaction in the presence of metal ions of biological interest may prove useful in determining the fate of dexrazoxane *in vivo*. Because little is known of the pharmacokinetics of dexrazoxane, characterization of its hydrolysis *in vitro* will provide valuable information about its hydrolysis rate *in vivo*. If dexrazoxane hydrolyzes significantly faster in the presence of biological metal ions, its activation rate *in vivo* may be much faster than in Tris buffer, pH 7.4 at 37 °C ($t_{½}$ = 28 h) [128].

4.2 Materials and methods

$MgCl_2 \cdot 6H_2O$, optical grade KCl, and volumetric Fe^{2+} standard were purchased from Aldrich (Milwaukee, WI). $FeCl_3 \cdot H_2O$, $MnCl_2 \cdot 4H_2O$, and $ZnCl_2$ were purchased from BDH

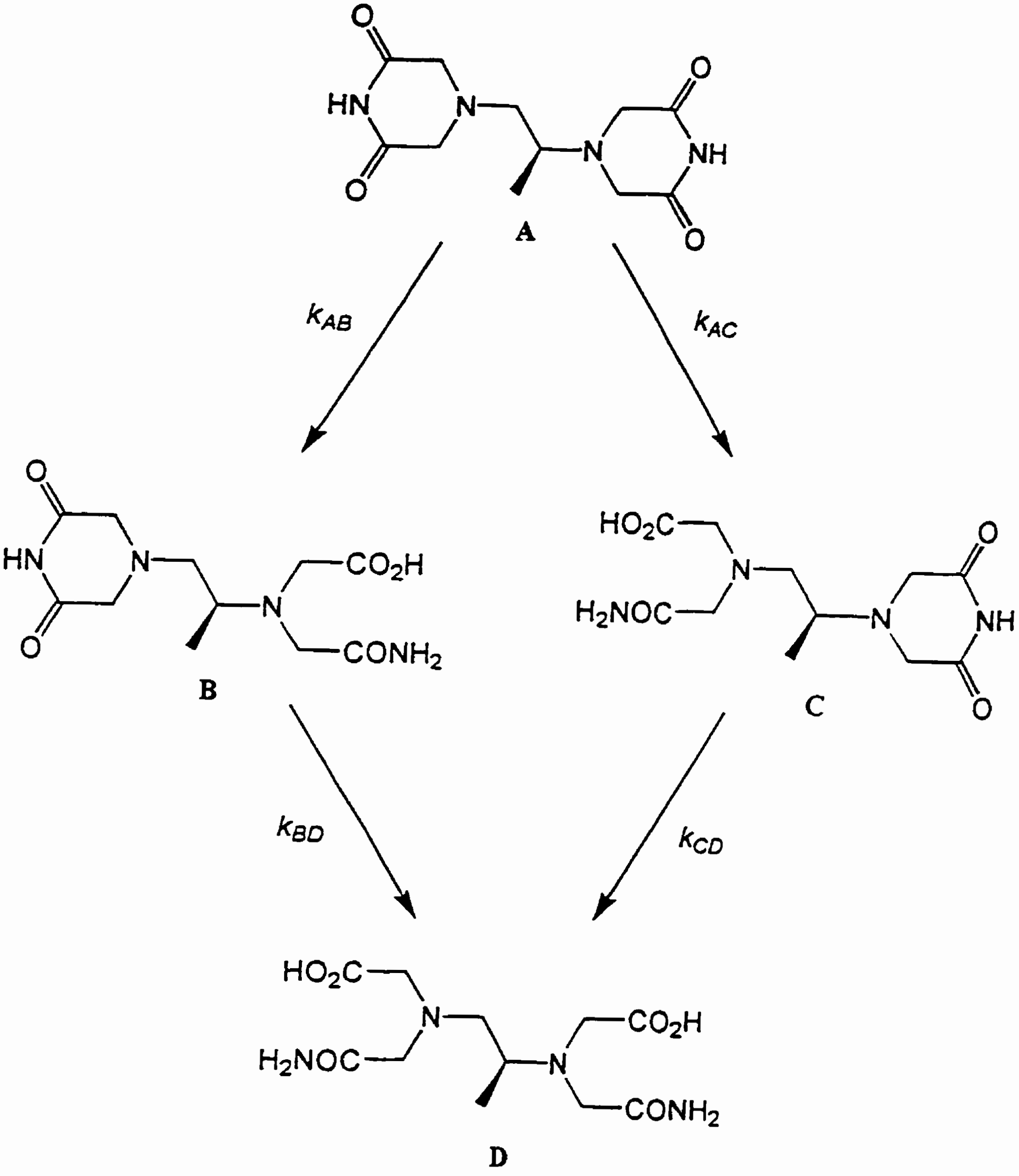

Figure 4. 1. Reaction scheme for the hydrolysis of ICRF-187 (Dexrazoxane, **A**) to its one-ring open intermediates (**B** and **C**), and its final hydrolysis product, ADR-925 (**D**). At constant pH, the reactions shown are pseudo-first-order, described by the rate constants k_{AB}, k_{AC}, k_{BD}, and k_{CD}.

(Montreal, Canada). $Ni(NO_3)_2 \cdot 6H_2O$ and disodium EDTA were purchased from Analar (Poole, England). $CoCl_2 \cdot 6H_2O$ was purchased from Fisher (Fair Lawn, NJ). $CuCl_2 \cdot 5H_2O$, $CaCl_2$ and KCl were purchased from Anachemia (Montreal, Canada). Tris base and Tris hydrochloride were obtained from Sigma (St. Louis, MO) in two grades; reagent and SigmaUltra, of which the latter was used for spectrophotometric measurements in the UV range, since it contributed less to the background absorbance. Dexrazoxane was obtained from Adria Laboratories (Columbus, OH). The one-ring open hydrolysis intermediates **B** and **C** were isolated as described in Section 2.2.

The time-course studies of dexrazoxane hydrolysis were performed by HPLC, using a Waters μBondapak 10 μm 3.9 x 300 mm reverse phase C_{18} column, as described in Section 2.2. **B**, **C**, and **D** were detected at 205 nm, and dexrazoxane was detected at 212 nm. Incubations were at pH 7.4 and 37 °C in a buffer of 50 mM Tris and 150 mM KCl. Samples were stored at -20 °C in 0.05 M HCl and 0.008 M EDTA until analyzed.

Stock solutions of dexrazoxane were prepared daily in 20 mM HCl, and were stored on ice until used. Kinetic studies of metal-ion-accelerated dexrazoxane hydrolysis were performed spectrophotometrically in quartz cells in a Cary 1 spectrophotometer (Varian, Mulgrave, Australia) thermostatted at 37 °C in 50/150 mM Tris/KCl buffer, pH 7.4, unless otherwise indicated. Reactions were initiated by addition of the metal ion, except in the case of Fe^{3+}. For this metal ion, the Fe^{3+} complexes were preformed in 20 mM HCl to prevent precipitation of ferric hydroxides, and reactions were initiated by addition of the complex to the buffer, to which NaOH had been added to neutralize the HCl. The hydrolysis of dexrazoxane was observed at 207 nm, except in pH dependence experiments, in which the absorbance was measured at 215 nm. The Tris buffer was titrated with Tris base, rather than NaOH, to minimize its absorbance at low wavelengths, except in the pH dependence experiments, in which the buffer was titrated with NaOH. For these experiments, pH values were measured immediately after each experiment.

4.3 Time-course studies of metal ion promoted dexrazoxane hydrolysis

The possibility that biological metal ions may accelerate the hydrolysis of dexrazoxane under physiological conditions was examined. Dexrazoxane and its hydrolysis products can be separated by HPLC and detected spectrophotometrically. A sample chromatogram is shown in Figure 4.2. The most polar species, **D**, is eluted near the solvent front, followed by a near baseline separation of **B** and **C**. Dexrazoxane is much less polar than its hydrolysis products, and is eluted in the presence of 10% methanol. The kinetics of dexrazoxane hydrolysis was determined at pH 7.4 and 37 °C (Figure 4.3a). Under these conditions, the dexrazoxane concentration (**A**) decreased exponentially, while **B** and **C** both increased, reached maximum levels at approximately 20 h, and decreased. The concentration of **D** increased sigmoidally. The data shown in Figure 4.3a-c were normalized such that the sum of the amount of the four species for each time point was one. The four hydrolysis reactions were fitted simultaneously by a non-linear least-squares method, to the integrated rate equations describing their kinetics [149]:

$$A = A_0 e^{-(k_{AB} + k_{AC})t} \qquad (4.1)$$

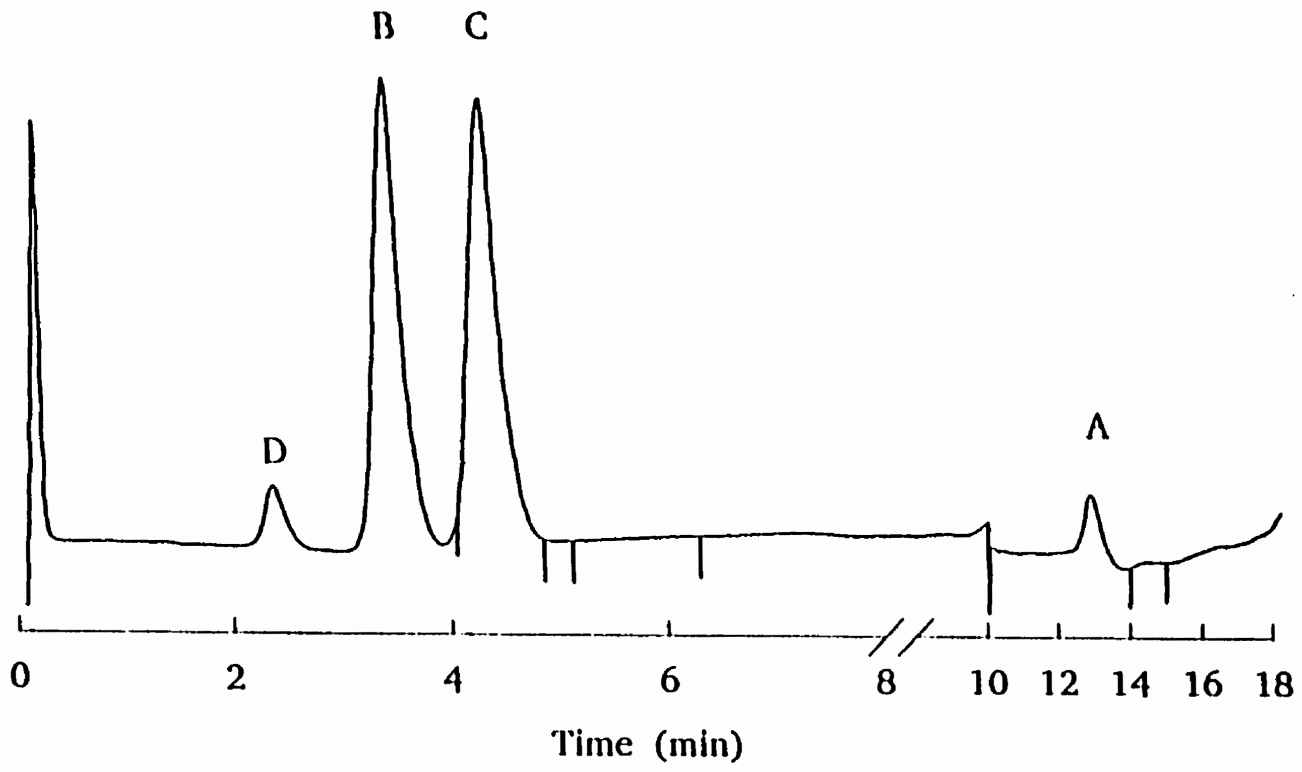

Figure 4.2. Sample HPLC chromatogram of dexrazoxane and its hydrolysis products. The retention times for **A**, **B**, **C**, and **D** are approximately 2.4, 3.5, 4.3, and 13 minutes, respectively. The sample was prepared by incubating 8.6 mg/mL dexrazoxane in 130 mM NaOH at 25 °C for 40 min, and then acidifying with 1 M HCl.

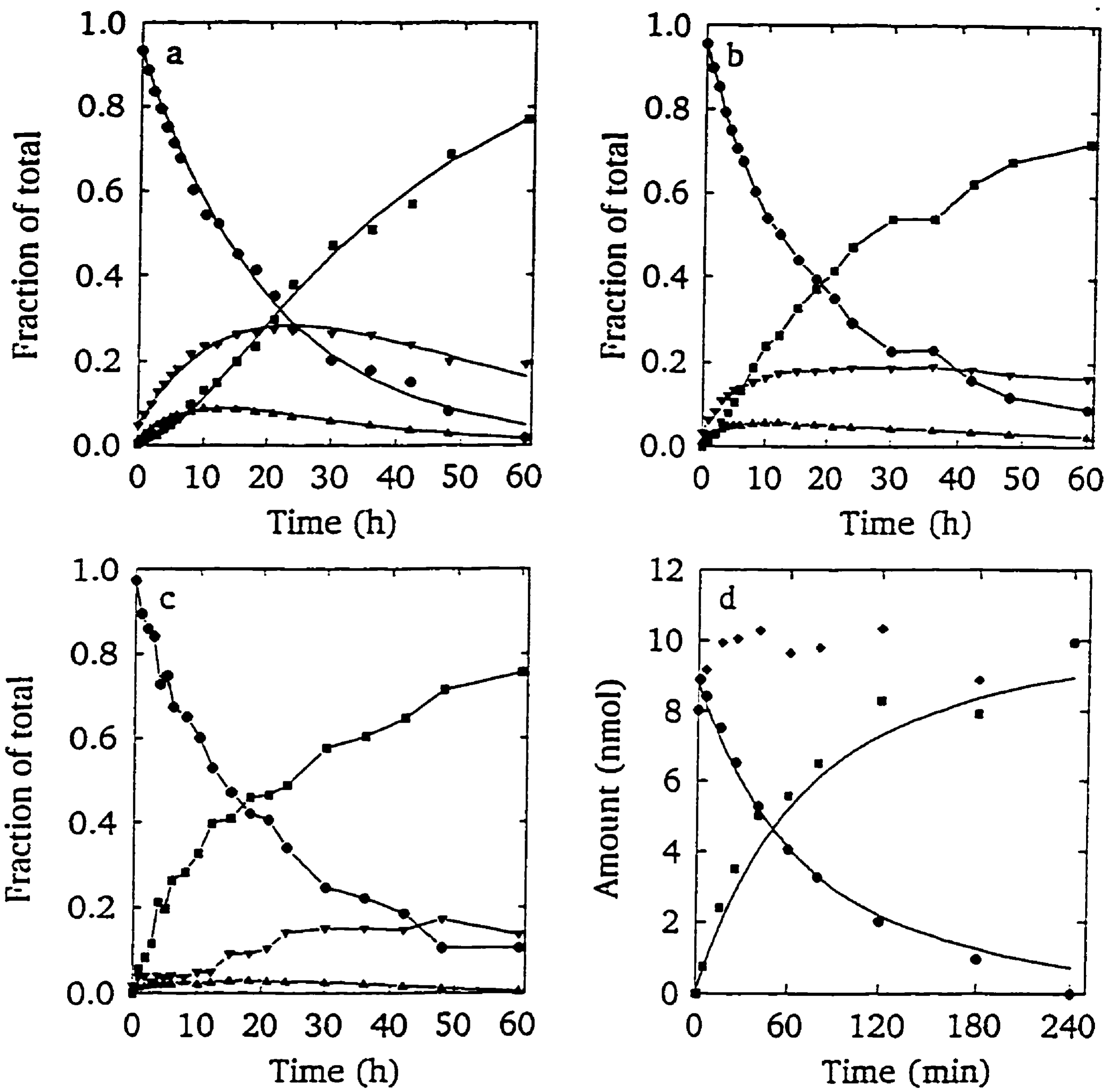

Figure 4.3. Kinetics of dexrazoxane hydrolysis at 37 °C, pH 7.40. Symbols represent dexrazoxane (●), **B** (▼), C(▲), and **D** (■). a) 5 mM dexrazoxane, no metal ion. Solid curves are the simultaneously solved eight-parameter integrated rate equations for the four species present. The half-time for the disappearance of dexrazoxane is 12 h, and the half-time for the production of **D** is 33 h. b) 5 mM dexrazoxane, 2.5 mM Mg^{2+}. The half-time for the disappearance of dexrazoxane is 12 h, and the half-time for the production of **D** is 27 h. c) 5 mM dexrazoxane, 2.5 mM Ca^{2+}. The half-time for the disappearance of dexrazoxane is 12 h, and the half-time for the production of **D** is 24 h. d) 1 mM dexrazoxane, 2.5 mM ZnCl$_2$. The half-times for the disappearance of dexrazoxane and production of **D** are 60 min. For a),b), and c), data are normalized; the sum of the four species is one. For d), the sum of the detected species is shown (◆).

$$B = \frac{k_{AB}A_0}{k_{BD} - (k_{AB} + k_{AC})} e^{-(k_{AB} + k_{AC})t} + \left(B_0 - \frac{k_{AB}A_0}{k_{BD} - (k_{AB} + k_{AC})}\right) e^{-k_{BD}t} \qquad (4.2)$$

$$C = \frac{k_{AC}A_0}{k_{CD} - (k_{AB} + k_{AC})} e^{-(k_{AB} + k_{AC})t} + \left(C_0 - \frac{k_{AC}A_0}{k_{CD} - (k_{AB} + k_{AC})}\right) e^{-k_{CD}t} \qquad (4.3)$$

$$D = A_0 + B_0 + C_0 + D_0 - (A + B + C) \qquad (4.4)$$

in which A_0, B_0, C_0, and D_0 are the concentrations of dexrazoxane, **B**, **C**, and **D** at t = 0, and k_{AB}, k_{AC}, k_{BD}, and k_{CD} are the pseudo-first-order rate constants describing the reactions shown in Figure 4.1. The fits were weighted according to the sensitivity of the spectrophotometric detector to each of the four species [128]. The values of the eight fitted parameters are shown in Table 4.1. At 37 °C and pH 7.4, in the absence of metal ions, the half-time for the disappearance of dexrazoxane is 12 h, while the half-time for the production of **D** is 33 h (Figure 4.3a). These values are in agreement with those of previous determinations [128, 149], as shown in Table 4.1.

Table 4.1. Values of calculated parameters for the simultaneous solution of the integrated rate equations for the hydrolysis of dexrazoxane at pH 7.4 and 37 °C.

Parameter	Value [a]	Value[b]
A_0	0.937 ± 0.007 [c]	n. r.[d]
B_0	0.047 ± 0.003[c]	n. r.[d]
C_0	0.016 ± 0.003[c]	n. r.[d]
D_0	indeterminate[c,e]	n. r.[d]
k_{AB}	0.0307 ± 0.0006 h^{-1}	0.052 ± 0.001 h^{-1}
k_{AC}	0.0185 ± 0.0009 h^{-1}	0.022 ± 0.001 h^{-1}
k_{BD}	0.032 ± 0.001 h^{-1}	0.040 ± 0.001 h^{-1}
k_{CD}	0.1042 ± 0.006 h^{-1}	0.082 ± 0.004 h^{-1}

[a] Errors are fitting errors only.
[b] determined previously [128].
[c] Since the data were normalized, these parameters are unitless.
[d] Not reported.
[e] This parameter converged to a very small number.

In the presence of physiological concentrations of Mg^{2+} and Ca^{2+} (Figure 4b&c, respectively), results were qualitatively similar. Half-times for the disappearance of dexrazoxane were estimated from the graphical data and calculated by determination of initial rates (Table 4.2) for the disappearance of dexrazoxane indicate that the half-times for the disappearance of dexrazoxane were unchanged in the presence of these metal ions, indicating that they do not affect the hydrolysis of the first imide ring. The half-times for the production of **D** were reduced to 27 and 24 h, respectively. Thus, the hydrolysis of the second ring has been accelerated in the presence of Mg^{2+} and Ca^{2+}. Since the waters of hydration of these ions are polarized, metal-bound hydroxide ion may be the nucleophile at neutral pH, rather than free hydroxide ion. However, since the presence of Ca^{2+} and Mg^{2+} had no effect on the hydrolysis of dexrazoxane, a mechanism specific to **B** and **C** is more likely. There must be an interaction between the one-ring open intermediates, which may act as tetradentate ligands (Section 2.5), and these metal ions. Weak complexes may be formed between these ions and **B** and **C**, which behave similarly to the proposed complex of Fe^{3+}-**C** (Section 2.5.2), either polarizing the ligand, or promoting an intramolecular nucleophilic attack.

Table 4.2. Initial rates for the metal ion promoted hydrolysis of dexrazoxane, and the half-times for its complete hydrolysis.[a]

Metal Ion	Metal Ion Concentration (mM)	Dexrazoxane Concentration (mM)	Initial Rate of Dexrazoxane Hydrolysis (h^{-1} ± SEM[b])	$t_{1/2}$ of Formation of **D** (h)
None	--	5.0	0.0411 ± 0.001	33
Mg^{2+}	2.5	5.0	0.0442 ± 0.002	27
Ca^{2+}	2.5	5.0	0.0410 ± 0.044	24
Zn^{2+}	2.4	1.0	0.11 ± 0.01	0.55

[a] Reactions were studied at 37 °C in Tris/KCl buffer, pH 7.4. Initial rates and their standard errors of the mean were calculated from the linear least-squares slopes over the first 10% of the data in Figure 4.3. Half-times were determined by interpolation.

[b] Standard error of the mean.

In the presence of 2.4 mM Zn^{2+} (Figure 4.3d), the half-time for the disappearance of 1 mM dexrazoxane was reduced to 0.55 h. Thus, Zn^{2+} interacts directly with dexrazoxane, as has been shown for Cu^{2+} [152]. Since **B** and **C** were not observed, their hydrolysis is accelerated such that they are hydrolyzed immediately, and do not accumulate in the reaction mixture. The first 60% of the data for dexrazoxane were fitted to a second order rate equation for unequal starting concentrations:

$$\ln\left(\frac{[D]_0\,([Zn^{2+}]_0 - [D])}{[Zn^{2+}]_0\,([D]_0 - [D])}\right) = ([Zn^{2+}]_0 - [D]_0)kt \qquad (4.5)$$

in which **D** is dexrazoxane, k is the apparent second-order rate constant, and t is the time in minutes. The data for dexrazoxane, subtracted from the initial concentration of dexrazoxane, were also fitted to Equation 4.5. The values obtained for k were 5.8 ± 0.2 and 10.0 ± 0.2 M^{-1} min^{-1} for the dexrazoxane and **D** data, respectively.

Since the one-ring open intermediates were not detected, it is not known whether **B** and **C** are produced in the same relative amounts as in the absence of Zn^{2+}. Although there is a difference between k_{AB} and k_{AC} at pH 7.4 (Table 4.1), at high pH, when the concentration of the preferred nucleophile is higher, the two rate constants are nearly identical [128]. Since Zn^{2+} promotes the hydrolysis rate by reducing the activation energy barrier, it may also be reducing the selectivity of the reaction.

4.4 Kinetics of Zn^{2+}-promoted dexrazoxane hydrolysis

The acceleration of dexrazoxane hydrolysis by Zn^{2+} was further investigated. The hydrolysis reactions of dexrazoxane in the presence of Zn^{2+} were studied spectrophotometrically at 207 nm. To permit the study of this reaction in the presence of low concentrations of Zn^{2+}, initial rates (Figure 4.4a) were analyzed. Since no dependence of the amplitude of the absorbance changes on $[Zn^{2+}]$ was observed, a value for $\Delta\epsilon$ of 13620 M^{-1}

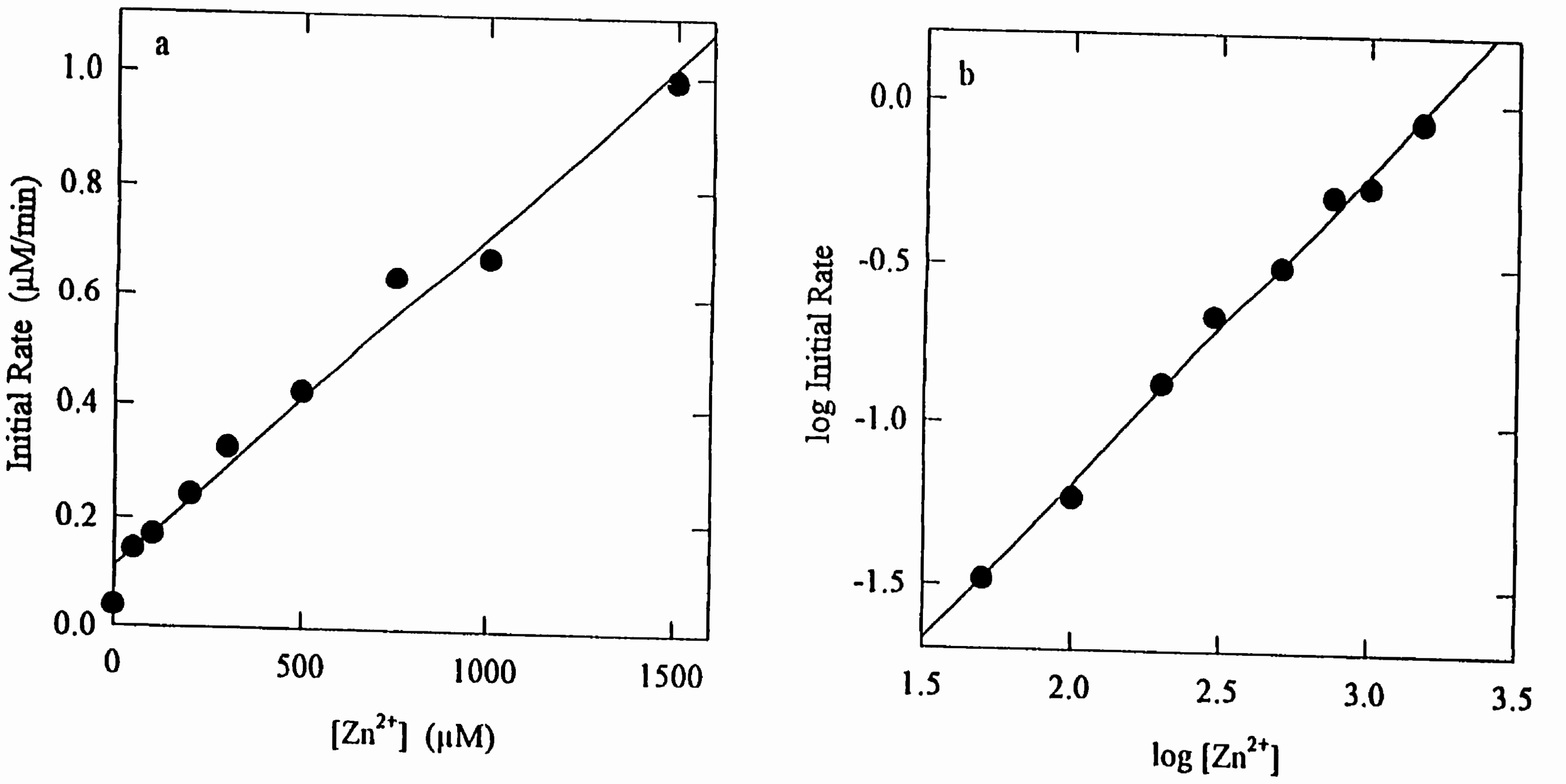

Figure 4.4. Dependence of Zn^{2+}-dexrazoxane hydrolysis rate at 37 °C and pH 7.40 on Zn^{2+}. Symbols (●) represent experimental data, and lines are the linear least squares fits of the data. a) dependence of the initial rate on [Zn^{2+}] at 100 μM dexrazoxane. b) log-log plot of the data, from which the Zn^{2+}-independent component has been subtracted (●), and linear least squares fit (line).

cm^{-1}, determined from first order experiments, was used. The hydrolysis of dexrazoxane in the presence of Zn^{2+} may be described by the following reactions:

$$\mathbf{A} \rightarrow \mathbf{D} \quad (4.6)$$

$$\mathbf{A} + Zn^{2+} \rightleftharpoons Zn^{2+}\text{-}\mathbf{A} \quad (4.7)$$

$$Zn^{2+}\text{-}\mathbf{A} \rightarrow Zn^{2+}\text{-}\mathbf{D} \quad (4.8)$$

Data were analyzed by curve fitting to a least squares linear equation:

$$Initial\ Rate = V_0 = -d[A]/dt = k_2[Zn^{2+}][A] + k_1[A] \quad (4.9)$$

in which **A** is dexrazoxane, and k_1 and k_2 are first- and second-order rate constants describing the Zn^{2+}-accelerated (Reaction 4.6) and unaccelerated (Reaction 4.8) hydrolysis pathways, respectively. The value obtained for the parameter k_2 was 6.0 M^{-1} min^{-1}, which is similar to the results obtained from HPLC data, for which the average of the values determined from dexrazoxane and **D** data is 7.9 M^{-1} min^{-1} (Figure 4.3d). The value of k_1, 0.0011 min^{-1}, determined from the intercept, compares reasonably well with the value of 0.050 h^{-1}, determined in this study from the HPLC data (the sum of k_{AB} and k_{AC} from Figure 4.3a), and other determinations of the observed first-order rate constant [128, 149]. Absorbance changes due to the Zn^{2+}-independent reaction, corresponding to the intercept of the fitted line in Figure 4.4a, were subtracted from each data point, and the resulting data were plotted on a log-log scale (Figure 4.4b). Since the slope of the fitted line was 0.98 ± 0.03, Zn^{2+}-promoted hydrolysis of dexrazoxane is first order in Zn^{2+}.

The initial rate of hydrolysis was also linearly dependent on the dexrazoxane concentration (Figure 4.5a), at a constant [Zn^{2+}] of 50 μM. Data were fitted to a least squares linear equation:

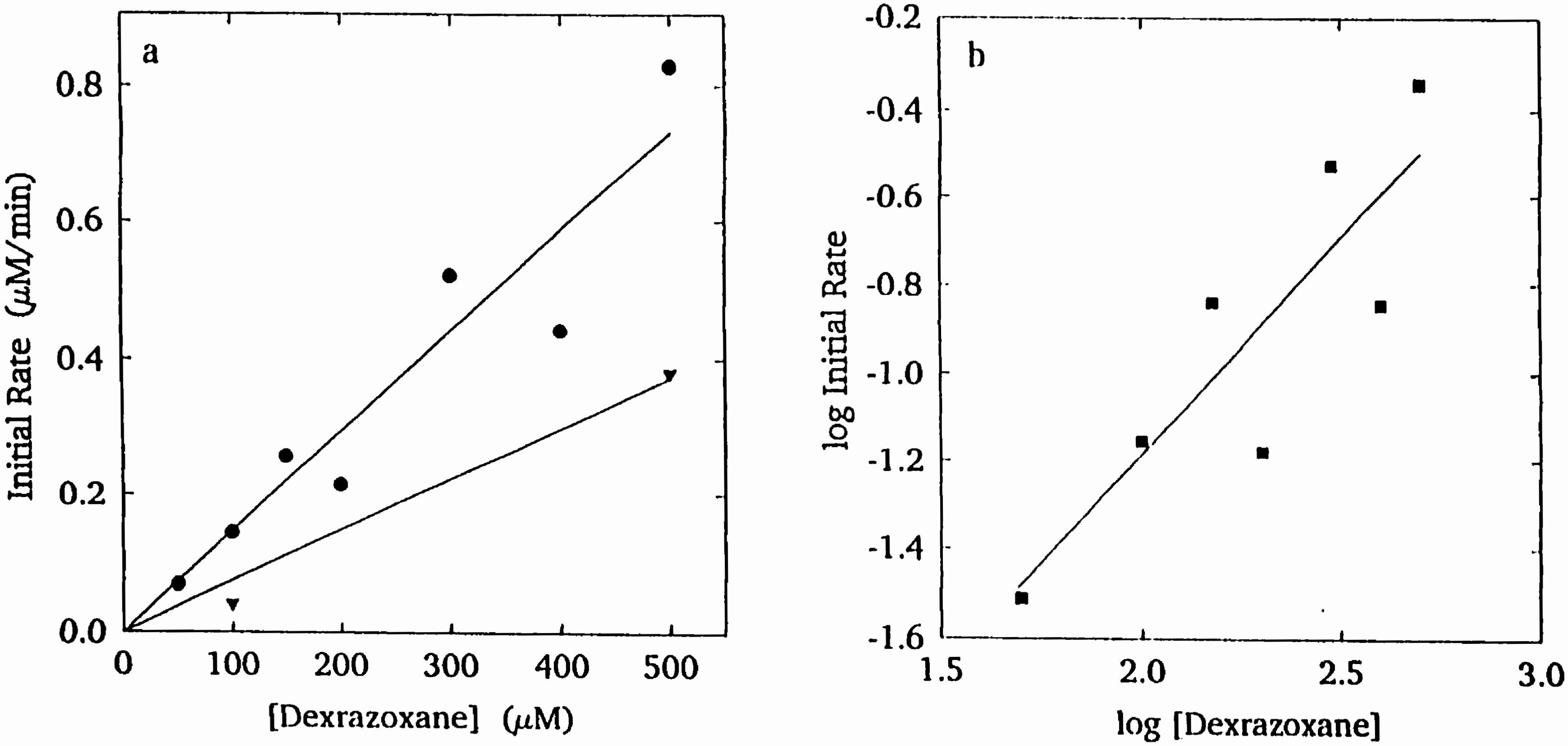

Figure 4.5. Dependence of Zn^{2+}-dexrazoxane hydrolysis at 37 °C and pH 7.40 on dexrazoxane. a) dependence of the initial rate on [dexrazoxane] in the presence (●) or absence (▼) of 50 μM Zn^{2+}. Straight lines were least squares calculated. b) log-log plot of the data corresponding to the Zn^{2+}-promoted pathway of hydrolysis only (■).

$$\textit{Initial Rate} = (k_2[Zn^{2+}] + k_1)[A] \qquad (4.10)$$

which accounts for Zn^{2+}-promoted and unpromoted hydrolysis pathways, both of which are significant over the concentration of Zn^{2+} used. The value of k_1, the pseudo-first-order rate constant describing the unaccelerated hydrolysis of dexrazoxane, was determined in the absence of Zn^{2+}, and subtracted from the total observed hydrolysis, yielding a value for k_2 of 13 M^{-1} min^{-1}. Given the relatively large error associated with this determination, since k_1 was estimated from two data points, this result compares well to other determinations (from data in Figures 4.3d and 4.4a). The slope of the log-log plot of the Zn^{2+}-promoted component was one (Figure 4.5b); this reaction was first order in dexrazoxane.

No curvature in the plot was observed up to 1.5 mM dexrazoxane, at which concentration the absorbance limited the experimentally accessible range. Therefore, the association between Zn^{2+} and dexrazoxane is weak, and only a small fraction of the total dexrazoxane concentration is present in its Zn^{2+}-associated state at any time. Thus, the rate enhancement due to this association must be large to cause the observed changes in overall reaction rate.

The pH dependence of the Zn^{2+}-promoted hydrolysis of dexrazoxane was studied, to provide information on the mechanism of the observed rate enhancement. Since the dependence of the molar absorptivity of the Zn^{2+}-dexrazoxane complex on pH is unknown, this reaction was not examined by its initial rate. Determinations of the pseudo-first-order rate constant, k_{obs}, were made by fitting the absorbance data to an equation describing first-order kinetics:

$$A = A_0 e^{-k_{obs}t} + A_\infty \qquad (4.11)$$

in which A_∞, A_0 and A are the absorbances at time infinity, 0 and t, respectively, and k_{obs} is the pseudo-first-order rate constant. The experimentally accessible pH range for determination of hydroxide ion dependence of this reaction is bounded at a lower limit of 7.0, at which the reaction becomes too slow to study, and an upper limit of 8.1, at which Zn^{2+} precipitates. The k_{obs} for the hydrolysis of dexrazoxane in the presence and absence of a 10-fold excess of Zn^{2+} were fitted to linear equations for descriptive purposes (Figure 4.6).

Although not as powerful a nucleophile as free hydroxide ion, Zn^{2+}-bound hydroxide ion would be present in much higher concentrations than free hydroxide ion at physiological pH, which may explain the faster hydrolysis of dexrazoxane in the presence of Zn^{2+}. It is possible that Zn^{2+} accelerates the hydrolysis of dexrazoxane by mechanisms analogous to those proposed for the acceleration of the hydrolysis of Fe^{3+}-C (Section 3.4), although the limited pH range over which this reaction was studied can not confirm a specific mechanism.

The hydrolysis of dexrazoxane in the presence of Zn^{2+} is first order in each species. Co^{2+}, Ni^{2+}, and Zn^{2+} have been shown to promote the hydrolysis of ICRF-154, an analog of dexrazoxane [166]. Since k_{obs} varied linearly with both [Zn^{2+}] and [dexrazoxane] over the experimentally accessible concentration ranges, there is no kinetic evidence for or against the formation of a Zn^{2+}-dexrazoxane complex. If such a complex exists, Zn^{2+} may bind the imide nitrogen or the carbonyl oxygen atoms, as Co^{2+} has been shown to do with succinimide [167]. Both interactions would result in a depletion of electron density on the carbonyl carbon atoms of the imide functional group, causing it to be more attractive to the nucleophile. Transition metals other than Zn^{2+} have been shown to bind dexrazoxane directly [166, 168]. Although the Cu^{2+}-dexrazoxane complex is known to have 1:2 stoichiometry [116], neither its structure

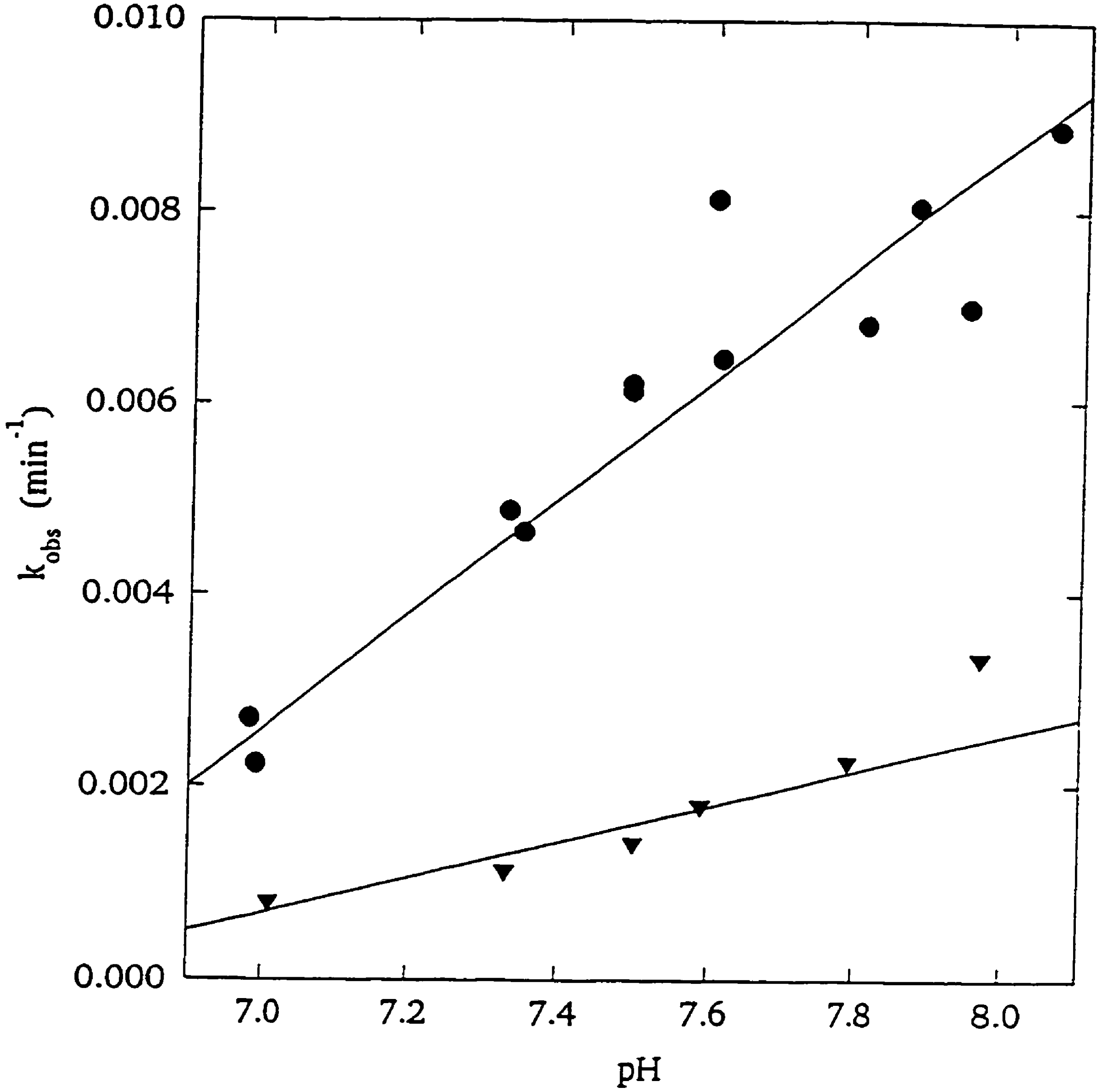

Figure 4.6. pH dependence of 40 μM dexrazoxane hydrolysis rate at 37 °C, in Tris buffer, in the presence (●) and absence (▼) of 400 μM Zn^{2+}. Solid lines are linear least squares fits of the data.

nor its mechanism of rate acceleration is known. A proposed complex for the Ga^{3+}-dexrazoxane complex involved metal ion co-ordination to the four nitrogen atoms of the drug [168], which seems unreasonable, since this requires the imide nitrogen atoms to leave the imide plane, reducing the stabilizing effect of electron delocalization.

4.5 Acceleration of hydrolysis of the one-ring open intermediates by other metal ions

Since Zn^{2+} had a significant effect on the hydrolysis of dexrazoxane, the effects of other metal ions were examined, as shown for **B** in Figure 4.7. Mn^{2+}, Fe^{2+}, Fe^{3+}, Co^{2+}, Ni^{2+}, Cu^{2+}, and Zn^{2+} promoted the hydrolysis of the one-ring open intermediates, **B** and **C**, when present in equimolar concentrations. Ca^{2+} and Mg^{2+} had no effect at this low concentration, but both significantly enhanced these hydrolysis reactions at 2.5 mM (Table 4.3). Data for **B** are shown in Figure 4.8. Since the amplitudes of the decreases in absorbance at 207 nm were consistent with those observed on hydrolysis of the imide ring [117], it was concluded that a complex was rapidly formed between the metal ion and the ligand, which hydrolyzed with pseudo-first-order kinetics, as was demonstrated for Fe^{3+} (Figure 3.4). The data were fitted to Equation 4.11, and k_{obs} are listed in Table 4.3. Many of the reactions were too fast to be accurately measured spectrophotometrically, as more than 50% of the reaction had occurred before the first absorbance measurement could be made. In all cases, hydrolysis of **C** was faster than **B**, which is consistent with their relative rates in the absence of metal ions (Table 4.3). At a 1:1 ratio of metal ion to ligand, the rate acceleration observed for **B** varied from 25-fold in the presence of Mn^{2+} to over 50,000-fold in the presence of Zn^{2+}. The fact that the

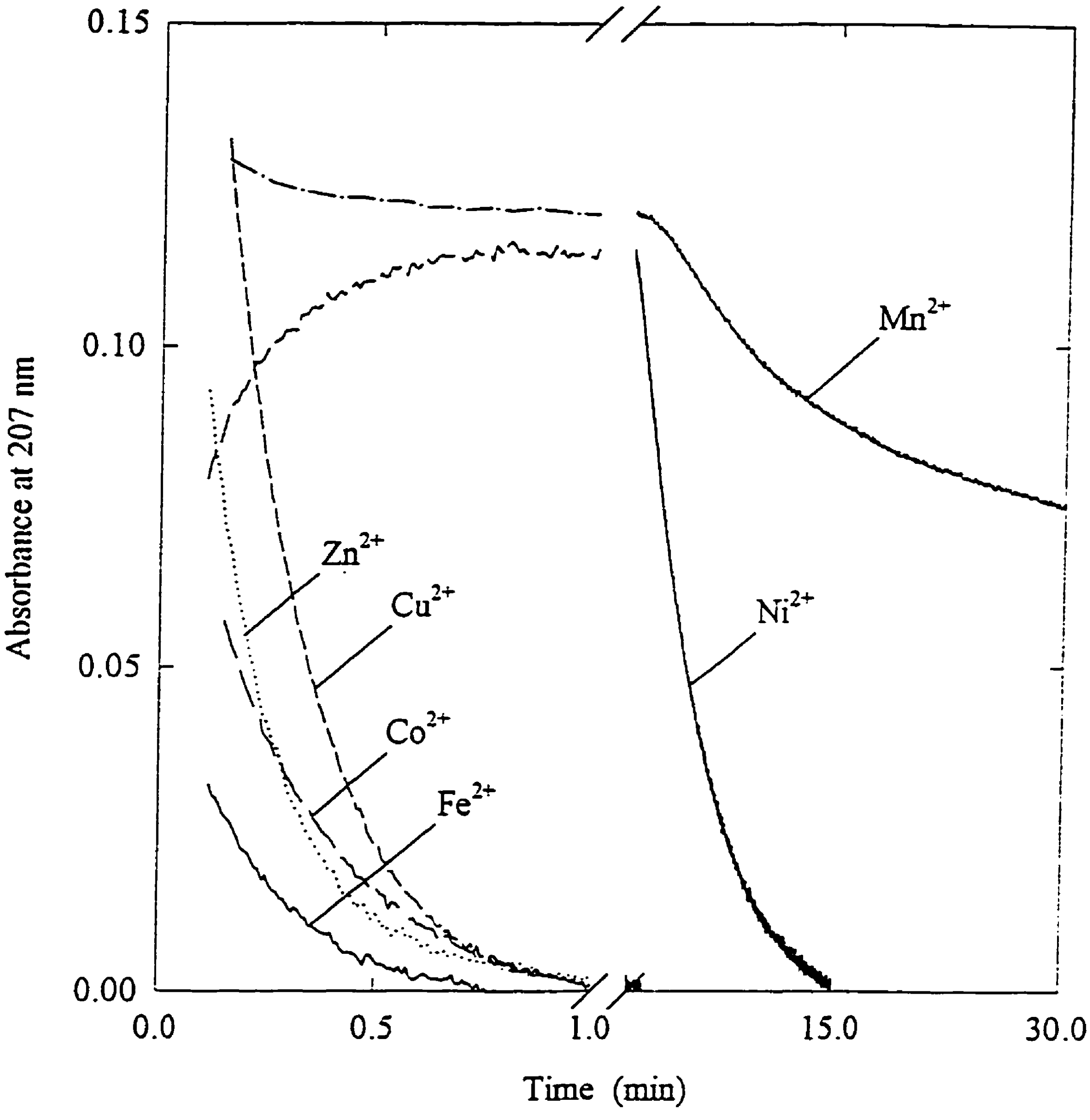

Figure 4.7. Decrease in absorbance with time for the metal ion promoted hydrolysis of **B**. Reactions were followed at 207 nm at 25 °C in Tris/KCl buffer, pH 7.4. Initial concentrations of metal ions and **B** were each 24 μM. These data were fitted (fits not shown) to Equation 4.8, and the first-order rate constants are listed in Table 4.3. The axis break on the abscissa marks the change in scale.

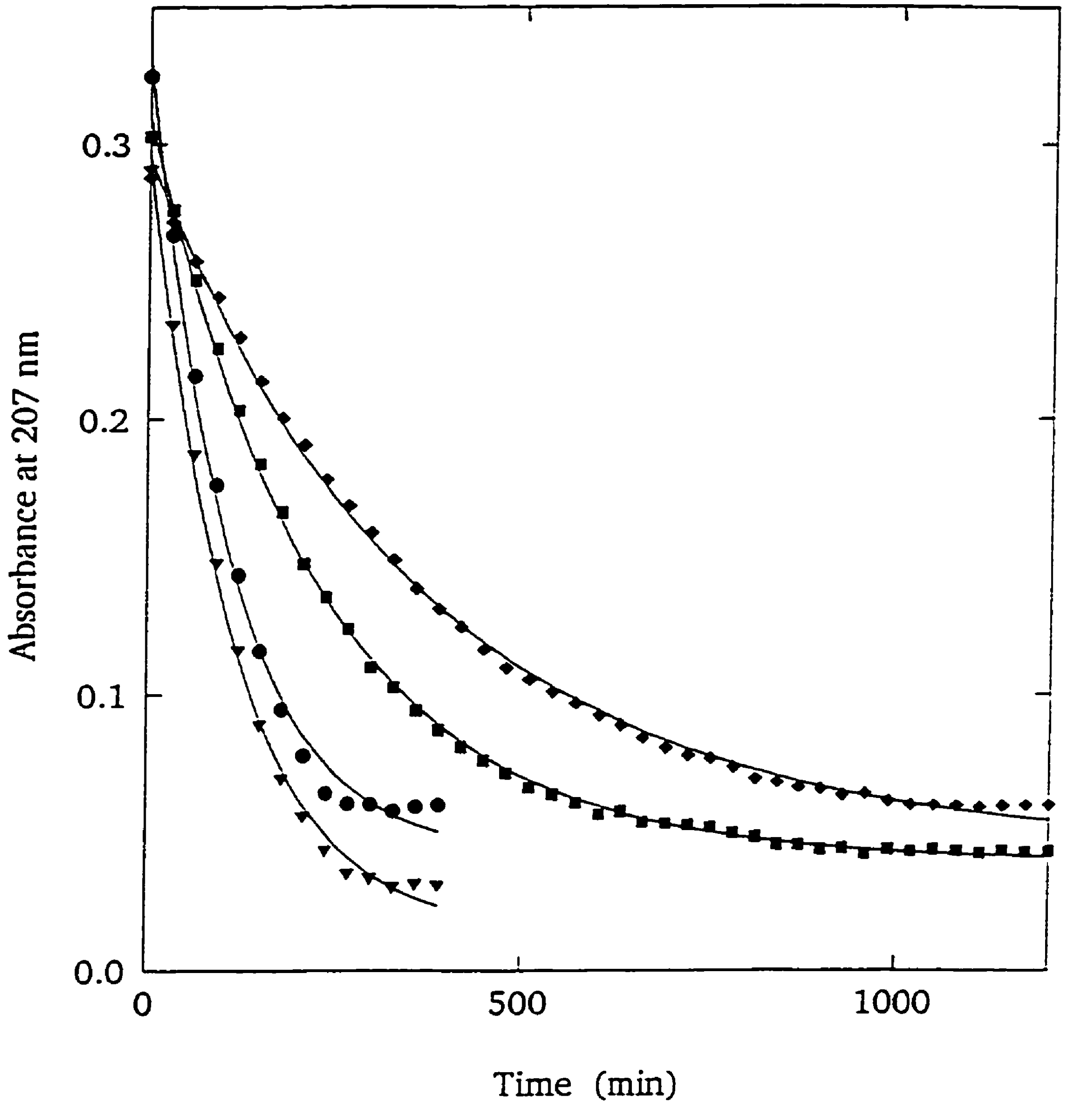

Figure 4.8. Decrease in absorbance with time for the hydrolysis of B and C in the presence of Mg^{2+} and Ca^{2+}. These reactions were followed at 207 nm at 25 °C in Tris/KCl buffer, pH 7.4, for Mg^{2+} and B (◆), Mg^{2+} and C (■), Ca^{2+} and B (▼), and Ca^{2+} and C (●). Data were fitted to Equation 4.8 (lines). Initial concentrations of B and C were 24 μM, and concentrations of Mg^{2+} and Ca^{2+} were 2.4 and 2.6 mM, respectively.

reactions of both **B** and **C** were too fast to be followed in the presence of equimolar Zn^{2+} is consistent with their absence as intermediates in the presence of 2.4 mM Zn^{2+} (Figure 4.3d).

Table 4.3. Rate constants for the pseudo-first-order hydrolysis of transition-metal-**B** complexes at 37 °C and pH 7.4.[a]

Metal ion	k_{obs} for **B** (min^{-1})	k_{obs} for **C** (min^{-1})
None [b]	0.00054[c]	0.00174[c]
Mg^{2+} [d]	0.0026[c]	0.0043[c]
Ca^{2+} [d]	0.0096[c]	0.0089[c]
Mn^{2+}	0.003[c]	0.202 ± 0.012[e]
Fe^{2+}	4.18 ± 0.13[f]	> 6 [c,g]
Co^{2+}	3.44 ± 0.07[f]	> 6 [c,g]
Ni^{2+}	0.231 ± 0.007[f]	3.46 ± 0.18[e]
Cu^{2+}	4.85 ± 0.08[e]	> 6 [c,g]
Zn^{2+}	> 6 [d,e]	> 6 [f,g]
Fe^{3+}	0.0042[c]	0.013[c]

[a] Reactions were studied at 207 nm in solutions containing 24 μM **B** or **C**, and 24 μM metal ion, except where otherwise indicated. Data were fitted to Equation 4.11.

[b] These data are k_{BD} and k_{CD}, respectively, determined in Section 4.3.

[c] These data are single measurements.

[d] These reactions were studied in the presence of 24 μM **B** or **C**, respectively, and either 2.4 mM Mg^{2+} or 2.6 mM Ca^{2+}.

[e] These data are the averages of two determinations. Errors are average deviations.

[f] These data are the averages of three determinations. Errors are standard errors of the mean.

[g] $t_{1/2} < 0.12$ min; reaction is too fast to be accurately measured.

The hydrolysis reaction in the presence of Ni^{2+} was preceded by a rapid increase in absorbance ($t_{1/2}$ of approximately 0.3 min, shown in Figure 4.7), likely corresponding to a change in the molar absorptivity of **B** as it forms a complex with the metal ion. Absorbance changes due to ligand association were not observed in the presence of other metal ions, which is likely due to their much faster rates of ligand substitution relative to Ni^{2+}. Ni^{2+} was much less effective than Cu^{2+}, Zn^{2+}, or Fe^{2+} at accelerating the hydrolysis of **B** and **C** (Figure 4.7 and Table 4.3). The rate enhancement observed in the presence of Ni^{2+}, and also for Fe^{3+} (Section 3.4), were smaller than for any of the other transition metal ions studied in this series. The lower rate enhancements observed in the presence of these two metal ions may also be due to their low ligand substitution rates, which may be rate-contributing.

Two fast spectral changes when **B** was incubated in the presence of Mn^{2+}, each of which was associated with a decrease in absorbance (Figure 4.7). These absorbance changes may be due to ligand association, or some other pre-equilibrium process. Since the third, slowest process had an amplitude similar to those observed in the presence of the other metal ions, it was assumed to be due to hydrolysis of the imide ring.

Although hydrolysis of the one-ring open intermediates in the presence of Fe^{2+} was not as well described by first-order kinetics as for the other metal ions, these data were also fitted to an exponential equation for comparison. Fe^{2+} oxidizes in air, causing absorbance changes in the UV range, which likely interfere with interpretation of the data. In addition, Fe^{2+} oxidation produces Fe^{3+}, which has a much smaller effect on hydrolysis; if the ratio of Fe^{2+} to Fe^{3+} changes significantly over the course of the reaction, the kinetics will be too complicated to analyze.

In the present experiments, the hydrolysis of **B** was accelerated by Fe^{2+} to a greater extent than observed in Section 3.5. There are some differences in experimental conditions which may account for this difference. The previously described experiments were observed in the presence of a 1.1-fold excess of **B** or **C**, while the present experiments were studied with a 1:1 ratio of Fe^{2+} to **B** or **C**. Thus, the equilibrium between Fe^{2+} and **B** shown in Figure 3.8 is shifted, and a larger fraction of the total **B** is present as the Fe^{2+}-associated species in the present experiments, causing an increase in the rate of the overall reaction. In addition, the concentrations of stock solutions of **B** and **C** were determined differently for the two experiments. Previously, they were determined spectrophotometrically, using half the molar absorptivity of dexrazoxane. Stock solutions for the present experiments were quantitated by HPLC, which is more accurate. Relatively small errors in the measurement of [**B**] cause the Fe^{2+}:**B** ratio to deviate from 1:1, changing the rate of the overall reaction.

Fe^{2+}, Co^{2+}, Zn^{2+}, and Cu^{2+} cause very similar rate enhancements of the hydrolysis of the one-ring open intermediates, and likely interact similarly with them. These ions cause much stronger rate enhancements than do Ca^{2+} and Mg^{2+}. These effects could be due to stronger binding of transition metals, which would result in a greater fraction of dexrazoxane bound as compared to Ca^{2+} and Mg^{2+}, and therefore a faster overall hydrolysis rate. The greater Lewis acidity of the transition metal ions is expected to have a stronger polarizing effect on either or both the imide and the nucleophile, thus increasing their reactivity. Metal ion promoted hydrolysis of amides has been studied as a model of metalloenzyme catalysis [160-162], and intramolecular nucleophilic attack of the metal-ion-bound amide by coordinated water has been demonstrated [160, 162]. In the case of a hydrated Zn^{2+}-

dexrazoxane complex, bound hydroxide ion would also be localized, increasing its nucleophilic efficiency.

A previous study reported crystallization of the Cu^{2+} complex of the one-ring open hydrolysis intermediates of dexrazoxane from a methanol-water solution [169]. Given the rapid hydrolysis rates observed for the Cu^{2+} complexes of **B** and **C** (Figure 4.7), it is unlikely that this species was correctly identified. The results of elemental analysis could not have been used to distinguish between the proposed complex and the more probable product, the Cu^{2+}-**D** complex.

4.6 Potential for metal ion accelerated hydrolysis of dexrazoxane *in vivo*

Neither Ca^{2+} nor Mg^{2+} promoted the hydrolysis of dexrazoxane itself. Both, however, had significant effects on the hydrolysis of its one-ring open intermediates at 2.5 mM (Table 4.2), the approximate total plasma or serum levels for these metal ions [170, 171]. The half-times for the production of **D** were decreased to 24 and 27 h in the presence of 2.5 mM Ca^{2+} and Mg^{2+}, respectively. Although it can not be expected that all the Ca^{2+} and Mg^{2+} in plasma is available to the chelators **B** and **C**, it is quite likely that these ions have a significant effect on the overall hydrolysis rate of dexrazoxane *in vivo*. Since Ca^{2+} is tightly sequestered in cells due to its regulatory role, its equilibrium concentration is low [170], and it is unlikely that it has an effect on intracellular dexrazoxane hydrolysis.

The total blood plasma Zn^{2+} concentration is approximately 8 μM [172]. Since Zn^{2+} is such a powerful catalyst for biological reactions, the majority is tightly sequestered, and therefore unavailable to promote the hydrolysis of dexrazoxane. The cellular concentration of Zn^{2+} has been estimated at 200 pM [172]. From the data of Figure 4.4a, it appears unlikely that biological levels of Zn^{2+} could significantly affect the hydrolysis of either dexrazoxane or its one-ring open intermediates, despite its strong rate enhancement.

Chapter 5 Quantitative structure-activity relationship between hydrolysis rate and molecular modelling parameters in imides, and prediction of the hydrolysis rates of new analogs

5.1 Relationship of the effectiveness of dexrazoxane as a cardioprotective agent to its hydrolysis rate

The results of Chapter 2 indicate that **B** and **C** are effective chelators, which are able to displace Fe^{3+} from its anthracycline complexes. Thus, the half-time for the production of effective species *in vitro* equals the half-time for the production of **B** and **C** (*i. e.* the sum of k_{AB} and k_{AC}, defined in the scheme of hydrolysis of dexrazoxane shown in Figure 5.1), which is approximately 9 h (Section 4.3) [120, 128]. The results of Chapters 3 and 4 indicate that the hydrolysis of dexrazoxane to **D** is accelerated in the presence of biological metal ions. Dexrazoxane likely has access to Mg^{2+} *in vivo*. However, 2.5 mM Mg^{2+} had no effect on the half-times for the first ring-opening reactions to be significantly affected (Section 4.5). Thus, any increase in the rate of dexrazoxane hydrolysis *in vivo* as compared to *in vitro* determinations (Section 4.3) [120, 128], is most likely due to the increased rate of production of **B** and **C** by dihydropyrimidine amidohydrolase [125].

Optimization of the rate of hydrolysis-activation of dexrazoxane *in vivo* is of interest in the development of analogs with improved cardioprotective properties. Since protection of the heart against doxorubicin-induced toxicity by dexrazoxane is due to its hydrolysis to **B**, **C**, and **D**, species which chelate Fe^{3+} (Chapter 2), increasing the rate at which the drug is activated may improve the cardioprotective ability of dexrazoxane, and it may also allow lower doses to be administered. In recent clinical trials, the dose of dexrazoxane was 1000

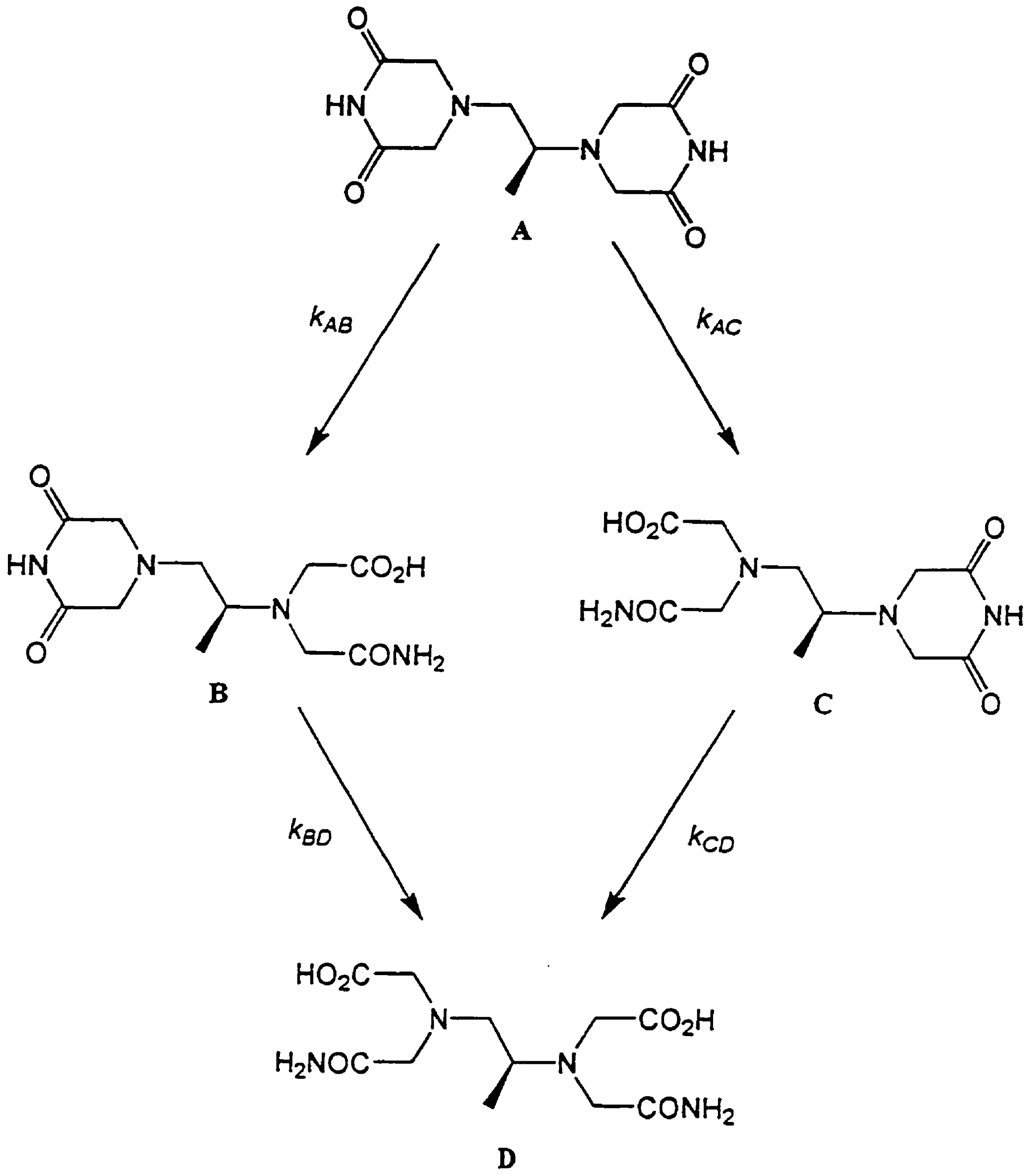

Figure 5.1. Reaction scheme for the hydrolysis of dexrazoxane (ICRF-187, **A**) to its one-ring open intermediates (**B** and **C**), and its final hydrolysis product, ADR-925 (**D**). At constant pH, the reactions shown are pseudo-first-order, described by the rate constants k_{AB}, k_{AC}, k_{BD}, and k_{CD}.

mg/m^2 body surface area [88], although it has been documented that doses above 600 mg/m^2 cause myelosuppression [100]. This is a serious side effect, especially since doxorubicin, with which dexrazoxane is administered, also causes myelosuppression. The development of an analog which hydrolyzes faster may allow lower doses to be administered, resulting in an improved therapeutic index. An analog with a two- to five-fold increase in the pH-dependent hydrolysis rate constant would produce significantly more chelating species. Such a moderate increase in hydrolysis rate would still permit distribution of the drug throughout the body tissues, since the hydrolysis rate constant would not exceed the distribution rate constant (approximately 1.4 h^{-1} [100]).

The objective of this study is to develop a quantitative structure-activity relationship between imide hydrolysis rate and molecular modelling parameters. An equation which predicts the hydrolysis rates of imides based on their theoretical structures will direct the synthesis of new analogs of dexrazoxane with faster hydrolysis rates. The hydrolysis reactions of a series of model imides will be characterized, and their structures will be optimized by molecular modelling algorithms, from which descriptors of their properties will be extracted. Equations describing imide hydrolysis in terms of these descriptors will be identified by multiple linear regression analysis, and the hydrolysis rates of a series of analogs of dexrazoxane will be predicted. Those with a two- to five-fold increase in hydrolysis rate will be identified as target compounds.

5.2 Mechanism of imide hydrolysis

The hydrolysis of imides occurs with the addition of water across one of the two C(carbonyl)-N bonds, *via* a base-catalyzed mechanism which follows pseudo-first-order kinetics at constant pH [173]. Studies of the pH dependence of imide hydrolysis [117, 120, 121, 174, 175] have demonstrated that, between pH values of approximately 7-13, the overall reaction depends on the concentrations of hydroxide ion and the fraction of the imide which is in its neutral form, as shown in Figure 5.2. Non-*N*-substituted imides are deprotonated at high pH, as has been shown for dexrazoxane [117]. The increased negative charge on the imide anion is, presumably, inductively and conjugatively distributed over the atoms of the functional group, thereby reducing its reactivity toward the negatively charged hydroxide ion. As a result, the pseudo-first-order rate constant describing imide hydrolysis reaches a limiting value; with increasing pH, the concentration of hydroxide ion increases and the concentration of neutral imide decreases. A similar pH dependence is expected for all imides in the data set which are not *N*-substituted. Base-catalyzed imide hydrolysis is thought to proceed *via* a tetrahedral intermediate, as shown in Figure 5.3.

While their mechanism of hydrolysis is similar, the *N*-substituted imides may be expected to have a simpler dependence on pH. Since they do not have a proton which dissociates, hydrolysis is first order in each of the involved species, hydroxide ion and imide, as has been shown for substituted maleimides [176, 177].

Some qualitative structure-activity studies have been reported [120, 177]. Electron-releasing *N*-substituents of maleimides have been shown to stabilize imides, reducing their hydrolysis rates [177]. The electron-withdrawing effect of the tertiary amine nitrogen atoms

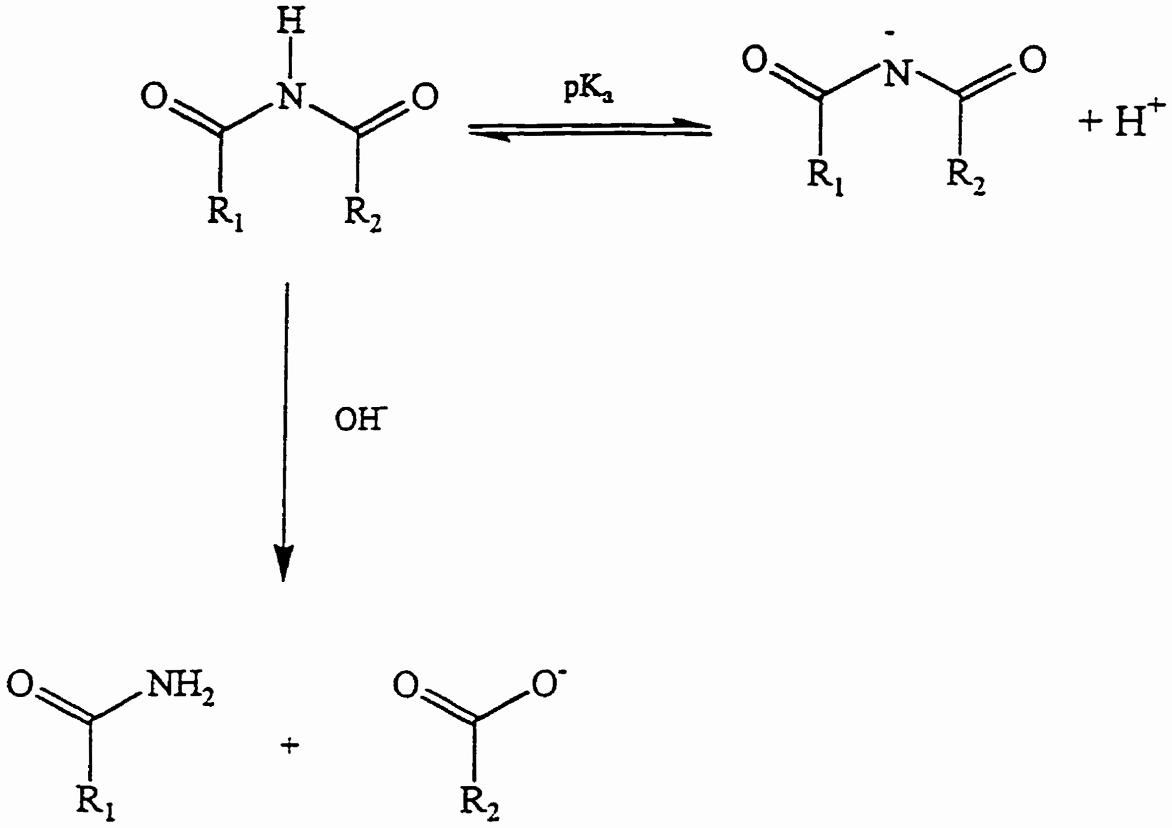

Figure 5.2. Scheme of hydroxide-ion-catalyzed imide hydrolysis in the pH range 8-13.

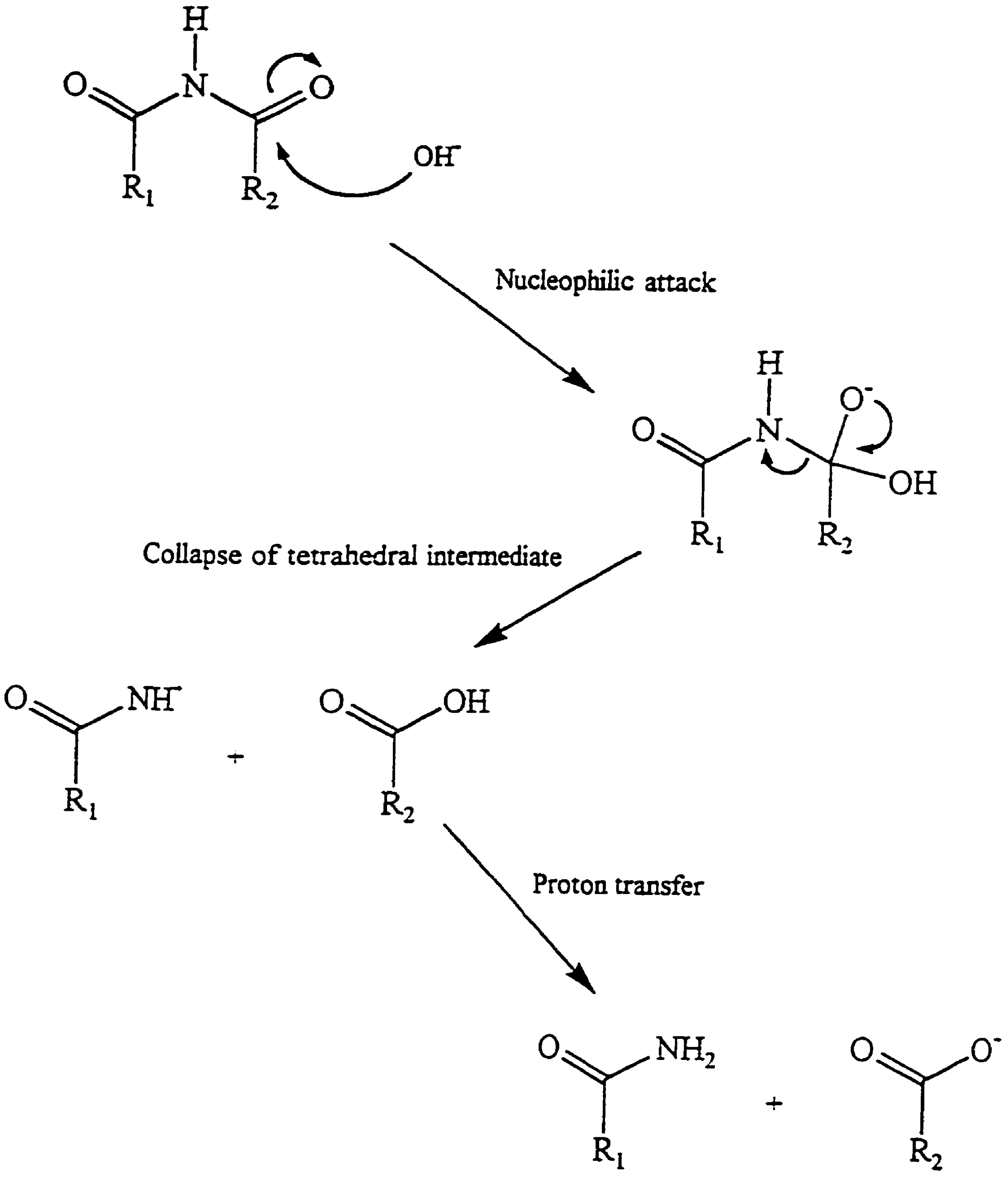

Figure 5.3. Mechanism of hydroxide-ion-catalyzed hydrolysis of imides.

of bisdioxopiperazines on pK_a and hydrolysis rate has been described in detail [120]. Both of these studies reflect the electronic effects of substituents near the imide functional group, and are consistent with their expected effects.

5.3 Kinetic analysis of imide hydrolysis

5.3.1 Materials

Diacetamide, *N*-methyldiacetamide, *N*-methylbis(trifluorodiacetamide), succinimide, *N*-methylsuccinimide, *N*-2,6-xylylsuccinimide, maleimide, *N*-methylmaleimide, *N*-ethylmaleimide, *N*-phenylmaleimide, *N*-4-chlorophenylmaleimide, *N*-3,4-xylylmaleimide, phthalimide, 1,2,3,6-tetrahydrophthalimide, 3,4,5,6-tetrachlorophthalimide, adipimide, and glutarimide (Figure 5.4) were obtained from Aldrich (Milwaukee, WI). Dexrazoxane (ICRF-187) and ICRF-154 (Figure 5.5) were gifts from A. M. Creighton. LYZ 17B, LYZ 19, LYZ 2, LYZ 8, and LYZ 22, synthesized in our laboratory by Yangzhi Ling, and BLPD B2, BLPD E1, BLPD TTHA, and BLPD G2A, synthesized in our laboratory by Bin Ling, are shown in Figure 5.6. The synthesis of ICRF-193 (Figure 5.5) is described in Section 5.3.2. The set of imides represents a variety of structures, including acyclic, five-, six-, and seven-membered rings, saturated and unsaturated, *N*-substituted and non-*N*-substituted, and nine bisdioxopiperazines, dexrazoxane analogs. Buffers were prepared using KCl (optical grade, Aldrich, Milwaukee, WI), and volumetric solutions of ammonium hydroxide (Aldrich), and KOH (Mallinkrodt, Paris, KY). All other materials were of the highest grade available.

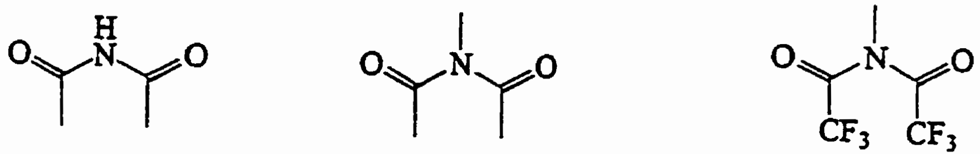

Diacetamide N-Methyldiacetamide N-Methylbis-(trifluorodiacetamide)

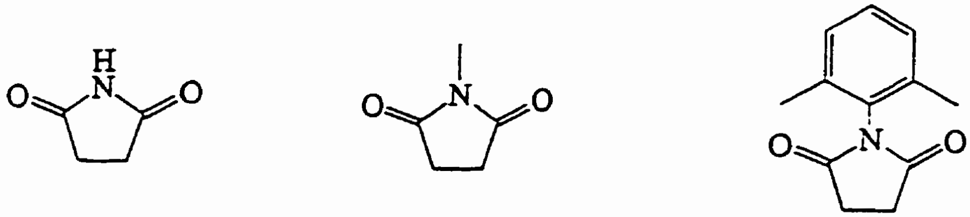

Succinimide N-Methylsuccinimide N-2,6-Xylylsuccinimide

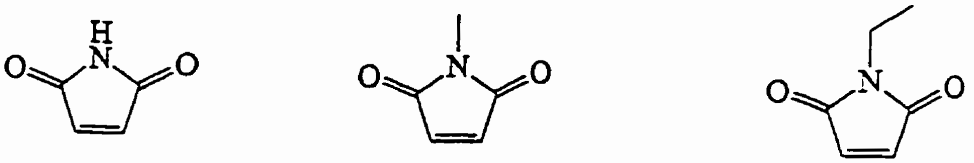

Maleimide N-Methylmaleimide N-Ethylmaleimide

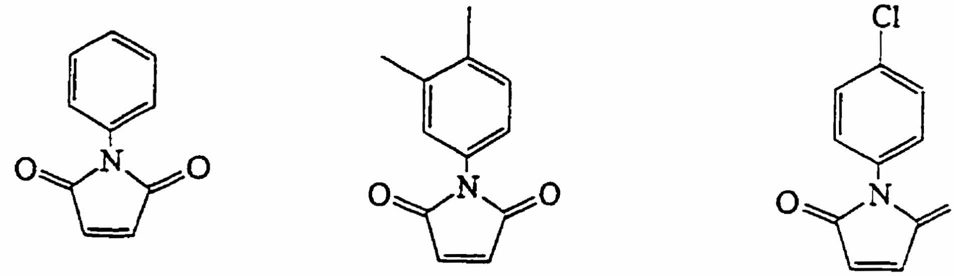

N-Phenylmaleimide N-3,4-Xylylmaleimide N-4-Chlorophenylmaleimide

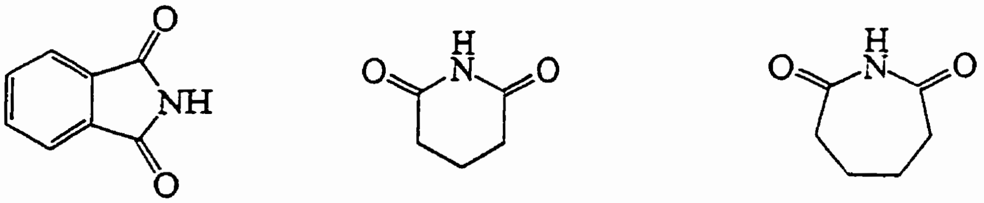

Phthalimide Glutarimide Adipimide

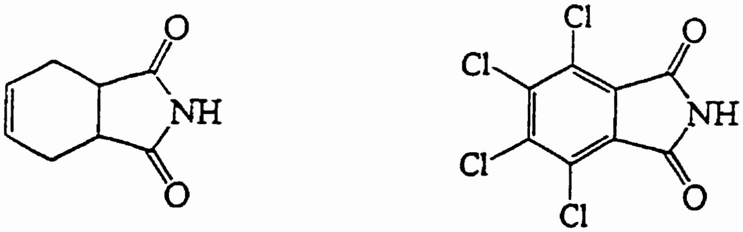

1,2,3,6-Tetrahydrophthalimide 3,4,5,6-Tetrachlorophthalimide

Figure 5.4. Structures of the imides purchased from Aldrich.

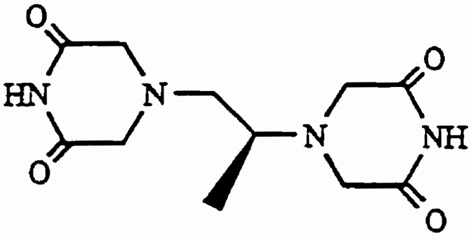

Dexrazoxane (ICRF-187)

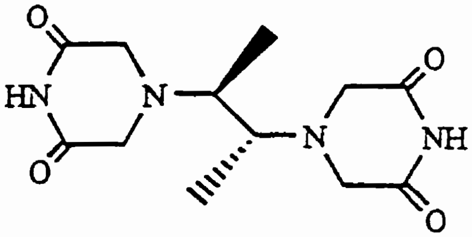

ICRF-193

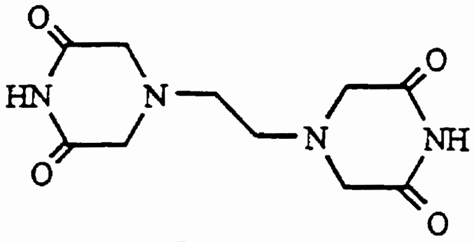

ICRF-154

Figure 5.5. Structures of dexrazoxane and two of its analogs.

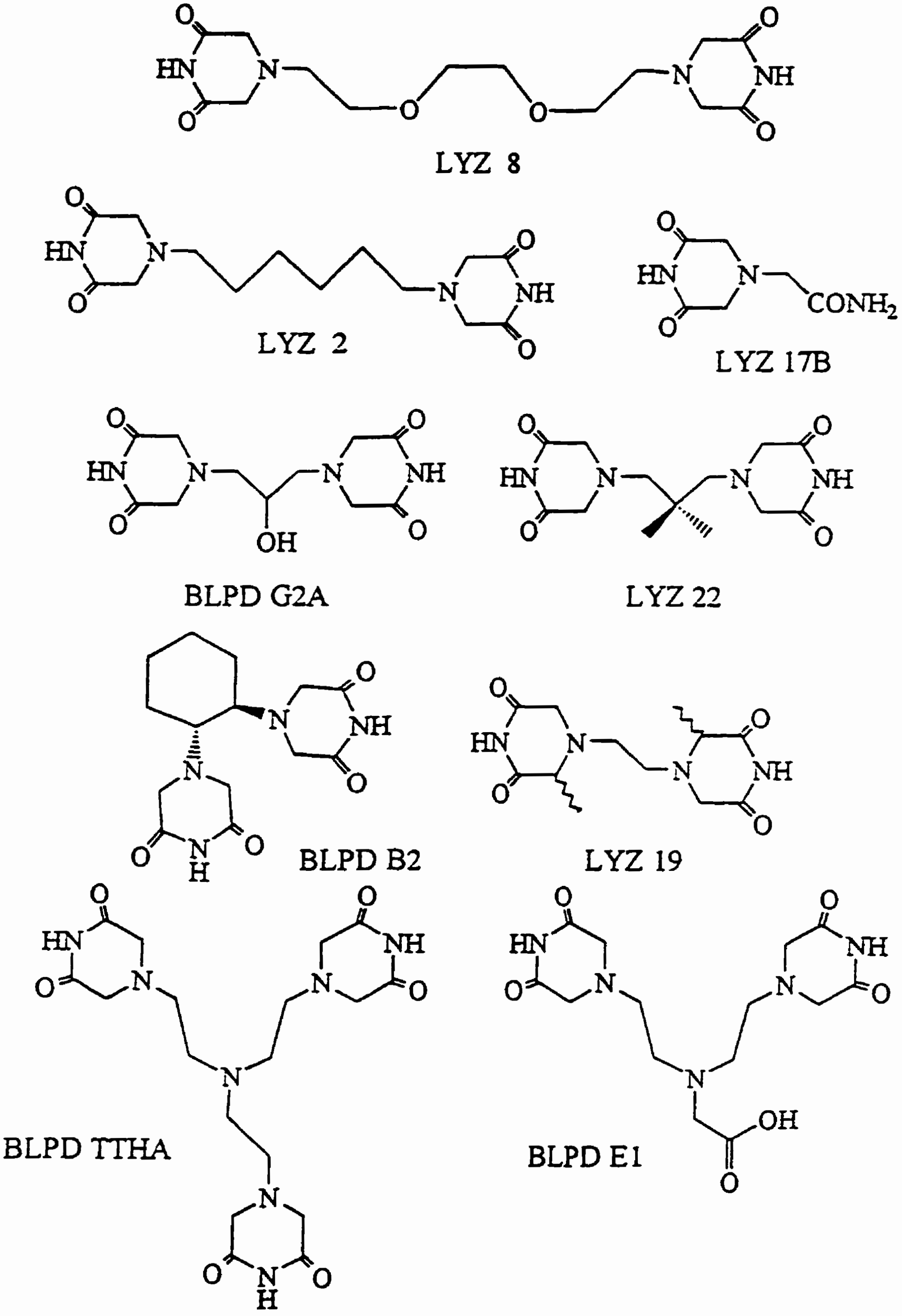

Figure 5.6. Structures of imides synthesized in our laboratory.

5.3.2 Synthesis of ICRF-193

ICRF-193 was synthesized in three steps, as shown in Figure 5.7. Dimethylglyoxime was reduced to butane-2,3-diamine as previously described [178]. Dimethylglyoxime (23.21 g) was dissolved in basic solution (74.31 g NaOH in 600 mL water). Raney nickel (49.6 g) was added in small portions such that the temperature remained at approximately 50 °C. Once all gas had evolved, the flask was stoppered. The temperature was maintained at 50 °C overnight. Amines and water were distilled from the reaction mixture, and the pH was then reduced to approximately 1 with concentrated HCl. The water was evaporated, and the residue washed with two 50 mL aliquots of methanol, yielding 63 g of a white solid. Separation of the *meso* diastereomer from the racemate was achieved by successive extractions with methanol [179]. Specifically, the solid was refluxed in 100 mL methanol, and the solution was cooled and filtered to yield 3.93 g white solid with a melting point of 234-255 °C, corresponding to that of the racemate [179]. This extraction process was repeated twice more, with 100 mL and 300 mL methanol. The remaining 5.0 g completely dissolved when refluxed in 250 mL methanol and 6 mL water. On concentration to 100 mL, this cooled solution yielded 3.04 g white solid, with a melting point of 318-322 °C, corresponding to the previously determined value of 325 °C for the pure *meso* diastereomer of butane-2,3-diamine dihydrochloride [61]. Melting points were measured on an Electrothermal capillary melting point apparatus (England) and are uncorrected. The overall yield was 17%. No attempt was made to isolate the *meso* diamine from any of the remaining solutions from the extraction process. The ^{1}H-NMR spectrum of this compound is shown in Figure 5.8; (D_2O) δ 3.7 (1H, m), δ 1.4 (3H, dd). The ^{1}H-NMR spectra were recorded on a Bruker AM-300 instrument,

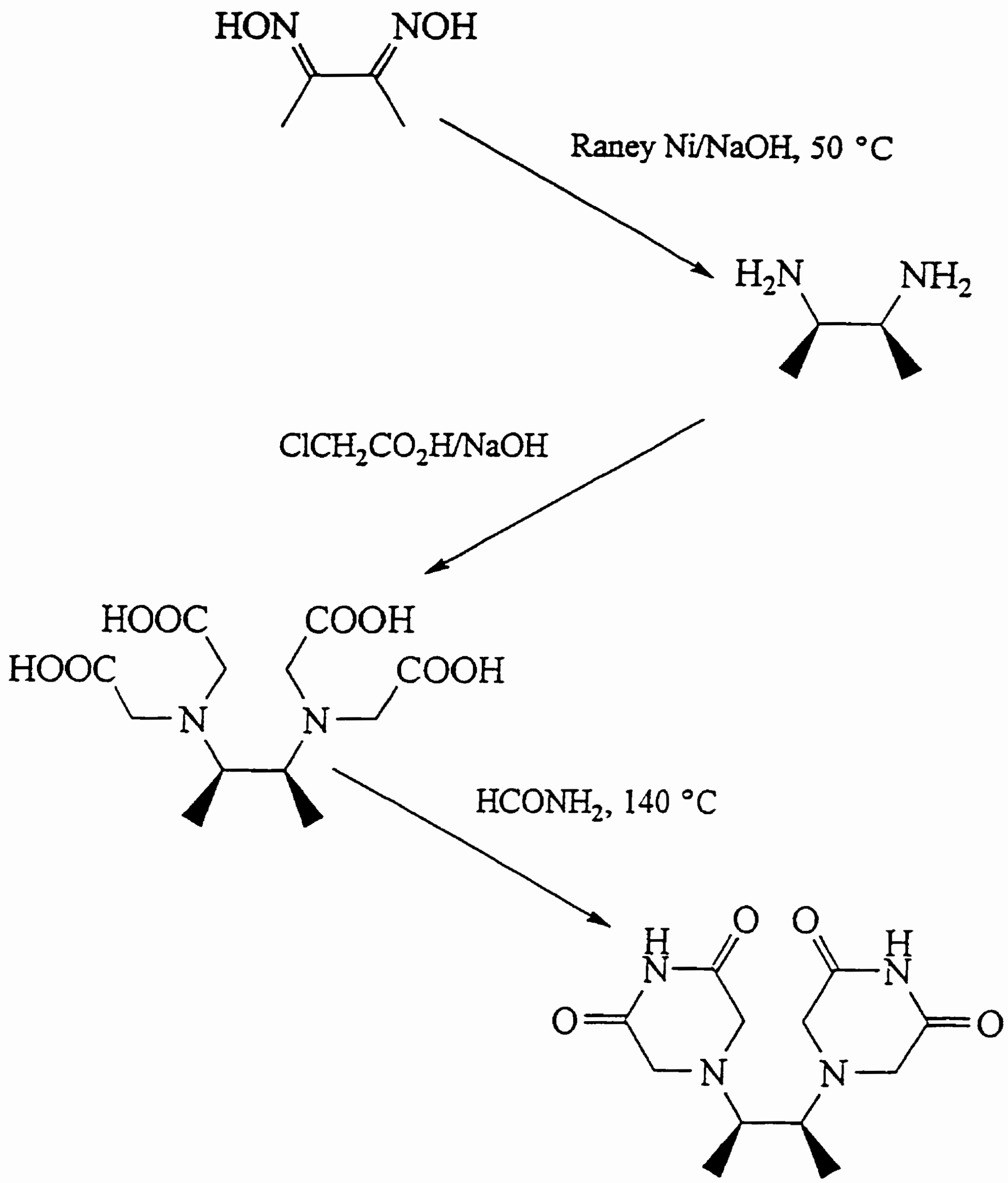

Figure 5.7. Synthetic scheme for ICRF-193.

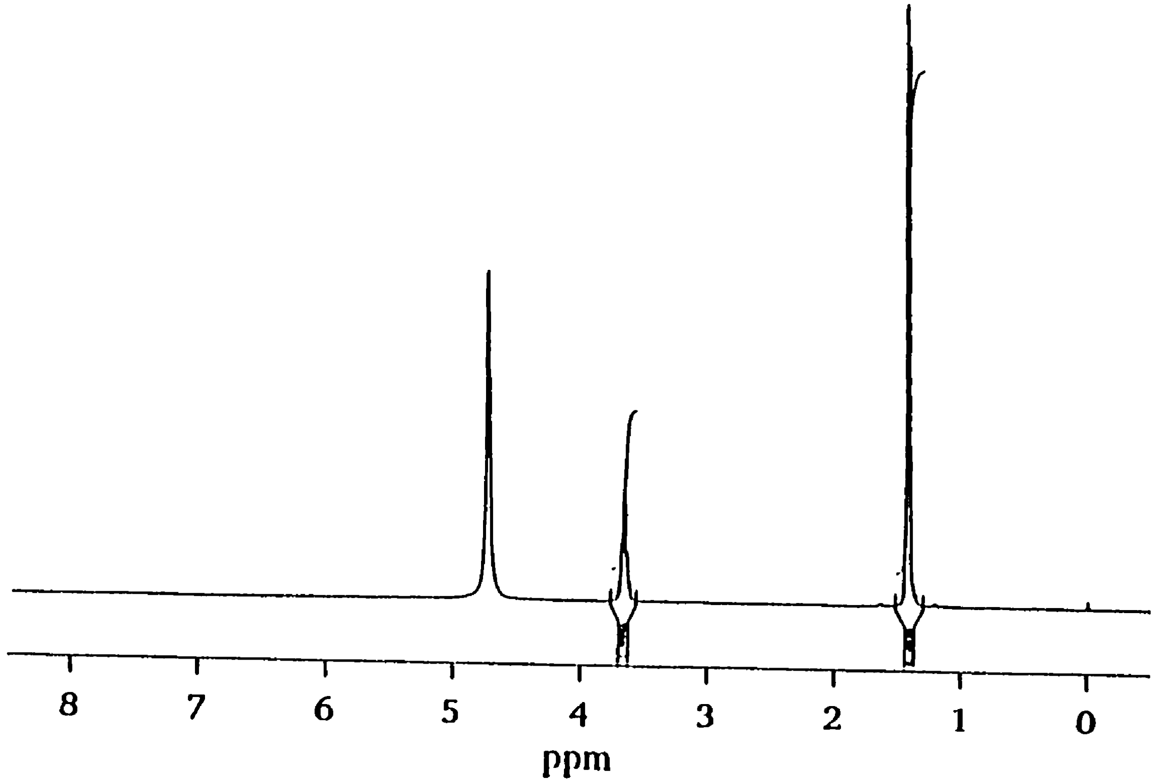

Figure 5.8. 300 MHz ^{1}H-NMR spectrum of *meso*-2,3-butanediamine in D_2O.

using tetramethylsilane and sodium 3-(trimethylsilyl)-propanesulfonate as internal standards in DMSO and D_2O, respectively.

Meso-2,3-butanediaminetetraacetic acid was synthesized as previously described [180], with 2 more equivalents of NaOH to titrate the amine dihydrochloride, as described [61]. NaOH (11.2 g) was dissolved in water (20 mL), cooled in an ice bath, and added dropwise to a cooled solution of chloroacetic acid (11.26 g) dissolved in water (6 mL), such that the temperature did not exceed 20 °C. The amine (3.22 g) was added, and the solution was stirred until homogeneous. The mixture was left at room temperature for 5 days, acidified to approximately pH 1 with HCl, cooled, and filtered to remove NaCl. The filtrate was evaporated to 20 mL, cooled, and filtered to yield 5.5 g of a white solid. This product was purified by ion exchange chromatography using 75 mL (dry volume) Dowex 50W-X8 resin (J. T. Baker Chemical Co., Phillipsburg, NJ). The column was prepared by washing first with 3 M HCl (150 mL), and then with boiling water (1 L). The product was loaded in 40 mL water, and eluted, first with cool water (600 mL) and then with boiling water. Ten fractions of approximately 150-200 mL were collected, and evaporated to approximately 20 mL. The fraction in which there was a precipitate was filtered, and recrystallized from boiling water (300 mL) to yield 2.1 g white solid, m. p. 153-156 °C, which agrees with the previously determined value of 144 °C [61]. The overall yield was 18%. The ^{1}H-NMR spectrum of this compound is shown in Figure 5.9; (DMSO) δ 3.3 (4H, dd) δ 2.7 (1H, s) δ 1.0 (3H, d).

The tetraacetic acid derivative was cyclized to ICRF-193 as previously described [61]. Formamide (2 mL) and *meso*-2,3-butanediaminetetraacetic acid (0.50 g) were vacuum-distilled for one hour at 110 °C to remove traces of water. The temperature was raised to 140

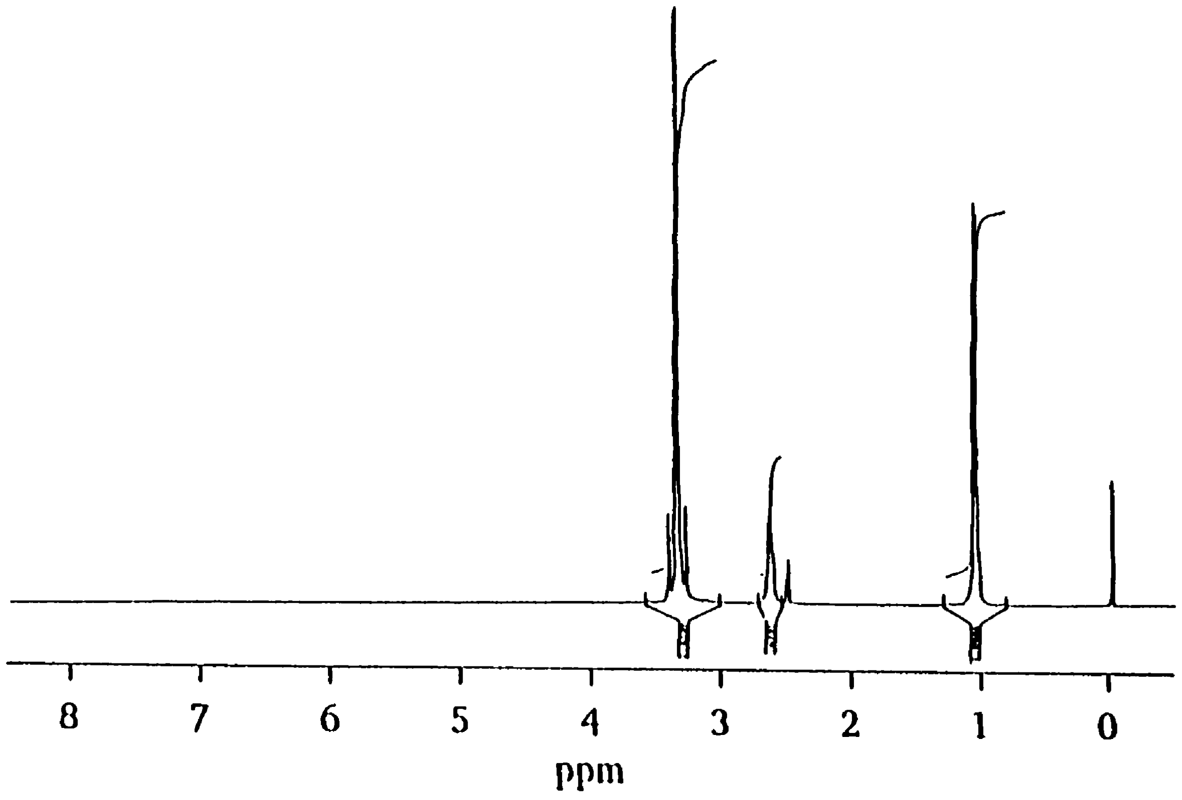

Figure 5.9. 300 MHz ^{1}H-NMR spectrum of *meso*-2,3-butanediamine-N,N,N',N'-tetraacetic acid in DMSO.

°C, and the solution was refluxed for four hours. Acetone was added to the cooled solution until it became turbid (approximately 8 mL), and the mixture was left overnight at -20 °C. Small, beige crystals (95 mg) were obtained, m. p. 300-306 °C. The crystals were recrystallized from DMSO (2.5 mL) and acetone (6 mL, added dropwise until turbid) [181]. The cooled solution was filtered, to yield 40 mg nearly white solid, m. p. 318-320 °C (9% overall yield). Further attempts to crystallize ICRF-193 from the mother liquor were not made. The ^{1}H-NMR spectrum of this compound is shown in Figure 5.10; (DMSO) δ 11.0 (1H, s) δ 3.3 (4H, dd) δ 2.5 (1H, dd) δ (3H, d).

5.3.3 Methods

The hydrolysis rates of the imides shown in Figures 5.4-5.6 were measured spectrophotometrically in 1 cm stoppered silica cells on a Cary 1 spectrophotometer (Varian, Mulgrave, Australia), equipped with a constant temperature bath, at 25 °C in 50 mM ammonia buffer and sodium hydroxide solutions over a pH range of approximately 8 to 13.2. The ionic strength was maintained at 150 mM with KCl. Below pH 11.1, reactions were carried out in ammonia buffer, and the pH was measured immediately following each experiment. Above pH 11.1, reactions were carried out in KOH solutions, and the pH was calculated from the amount of KOH added. Since many of the imides in this study were sparingly soluble in water, stock solutions were made in ethanol or DMSO, such that the final concentration of co-solvent remained less than 1%, and the final concentration of imide was 100 μM. Reactions were initiated by the addition of imide to the buffer. The first-order decrease in absorbance was observed at approximately 210 nm, corresponding to a decrease

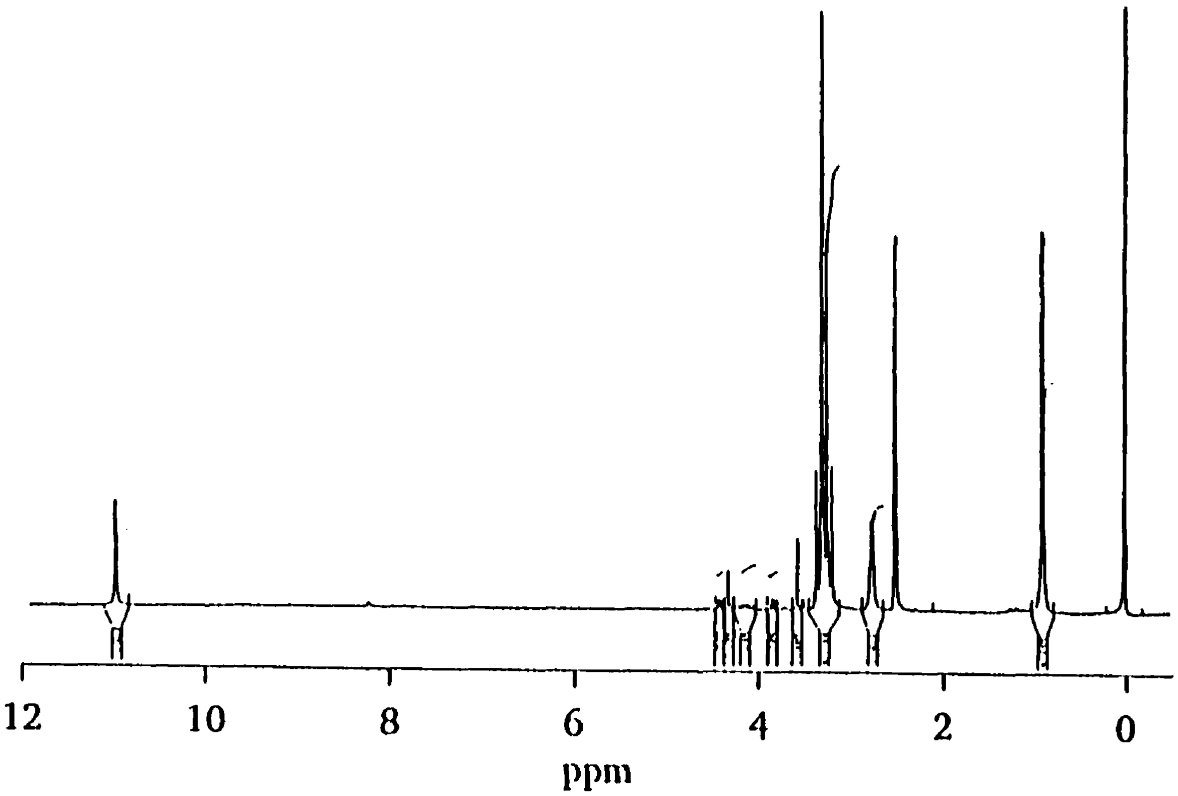

Figure 5.10. 300 MHz ^{1}H-NMR spectrum of ICRF-193 in DMSO.

in the concentration of the imide, or at 230 nm, corresponding to a decrease in the concentration of the imide anion. Data were analyzed using Cary 1/3E software, version 3 (Varian, Mulgrave, Australia) and Sigmaplot 5.0 for DOS (Jandel Scientific, San Rafael, CA).

5.3.4 pH dependence of *N*-substituted imides

Imides hydrolyze *via* base-catalyzed nucleophilic attack. On incubation with NaOH, a decrease in absorbance characteristic of imide hydrolysis [117] was observed. Absorbance-time data in the far UV range, following the first order disappearance of imide, were recorded for *N*-methylbis(trifluorodiacetamide), *N*-methylmaleimide, *N*-phenylmaleimide, *N*-4-chlorophenylmaleimide, and *N*-3,4-xylylmaleimide. Data for *N*-methylmaleimide are shown in Figure 5.11. For *N*-methyldiacetamide, *N*-methylsuccinimide, *N*-2,6-xylylsuccinimide, and *N*-ethylmaleimide, the imides which hydrolyzed sufficiently slowly, spectra within the wavelength range of 190 to 300 nm were recorded at fixed time intervals. Data for *N*-methylsuccinimide are shown in Figure 5.12a, from which single-wavelength data were obtained (Figure 5.12b). Regardless of the method of data collection, the single-wavelength data were fitted to an exponential equation:

$$A = Amp \cdot e^{-k_{obs}t} + A_{\infty} \qquad (5.1)$$

in which A and A_{∞} are the absorbances at time t and infinity, respectively, k_{obs} is the pseudo-first-order rate constant, and *Amp* is the amplitude of the absorbance change. k_{obs} varied linearly with hydroxide-ion concentration in the case of *N*-substituted imides (Figures 5.13-5.16). Weighted data were fitted to a linear equation:

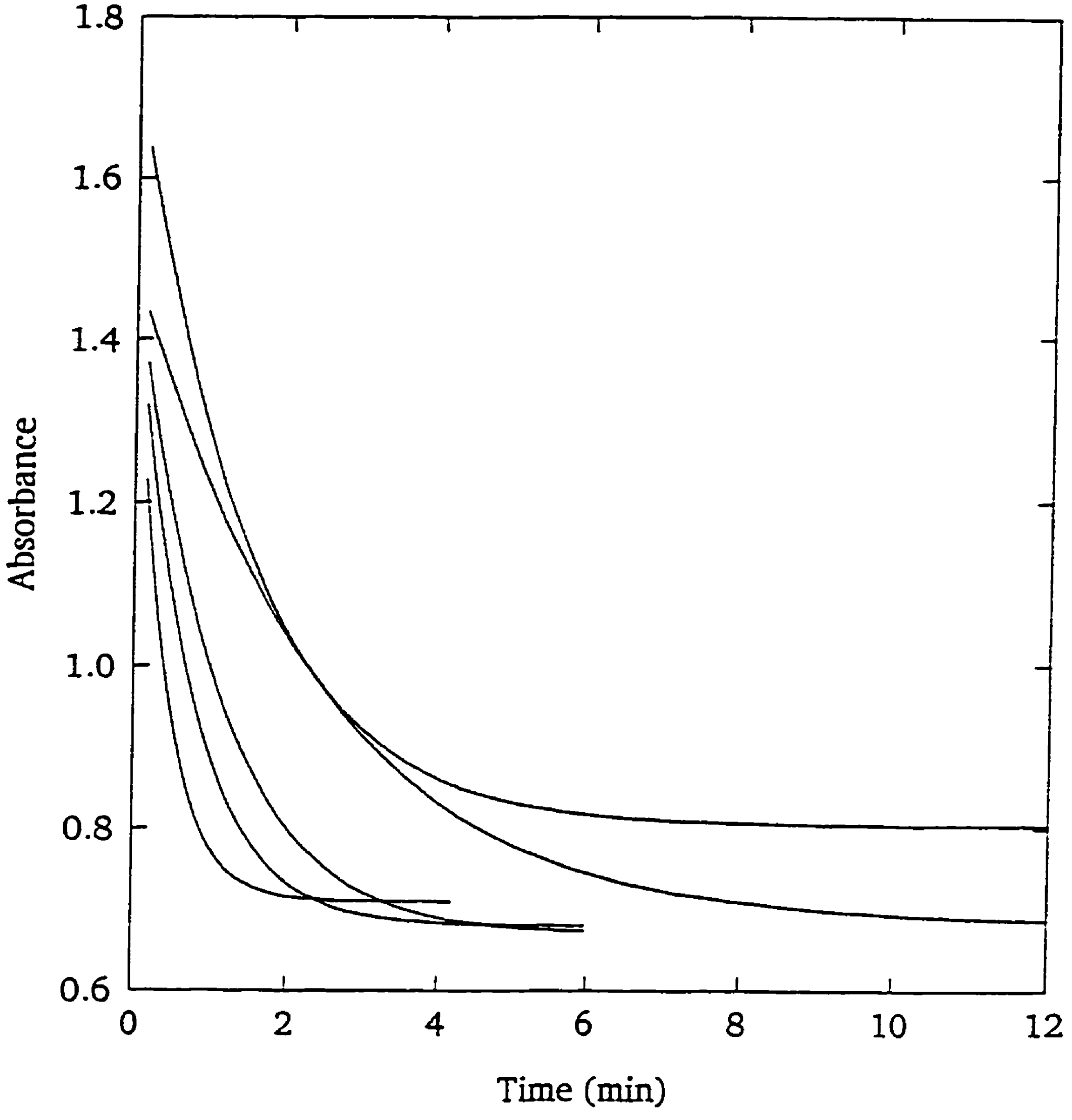

Figure 5.11. Absorbance-time data for *N*-methylmaleimide, at 220 nm, measured at 25 °C at pH values of 10.19, 9.99, 10.30, 10.45, and 10.66 (in order of increasing absorbance at time zero), in ammonia buffer. Ionic strength was maintained at 150 mM.

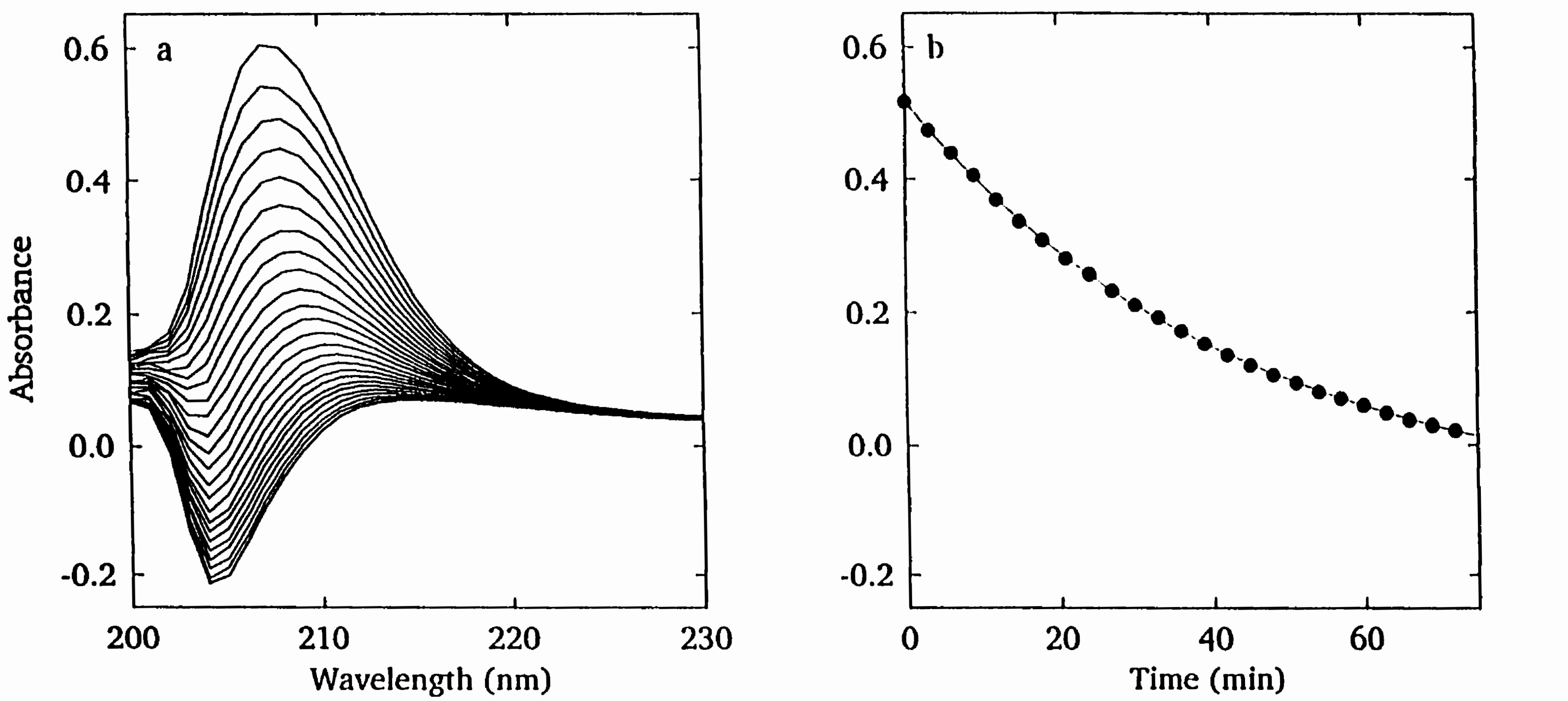

Figure 5.12. Absorbance data for *N*-methylsuccinimide. a) Spectra at pH 11.12 were recorded every 3 minutes in ammonia buffer. Ionic strength was maintained at 150 mM with KCl. b) Absorbance-time data at 210 nm, extracted from the spectra (●) and fit to Equation 5.1.

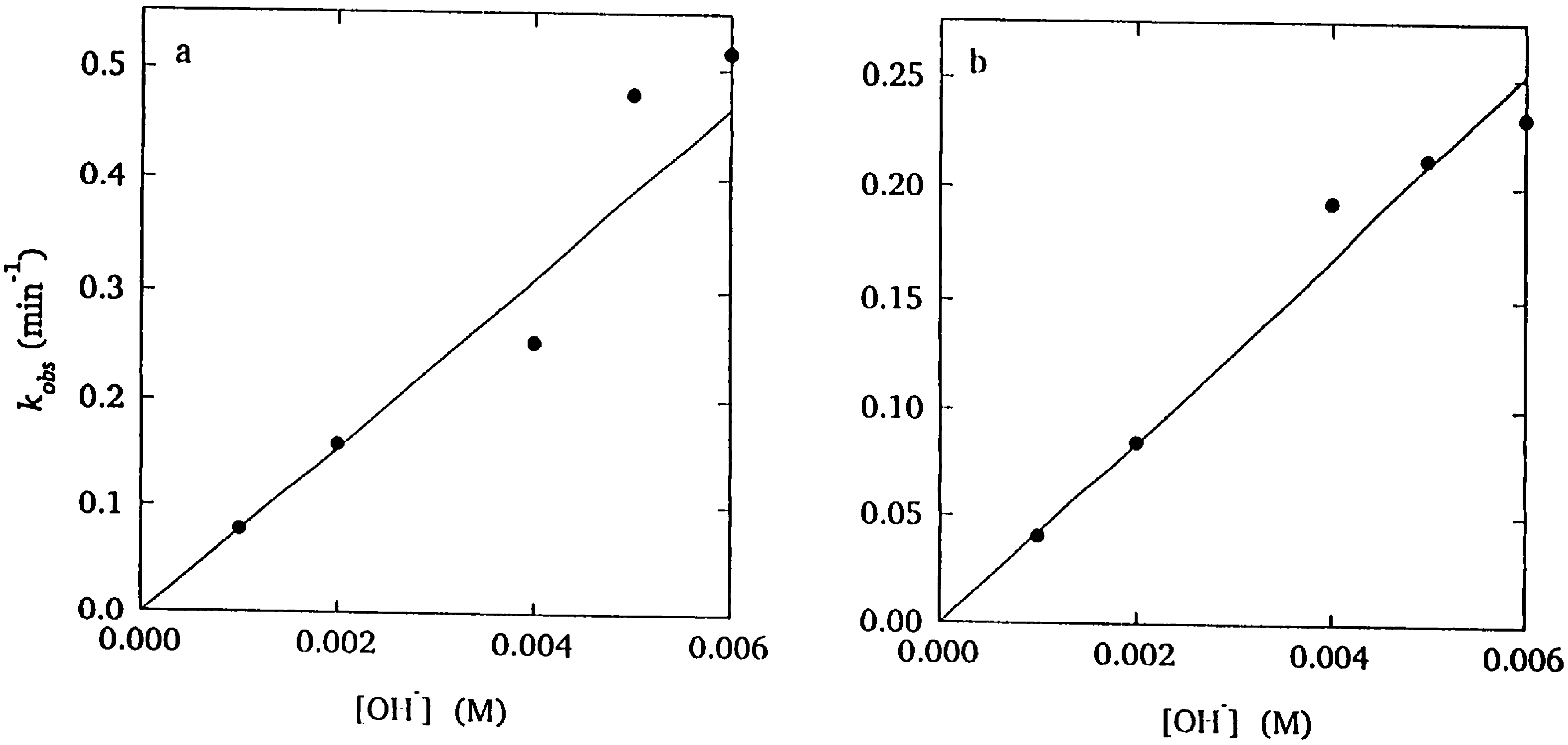

Figure 5.13. Hydroxide ion dependence of hydrolysis of a) *N*-methyldiacetamide and b) *N*-methylbis(trifluorodiacetamide) at 25 °C in NaOH solutions. Experimental data (●) were fitted to weighted least squares linear equations (lines). Hydrolysis rates were studied in NaOH solutions. Ionic strength was maintained at 150 mM with KCl.

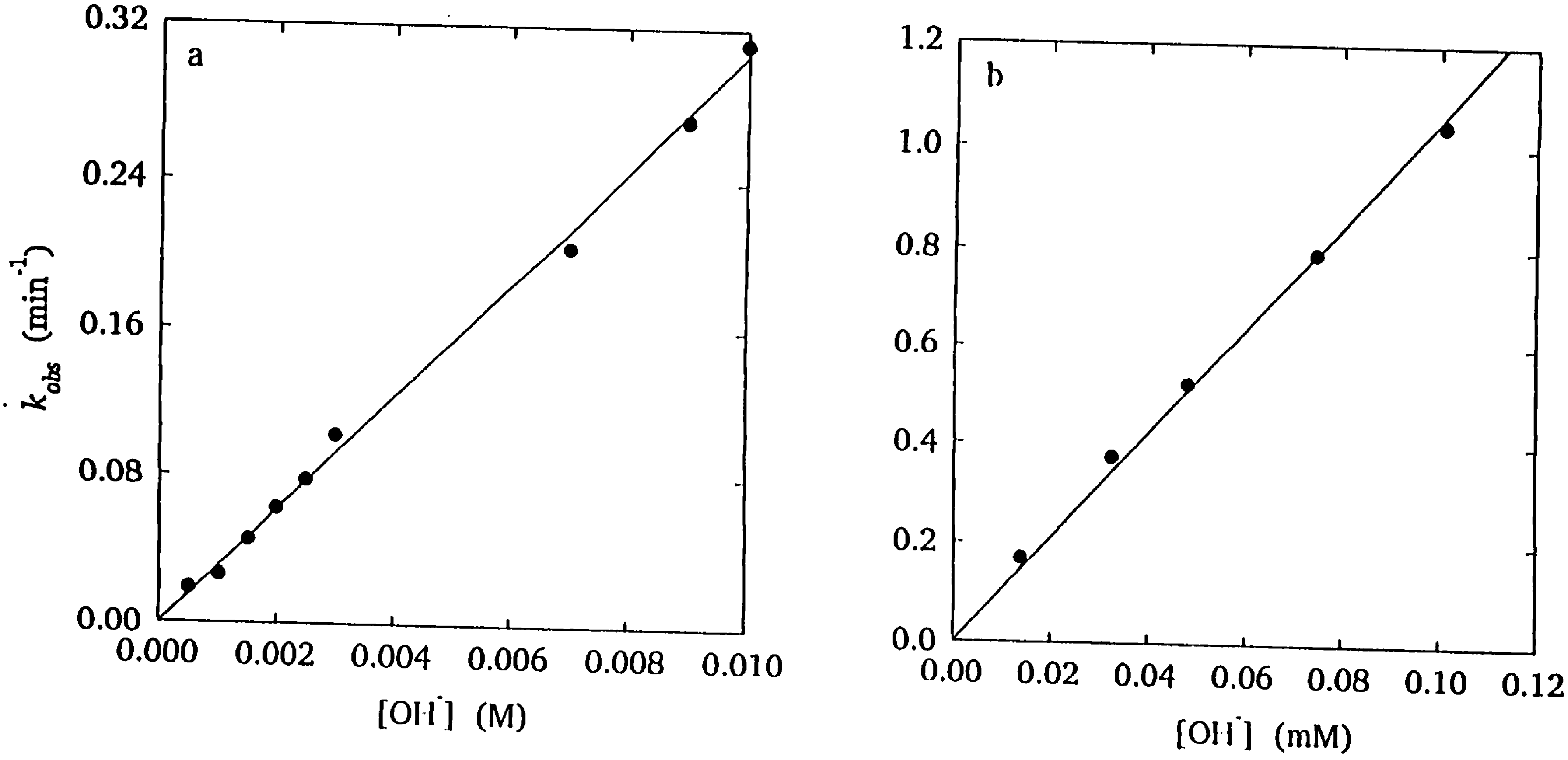

Figure 5.14. Hydroxide ion dependence of hydrolysis of a) *N*-2,6-xylylsuccinimide and b) *N*-phenylmaleimide at 25 °C in NaOH solutions. Experimental data (●) were fitted to weighted least squares linear equations (lines). Hydrolysis rates were studied in NaOH solutions and ammonia buffer, respectively. Ionic strength was maintained at 150 mM with KCl.

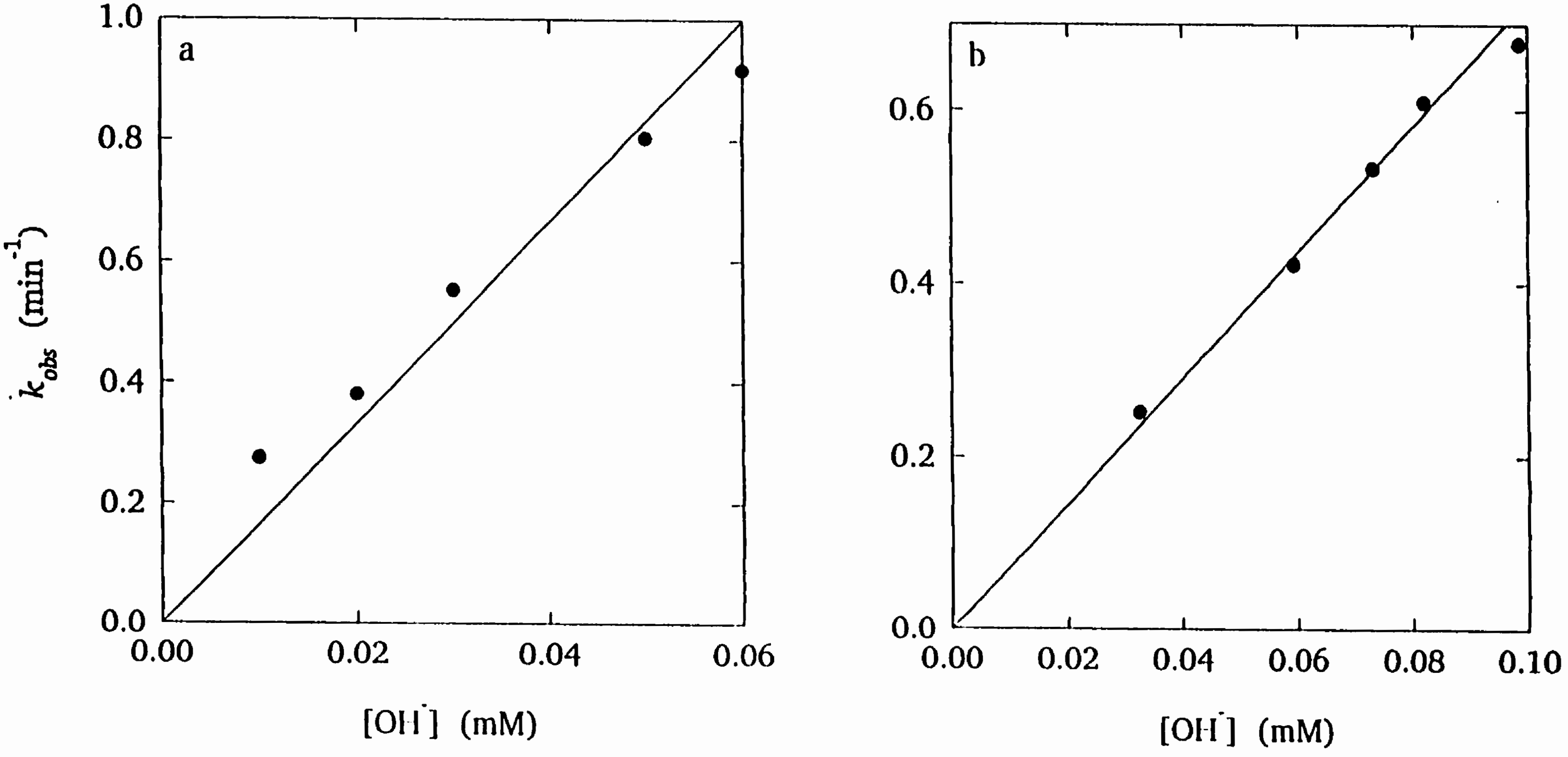

Figure 5.15. Hydroxide ion dependence of hydrolysis of a) *N*-4-chlorophenylmaleimide and b) *N*-3,4-xylylmaleimide at 25 °C in NaOH solutions. Experimental data (●) were fitted to weighted least squares linear equations (lines). Hydrolysis rates were studied in ammonia buffer. Ionic strength was maintained at 150 mM with KCl.

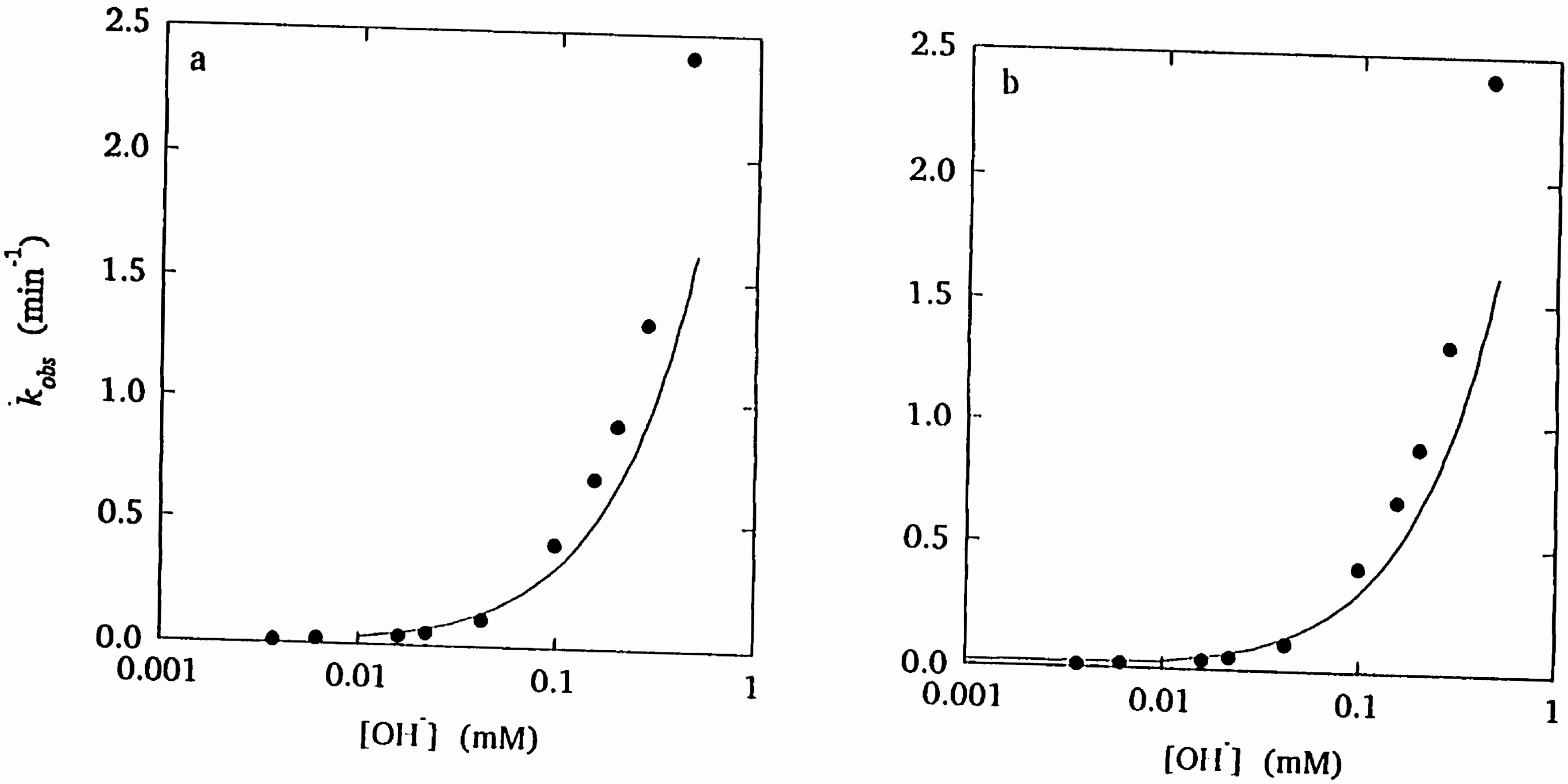

Figure 5.16. Hydroxide ion dependence of hydrolysis of a) *N*-methylmaleimide and b) *N*-ethylmaleimide at 25 °C in NaOH solutions. Lines represent the weighted fit of the experimental data (●) to Equation 5.2. Data are shown on a log scale. Hydrolysis rates were studied in ammonia buffer. Ionic strength was maintained at 150 mM with KCl.

$$k_{obs} = k_2[OH^-] \qquad (5.2)$$

in which k_2 is a second order rate constant, describing the dependence of imide hydrolysis on the hydroxide ion and imide concentrations for all *N*-substituted imides, except *N*-methylsuccinimide (Figure 5.17). Since these data were not well described by Equation 5.2, it was modified by the addition of a quadratic term, $k_3[OH^-]^2$. The calculated value of k_3 for these imides was 6900 ± 1400 M^{-2}. The addition of a constant term to Equation 5.2, corresponding to nucleophilic attack by water, did not significantly improve the fits to the rate constant data for any of the *N*-substituted imides, and the fitting errors on this parameter were large, indicating that it was poorly defined. If water can act as a nucleophile toward *N*-substituted imides, its contribution to k_{obs} was too small to be detected over the pH range studied. Calculated values of k_2 obtained from Equation 5.2 are listed in Table 5.1.

5.3.5 pH dependence of hydrolysis of non-*N*-substituted imides

Similar to the *N*-substituted imides, non-*N*-substituted imides have a characteristic absorbance peak at approximately 210 nm, as has been shown for dexrazoxane [117]. At a pH of approximately 10, the imide proton dissociates, causing a shift of this peak to a longer wavelength. The maximum absorbance of the deprotonated imide occurs at 227 nm for dexrazoxane [117].

Single-wavelength data were recorded for phthalimide, 3,4,5,6-tetrachlorophthalimide, adipimide, and glutarimide. Data for glutarimide are shown in Figure 5.18. For the imides which hydrolyzed sufficiently slowly, spectra were recorded at fixed time intervals, from

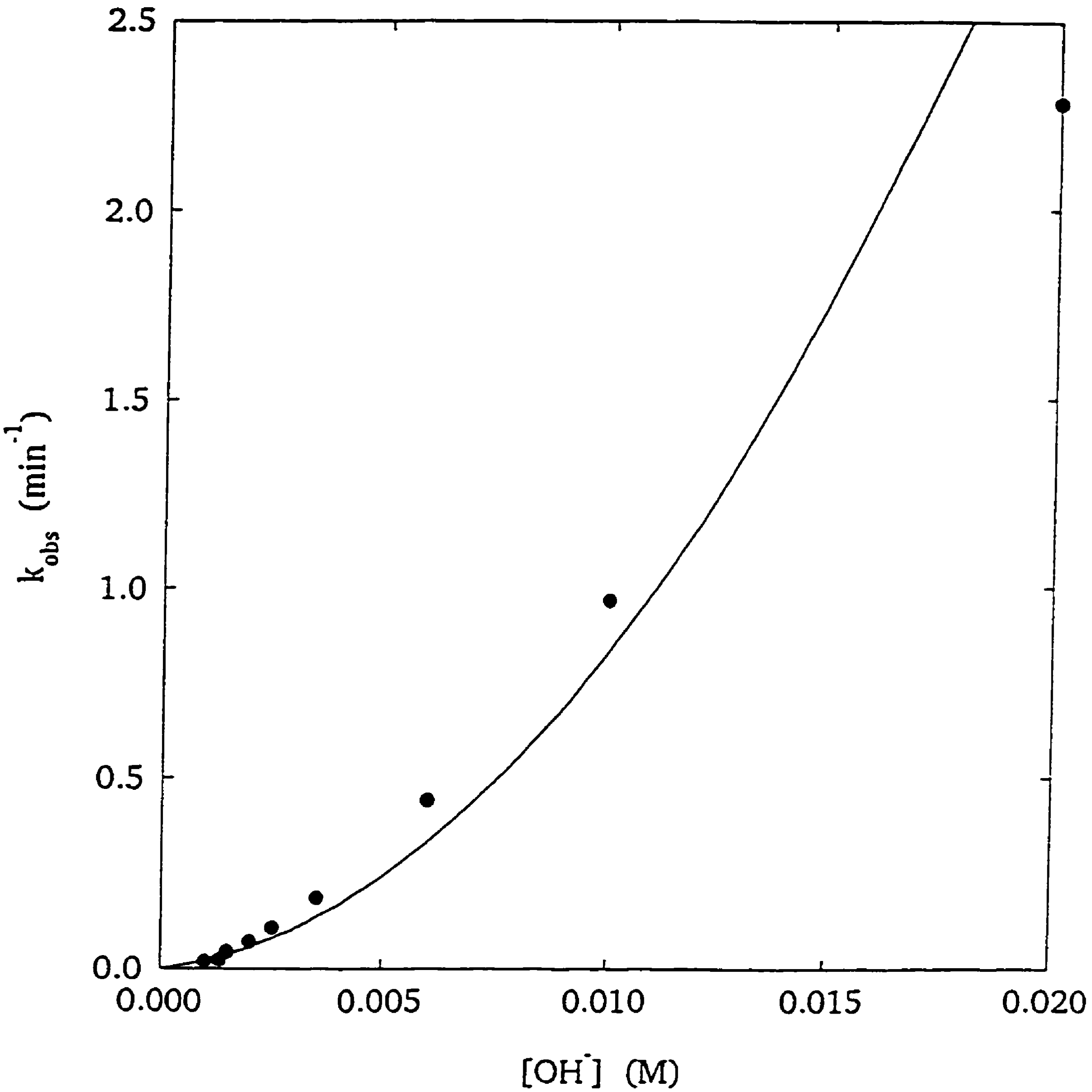

Figure 5.17. Hydroxide ion dependence of hydrolysis of *N*-methylsuccinimide at 25 °C in NaOH solutions. Experimental data (●) were fitted to a weighted quadratic equation: $k_{obs} = k_2[OH^-] + k_3[OH^-]^2$ (line). Hydrolysis rates were studied in NaOH solutions. Ionic strength was maintained at 150 mM with KCl.

Table 5.1. Kinetic and static parameters describing base-catalyzed hydrolysis of imides.[a]

Imide	k_2[b] (min^{-1} M^{-1})	pK_a[b] (kinetic)	pK_a[c] (static)	Amp_{max}[c]
diacetamide	64.96 ± 0.2	12.77 ± 0.01	12.73 ± 0.2	10910 ± 4000
N-methyl-"	77.49 ± 5	–	–	–
N-methylbis(trifluoro-")	42.03 ± 2	–	–	–
succinimide	5.48 ± 0.9	10.86 ± 0.08	9.633 ± 0.3	16430 ± 232
N-methyl-"	14.14 ± 4	–	–	–
N-2,6-xylyl-"	30.67 ± 1	–	–	–
maleimide	1689 ± 200	10.41 ± 0.06	–	–
N-methyl-"	3228 ± 300	–	–	–
N-ethyl-"	1437 ± 200	–	–	–
N-phenyl-"	10560 ± 200	–	–	–
N-3,4-xylyl-"	7272 ± 100	–	–	–
N-4-chlorophenyl-"	16650 ± 300	–	–	–
phthalimide	560.4 ± 3	10.08 ± 1	–	–
adipimide	150.5 ± 3	11.41 ± 0.05	11.50 ± 0.06	–
glutarimide	91.02 ± 8	12.01 ± 0.05	12.00 ± 0.08	–
ICRF-154	125.2 ± 20	10.10 ± 0.09	10.08 ± 0.03	13010 ± 200
ICRF-193	220.1 ± 30	10.41 ± 0.07	10.48 ± 0.05	11460 ± 300
LYZ 17B	322.4 ± 30	10.10 ± 0.06	10.06 ± 0.1	7319 ± 600
LYZ 19	88.19 ± 20	9.90 ± 0.1	10.32 ± 0.1	18540 ± 500
LYZ 2	65.01 ± 10	10.02 ± 0.08	10.14 ± 0.07	13650 ± 500
LYZ 8	115.7 ± 30	9.787 ± 0.09	10.16 ± 0.07	13080 ± 500
LYZ 22	151.3 ± 30	10.06 ± 0.1	10.45 ± 0.04	14710 ± 300
BLPD B2	199.2 ± 30	10.20 ± 0.08	10.53 ± 0.08	9518 ± 600
BLPD G2A	2803 ± 300	10.24 ± 0.05	10.45 ± 0.05	12480 ± 400
dexrazoxane[d]	51.23 ± 6	10.47 ± 0.06	10.44 ± 0.08	17960 ± 600
1,2,3,6-tetrahydrophthalimide	0.4714 ± 0.08	11.61 ± 0.08	–	–
3,4,5,6-tetrachlorophthalimide	1.407 ± 0.06	–	–	–
BLPD E1	66.9 ± 16	10.43 ± 0.1	10.06 ± 0.07	13580 ± 500
TTHA	273.2 ± 2	–	–	–

[a] Experimental conditions are described in Section 5.3.3.

[b] Calculated from Equations 5.2 and 5.5 for *N*-substituted and non-substituted imides, respectively. Errors are standard errors of the mean from non-linear least squares curve fitting.

[c] Calculated from Equation 5.6. Errors are standard errors of the mean from non-linear least squares curve fitting. Data were measured at 240 nm, except for diacetamide and succinimide, which were measured at 239 and 220 nm, respectively.

[d] Since dexrazoxane is asymmetrical, the rate constant measured is a composite of k_{AB} and k_{AC}, defined in Figure 5.1.

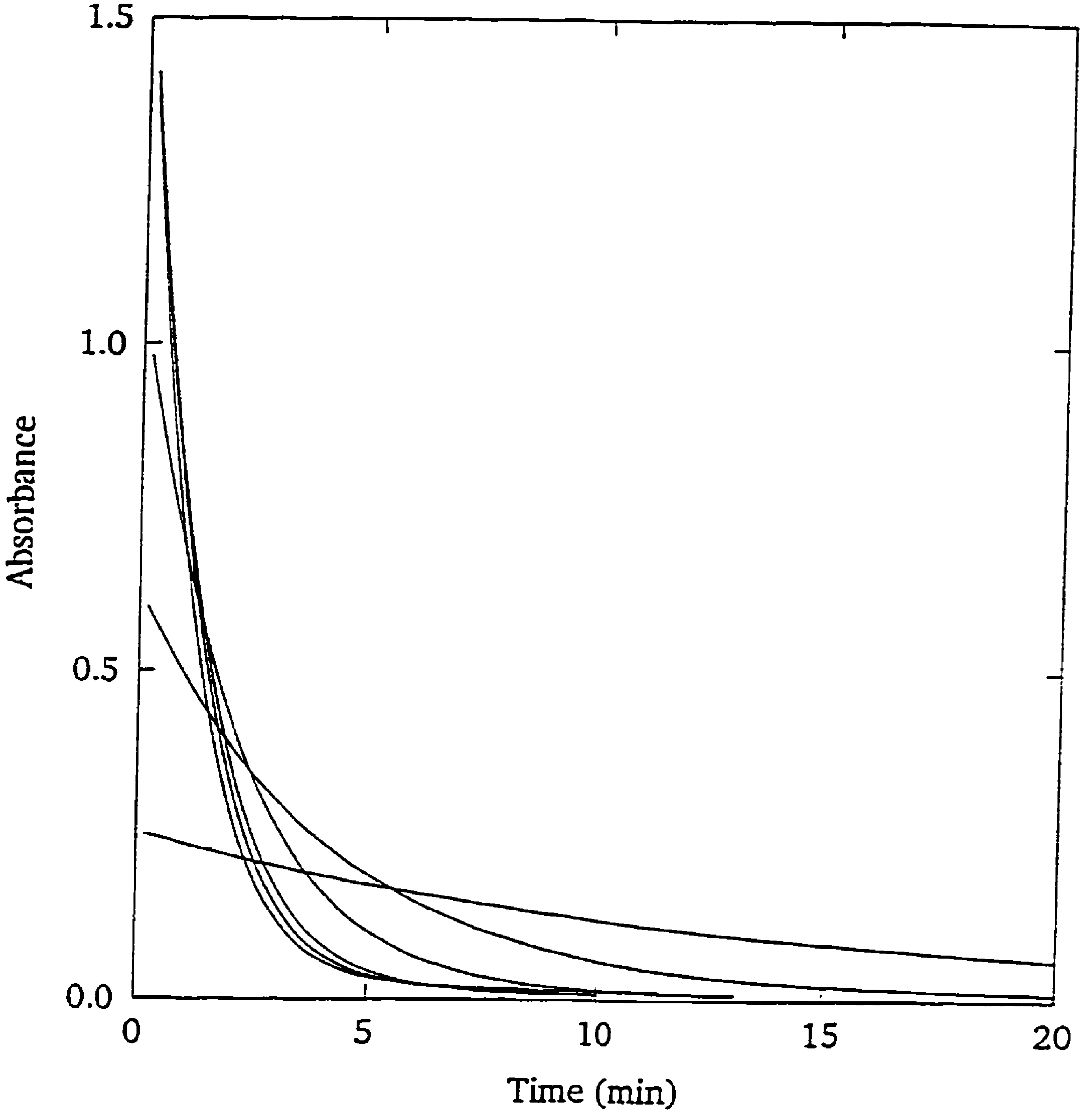

Figure 5.18. Absorbance-time data for glutarimide at 239 nm, at 25 °C, measured at pH values of 12.73, 12.57, 12.51, 12.12, 11.72, and 11.20 (in order of decreasing absorbance at time zero), in NaOH solutions. Ionic strength was maintained at 150 mM with KCl.

which single wavelength data were obtained. Data for diacetamide, maleimide, adipimide, glutarimide, and 1,2,3,6-tetrahydrophthalimide were collected by this method. Spectral data, and the single wavelength data derived from it, are shown in Figure 5.19 for diacetamide. Regardless of the method of data collection, the single wavelength data were fitted to Equation 5.1, to give a determination of k_{obs} at each pH.

The one-ring open intermediates of dexrazoxane do not hydrolyze at the same rates as dexrazoxane. Hydrolysis rates of **B** and **C**, described by k_{3D} and k_{CD}, are approximately twice as fast as the corresponding hydrolysis steps of dexrazoxane, described by k_{AC} and k_{AB}, respectively (Table 4.1). Since the kinetics of complete bis-imide hydrolysis may therefore be too complicated to study spectrophotometrically, only the first hydrolysis reaction was characterized. For succinimide, due to its slow hydrolysis rate, and for all bis-imides, including ICRF-154, ICRF-193, LYZ 17B, LYZ 19, LYZ 2, LYZ 22, and BLPD B2, the pseudo-first-order rate constants describing imide hydrolysis were determined by initial rates. By using this method for the bis-imides, only the first hydrolysis reaction was observed, without a significant contribution from the second. Thus, for all bis-imides, the kinetic data reported describe only the first hydrolysis step (*i. e.* the opening of the first ring). Under initial rate conditions,

$$A = -V_0 t - A_0 \qquad (5.3)$$

in which A and A_0 are the absorbances at time t and time zero, respectively, and V_0 is the initial rate, expressed in absorbance units/min.

The absorbance of imides varies with pH, while the absorbance of the hydrolysis products did not. Thus, either the amplitude of the reaction or the absorbance at time zero

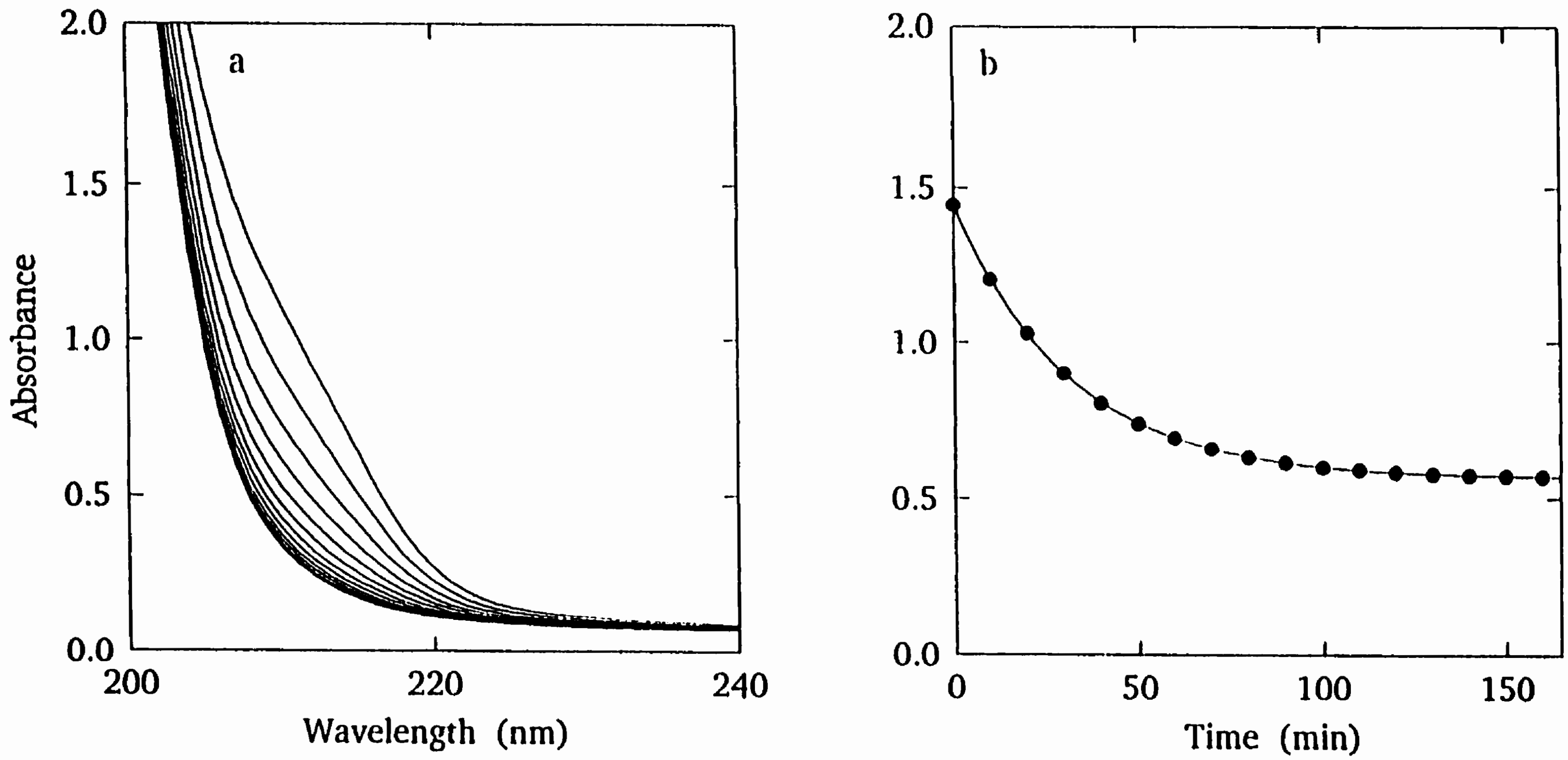

Figure 5.19. Absorbance data for diacetamide. a) Spectra at pH 10.79 and 25 °C were recorded every 5 minutes (data are shown at ten minute intervals) in ammonia buffer. Ionic strength was maintained at 150 mM with KCl. b) Absorbance-time data at 207 nm, extracted from the spectra (●) and their fit to Equation 5.1 (line).

must be determined for each data point for conversion of the initial rate data from units of absorbance to units of concentration. After collecting the initial rate data, solutions were heated to 50 °C to accelerate the hydrolysis reactions. When the absorbance changes were complete (4-24 h), solutions were returned to 25 °C, and the final absorbances were measured. Data for ICRF-154 are shown in Figure 5.20. Data for adipimide and glutarimide were analyzed using the absorbance of the solutions at time zero. All other imides were analyzed using the amplitudes of the observed absorbance changes. Initial rates were converted to units of μM/min using Beer's law, and to k_{obs} by

$$k_{obs} = \frac{V_0}{C_0} \qquad (5.4)$$

in which C_0 is the initial concentration of imide. The k_{obs} data describing the pH dependence of non-*N*-substituted imide hydrolysis are shown in Figures 5.21-5.38. The wavelengths at which each imide was analyzed are reported in the figure captions. Over the pH range used in this study, k_{obs} increased sigmoidally, with an inflection point corresponding to the pK_a of the imide functional group, with the exceptions of BLPD TTHA and 3,4,5,6-tetrachlorophthalimide, for which the relationship of k_{obs} to hydroxide ion was linear. It has been previously shown for maleimide [182], succinimide [122] and ethosuximide [123] that the imide anion, being less electrophilic than the protonated species, is resistant to nucleophilic attack by hydroxide ion in the pH range of interest in this study. A scheme for the base-catalyzed hydrolysis of imides is shown in Figure 5.2, from which the following equation was derived (Appendix):

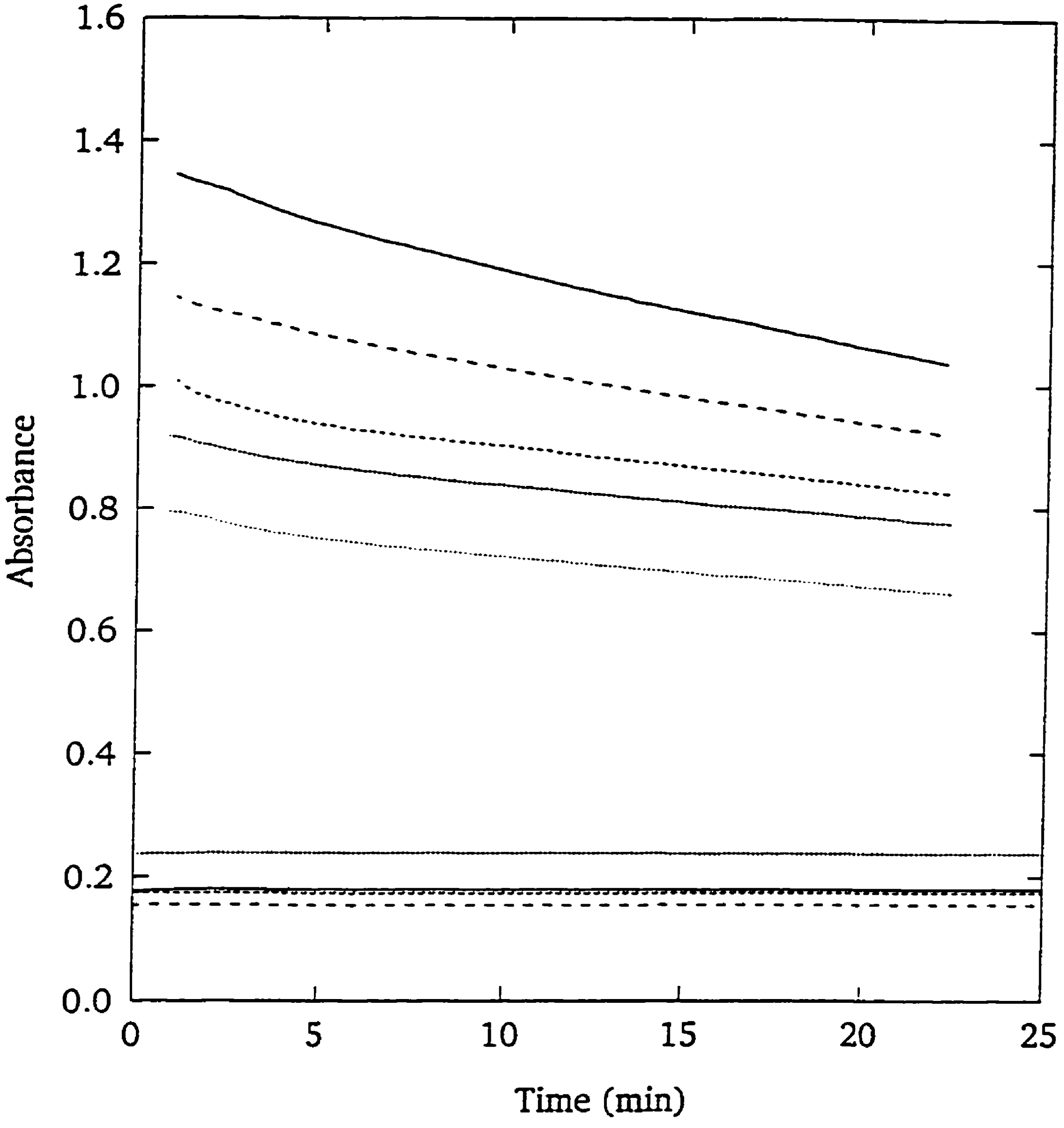

Figure 5.20. Initial rate data for ICRF-154. Absorbance data were collected at 25 °C and 240 nm in ammonia buffer, at pH values of 11.15, 10.69, 10.42, 10.14, and 9.24, from top to bottom. Ionic strength was maintianed at 150 mM with KCl. Absorbance values near 0.2, corresponding to 100% reaction, which were recorded after the solutions were incubated at 50 °C, are also shown.

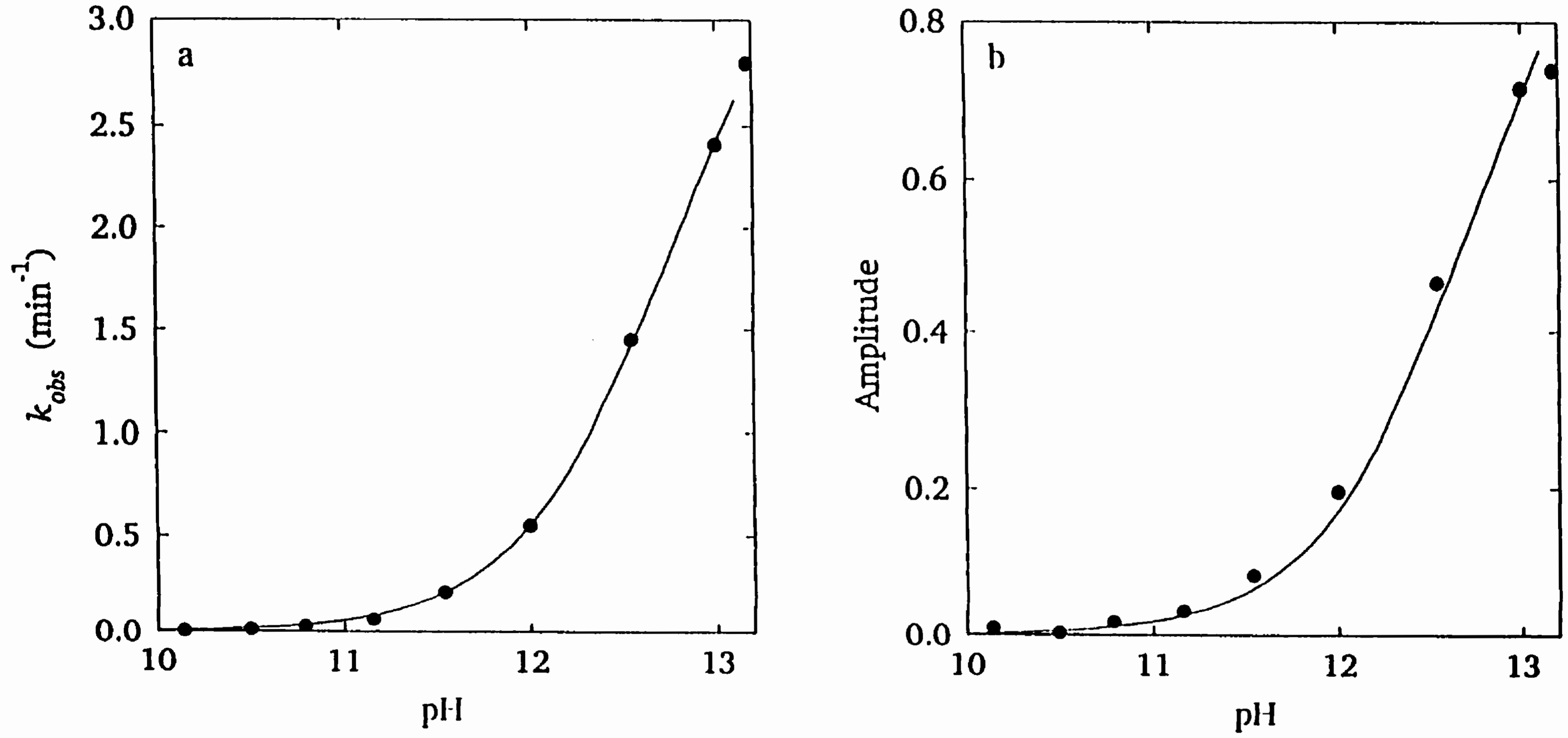

Figure 5.21. pH dependence of hydrolysis of diacetamide at 25 °C in ammonia buffer and NaOH solutions. Experimental measurements (●) of a) k_{obs}, measured at 239 and 207 nm above and below pH 11, respectively, and b) Amplitude of the absorbance change, measured at 239 nm, are shown with their least squares fits (lines) to Equations 5.5 and 5.6, respectively.

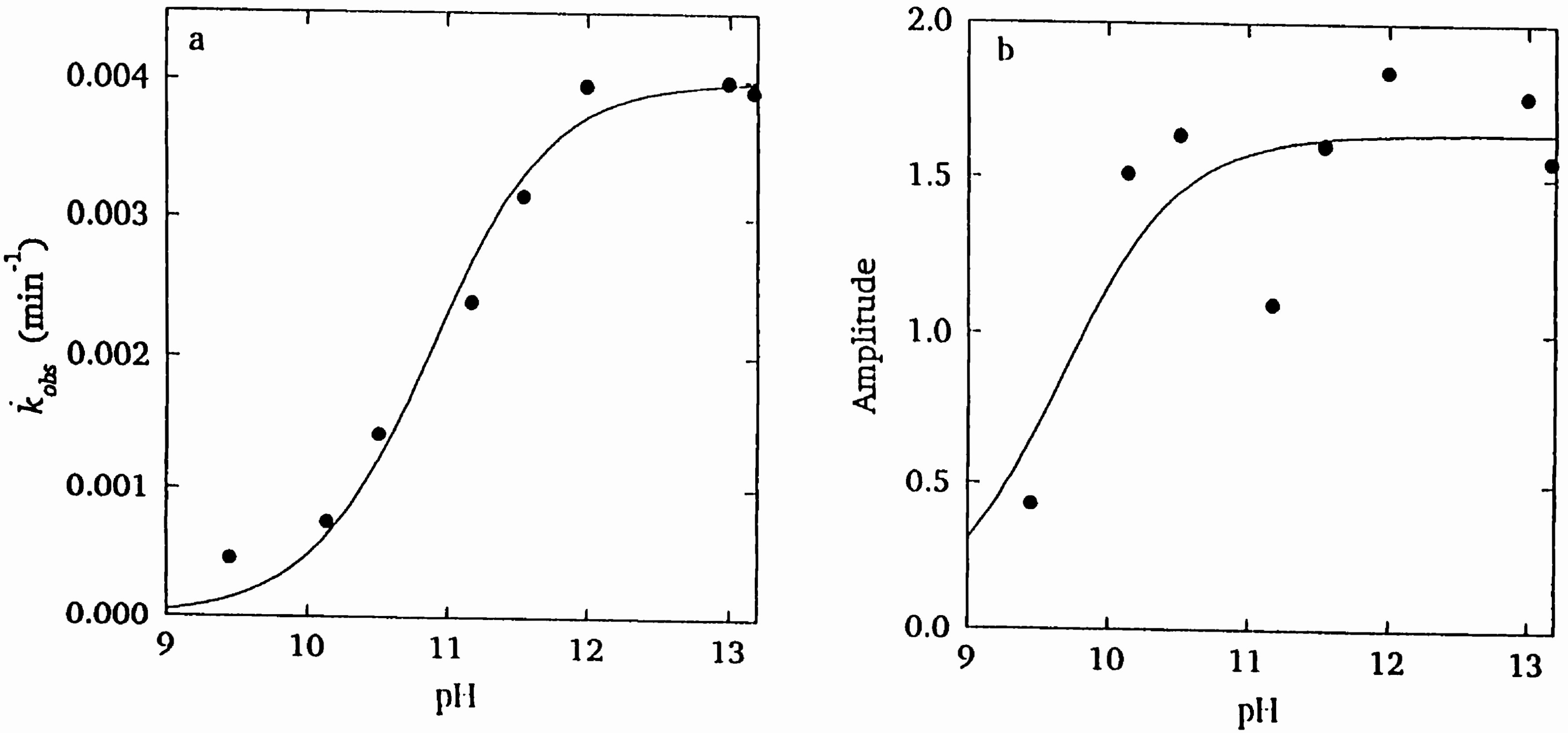

Figure 5.22. pH dependence of hydrolysis of succinimide at 25 °C in ammonia buffer and NaOH solutions. Experimental measurements (●) of a) k_{obs} and b) Amplitude of the absorbance change, both measured at 220 nm, are shown with their least squares fits (lines) to Equations 5.5 and 5.6, respectively.

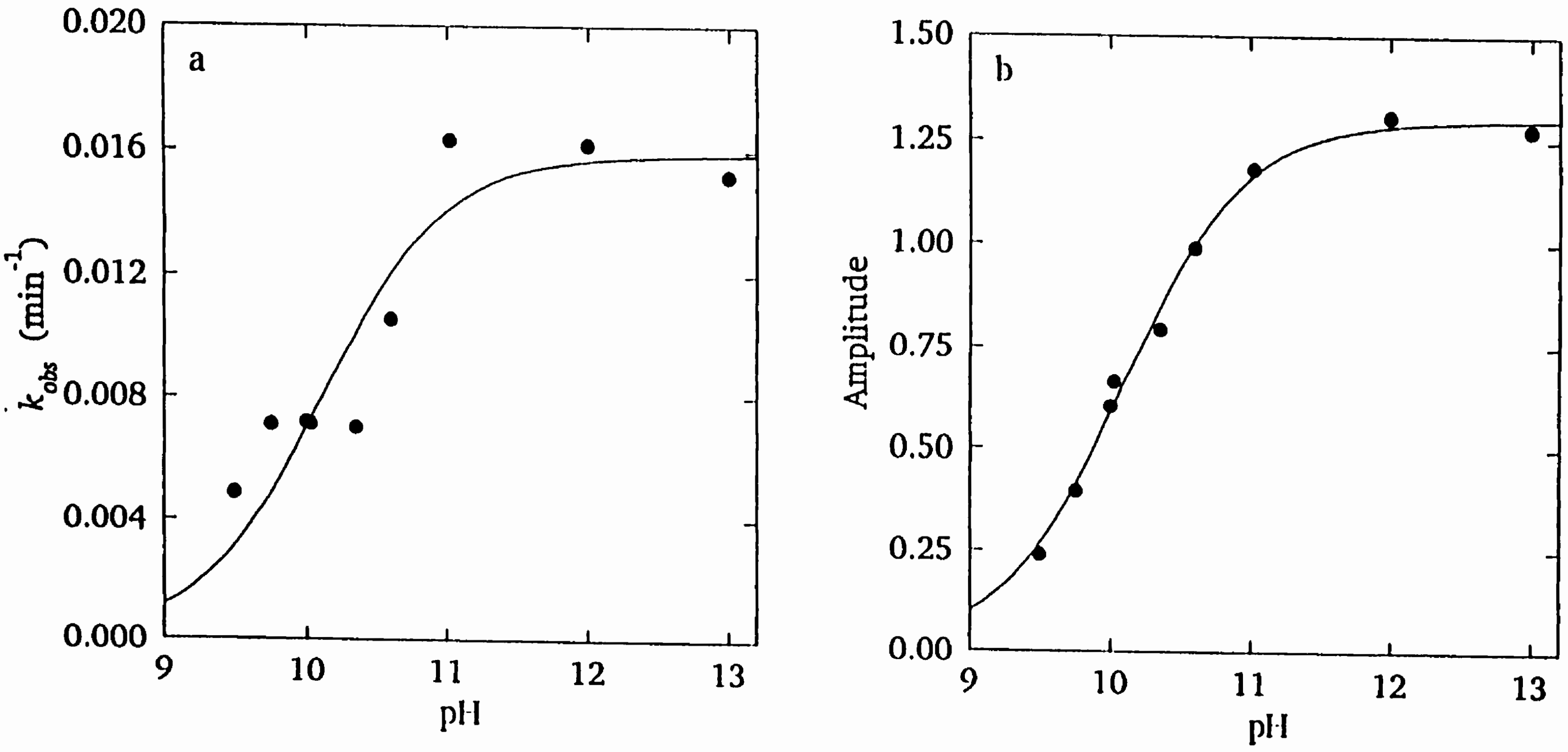

Figure 5.23. pH dependence of hydrolysis of ICRF-154 at 25 °C in ammonia buffer and NaOH solutions. Experimental measurements (●) of a) k_{obs} and b) Amplitude of the absorbance change, both measured at 240 nm, are shown with their least squares fits (lines) to Equations 5.5 and 5.6, respectively.

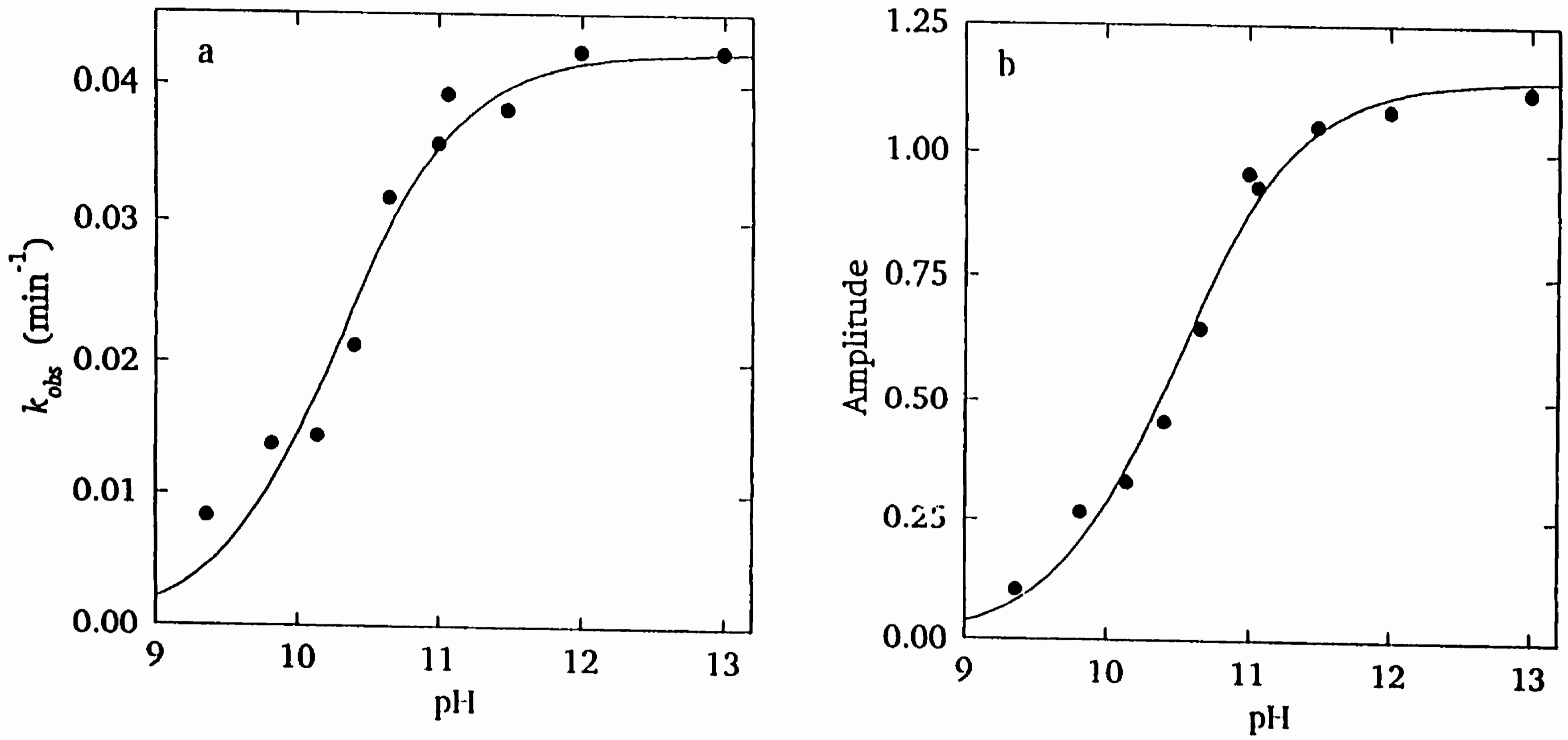

Figure 5.24. pH dependence of hydrolysis of ICRF-193 at 25 °C in ammonia buffer and NaOH solutions. Experimental measurements (●) of a) k_{obs} and b) Amplitude of the absorbance change, both measured at 240 nm, are shown with their least squares fits (lines) to Equations 5.5 and 5.6, respectively.

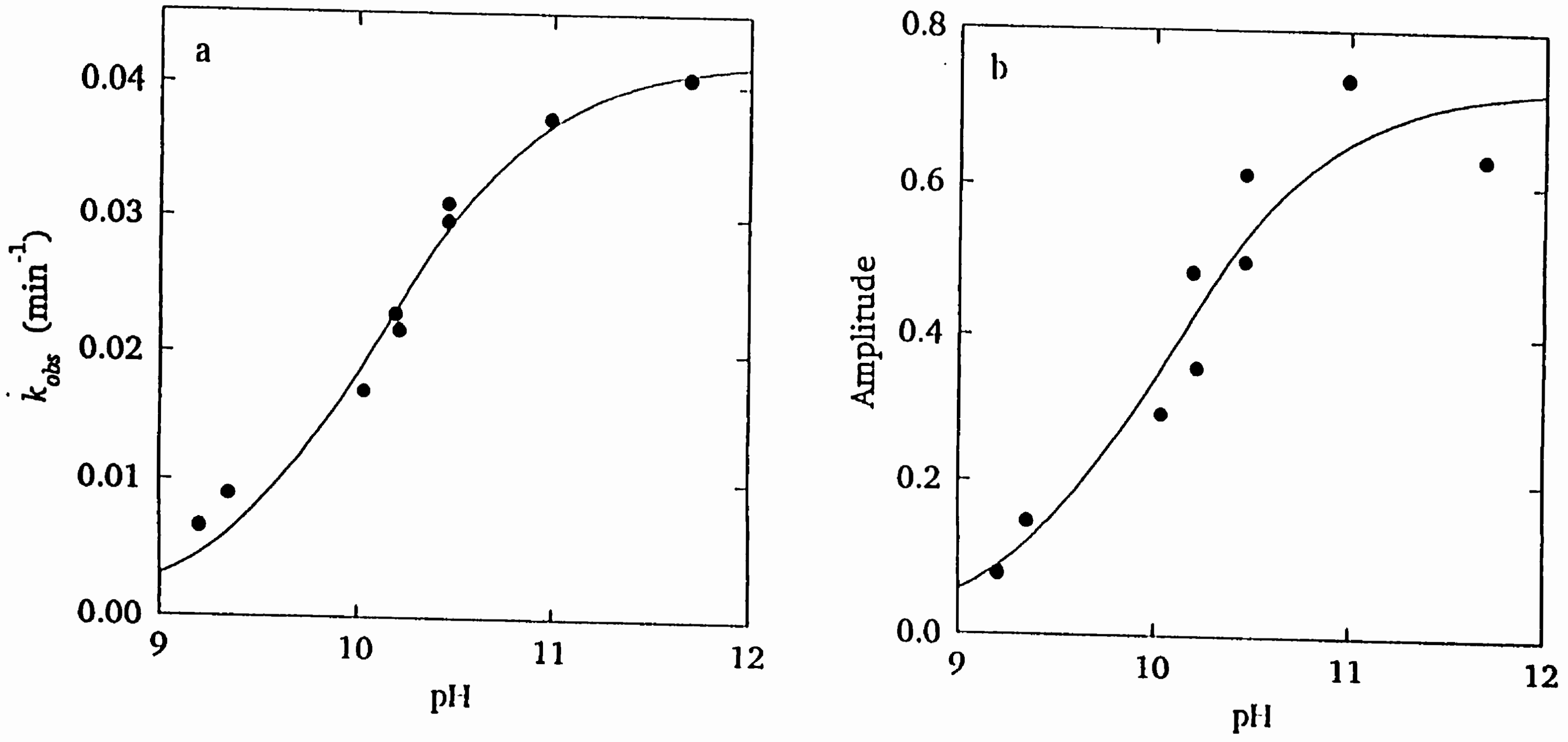

Figure 5.25. pH dependence of hydrolysis of LYZ 17B at 25 °C in ammonia buffer and NaOH solutions. Experimental measurements (●) of a) k_{obs} and b) Amplitude of the absorbance change, both measured at 240 nm, are shown with their least squares fits (lines) to Equations 5.5 and 5.6, respectively.

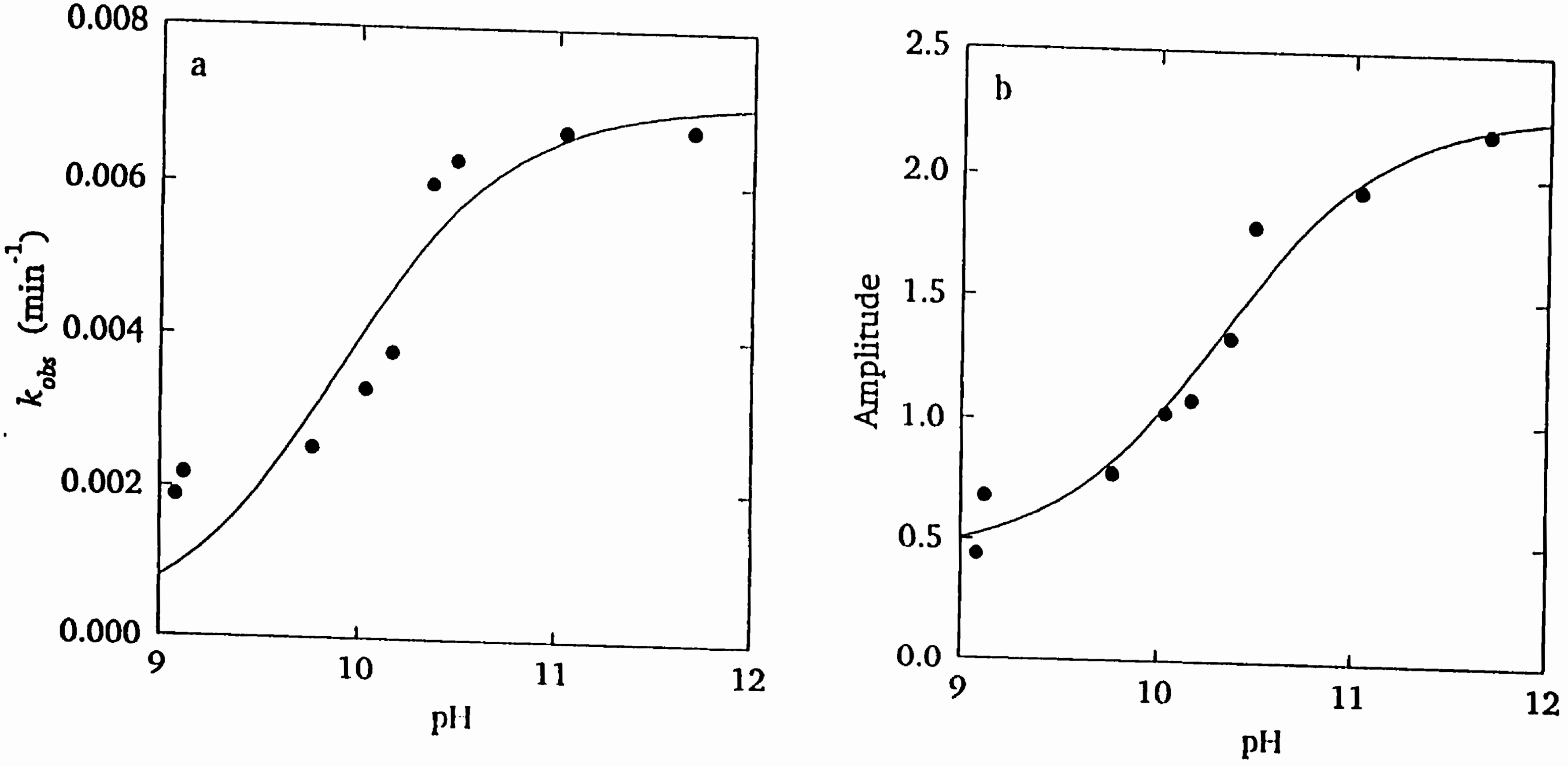

Figure 5.26. pH dependence of hydrolysis of LYZ 19 at 25 °C in ammonia buffer and NaOH solutions. Experimental measurements (●) of a) k_{obs} and b) Amplitude of the absorbance change, both measured at 240 nm, are shown with their least squares fits (lines) to Equations 5.5 and 5.6, respectively.

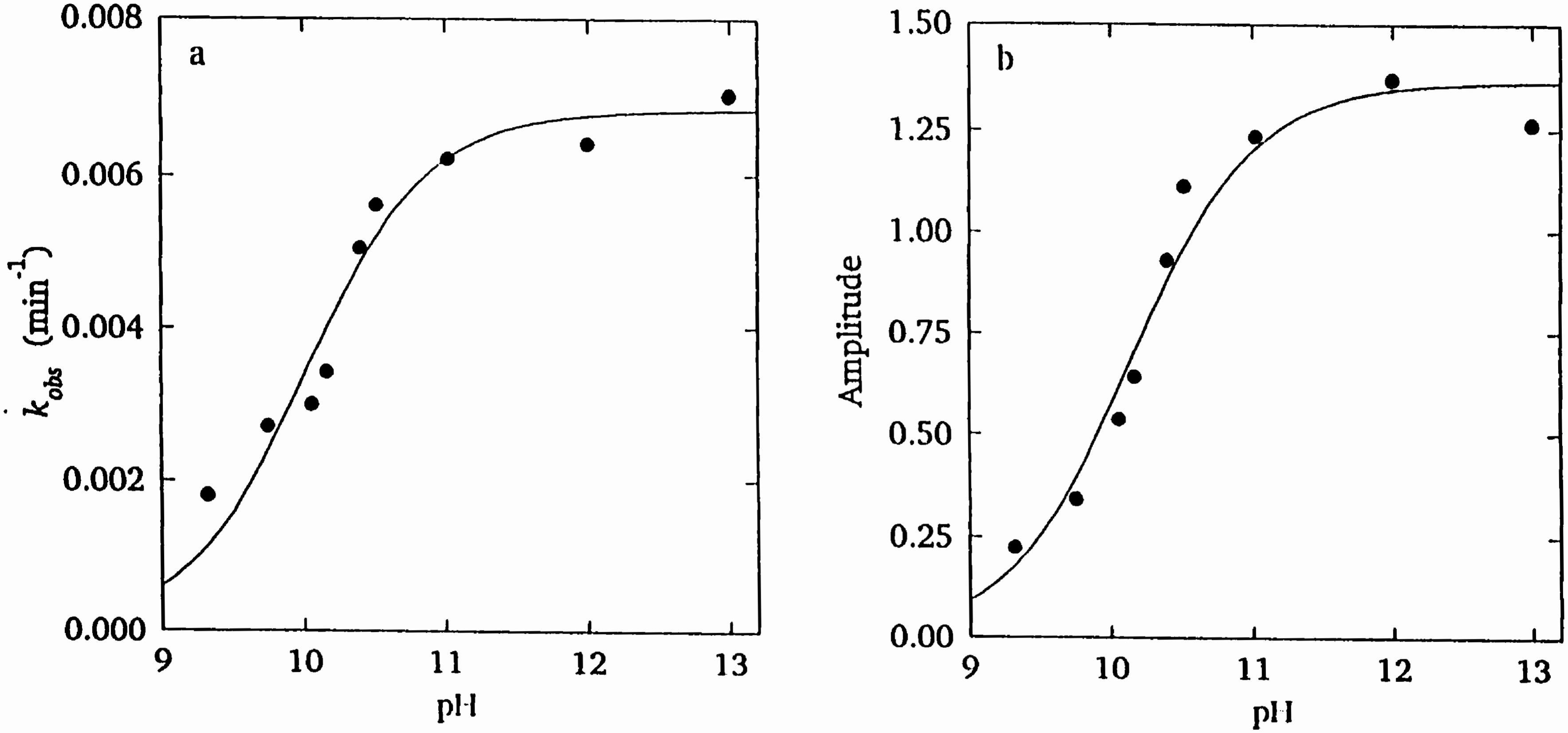

Figure 5.27. pH dependence of hydrolysis of LYZ 2 at 25 °C in ammonia buffer and NaOH solutions. Experimental measurements (●) of a) k_{obs} and b) Amplitude of the absorbance change, both measured at 240 nm, are shown with their least squares fits (lines) to Equations 5.5 and 5.6, respectively.

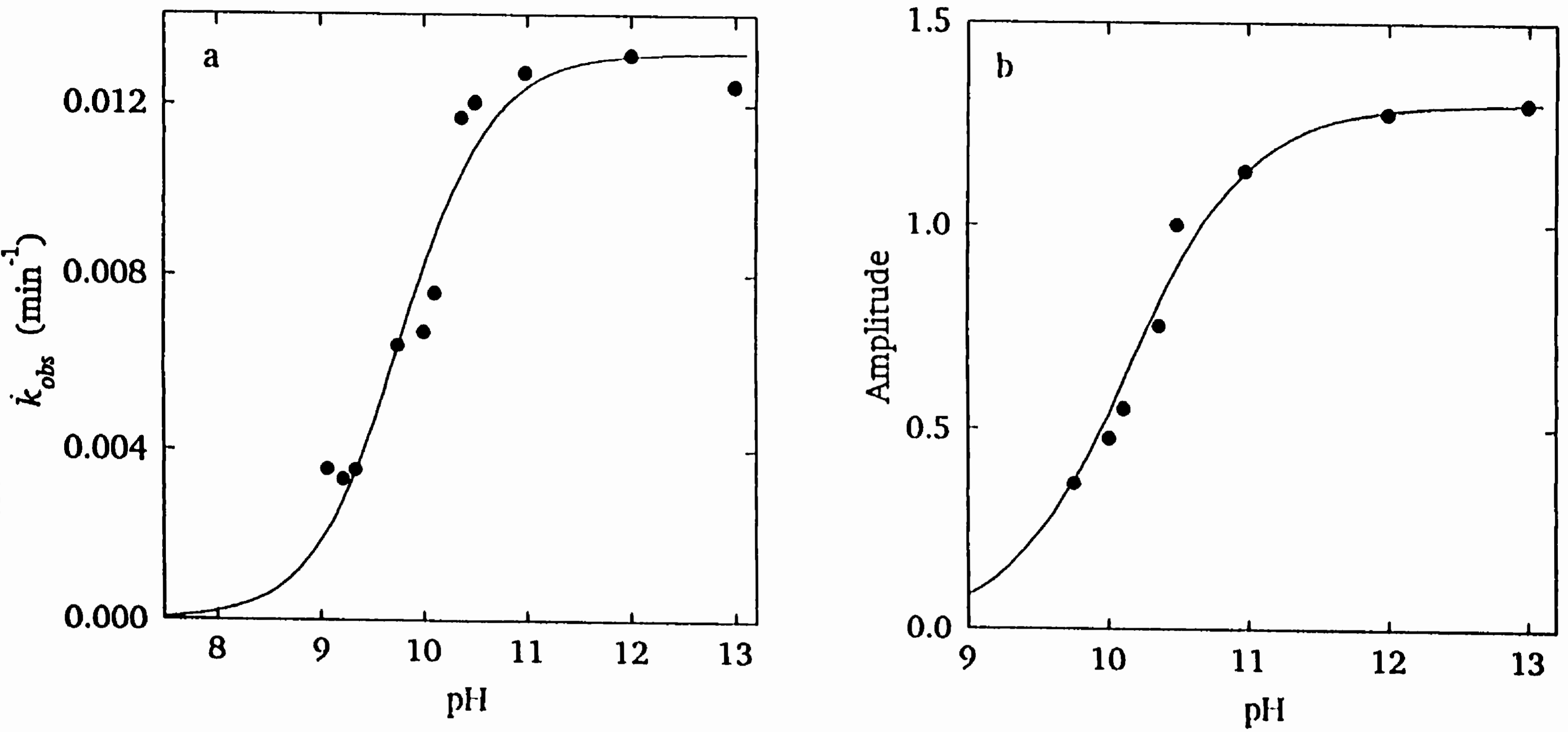

Figure 5.28. pH dependence of hydrolysis of LYZ 8 at 25 °C in ammonia buffer and NaOH solutions. Experimental measurements (●) of a) k_{obs} and b) Amplitude of the absorbance change, both measured at 240 nm, are shown with their least squares fits (lines) to Equations 5.5 and 5.6, respectively.

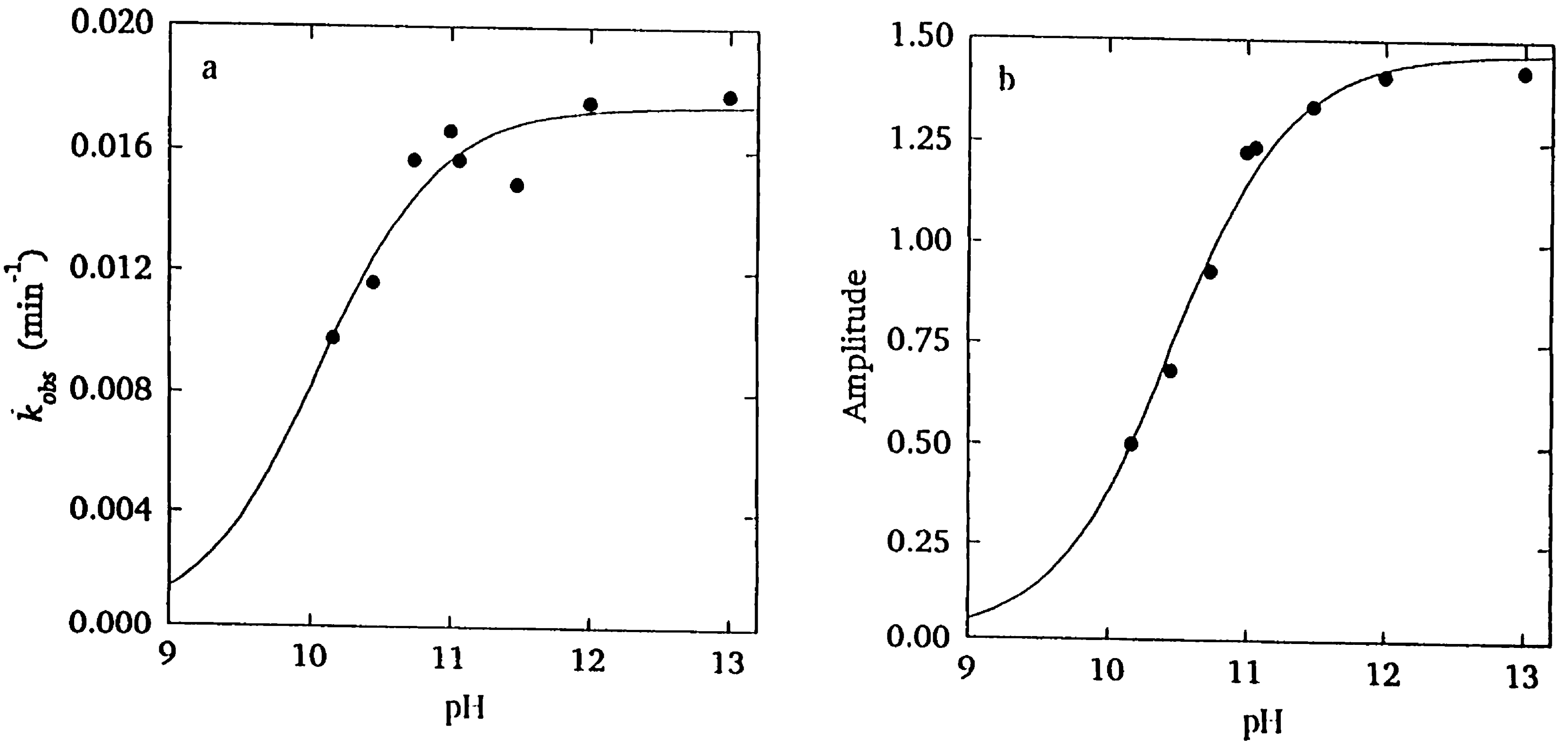

Figure 5.29. pH dependence of hydrolysis of LYZ 22 at 25 °C in ammonia buffer and NaOH solutions. Experimental measurements (●) of a) k_{obs} and b) Amplitude of the absorbance change, both measured at 240 nm, are shown with their least squares fits (lines) to Equations 5.5 and 5.6, respectively.

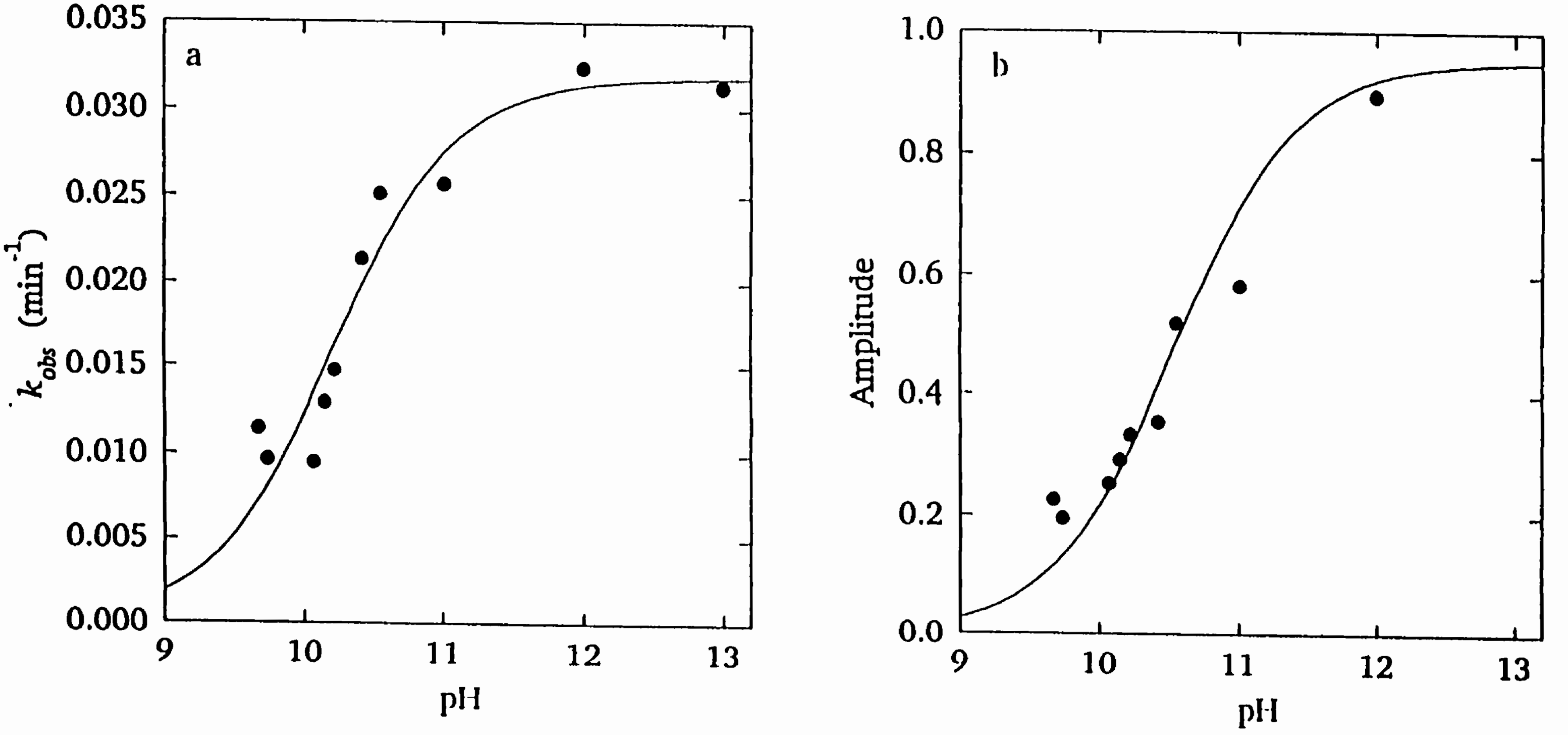

Figure 5.30. pH dependence of hydrolysis of BLPD B2 at 25 °C in ammonia buffer and NaOH solutions. Experimental measurements (●) of a) k_{obs} and b) Amplitude of the absorbance change, both measured at 240 nm, are shown with their least squares fits (lines) to Equations 5.5 and 5.6, respectively.

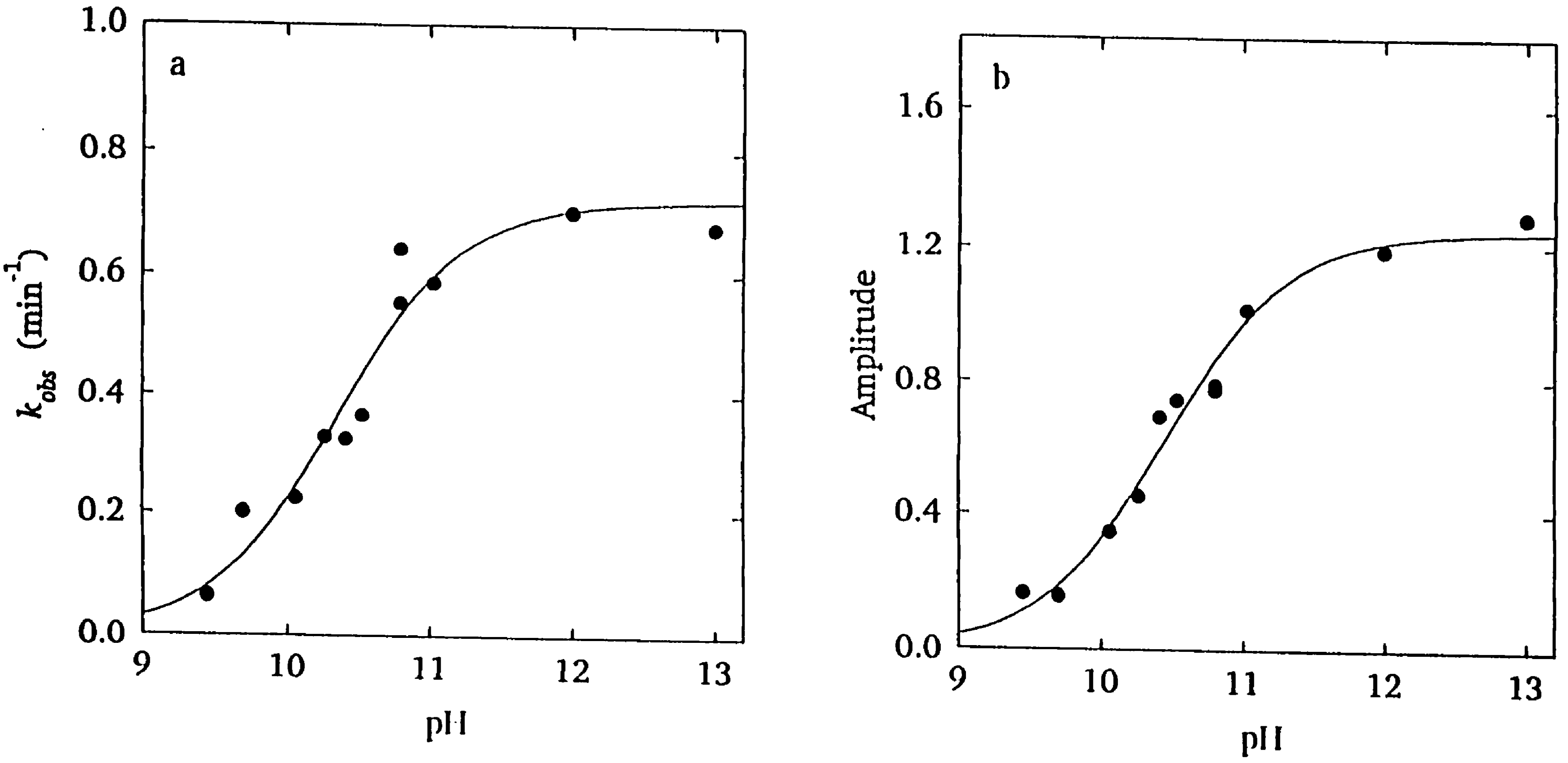

Figure 5.31. pH dependence of hydrolysis of BLPD G2A at 25 °C in ammonia buffer and NaOH solutions. Experimental measurements (●) of a) k_{obs} and b) Amplitude of the absorbance change, both measured at 240 nm, are shown with their least squares fits (lines) to Equations 5.5 and 5.6, respectively.

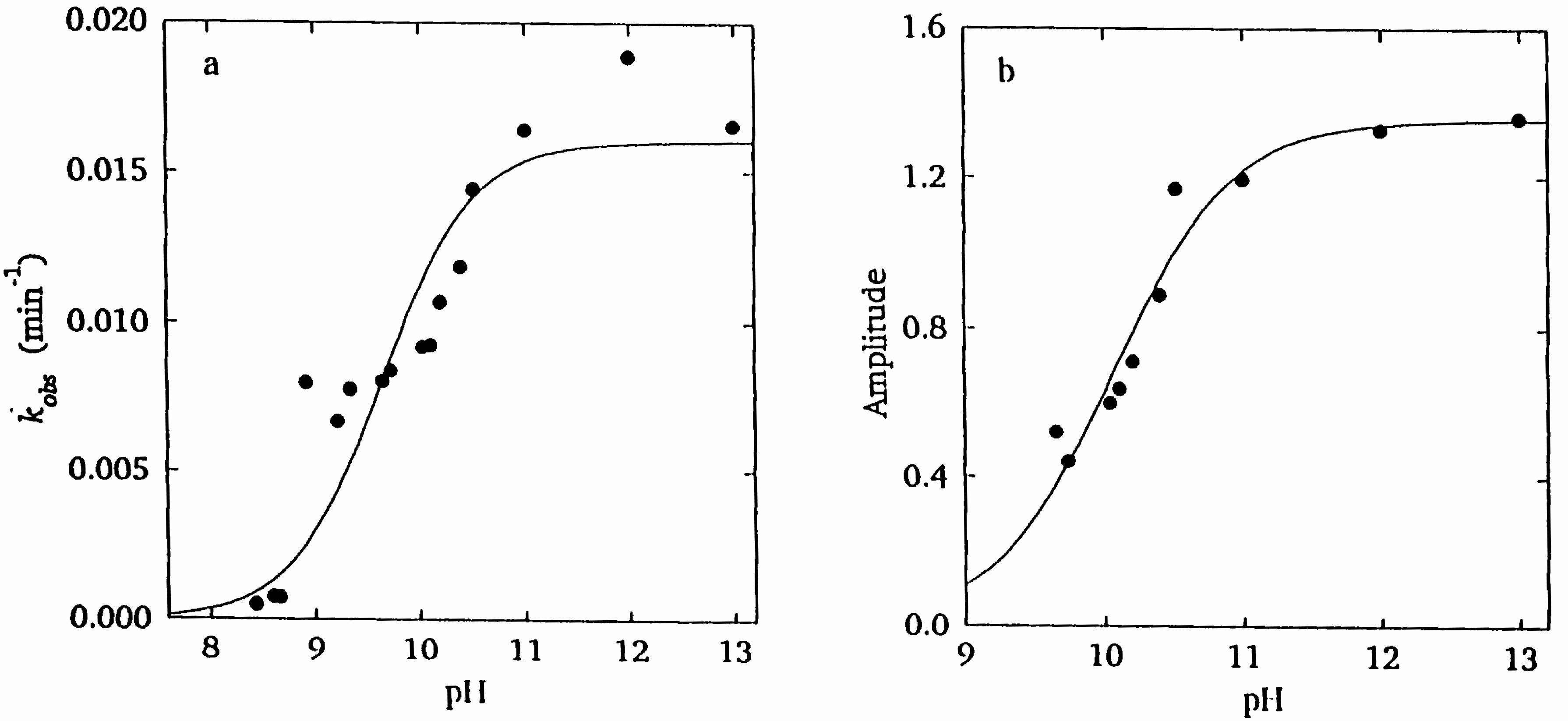

Figure 5.32. pH dependence of hydrolysis of BLPD E1 at 25 °C in ammonia buffer and NaOH solutions. Experimental measurements (●) of a) k_{obs} and b) Amplitude of the absorbance change, both measured at 240 nm, are shown with their least squares fits (lines) to Equations 5.5 and 5.6, respectively.

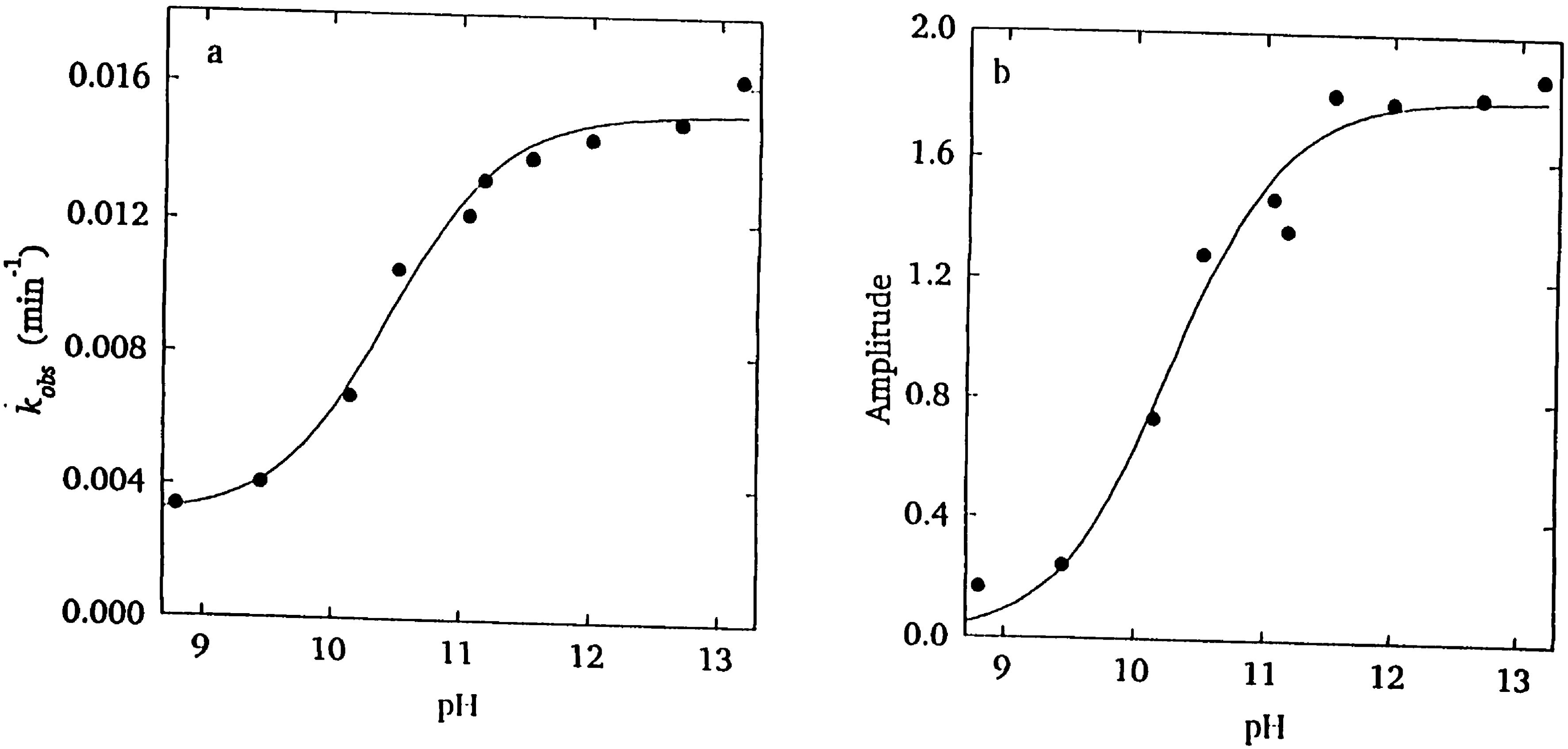

Figure 5.33. pH dependence of hydrolysis of dexrazoxane at 25 °C in ammonia buffer and NaOH solutions. Experimental measurements (●) of a) k_{obs} and b) Amplitude of the absorbance change, both measured at 237 nm, are shown with their least squares fits (lines) to Equations 5.5 and 5.6, respectively.

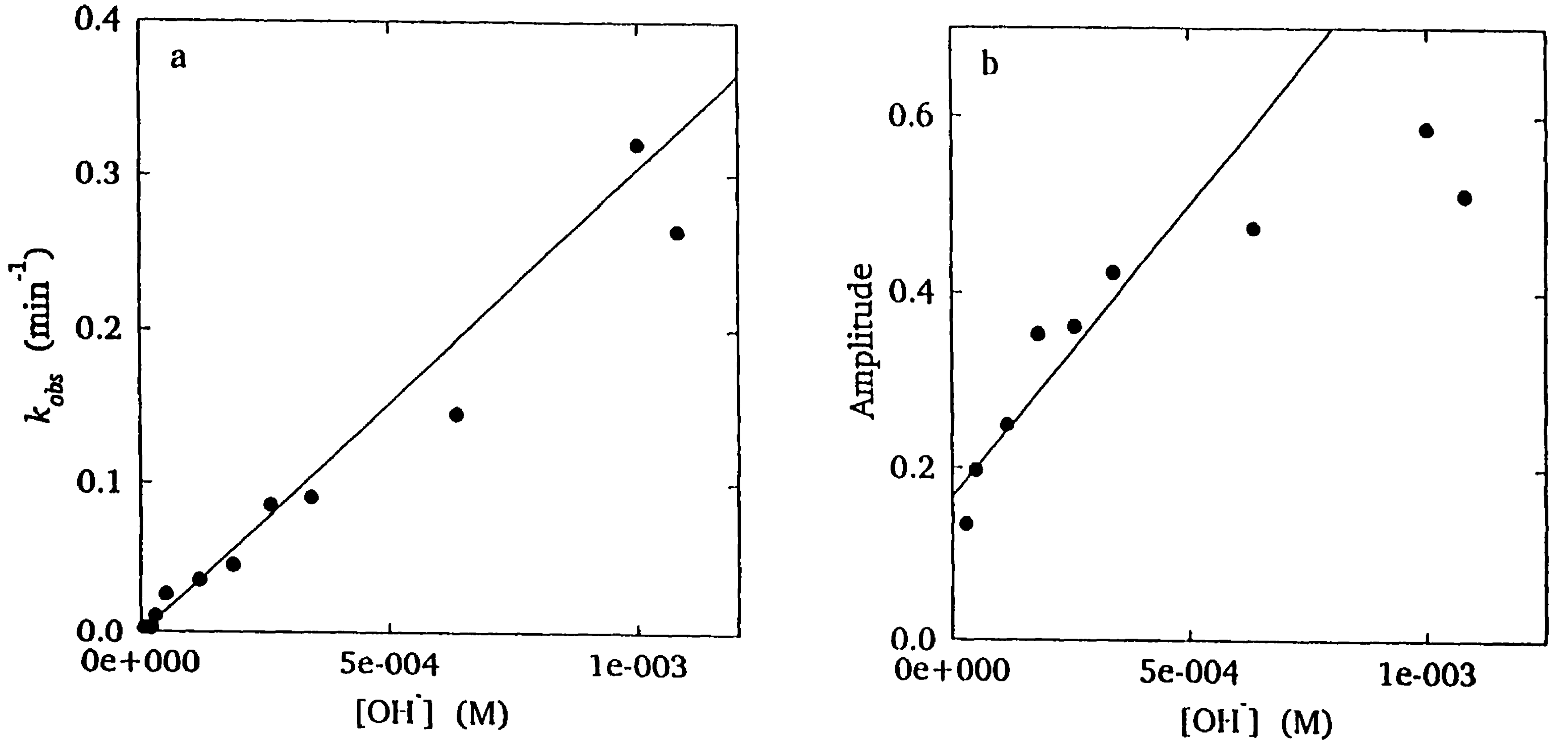

Figure 5.34. pH dependence of hydrolysis of BLPD TTHA at 25 °C in NaOH solutions. Experimental measurements (●) of a) k_{obs} and b) Amplitude of the absorbance change, both measured at 240 nm. Since a pK_a was not observed over the pH range studied, data were fitted to weighted linear equations (lines) with and without a *y*-intercept term, respectively.

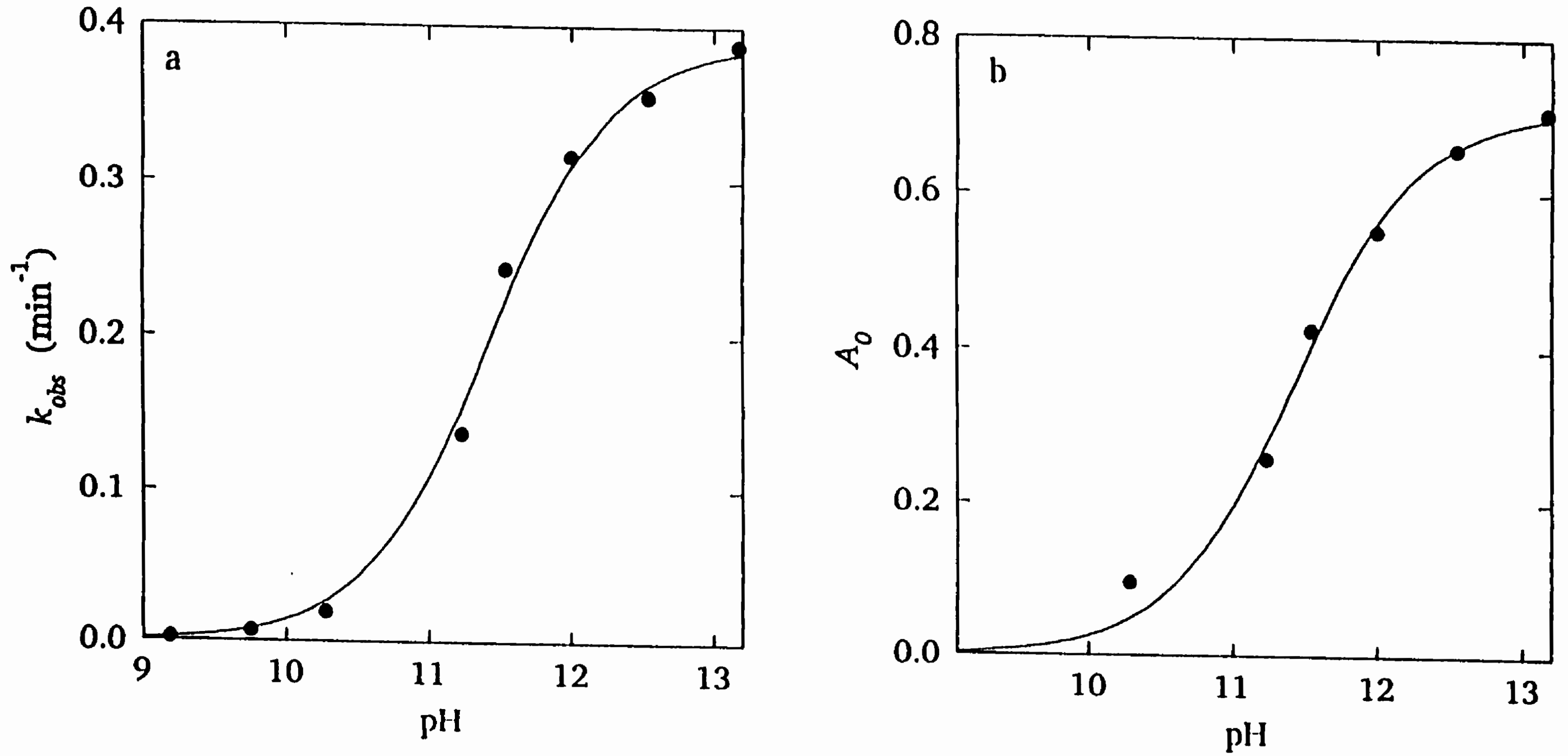

Figure 5.35. pH dependence of hydrolysis of adipimide at 25 °C in ammonia buffer and NaOH solutions. Experimental measurements (●) of a) k_{obs} and b) Absorbance at time zero, both measured at 239 nm, are shown with their least squares fits (lines) to Equations 5.5 and 5.6, respectively.

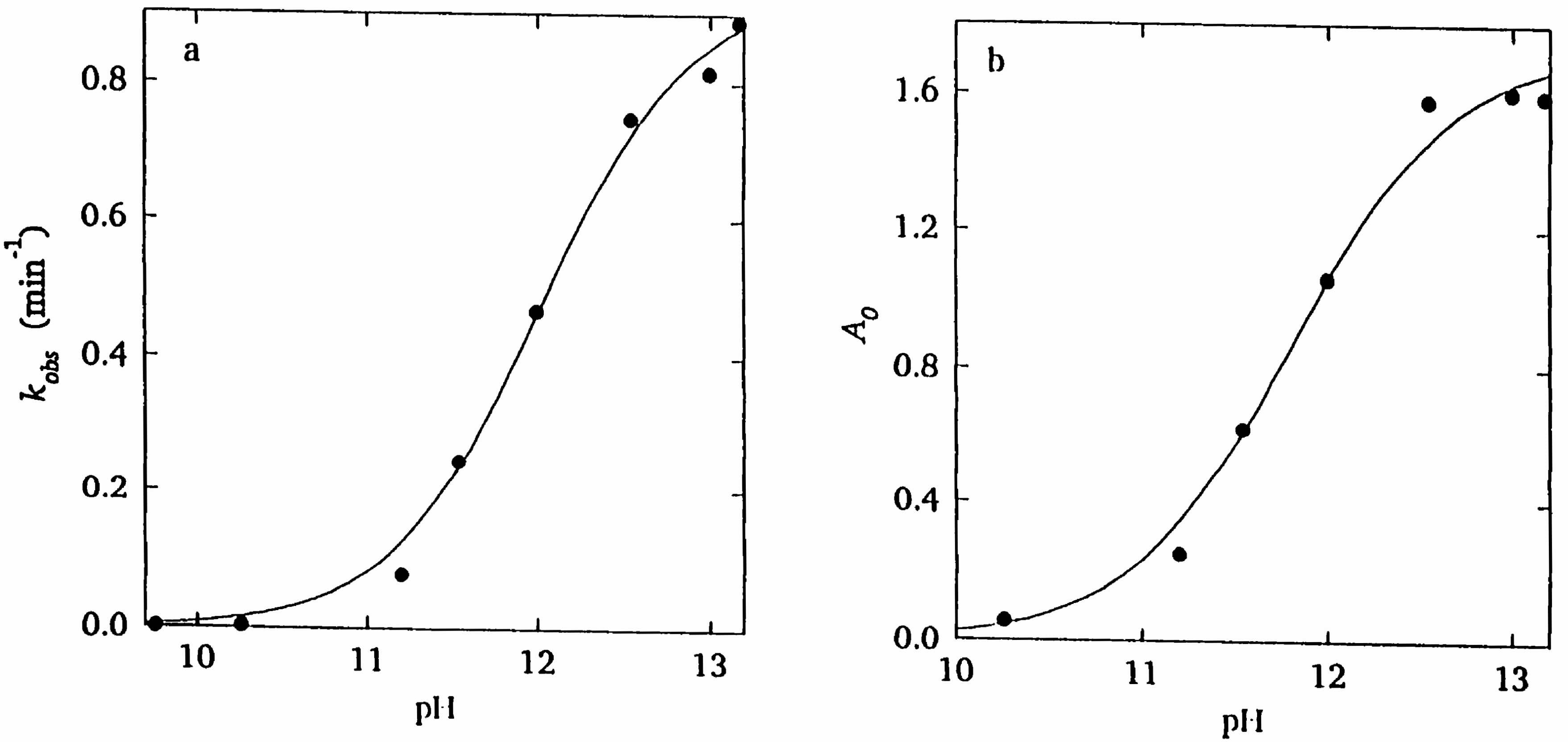

Figure 5.36. pH dependence of hydrolysis of glutarimide at 25 °C in ammonia buffer and NaOH solutions. Experimental measurements (●) of a) k_{obs} and b) Absorbance at time zero, both measured at 239 nm, are shown with their least squares fits (lines) to Equations 5.5 and 5.6, respectively.

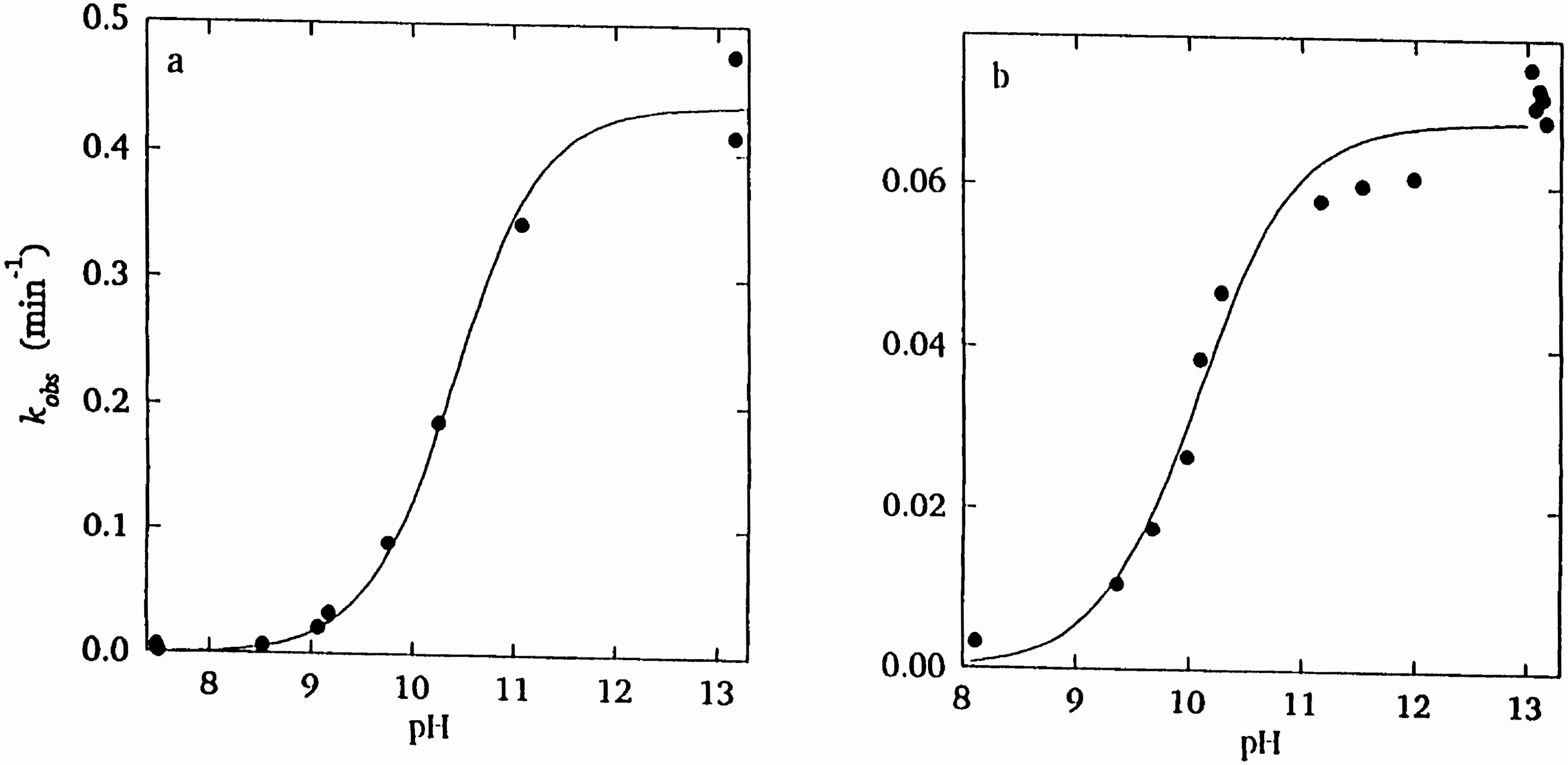

Figure 5.37. pH dependence of hydrolysis of a) maleimide and b) phthalimide at 25 °C in ammonia buffer and NaOH solutions. Experimental measurements (●) of k_{obs} were measured at 217 and 220 nm, respectively, and fitted to Equation 5.5. No change in the amplitude of the absorbance change with pH was observed for these imides.

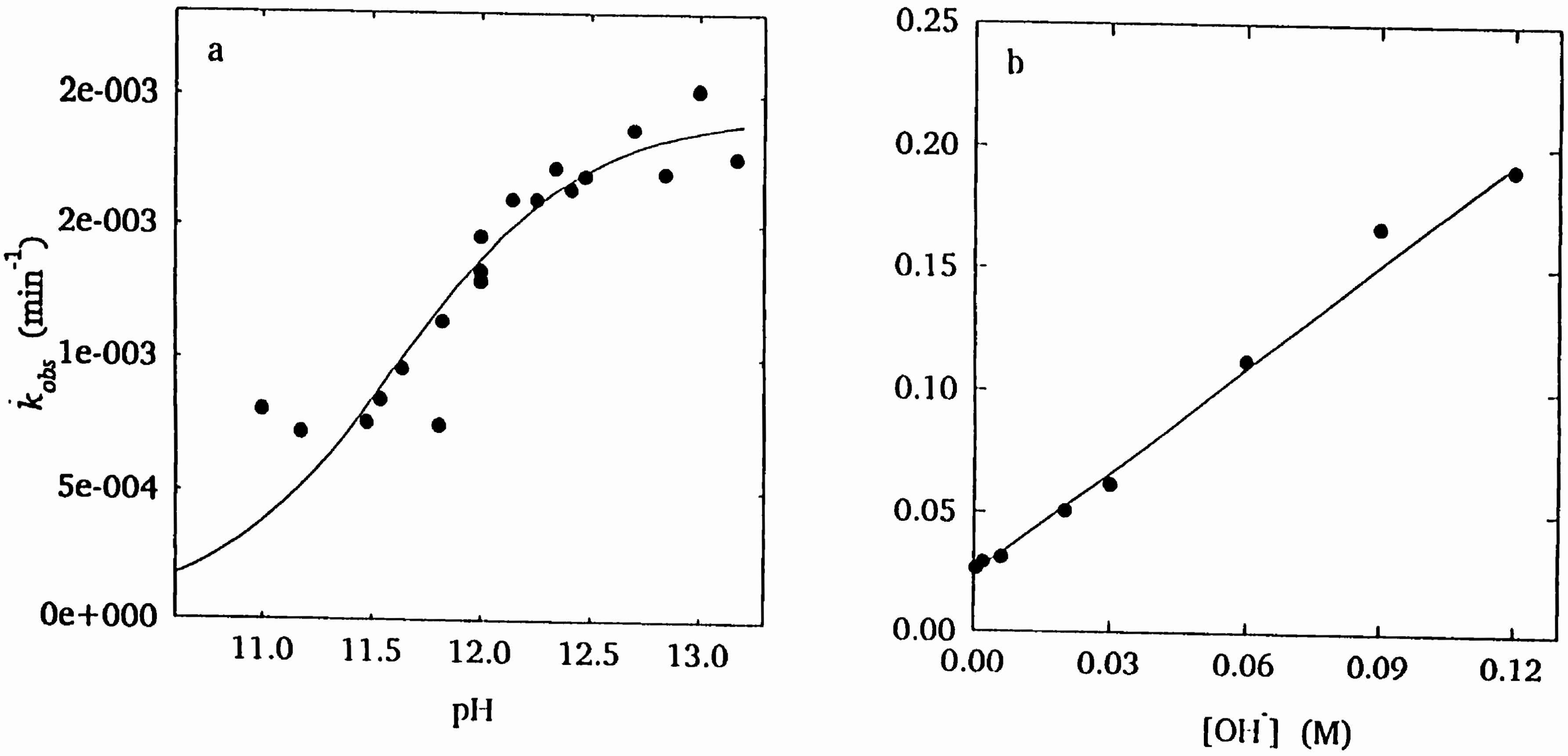

Figure 5.38. pH dependence of hydrolysis of a) 1,2,3,6-tetrahydrophthalimide and b) 3,4,5,6-tetrachlorophthalimide at 25 °C in ammonia buffer and NaOH solutions. Experimental measurements (●) of k_{obs} were measured at 220 nm. Data for 1,2,3,6-tetrahydrophthalimide were fitted to Equation 5.5. Since no pK_a was observed for 3,4,5,6-tetrachlorophthalimide over the pH range studied, data were fitted to a weighted linear equation. No change in the amplitude of the absorbance change with pH was observed for these imides.

$$k_{obs} = \frac{k_2[OH^-]}{\frac{K_a}{[H^+]} + 1} \qquad (5.5)$$

in which K_a is the acid dissociation constant for the imide proton, and k_2 is a second-order rate constant, describing the dependence of imide hydrolysis on the hydroxide ion and imide concentrations. Values of k_2 and pK_a are listed in Table 5.1.

For all the non-*N*-substituted imides, Equation 5.5 adequately described the data, confirming the reaction scheme shown in Figure 5.2. If nucleophilic attack by water also occurs, its contribution to k_{obs} is small enough to be undetectable in these experiments. When a constant term was included in Equation 5.5, representing hydrolysis due to nucleophilic attack by water, the fitting errors on this parameter were large, indicating that this parameter was poorly defined, with the exception of dexrazoxane, for which water-catalyzed hydrolysis has been described in detail [120]. The experimental difficulties which prevented the study of imide hydrolysis at lower pH include low water solubility and very slow hydrolysis rates of imides below the pK_a. As pH decreases below the pK_a, the fraction of the imide present as the anion decreases. When the absorbance of the imide peak becomes too small, measurement of the absorbance changes at this wavelength is no longer possible. Due to the high background absorbance of the buffer at shorter wavelengths, it is not possible to measure the absorbance of the neutrally charged imide directly.

Due to the shift of the absorbance maximum on imide deprotonation, a static determination of the imide pK_a can be made. The pH-dependent changes in amplitude at the wavelengths analyzed for each imide were consistent with a scheme in which the absorbance of the imide anion is much greater than that of the protonated species, as has been shown at 227 nm for dexrazoxane [117]. The amplitude data were fitted to an equation derived from this scheme (Appendix),

$$Amp = \frac{Amp_{max} \cdot K_a}{[H^+] + K_a} + C \qquad (5.6)$$

in which *Amp* is the amplitude at a given pH, Amp_{max} is the maximum amplitude from the kinetic study, and *C* is the absorbance of the completely hydrolyzed species.

5.3.6 Discussion of kinetic results

The values of Amp_{max}, determined from Equation 5.6 at 239 or 240 nm for all non-*N*-substituted imides except succinimide (Table 5.1), fell within a narrow range, indicating that this parameter is not greatly affected by changes in the structural environment of the imide. It was expected, but not observed, that the bis-imides would have values of Amp_{max} approximately two-fold larger than those of the mono-imides.

The kinetically and statically determined pK_a values did not agree well for a number of the imides in the series: succinimide, LYZ 8, LYZ 19, LYZ 22, BLPD E1, BLPD G2A, and BLPD B2. The pK_a of succinimide has been reported as 9.6 (measured potentiometrically at 25 °C, ionic strength 0.01) [183] and 10.5 (measured kinetically at 25 °C in 0.05 M NaOH) [184], which agree well with the statically (9.6 ± 0.3) and kinetically (10.9 ± 0.08) determined values of pK_a in this study. Thus, the kinetically determined values of pK_a, which describe the hydrolysis reaction, may not depend solely on the microscopic pK_a values of these imides. The pK_a values for glutarimide (determined potentiometrically at 25 °C) [185] and dexrazoxane (determined spectrophotometrically at 25 °C and ionic strength = 0.5) [120] were higher than in previous determinations, perhaps for the same reason. Since it is the kinetic determination of pK_a which, with k_2, quantitatively describes the pH dependence of imide hydrolysis, the kinetically determined values of pK_a will be used for the statistical analysis.

The pH range over which kinetic data were measured for diacetamide was not optimal for kinetic analysis. Because of its high pK_a, very few data points characterize the region above this pH. However, due to the excellent agreement of the determination of the pK_a (12.8) with the value of 12.9 (determined kinetically at 25 °C) reported previously [174], it was concluded that the data had been collected over a sufficient range to permit accurate determination of the kinetic parameters, k_2 and pK_a. Thus, data for diacetamide were included in the kinetic analysis.

The results of kinetic analysis of hydrolysis of imides, listed in Table 5.1, reveal trends in pK_a and k_2 with structure. The imides in the series can be compared to determine the effects of ring size, unsaturation, *N*-substitution, and other structural variations on imide hydrolysis.

Any differences in pK_a and k_2 between glutarimide and diacetamide are likely to be due to steric effects, since the electronic effects of the additional methylene group of glutarimide should be minimal. The k_2 of glutarimide was 1.4 times larger than that of diacetamide, and the pK_a of glutarimide was 0.7 pH units lower than that of diacetamide, indicating the minimal effect of a six-membered ring on imide hydrolysis. The differences in both of these parameters suggest a small destabilization of glutarimide, which may be explained by the rigidity imposed on the imide functional group by its six-membered ring. In the solid state, diacetamide prefers an *E,Z* conformation about the carbon-nitrogen bonds [186], through which it minimizes steric and electronic strain by keeping the bulky methyl groups and the electron-rich carbonyl oxygen atoms as far apart as possible. Thus, deprotonation, which increases the electron density on the two oxygen atoms, is more favored for diacetamide than for glutarimide, which must maintain an *E,E* conformation. Diacetamide may also deviate from a planar conformation to further relieve strain, while glutarimide, presumably, is more rigid. Another kinetic study on the relative hydrolysis rates of imides reported that the *N*-methyl derivatives of diacetamide and glutarimide also hydrolyzed at similar rates [187]. Adipimide, a seven-membered ring, had a k_2 1.7 times higher than that of glutarimide, which is consistent with the observation that stability decreases with increasing ring size.

In agreement with previous predictions that the stabilities of five-membered rings containing *exo* double bonds are greater than their six-membered analogs [188], the k_2 of succinimide was approximately 17 and 12 times lower than those of glutarimide and diacetamide. A previous study reported a ten-fold decrease in the hydrolysis rate of *N*-methylsuccinimide relative to *N*-methyldiacetamide [187], which is in good agreement with the six-fold difference observed in this study. It was determined [188] that the *exo* double bonds decreased the number of bond oppositions, and therefore ring strain, in five-membered rings, which should apply especially to five-membered cyclic imides, due to their planarity. The k_2 of 1,2,3,6-tetrahydrophthalimide, which may be considered an analog of succinimide, was 12 times lower than that of succinimide. The fused ring must confer additional stability to the molecule, which overcomes any increase in strain caused by steric factors.

Values for phthalimide of 560 ± 3 M^{-1} min^{-1} and 10.1 ± 1 for the kinetic parameters, k_2 and pK_a, are in excellent agreement with previously reported determinations of 684 M^{-1} min^{-1} and 10.2 (determined at 25 °C in 10% aqueous ethanol) [175]. Phthalimide and maleimide, both of which are unsaturated imides, had high values of k_2 relative to the rest of the imides in the series, although the k_2 of phthalimide was three times lower than that of maleimide. This is unlikely to be due to steric effects, since both of these imides may be expected to be rigidly planar, to maximize electron delocalization. The benzene ring of phthalimide may donate electrons to the imide ring, increasing the electron density of the imide functional group, making it less attractive to the negatively charged nucleophile, hydroxide ion. By the same argument, the analog of phthalimide, 3,4,5,6-tetrachlorophthalimide, is expected to hydrolyze significantly faster than phthalimide, due to the strong electron-withdrawing effect of the four chlorine atoms. However, 3,4,5,6-tetrachlorophthalimide has a k_2 400 times lower than that of phthalimide.

Maleimide hydrolyzed 300 times faster than its saturated analog, succinimide. Although the overall geometry of these imides is similar, it may be expected that maleimide may have additional ring strain, both due to the rigidity required for maximal electron delocalization of the ring, and to the larger number of in-plane steric interactions of the substituents of the five-membered ring oppositions for maleimide (five) as compared to succinimide (four) [188].

The bisdioxopiperazines have similar values of k_2 and pK_a, indicating that, in this series, structural features outside the dioxopiperazine ring have little influence on the geometric and electronic properties of the imide functional group, as previously observed for a series of bisdioxopoiperazines [189]. Both of these parameters, however, are quite different between the bisdioxopiperazines and glutarimide, their carbon isostere. The tertiary nitrogen atom decreases the pK_a of the imide group without significantly affecting k_2. The effect on pK_a must be due to the electron-withdrawing effect of the nitrogen atom, as is it unlikely that substitution of nitrogen for carbon would result in a significant change in ring strain.

Effects of *N*-substituents on the hydrolysis rates of imides are also observed. *N*-methyl groups on diacetamide, succinimide, and maleimide increase k_2 by a factor of approximately two. This small effect may be due to the expected increase in steric strain by the substitution of a small group, the hydrogen atom, with a somewhat larger methyl group. In the case of the maleimides, for which a variety of *N*-substituted imides were studied, it can be seen that k_2 increases with the electron-withdrawing properties of the imide, *i. e.* in the order *N*-ethyl ≈ *N*-methyl < *N*-3,4-xylyl < *N*-phenyl < *N*-4-chlorophenyl. σ_I parameters, calculated from pK_a values of the corresponding α-substituted acetic acids, are known for each of these substituents [190]. The log k_2 *vs.* σ_I data were fitted to a linear equation with a slope of 5.0 ± 1.6. Thus, the *N*-substituent is able to withdraw electrons from the imide group, thereby increasing its reactivity toward hydroxide ion.

5.4 Molecular Modelling

5.4.1 Introduction

Imides hydrolyze *via* a $B_{AC}2$ mechanism [191]. This classification denotes second-order, base-catalyzed acyl cleavage. Thus, it is expected that the products of imide hydrolysis will be a carboxylic acid and an amide, due to the addition of water across the C(carbonyl)-N bond, and that hydrolysis will depend on the concentrations of the nucleophile (hydroxide ion) and the imide. Imide hydrolysis is analogous to ester and amide hydrolysis, all of which hydrolyze by a similar, two-step mechanism (Figure 5.3). In the first step, hydroxide ion attacks the electrophilic carbonyl carbon atom, reversibly producing an intermediate with a tetrahedral sp^3 carbon atom. The second step involves the decomposition of the tetrahedral intermediate, during which the C-N bond is broken. At neutral pH, the expected products are a carboxylate and an amide.

The base-promoted hydrolysis rates of imides depend on geometric and electronic factors, which determine their reactivities as electrophiles toward hydroxide ion. Since hydrolysis begins with the attack of the carbonyl carbon atom of the imide by hydroxide ion, this atom and its environment are of great significance. Since the hydroxide ion must first attack the carbonyl carbon atom, the charge on this atom, and those surrounding it, may influence hydrolysis rate. It is expected that the hydrolysis rate constant will increase with the positive charge on the imide functional group. Bond lengths depend on the interaction between the atoms; as the strength of the interaction increases, bond length decreases. The length of the C-N bond, which is broken during hydrolysis, may reflect the hydrolysis rate. The π electrons of the imide functional group are delocalized, as is the case for amides. Thus, it is expected that deviations from planarity of the atoms in the imide functional group will reduce the electron delocalization and stability, increasing their susceptibility to nucleophilic attack. According to frontier molecular orbital theory, the LUMO (lowest unoccupied molecular orbital) of the imide will accept electrons from the nucleophile, hydroxide ion, during the first step of imide hydrolysis. The lower the energy of this orbital, the more favorable will be the production of the tetrahedral intermediate, and therefore, the faster will be the hydrolysis rate. Many of the imides in the data set are cyclic. Thus, ring strain may also be a factor in the relative hydrolysis rates of these imides. The greater the deviations of bond lengths and angles from their optimum (unstrained) values, the faster the imide group may hydrolyze to relieve this strain. These and other factors were examined by extraction of estimates of atomic charges, frontier molecular orbital energies, bond lengths and angles, and other descriptors from the geometry-optimized structures of the imides in the data set.

The most useful information for prediction of imide hydrolysis rates should come from studying the transition state of the rate-determining step in the mechanism, since the production and decomposition of this species govern the rate of the overall reaction. However, there is some disagreement in the literature regarding which of the two steps is rate-determining. Studies of succinimide and diacetamide [174] and maleimides [177] have concluded that nucleophilic attack is rate-determining, while other studies of succinimide [121] and maleimide [192] have concluded that the collapse of the tetrahedral intermediate is rate-determining. In either case, it may be worthwhile to examine the electronic and geometric properties of the tetrahedral intermediate structure as well as the imide structure, since, regardless of which step is rate-determining, it may more closely resemble the transition state of interest. Thus, the structures of the tetrahedral intermediates, as well as those of the imides themselves, were modelled, and similar measurements of descriptors were made, as described for the imide structures.

Molecular modelling produces an energy-minimized structure, *i. e.* a minimum-energy conformation, with optimized geometry. Properties of the resulting energy-minimized conformation may be calculated, such as bond lengths, orbital energies, and partial charges. Parameters calculated from the minimized imide structures were used as independent variables in a multiple linear regression analysis to predict k_2.

Molecular mechanics (MMX) and semi-empirical (AM1) algorithms were both used in the study, as each has its advantages. Molecular mechanics calculations are empirically parameterized. Each parameter is based on a series of model compounds. Since molecular mechanics methods have been adapted specifically for small molecules, and since imides are homologous to the peptide bonds in proteins, for which these algorithms have been well parameterized, they are likely to be suitable for geometric parameters such as bond lengths and angles, and torsion angles. Properties which are electronic in nature, such as orbital energies and partial charges, were more appropriately calculated by semi-empirical methods, which explicitly calculate the molecular orbitals of the electrons from the partially parameterized Schrödinger equations.

5.4.2 Structure optimization with a molecular mechanics algorithm

For diacetamide [186], *N*-methylbis(trifluorodiacetamide) [193], succinimide [194], *N*-ethylmaleimide [195], phthalimide [196], 1,2,3,6-tetrahydrophthalimide [197], glutarimide [198], and ICRF-154 [199], the X-ray crystal structures are known. These structures were used as starting points for structure optimization. The starting structures for *N*-methyldiacetamide, the substituted succinimides, the remaining maleimides, 3,4,5,6-

tetrachlorophthalimide, and the remaining dexrazoxane analogs were obtained by modification of the crystal structures of *N*-methylbis(trifluorodiacetamide), succinimide, *N*-ethylmaleimide, phthalimide, and ICRF-154, respectively. Two starting structures for adipimide were manually entered, both of which had planar sp^2 atoms. One of these structures had one sp^3 carbon atom on each side of the imide plane, while the other had both sp^3 carbon atoms on the same side of the plane. The selection of the preferred conformation is discussed in Section 5.4.3.

Structure minimization by the MMX algorithm was done with PCModel (Serena Software, Bloomington, IN), version 4.0, which uses the MMX algorithm, adapted from the Allinger MM2 algorithm [150], on an IBM-compatible 486 computer. The diacetamides, which are acyclic, were minimized from three starting structures, corresponding to the *E,E*, *E,Z*, and *Z,Z* conformations, and of the resulting minimized structures, that with the lowest-energy was selected. For the analogs of dexrazoxane, structures with significant conformational flexibility, optimization was attempted from multiple starting points, based on the results of initial structure optimization. Conformations with torsion angles of the flexible bonds rotated 0, 120, and 240° from the angles of the initial optimized structure were minimized. When more than one optimized conformation resulted from these multiple starting structures, that with the lowest energy was chosen as the final structure. Structures were minimized with a dielectric constant of 1.5, as is usual. Minimization was repeated at least three times, until the binding energy no longer decreased. Aromatic rings, and the carbon, oxygen, and nitrogen atoms of the imide functional group were modelled as π atoms, and minimization was performed using restricted Hartree-Fock self-consistent field calculations.

Optimized structures of the anionic tetrahedral hydrolysis intermediates were generated using the corresponding minimized imide structures as the starting points, and were minimized at least three times, until the binding energy no longer decreased. No further exploration of conformational flexibility was made for the structures of the tetrahedral intermediates. The intermediates were modelled as mono-anions, as was done in previous studies of esters [200] and lactams [201].

Due to the geometric restrictions of cyclic molecules, and to the stabilization of the imide functional group due to electron delocalization, the optimized structures tended toward planarity. Thus, the succinimides, maleimides, and phthalimides, which have five-membered rings, had nearly planar conformations. Glutarimide and the dexrazoxane analogs, compounds with six-membered imide rings, preferred a half-chair conformation, which permitted a planar arrangement of the atoms of the imide functional group. Although *N*-methyldiacetamide and *N*-methylbis(trifluorodiacetamide) preferred an *E,E* conformation, diacetamide, with no bulky *N*-substituent, preferred an *E,Z* conformation, which minimized steric interaction between the two acetyl groups. Bond angles of the optimized imide structures were consistent with the π delocalization expected of the imide functional group. The C(carbonyl)-N-C(carbonyl) and Cα-C(carbonyl)-N angles for the acyclic and six-membered ring imides, which may be expected to have minimal strain, were approximately 120°, consistent with partial sp^2 character.

The tetrahedral hydrolysis intermediates of the five- and six-membered imides preferred envelope and cyclohexene conformations, respectively, which retained the planar arrangement of the sp^2 centers. The Cα-C(carbonyl)-N bond angles decreased, corresponding to the shift from sp^2 to sp^3 hybridization. The species with five-membered rings, the succinimides and maleimides, had angles from 100 to 104°, reflecting the Baeyer strain due to the two remaining sp^2 centers. The other species had angles from 110 to 114°, consistent with sp^3 hybridization. The C-N bond length increased to 1.44-1.49 Å, reflecting the decrease in electron density from the nitrogen atom, due to the loss of π character.

5.4.3 Structure optimization with a semi-empirical algorithm

All structures were also optimized by the AM1 algorithm using Hyperchem, release 4 for Windows (Hypercube Inc., Gainesville, FL), on an IBM-compatible 486 computer. The MMX-optimized structures obtained from PCModel were used as the starting points for semi-empirical optimization. Structures were minimized *in vacuo*, using a restricted Hartree-Fock self-consistent field. Optimization proceeded by a Polak-Ribière algorithm, which iterates based on the gradients of the current and previous iterations. Since minimization until the gradient was less than either 0.01 or 0.1 kcal/Å yielded binding energies which differed only in the seventh significant figure, the cutoff for structure optimization was set at a gradient of 0.1 kcal/Å.

The structures optimized by the AM1 algorithm were qualitatively similar to those obtained from the MMX algorithm of PCModel. The results of a root-mean-square (RMS) comparison of atomic positions for the series of compounds for which MMX-optimized, AM1-optimized, and X-ray imide structures are available are shown in Table 5.2. Since the root-mean-square distances are generally small, and the optimized structures are intuitively reasonable, these structures likely represent stable conformations. Although X-ray structures of *N*-methylbis(trifluorodiacetamide) and ICRF-154 were available, they were not included in the analysis, since the optimized structures had adopted significantly different conformations.

Table 5.2. Comparison of x-ray structures with those obtained from molecular modelling.[a]

Compound	**RMS Distance X-ray *vs.* MMX (Å)**	**RMS Distance X-ray *vs.* AM1 (Å)**	**RMS Distance MMX *vs.* AM1 (Å)**
Diacetamide	0.077	0.078	0.039
Succinimide	0.078	0.050	0.067
N-Ethylmaleimide	0.056[b]	0.045[b]	0.131
Phthalimide	0.029	0.037	0.029
1,2,3,6-Tetrahydrophthalimide	0.078	0.062	0.082
Glutarimide	0.035	0.033	0.036

[a] Hydrogen atoms were not included in the calculations, which were done using the Compare Structures feature of PCModel.

[b] The terminal carbon atom of the *N*-ethyl substituent was not included in the calculations.

Two energy minima were found for adipimide, both of which were qualitatively similar to their respective starting structures (described in Section 5.4.2). In the case of the structures optimized by the MMX algorithm, the energy of the conformation in which the two sp^3 carbon atoms are on opposite sides of the imide plane was 1.25 kcal higher than that with the sp^3 atoms on opposite sides. In the case of the structures optimized by the AM1 algorithm, the energy of the former structure was 1.28 kcal lower than the latter. It was expected that the AM1 algorithm results would be more useful, since the calculation of electronic parameters is more reliable, the structure with the sp^3 carbon atoms on opposite sides of the imide plane was chosen for the statistical analysis.

Measurements of 80 descriptors which measure electronic and geometric properties were made on the MMX- and AM1-optimized structures of the imides and tetrahedral intermediates.Forty-four compound descriptors were generated by simple transformations. Examples include the squares and absolute values of individual descriptors, which may better describe any non-linear relationships with the dependent variables. Sums and differences of partial charges of adjacent atoms and differences between HOMO and LUMO energies were also included, as they may describe properties which the individual descriptors do not. For some partial charges, bond lengths and angles, and the HOMO energy, the differences between measurements of each imide were subtracted from that of diacetamide, and squared. Since diacetamide is the smallest, simplest molecule in the data set, it likely represents the least strained system. Due to their structural variations, values of the descriptors for the other imides in the series may deviate from those of diacetamide. Thus, a measure of this deviation may also provide useful information. A total of 124 descriptors was compiled, to be used as independent variables in the prediction of imide hydrolysis rates. The abbreviations used to identify each of these descriptors are defined in Table 5.3, and their values for each imide are listed in Table 5.4.

Table 5.3. Definitions of descriptors extracted from molecular modelling of imides.

Descriptor	Structure[a]	Algorithm[b]	Average[c]	Description
IZO	I	AM1	A	Charge; carbonyl oxygen
IZC	I	AM1	A	Charge; carbonyl carbon
IZN	I	AM1	A	Charge; imide nitrogen
IZR	I	AM1	A	Charge; imide *N*-substituent (sum of charges of all atoms)
IRCO	I	AM1	A	Bond distance; carbonyl carbon - carbonyl oxygen (Å)
IRCN	I	AM1	A	Bond distance; carbonyl carbon - nitrogen (Å)
IRCR	I	AM1	A	Bond distance; carbonyl carbon - α carbon (Å)
ITOCNC	I	AM1	A	Absolute value of torsion angle; carbonyl oxygen-carbonyl carbon-imide nitrogen-carbonyl carbon (°)
IPLAN	I	AM1	A	Absolute value of torsion angle; carbonyl oxygen-carbonyl carbon-imide nitrogen-imide R group (°)
ICCN	I	AM1	A	Bond angle; imide nitrogen-carbonyl carbon-α carbon (°)
IRING	I	AM1	A	Sum of the angles in the imide ring (°)
IHOMO	I	AM1	--	Energy; highest occupied molecular orbital (eV)
ILUMO	I	AM1	--	Energy; lowest unoccupied molecular orbital (eV)
IDPM	I	AM1	--	Dipole moment (Debyes)
IBIN	I	AM1	--	Binding energy (kcal/mol)
IHF	I	AM1	--	Heat of formation (kcal/mol)
IELEC	I	AM1	--	Electronic energy (kcal/mol)
ICORE	I	AM1	--	Core-core interaction energy (kcal/mol)

IATOM	I	AM1	--	Isolated atom energy (kcal/mol)
ITOT	I	AM1	--	Total energy (kcal)
IZO2	I	AM1	A	$(IZO)^2$
IZN2	I	AM1	A	$(IZN)^2$
IRCO2	I	AM1	A	$(IRCO)^2$ (Å^2)
IRCN2	I	AM1	A	$(IRCN)^2$ (Å^2)
IRCR2	I	AM1	A	$(IRCR)^2$ (Å^2)
ITOC2	I	AM1	A	$(ITOCNC)^2$ ($^{\circ 2}$)
ICCN2	I	AM1	A	$(ICCN)^2$ ($^{\circ 2}$)
IRING2	I	AM1	A	$(IRING)^2$ ($^{\circ 2}$)
IHOMO2	I	AM1	--	$(IHOMO)^2$ (eV^2)
ILUMO2	I	AM1	--	$(ILUMO)^2$ (eV^2)
I4+5	I	AM1	--	(IZO) + (IZC)
I5+6	I	AM1	--	(IZC) + (IZN)
I6+7	I	AM1	--	(IZN) + (IZR)
I4-5	I	AM1	--	(IZO) - (IZC)
I5-6	I	AM1	--	(IZC) - (IZN)
I6-7	I	AM1	--	(IZN) - (IZR)
I15-16	I	AM1	--	(IHOMO) - (ILUMO) (eV)
I8-9	I	AM1	--	(IRCO) - (IRCN) (Å)
IZON	I	AM1	A	$[(IZO) - (IZO)_{diacetamide}]^2$
IZCN	I	AM1	A	$[(IZC) - (IZC)_{diacetamide}]^2$
IZNN	I	AM1	A	$[(IZN) - (IZN)_{diacetamide}]^2$
IRCON	I	AM1	A	$[(IRCO) - (IRCO)_{diacetamide}]^2$ (Å^2)
IRCNN	I	AM1	A	$[(IRCN) - (IRCN)_{diacetamide}]^2$ (Å^2)
IRCRN	I	AM1	A	$[(IRCR) - (IRCR)_{diacetamide}]^2$ (Å^2)
ICCNN	I	AM1	A	$[(ICCN) - (ICCN)_{diacetamide}]^2$ ($^{\circ 2}$)

IHOMON	I	AM1	–	$[(\mathrm{IHOMO}) - (\mathrm{IHOMO})_{\mathrm{diacetamide}}]^2$ (eV^2)
IZO-	I	AM1	–	Charge; carbonyl oxygen (most negative of all in molecule)
IZC+	I	AM1	–	Charge; carbonyl carbon (most positive of all in molecule)
IZN-	I	AM1	–	Charge; imide nitrogen (most negative of all in molecule)
IRCOL	I	AM1	–	Bond length; carbonyl carbon - carbonyl oxygen (longest of all in molecule) (Å)
IRCNL	I	AM1	–	Bond length; carbonyl carbon-imide nitrogen (longest of all in molecule) (Å)
IRCRL	I	AM1	–	Bond length; carbonyl carbon-α carbon (longest of all in molecule) (Å)
TZO-	T	AM1	–	Charge; unprotonated oxygen on tetrahedral carbon
TZO	T	AM1	–	Charge; protonated oxygen on tetrahedral carbon
TZ=O	T	AM1	–	Charge; intact carbonyl oxygen
TZC	T	AM1	–	Charge; tetrahedral carbon
TZN	T	AM1	–	Charge; imide nitrogen
TZR	T	AM1	–	Charge; imide *N*-substituent (sum of charges of all atoms)
TRCO	T	AM1	–	Bond length; tetrahedral carbon-protonated oxygen (Å)
TRCO-	T	AM1	–	Bond length; tetrahedral carbon-unprotonated oxygen (Å)
TRCN	T	AM1	–	Bond length; tetrahedral carbon-nitrogen (Å)
TRCR	T	AM1	–	Bond length; tetrahedral carbon-α carbon (Å)
TRING	T	AM1	–	Sum of angles in ring (°)

TCCN	T	AM1	--	Bond angle; nitrogen-tetrahedral carbon-α carbon (°)
THOMO	T	AM1	--	Energy; highest occupied molecular orbital (eV)
TLUMO	T	AM1	--	Energy; lowest unoccupied molecular orbital (eV)
TDPM	T	AM1	--	Dipole moment (Debyes)
TBIN	T	AM1	--	Binding energy (kcal/mole)
THF	T	AM1	--	Heat of formation (kcal/mole)
TELEC	T	AM1	--	Electronic energy (kcal/mole)
TCORE	T	AM1	--	Core-core interaction energy (kcal/mole)
TATOM	T	AM1	--	Isolated atom energy (kcal/mole)
TRCO2	T	AM1	--	(TRCO)^2 (Å^2)
TRCO-2	T	AM1	--	(TRCO-)^2 (Å^2)
TRCN2	T	AM1	--	(TRCN)^2 (Å^2)
TRCR2	T	AM1	--	(TRCR)^2 (Å^2)
TCCN2	T	AM1	--	(TCCN)^2 ($°^2$)
T4+7	T	AM1	--	(TZO-) + (TZC)
T4-7	T	AM1	--	(TZO-) - (TZC)
T5+7	T	AM1	--	(TZO) + (TZC)
T5-7	T	AM1	--	(TZO) - (TZC)
T7+8	T	AM1	--	(TZC) + (TZN)
T7-8	T	AM1	--	(TZC) - (TZN)
T8+9	T	AM1	--	(TZN) + (TZR)
T8-9	T	AM1	--	(TZN) - (TZR)
T17-16	T	AM1	--	(THOMO) - (TLUMO) (eV)
T10-11	T	AM1	--	(TRCO) - (TRCO-) (Å)
T10-12	T	AM1	--	(TRCO) - (TRCN) (Å)

T11-12	T	AM1	--	(TRCO-) - (TRCN) (Å)
PIRCN	I	MMX	A	Bond length; imide nitrogen-carbonyl carbon (Å)
PIZR	I	MMX	A	Charge; imide *N*-substituent (sum of charges of all atoms)
PIRCO	I	MMX	A	Bond length; carbonyl (Å)
PIZC	I	MMX	A	Charge; carbonyl carbon
PIZN	I	MMX	A	Charge; imide nitrogen
PICCN	I	MMX	A	Bond angle; imide nitrogen-carbonyl carbon-α carbon (°)
PITOCNC	I	MMX	A	Torsion angle; carbonyl oxygen-carbonyl carbon-imide nitrogen-carbonyl carbon (°)
PIRING	I	MMX	A	Sum of angles in ring (°)
PIRCR	I	MMX	A	Bond length; carbonyl carbon-α carbon (Å)
PIZO	I	MMX	A	Charge; carbonyl oxygen
PIPLAN	I	MMX	A	Absolute value of torsion angle; |(carbonyl oxygen-carbonyl carbon-imide nitrogen-imide R group)| (°)
PISTR	I	MMX	--	Energy; strain term (kcal/mole)
PIBND	I	MMX	--	Energy; bond distortion term (kcal/mole)
PITOR	I	MMX	--	Energy; torsional strain term (kcal/mole)
PIVDW	I	MMX	--	Energy; van der Waals strain term (kcal/mole)
PIDDQQ	I	MMX	--	Energy; dipole-dipole, charge-charge interaction term (kcal/mole)
PIDPM	I	MMX	--	Dipole moment (Debyes)
PTZO-	T	MMX	--	Charge; unprotonated oxygen on tetrahedral carbon

PTZN	T	MMX	--	Charge; imide nitrogen
PTZC	T	MMX	--	Charge; carbonyl carbon
PTZ=O	T	MMX	--	Charge; intact carbonyl oxygen
PTZR	T	MMX	--	Charge; *N*-substituent (sum of charges of all atoms)
PTRCO-	T	MMX	--	Bond length; tetrahedral carbon-unprotonated oxygen (Å)
PTRCOH	T	MMX	--	Bond length; tetrahedral carbon-protonated oxygen (Å)
PTRCN	T	MMX	--	Bond length; tetrahedral carbon-nitrogen (Å)
PTRCR	T	MMX	--	Bond length; tetrahedral carbon-α carbon (Å)
PTCCN	T	MMX	--	Bond angle; nitrogen-tetrahedral carbon-α carbon (°)
PTRING	T	MMX	--	Sum of angles in ring (°)
PTSTR	T	MMX	--	Energy; strain term (kcal/mole)
PTBND	T	MMX	--	Energy; bond distortion term (kcal/mole)
PTTOR	T	MMX	--	Energy; torsional strain term (kcal/mole)
PTVDW	T	MMX	--	Energy; van der Waals strain term (kcal/mole)
PTDDQQ	T	MMX	--	Energy; dipole-dipole, charge-charge interaction term (kcal/mole)
PTDPM	T	MMX	--	Dipole moment (Debyes)

[a] Descriptors were extracted from imide structures (I) or tetrahedral intermediate structures (T).

[b] Descriptors were extracted from structures optimized by the MMX or AM1 algorithm.

[c] Descriptors marked (A) are the averages of all like measurements on the structure. In the cases of the bisdioxopiperazines, which have two imide rings, both rings were measured for symmetrical structures only.

Table 5.4. Values of log k_2, pK_a, and descriptors from molecular modelling for each imide.

	log (k_2)	pK_a	IZO	IZC	IZN	IZR	IRCO	IRCN
diacetamide	1.8130	12.77	-0.3445	0.3140	-0.3910	0.2380	1.243	1.400
***N*-methyl-"**	1.8890	--	-0.2900	0.3045	-0.3570	0.1680	1.238	1.414
***N*-methylbis(trifluoro-")**	1.6240	--	-0.2100	0.2745	-0.3160	0.2310	1.229	1.404
succinimide	0.7388	10.86	-0.3090	0.3070	-0.3930	0.2610	1.234	1.406
***N*-methyl-"**	1.1504	--	-0.3085	0.3065	-0.3460	0.2170	1.234	1.411
***N*-2,6-xylyl-"**	1.4867	--	-0.2980	0.3110	-0.3050	0.1480	1.233	1.416
maleimide	3.2280	10.41	-0.2810	0.3260	-0.4110	0.1650	1.231	1.416
***N*-methyl-"**	3.5089	--	-0.2810	0.3260	-0.3630	0.2200	1.231	1.420
***N*- ethyl-"**	3.1575	--	-0.2820	0.3250	-0.3590	0.2250	1.231	1.421
***N*-phenyl-"**	4.0240	--	-0.2720	0.3310	-0.3120	0.1330	1.230	1.428
***N*-3,4-xylyl-"**	4.2210	--	-0.2700	0.3320	-0.3130	0.1230	1.230	1.429
***N*-4-chlorophenyl-"**	3.8620	--	-0.2730	0.3310	-0.3100	0.1320	1.230	1.428
phthalimide	2.7485	10.08	-0.2950	0.3600	-0.4030	0.2620	1.233	1.417
adipimide	2.1780	11.41	-0.3350	0.3150	-0.3920	0.2490	1.245	1.396
glutarimide	1.9591	12.01	-0.3310	0.3100	-0.3800	0.2520	1.242	1.397
ICRF-154	2.0976	10.10	-0.3238	0.3013	-0.3705	0.2540	1.240	1.395
ICRF-193	2.3430	10.41	-0.3253	0.2995	-0.3710	0.2545	1.240	1.395
LYZ 17B	2.5080	10.10	-0.3190	0.3130	-0.3730	0.2560	1.240	1.395
LYZ 19	1.9450	909.00	-0.3218	0.2953	-0.3745	0.2525	1.240	1.395
LYZ 2	1.8130	10.02	-0.3250	0.3135	-0.3720	0.2545	1.240	1.394
LYZ 8	2.0633	9.79	-0.3230	0.3140	-0.3720	0.2550	1.240	1.394
LYZ 22	2.2750	10.06	-0.3260	0.3140	-0.3705	0.2550	1.240	1.394
BLPD B2	2.2990	10.20	-0.3235	0.3120	-0.3720	0.2550	1.240	1.395
BLPD G2A	3.4476	10.24	-0.3228	0.3120	-0.3740	0.2545	1.240	1.395
1,2,3,6-tetrahydrophthalimide	--	--	--	--	--	--	--	--
3,4,5,6-tetrachlorophthalimide	--	--	--	--	--	--	--	--

IRCR	ITOCNC	IPLAN	ICCN	IRING	IHOMO	ILUMO	IDPM	IBIN	IHF
1.504	0.27393	0.28400	118.389	--	-11.01910	0.39279	2.72459	-1367.65	-87.2604
1.509	12.16903	20.80930	118.226	--	-10.26920	0.75549	6.06707	-1628.90	-73.4168
1.579	12.84057	21.24200	118.046	--	-11.59540	-0.94071	3.46261	-1716.40	-360.1840
1.526	0.00250	0.01180	109.063	540.001	-11.14780	0.27761	2.47459	-1253.71	-77.5244
1.526	0.15250	0.01565	109.171	540.000	-10.46070	0.35162	2.02878	-1523.72	-72.4370
1.527	0.06400	0.30279	109.133	540.000	-9.32120	0.22818	2.11679	-3009.01	-48.8824
1.516	0.00000	0.00000	106.463	540.000	-11.26590	-1.20946	1.93859	-1105.81	-33.8239
1.516	0.01450	0.07042	106.570	539.998	-10.51220	-1.14112	1.50761	-1376.11	-29.0301
1.516	0.79750	0.04248	106.619	539.969	-10.55140	-1.10162	1.34930	-1657.35	-35.1731
1.515	0.24950	1.29975	106.664	539.998	-9.16939	-1.23788	1.70302	-2300.11	5.6216
1.514	0.20800	1.08501	106.687	539.999	-9.14492	-1.36232	3.14972	-2284.03	-1.4065
1.515	0.16500	0.86494	106.687	540.001	-8.87426	-1.19878	1.25459	-2864.94	-9.0152
1.499	0.00050	0.00154	106.510	540.001	-10.48050	-1.12829	3.35033	-1886.73	-26.2779
1.510	17.67300	49.80320	122.244	831.054	-10.85780	0.30470	3.91913	-1816.73	-90.3570
1.512	0.74600	0.20664	118.639	697.615	-11.02900	0.28318	3.69385	-1541.49	-90.2068
1.529	1.98025	2.74675	118.233	702.087	-9.94386	0.16762	5.63398	-3255.62	-127.0590
1.530	2.44525	6.12343	118.166	700.528	-9.77753	0.23164	6.12568	-3808.39	-129.6350
1.527	1.63500	1.25965	118.440	699.686	-10.45560	0.03511	2.11599	-2116.65	-104.7180
1.535	1.27050	2.44260	118.283	699.761	-10.19470	0.01068	3.28928	-3810.66	-131.9100
1.526	1.66925	0.83303	118.534	700.903	-10.12980	0.16954	1.80639	-4381.64	-152.7010
1.527	1.51850	0.19590	118.523	700.559	-10.20960	0.13662	2.52108	-4565.29	-217.2360
1.527	1.90200	0.81119	118.631	701.672	-9.80231	0.25086	7.15269	-4085.42	-131.5690
1.529	2.09125	3.53599	118.380	698.369	-10.00360	0.13518	4.70510	-4258.09	-133.3550
1.527	1.77700	2.55741	118.494	700.158	-10.03060	0.07914	5.34925	-3637.43	-174.2170
--	--	--	--	--	--	--	--	--	--
--	--	--	--	--	--	--	--	--	--

IELEC	ICORE	IATOM	ITOT	IZO2	IZN2	IRCO2	IRCN2	IRCR2	ITOC2
-123669	90070.7	-32231.1	-33598.7	0.118680	0.152881	1.546218	1.958712	2.262678	0.075036
-154417	117245.4	-35542.8	-37171.7	0.084100	0.127449	1.533696	1.999127	2.277639	148.0853
-424585	322170.1	-100699.0	-102415.0	0.044100	0.099856	1.510539	1.970626	2.494094	164.8801
-117250	84290.9	-31705.5	-32959.2	0.095481	0.154449	1.523472	1.977483	2.329485	6.25E-06
-146524	109982.6	-35017.2	-36540.9	0.095172	0.119716	1.523879	1.990977	2.328096	0.023256
-350574	291467.6	-56097.0	-59106.0	0.088804	0.093025	1.521448	2.006002	2.330874	0.004096
-108145	75859.5	-31179.9	-32285.7	0.078961	0.168921	1.515743	2.003853	2.299287	0
-136468	100600.1	-34491.6	-35867.7	0.078961	0.131769	1.516198	2.017707	2.297271	0.00021
-165701	126240.1	-37803.3	-39460.7	0.079524	0.128881	1.516420	2.019539	2.298059	0.636006
-254687	203438.7	-48947.9	-51248.0	0.073984	0.097344	1.514081	2.038798	2.294468	0.06225
-289394	229841.2	-57268.4	-59552.4	0.072900	0.097969	1.513171	2.042927	2.292847	0.043264
-325342	266905.5	-55571.4	-58436.3	0.074529	0.096100	1.514020	2.040012	2.294967	0.027225
-198114	153378.4	-42850.0	-44736.0	0.087025	0.162409	1.519303	2.007591	2.247301	2.50E-07
-176896	136750.0	-38329.0	-40145.7	0.112225	0.153664	1.549315	1.948300	2.279632	312.3349
-146130	109571.3	-35017.2	-36558.7	0.109561	0.144400	1.542353	1.950673	2.286325	0.556516
-519891	437265.9	-79369.9	-82625.5	0.104814	0.137270	1.537612	1.945383	2.338170	3.92139
-627411	537609.6	-85993.4	-89801.8	0.105788	0.137641	1.537854	1.945753	2.340303	5.979248
-271409	214338.7	-54954.0	-57070.7	0.101761	0.139129	1.536720	1.945286	2.331530	2.673225
-584718	494913.6	-85993.4	-89804.0	0.103523	0.140250	1.537160	1.946220	2.357092	1.61417
-613375	516376.5	-92616.9	-96998.5	0.105625	0.138384	1.538146	1.944428	2.329866	2.786396
-700711	588949.4	-107196.0	-111761.0	0.104329	0.138384	1.537904	1.944337	2.330584	2.305842
-655262	561871.7	-89305.1	-93390.5	0.106276	0.137270	1.538580	1.942156	2.330279	3.617604
-678228	581878.9	-92091.2	-96349.3	0.104652	0.138384	1.537433	1.945753	2.337680	4.373327
-593985	500296.3	-89971.2	-93608.6	0.104168	0.139876	1.537780	1.945439	2.330828	3.157729
--	--	--	--	--	--	--	--	--	--
--	--	--	--	--	--	--	--	--	--

ICCN2	IRING2	IHOMO2	ILUMO2	I4+5	I5+6	I6+7	I4-5	I5-6	I6-7	I15-16
14016.0	--	121.41968	0.15428	-0.031	-0.077	-0.153	-0.659	0.705	-0.629	-11.41180
13977.3	--	105.45556	0.57076	0.015	-0.053	-0.189	-0.595	0.662	-0.525	-11.02460
13934.7	--	134.45284	0.88493	0.065	-0.042	-0.085	-0.485	0.591	-0.547	-10.65470
11894.7	291601.1	124.27414	0.07707	-0.002	-0.086	-0.132	-0.616	0.700	-0.654	-11.42540
11918.2	291600.0	109.42687	0.12364	-0.002	-0.040	-0.129	-0.615	0.653	-0.563	-10.81240
11910.0	291600.0	86.88468	0.05206	0.013	0.006	-0.157	-0.609	0.616	-0.453	-9.54937
11334.3	291600.0	126.92118	1.46279	0.045	-0.085	-0.246	-0.607	0.737	-0.576	-10.05650
11357.1	291597.8	110.50662	1.30215	0.045	-0.037	-0.143	-0.607	0.689	-0.583	-9.37109
11367.5	291566.5	111.33162	1.21357	0.043	-0.034	-0.134	-0.607	0.684	-0.584	-9.44976
11377.1	291597.8	84.07764	1.53234	0.059	0.019	-0.179	-0.603	0.643	-0.445	-7.93151
11382.0	291598.9	83.62949	1.85592	0.062	0.019	-0.190	-0.602	0.645	-0.436	-7.78259
11382.0	291601.1	78.75244	1.43707	0.058	0.021	-0.178	-0.604	0.641	-0.442	-7.67548
11344.3	291601.1	109.84109	1.27304	0.065	-0.043	-0.141	-0.655	0.763	-0.665	-9.35222
14943.6	690650.8	117.89226	0.09284	-0.020	-0.077	-0.143	-0.650	0.707	-0.641	-11.16250
14075.2	486666.7	121.63928	0.08019	-0.021	-0.070	-0.128	-0.641	0.690	-0.632	-11.31220
13979.0	492926.2	98.88029	0.02810	-0.023	-0.069	-0.117	-0.625	0.672	-0.625	-10.11150
13963.1	490738.8	95.60007	0.05366	-0.026	-0.072	-0.117	-0.625	0.671	-0.626	-10.00920
14028.0	489560.5	109.31978	0.00123	-0.006	-0.060	-0.117	-0.632	0.686	-0.629	-10.49070
13990.7	489664.8	103.93191	0.00011	-0.027	-0.079	-0.122	-0.617	0.670	-0.627	-10.20540
14050.3	491264.3	102.61228	0.02874	-0.012	-0.059	-0.118	-0.639	0.686	-0.627	-10.29930
14047.7	490782.9	104.23552	0.01866	-0.009	-0.058	-0.117	-0.637	0.686	-0.627	-10.34620
14073.3	492342.9	96.08528	0.06293	-0.012	-0.057	-0.116	-0.640	0.685	-0.626	-10.05320
14013.8	487718.6	100.07261	0.01827	-0.012	-0.060	-0.117	-0.636	0.684	-0.627	-10.13880
14040.8	490220.5	100.61334	0.00626	-0.011	-0.062	-0.120	-0.635	0.686	-0.629	-10.10980
--	--	--	--	--	--	--	--	--	--	--
--	--	--	--	--	--	--	--	--	--	--

I8-9	IZON	IZCN	IZNN	IRCON	IRCNN	IRCRN	ICCNN	IHOMON	IZO-
-0.15607	2.50E-07	0	0	2.21E-07	2.12E-07	4.84E-08	0.0000	3.6 E-9	-0.344
-0.17548	0.003025	9.03E-05	0.001156	2.09E-05	0.000193	2.69E-05	0.0267	0.562266	-0.294
-0.17475	0.018225	0.00156	0.005625	0.000195	1.44E-05	0.005666	0.1180	0.332214	-0.214
-0.17194	0.001296	4.90E-05	4.00E-06	7.59E-05	3.88E-05	0.000496	86.9743	0.016597	-0.309
-0.17657	0.001332	5.63E-05	0.002025	7.30E-05	0.000121	0.000476	84.9807	0.311665	-0.310
-0.18286	0.002209	9.00E-06	0.007396	9.08E-05	0.000267	0.000516	85.6735	2.882542	-0.298
-0.18442	0.004096	0.000144	0.0004	0.00014	0.000243	0.000152	142.2414	0.060974	-0.281
-0.18912	0.004096	0.000144	0.000784	0.000136	0.000419	0.000136	139.7006	0.256833	-0.281
-0.18968	0.003969	0.000121	0.001024	0.000134	0.000445	0.000142	138.5447	0.218668	-0.282
-0.19739	0.005329	0.000289	0.006241	0.000157	0.000776	0.000116	137.4874	3.421072	-0.272
-0.19920	0.005625	0.000324	0.006084	0.000166	0.000859	0.000104	136.9485	3.512191	-0.270
-0.19784	0.005184	0.000289	0.006561	0.000157	0.0008	0.000119	136.9485	4.599923	-0.273
-0.18430	0.0025	0.002116	0.000144	0.000108	0.000285	2.40E-05	141.1225	0.289971	-0.295
-0.15110	1.00E-04	1.00E-06	1.00E-06	2.94E-06	1.75E-05	3.42E-05	14.8610	0.025979	-0.335
-0.15475	0.000196	1.60E-05	0.000121	1.18E-06	1.11E-05	6.50E-05	0.0625	0.000100	-0.331
-0.15477	0.000452	0.000163	0.00042	8.97E-06	2.74E-05	0.00063	0.0243	1.155932	-0.332
-0.15480	0.00039	0.00021	0.0004	8.40E-06	2.60E-05	0.000666	0.0500	1.541250	-0.333
-0.15509	0.000676	1.00E-06	0.000324	1.13E-05	2.77E-05	0.000526	0.0026	0.317408	-0.321
-0.15525	0.000541	0.000352	0.000272	1.01E-05	2.43E-05	0.000979	0.0113	0.679470	-0.323
-0.15421	0.0004	2.50E-07	0.000361	7.73E-06	3.11E-05	0.000501	0.0210	0.790726	-0.326
-0.15427	0.000484	0	0.000361	8.28E-06	3.14E-05	0.000512	0.0180	0.655161	-0.324
-0.15322	0.000361	0	0.00042	6.79E-06	4.08E-05	0.000507	0.0586	1.480335	-0.329
-0.15497	0.000462	4.00E-06	0.000361	9.41E-06	2.60E-05	0.000622	0.0001	1.030976	-0.325
-0.15472	0.000495	4.00E-06	0.000289	8.57E-06	2.71E-05	0.000516	0.0110	0.976895	-0.326
--	--	--	--	--	--	--	--	--	--
--	--	--	--	--	--	--	--	--	--

IZC+	IZN-	IRCOL	IRCNL	IRCRL	TZO-	TZO	TZ=O	TZC	TZN	TZR
0.312	-0.391	1.24311	1.40419	1.50909	-0.709	-0.456	-0.501	0.383	-0.389	0.185
0.304	-0.357	1.23878	1.41527	1.50920	-0.680	-0.410	-0.438	0.400	-0.367	0.081
0.275	-0.316	1.22945	1.40492	1.57967	-0.608	-0.412	-0.404	0.405	-0.370	0.224
0.307	-0.393	1.23431	1.40624	1.52627	-0.690	-0.437	-0.481	0.387	-0.398	0.202
0.307	-0.346	1.23457	1.41115	1.52587	-0.678	-0.436	-0.473	0.395	-0.359	0.125
0.311	-0.305	1.23350	1.41608	1.52673	-0.643	-0.434	-0.440	0.404	-0.341	-0.008
0.326	-0.411	1.23119	1.41558	1.51636	-0.680	-0.421	-0.458	0.391	-0.404	0.196
0.326	-0.363	1.23135	1.42047	1.51568	-0.667	-0.420	-0.458	0.402	-0.370	0.120
0.325	-0.359	1.23143	1.42111	1.51599	-0.661	-0.426	-0.461	0.410	-0.379	0.112
0.331	-0.312	1.23049	1.42787	1.51476	-0.632	-0.411	-0.427	0.415	-0.341	-0.050
0.332	-0.313	1.23016	1.42933	1.51424	-0.627	-0.408	-0.421	0.415	-0.343	-0.073
0.331	-0.310	1.23047	1.42793	1.51495	-0.632	-0.410	-0.427	0.415	-0.341	-0.051
0.360	-0.403	1.23262	1.41690	1.49911	-0.667	-0.417	-0.450	0.418	-0.404	0.203
0.315	-0.392	1.24472	1.39586	1.50985	-0.693	-0.452	-0.501	0.395	-0.381	0.193
0.310	-0.380	1.24194	1.39667	1.51208	-0.693	-0.448	-0.497	0.391	-0.377	0.196
0.317	-0.375	1.24120	1.39875	1.53158	-0.636	-0.392	-0.473	0.375	-0.403	0.197
0.315	-0.377	1.24130	1.39846	1.53114	-0.678	-0.456	-0.476	0.388	-0.385	0.213
0.313	-0.373	1.23995	1.39575	1.52765	-0.682	-0.438	-0.482	0.398	-0.376	0.207
0.316	-0.379	1.24023	1.39647	1.54434	-0.684	-0.436	-0.484	0.398	-0.369	0.205
0.314	-0.372	1.24034	1.39470	1.52658	-0.683	-0.453	-0.480	0.383	-0.387	0.211
0.314	-0.372	1.24027	1.39468	1.52676	-0.678	-0.455	-0.489	0.371	-0.383	0.203
0.315	-0.371	1.24078	1.39435	1.52763	-0.698	-0.438	-0.482	0.390	-0.370	0.202
0.312	-0.372	1.24001	1.39519	1.52936	-0.709	-0.434	-0.473	0.362	-0.383	0.201
0.313	-0.375	1.24037	1.39570	1.52736	-0.679	-0.451	-0.479	0.399	-0.380	0.210
--	--	--	--	--	--	--	--	--	--	--
--	--	--	--	--	--	--	--	--	--	--

TRCO	TRCO-	TRCN	TRCR	TRING	TCCN	THOMO	TLUMO	TDPM	TBIN
1.45512	1.31012	1.50154	1.56043	--	108.969	-4.26151	5.91479	0.80766	-1552.36
1.43052	1.29814	1.57665	1.55355	--	106.491	-4.18874	5.81233	6.23522	-1812.55
1.43040	1.28640	1.49179	1.64465	--	105.439	-5.77051	4.33433	2.17514	-1938.55
1.44932	1.30024	1.52710	1.57595	539.624	103.007	-4.43531	5.80938	2.88863	-1442.97
1.44768	1.29771	1.54414	1.57269	539.736	102.705	-4.52885	5.78740	2.03171	-1712.65
1.44313	1.28878	1.58572	1.56999	535.378	101.679	-4.68023	3.89202	2.81692	-3199.40
1.44252	1.29968	1.54357	1.55858	539.126	100.776	-4.63284	4.57780	2.33116	-1300.72
1.44146	1.29696	1.56059	1.55558	539.452	100.335	-4.70095	4.56270	1.42697	-1570.58
1.44349	1.29547	1.55637	1.55546	539.969	100.071	-4.74725	4.56553	2.13036	-1851.46
1.43366	1.28918	1.60372	1.54612	539.979	99.865	-4.69278	3.74098	2.66667	-2502.76
1.43183	1.28802	1.61069	1.54428	539.982	99.715	-4.86228	3.42024	4.17965	-2490.37
1.43336	1.28937	1.60359	1.54613	539.754	99.846	-4.63352	3.66557	4.88668	-3067.10
1.44206	1.29719	1.54581	1.55224	539.427	100.517	-4.91372	3.50647	5.49473	-2079.57
1.45926	1.30402	1.51952	1.55802	811.170	109.786	-4.48852	5.79935	4.44341	-2003.12
1.45696	1.30391	1.51734	1.55771	689.204	109.554	-4.46541	5.76065	4.29876	-1726.40
1.44577	1.29379	1.52725	1.58564	690.197	107.235	-4.58741	2.17695	12.57640	-3444.33
1.44572	1.30101	1.50086	1.57907	690.448	109.453	-4.90922	2.08533	15.52124	-3998.44
1.45137	1.30249	1.50386	1.57463	698.685	109.656	-4.93285	4.05720	6.53018	-2311.03
1.45137	1.30319	1.50380	1.57340	697.393	110.030	-4.86209	2.00761	17.15489	-4002.31
1.45491	1.30183	1.50171	1.57517	693.642	108.714	-4.70422	1.38760	25.80238	-4759.41
1.45514	1.30121	1.50917	1.57199	698.431	108.847	-4.65539	1.20595	30.49610	-4759.97
1.44924	1.30711	1.50882	1.57750	689.519	109.112	-4.85822	2.84876	10.72144	-4284.16
1.44996	1.30942	1.50431	1.57688	701.178	110.302	-4.92290	2.57689	9.24812	-4457.17
1.45628	1.30096	1.50428	1.57609	693.377	108.364	-4.99541	2.68517	11.66608	-3832.34
--	--	--	--	--	--	--	--	--	--
--	--	--	--	--	--	--	--	--	--

THF	TELEC	TCORE	TATOM	TRCO2	TRCO-2	TRCN2	TRCR2	TCCN2	T4+7
-160.32	-164386	123050	-39784	2.11737	1.71641	2.25462	2.43494	11874.24	-0.326
-145.40	-198710	153802	-43095	2.04639	1.68517	2.48583	2.41352	11340.33	-0.280
-470.68	-499269	389079	-100251	2.04604	1.65482	2.22544	2.70487	11117.38	-0.203
-155.12	-156421	115720	-39258	2.10053	1.69062	2.33203	2.48362	10610.44	-0.303
-149.70	-189538	145255	-42570	2.09578	1.68405	2.38437	2.47335	10548.32	-0.283
-127.61	-410657	343808	-63649	2.08262	1.66095	2.51451	2.46487	10338.62	-0.239
-117.08	-146032	105999	-38732	2.08086	1.68917	2.38261	2.42917	10155.80	-0.289
-111.84	-178219	134605	-43615	2.07781	1.68211	2.43544	2.41983	10067.11	-0.265
-117.62	-210639	163431	-45356	2.08366	1.67824	2.42229	2.41946	10014.21	-0.251
-85.36	-306741	247737	-56500	2.05538	1.66199	2.57192	2.39049	9973.06	-0.217
-96.09	-343258	275947	-64821	2.05014	1.65900	2.59432	2.38480	9943.16	-0.212
-99.52	-381838	315647	-63124	2.05452	1.66248	2.57150	2.39052	9969.30	-0.217
-108.16	-245020	192538	-50402	2.07954	1.68270	2.38953	2.40945	10103.67	-0.249
-165.08	-224187	176302	-45881	2.12944	1.70047	2.30894	2.42743	12052.97	-0.298
-163.45	-188602	144306	-42570	2.12273	1.70018	2.30232	2.42646	12002.08	-0.302
-204.10	-549147	458780	-86922	2.09025	1.67389	2.33249	2.51425	11499.35	-0.261
-208.02	-659355	561811	-93546	2.09011	1.69263	2.25258	2.49346	11979.96	-0.290
-187.43	-323250	258433	-62506	2.10647	1.69648	2.26159	2.47946	12024.44	-0.284
-211.90	-647060	549512	-93546	2.10647	1.69830	2.26141	2.47559	12106.60	-0.286
-232.81	-678300	573557	-100169	2.11676	1.69476	2.25513	2.29574	11818.73	-0.300
-300.26	-772498	652990	-114748	2.11743	1.69315	2.27759	2.47115	11847.67	-0.307
-218.65	-724503	623361	-96858	2.10030	1.70854	2.27654	2.48851	11905.43	-0.308
-220.78	-771099	666999	-99644	2.10238	1.71458	2.26295	2.48655	12166.53	-0.347
-257.47	-676350	574994	-97524	2.12075	1.69250	2.26286	2.48406	11742.76	-0.280
--	--	--	--	--	--	--	--	--	--
--	--	--	--	--	--	--	--	--	--

T4-7	T5+7	T5-7	T7+8	T7-8	T8+9	T8-9	T17-16	T10-11	T10-12	T11-12
-1.092	-0.073	-0.839	-0.006	0.772	-0.204	-0.574	10.17630	0.14500	-0.04642	-0.19142
-1.080	-0.010	-0.810	0.033	0.767	-0.286	-0.448	10.00106	0.13238	-0.14613	-0.27851
-1.013	-0.007	-0.817	0.035	0.775	-0.146	-0.594	10.10483	0.14400	-0.06139	-0.20539
-1.077	-0.050	-0.824	-0.011	0.785	-0.196	-0.600	10.24469	0.14908	-0.07778	-0.22686
-1.073	-0.041	-0.831	0.036	0.754	-0.234	-0.484	10.31624	0.14997	-0.09646	-0.24643
-1.047	-0.030	-0.838	0.063	0.745	-0.349	-0.333	8.57225	0.15435	-0.14259	-0.29694
-1.071	-0.030	-0.812	-0.013	0.795	-0.208	-0.600	9.21064	0.14284	-0.10105	-0.24389
-1.069	-0.018	-0.822	0.032	0.772	-0.250	-0.490	9.26365	0.14450	-0.11913	-0.26363
-1.071	-0.016	-0.836	0.031	0.789	-0.267	-0.491	9.31278	0.14802	-0.11288	-0.26090
-1.047	0.004	-0.826	0.074	0.756	-0.391	-0.291	8.43376	0.14448	-0.17006	-0.31454
-1.042	0.007	-0.823	0.072	0.758	-0.416	-0.270	8.28252	0.14381	-0.17886	-0.32267
-1.047	0.005	-0.825	0.074	0.756	-0.392	-0.290	8.29909	0.14399	-0.17023	-0.31422
-1.085	0.001	-0.835	0.014	0.822	-0.201	-0.607	8.42019	0.14487	-0.10375	-0.24862
-1.088	-0.057	-0.847	0.014	0.776	-0.188	-0.574	10.28787	0.15524	-0.06026	-0.21550
-1.084	-0.057	-0.839	0.014	0.768	-0.181	-0.573	10.22606	0.15305	-0.06038	-0.21343
-1.011	-0.017	-0.767	-0.028	0.778	-0.206	-0.600	6.76437	0.15198	-0.08148	-0.23346
-1.066	-0.068	-0.844	0.003	0.773	-0.172	-0.598	6.99454	0.14471	-0.05514	-0.19985
-1.080	-0.040	-0.836	0.022	0.774	-0.169	-0.583	8.99005	0.14888	-0.05249	-0.20137
-1.082	-0.038	-0.834	0.029	0.767	-0.164	-0.574	6.86969	0.14818	-0.05243	-0.20061
-1.066	-0.070	-0.836	-0.004	0.770	-0.176	-0.598	6.09182	0.15308	-0.04680	-0.19988
-1.049	-0.084	-0.826	-0.012	0.754	-0.180	-0.586	5.86134	0.15393	-0.05403	-0.20796
-1.088	-0.048	-0.828	0.020	0.760	-0.168	-0.572	7.70697	0.14213	-0.05958	-0.20171
-1.071	-0.072	-0.796	-0.021	0.745	-0.182	-0.584	7.49979	0.14054	-0.05435	-0.19489
-1.078	-0.052	-0.850	0.019	0.779	-0.170	-0.590	7.68058	0.15532	-0.04800	-0.20332
--	--	--	--	--	--	--	--	--	--	--
--	--	--	--	--	--	--	--	--	--	--

PIRCN	PIZR	PIRCO	PIZC	PIZN	PICCN	PITOC	PIRING	PIRCR	PIZO	PIPLAN
1.3735	0.15	1.2255	0.345	-0.09	121.290	179.965	--	1.5165	-0.42	0.10
1.3905	0.09	1.2265	0.330	-0.04	120.950	164.940	--	1.5250	-0.29	22.96
1.3950	0.09	1.2280	0.330	-0.04	121.720	166.800	--	1.5335	-0.29	45.59
1.3670	0.15	1.2230	0.340	-0.08	115.820	180.000	240.00	1.5180	-0.41	0.00
1.3710	0.09	1.2240	0.340	-0.01	115.700	176.020	539.90	1.5180	-0.41	12.68
1.3720	0.15	1.2230	0.330	-0.09	115.650	178.220	539.98	1.5180	-0.41	3.91
1.3770	0.15	1.2230	0.240	-0.08	108.410	180.000	540.00	1.4800	-0.19	0.00
1.3820	0.09	1.2240	0.240	-0.01	108.450	176.795	539.91	1.4800	-0.19	14.25
1.3775	0.09	1.2210	0.270	0.01	108.455	178.770	539.98	1.4145	-0.21	2.57
1.3870	0.16	1.2240	0.230	-0.09	108.795	178.520	539.99	1.4800	-0.18	2.87
1.3870	0.16	1.2230	0.230	-0.09	108.805	178.505	539.99	1.4800	-0.18	3.00
1.3865	0.12	1.2240	0.230	-0.09	108.775	178.535	539.99	1.4800	-0.19	2.85
1.3820	0.15	1.2230	0.250	-0.07	107.340	180.000	540.01	1.4780	-0.21	0.02
1.3750	0.15	1.2280	0.340	-0.09	125.280	175.445	848.84	1.5180	-0.31	9.11
1.3710	0.15	1.2240	0.340	-0.08	120.855	176.430	698.12	1.5180	-0.31	2.02
1.3703	0.15	1.2240	0.340	-0.08	120.155	179.088	693.02	1.5175	-0.41	1.57
1.3705	0.15	1.2260	0.335	-0.08	120.013	178.675	693.79	1.5163	-0.31	2.60
1.3710	0.15	1.2260	0.330	-0.08	120.060	179.325	692.72	1.5175	-0.31	0.17
1.3710	0.15	1.2260	0.338	-0.08	120.185	178.993	694.56	1.5193	-0.31	1.09
1.3700	0.15	1.2260	0.340	-0.08	120.133	178.100	693.26	1.5165	-0.31	-1.09
1.3700	0.15	1.2260	0.330	-0.08	120.120	177.815	693.04	1.5165	-0.31	-2.11
1.3700	0.15	1.2260	0.340	-0.08	120.098	178.125	693.16	1.5165	-0.31	-0.67
1.3710	0.15	1.2260	0.340	-0.08	119.940	178.150	690.33	1.5175	-0.31	-0.52
1.3705	0.15	1.2260	0.333	-0.08	120.043	178.805	692.11	1.5170	-0.31	-0.11
1.3650	0.15	1.2230	0.340	-0.08	116.050	179.390	539.99	1.5220	-0.42	0.00
1.3800	0.15	1.2220	0.250	-0.07	107.630	180.000	540.00	1.4820	-0.21	0.11

PISTR	PIBND	PITOR	PIVDW	PIDDQQ	PIDPM	PTZO-	PTZN	PTZC	PTZ=O	PTZR	PTRCO-
0.04	1.35	-0.12	1.78	-20.81	2.54	-0.96	-0.11	0.32	-0.49	0.15	1.430
0.58	1.21	1.84	5.51	-10.88	5.87	-0.85	-0.05	0.32	-0.38	0.09	1.445
0.96	1.12	16.93	5.36	22.49	3.93	-0.85	-0.05	0.32	-0.38	0.09	1.447
0.25	6.00	1.42	0.27	-19.51	1.38	-0.96	-0.11	0.32	-0.49	0.15	1.426
0.19	6.57	0.55	1.04	-14.52	1.38	-0.96	-0.04	0.32	-0.49	0.09	1.432
0.49	6.95	8.47	3.76	-10.56	0.20	-0.96	-0.10	0.31	-0.46	0.14	1.425
0.06	11.03	3.00	-0.34	-11.71	0.87	-0.85	-0.12	0.23	-0.29	0.15	1.430
0.11	11.42	2.20	0.20	-9.01	0.90	-0.85	-0.05	0.23	-0.28	0.09	1.434
0.12	10.23	1.45	0.66	-9.70	0.54	-0.85	-0.03	0.25	-0.29	0.09	1.429
0.29	11.66	8.37	3.78	-8.24	0.17	-0.85	-0.11	0.22	-0.25	0.11	1.436
0.31	11.68	8.07	4.00	-8.96	1.88	-0.85	-0.10	0.22	-0.25	0.11	1.435
0.44	11.97	6.56	4.78	-7.93	0.55	-0.85	-0.10	0.22	-0.25	0.12	1.436
0.27	13.81	13.40	1.53	-10.54	2.47	-0.85	-0.11	0.23	-0.29	0.15	1.431
0.14	8.35	1.82	4.00	-18.59	3.20	-0.85	-0.11	0.32	-0.39	0.15	1.468
0.13	0.42	1.18	2.76	-18.22	2.51	-0.85	-0.11	0.32	-0.39	0.15	1.436
0.95	4.21	1.17	9.16	-38.71	0.03	-0.96	-0.11	0.32	-0.42	0.15	1.427
2.33	7.90	12.30	12.84	-34.66	0.01	-0.96	-0.11	0.32	-0.42	0.15	1.427
0.38	1.11	0.59	5.02	-27.67	2.80	-0.85	-0.11	0.32	-0.14	0.15	1.434
1.51	4.73	4.13	11.04	-35.20	2.69	-0.85	-0.11	0.32	-0.14	0.15	1.433
1.25	3.07	0.94	12.56	-36.45	1.38	-0.85	-0.11	0.32	-0.39	0.15	1.422
2.12	6.57	5.50	10.89	-35.64	4.89	-0.85	-0.11	0.32	-0.39	0.15	1.435
1.55	4.52	1.01	16.86	-38.91	1.89	-0.85	-0.11	0.32	-0.39	0.15	1.435
2.10	8.57	11.52	13.81	-36.19	3.57	-0.85	-0.11	0.32	-0.39	0.15	1.435
1.09	3.52	2.82	9.86	-36.33	5.04	-0.85	-0.11	0.32	-0.39	0.15	1.435
0.55	6.69	4.65	2.32	-19.76	1.38	-0.96	-0.11	0.32	-0.49	0.15	1.428
0.67	14.12	13.40	5.54	-13.16	0.98	-0.85	-0.11	0.23	-0.42	0.15	1.428

PTRCOH	PTRCN	PTRCR	PTCCN	PTRING	PTSTR	PTBND	PTTOR	PTVDW	PTDDQQ	PTDPM
1.405	1.453	1.538	109.70	--	0.13	1.86	2.19	5.46	-1.91	5.94
1.411	1.475	1.542	110.84	--	0.83	2.42	1.34	8.46	8.02	10.68
1.415	1.485	1.564	115.27	--	1.85	4.09	7.57	7.80	20.08	41.77
1.405	1.447	1.548	103.86	533.06	0.42	6.01	3.99	3.89	-2.10	18.04
1.405	1.458	1.549	103.25	531.94	0.37	6.33	3.71	5.25	0.77	25.16
1.405	1.458	1.552	102.93	530.23	0.77	7.12	14.43	5.64	14.71	55.50
1.406	1.456	1.511	101.02	539.94	0.11	8.42	4.42	1.83	-3.10	30.75
1.408	1.466	1.511	101.29	539.71	0.21	8.56	4.47	2.57	-0.75	36.56
1.405	1.468	1.510	100.32	539.96	0.29	8.32	5.07	1.62	11.68	25.21
1.408	1.472	1.512	101.91	539.67	0.53	9.09	10.25	7.43	0.07	41.20
1.407	1.470	1.512	101.88	539.72	0.50	9.09	9.66	7.50	-1.80	45.15
1.408	1.472	1.512	101.83	539.71	0.65	9.43	8.13	8.32	1.83	62.68
1.406	1.463	1.509	100.71	539.98	0.25	10.30	12.58	3.51	-0.08	45.15
1.430	1.490	1.573	88.28	779.20	2.57	54.47	8.52	18.79	16.09	38.13
1.410	1.452	1.536	113.05	581.64	0.21	1.51	2.06	6.38	-0.96	37.49
1.406	1.445	1.536	112.12	689.05	0.88	4.24	4.48	10.05	-14.59	62.53
1.406	1.447	1.539	112.65	687.26	2.17	8.93	9.09	13.01	-14.74	59.97
1.419	1.454	1.543	111.55	687.87	0.63	5.13	2.79	7.97	-9.36	18.21
1.420	1.453	1.542	112.00	690.01	1.80	8.63	6.53	13.86	-13.07	21.51
1.409	1.447	1.537	113.20	688.50	1.46	6.47	2.30	14.17	-12.97	32.08
1.410	1.447	1.534	112.20	688.58	2.17	6.86	6.89	13.84	-20.04	49.36
1.409	1.446	1.535	111.79	690.84	1.70	5.53	3.36	20.23	-22.13	97.74
1.409	1.448	1.537	112.63	688.82	2.23	9.17	14.16	16.87	-20.18	69.03
1.410	1.448	1.535	112.57	686.91	1.17	4.21	3.79	12.95	-22.25	64.73
1.405	1.445	1.559	105.81	539.83	0.99	5.72	9.10	6.62	-1.63	21.60
1.404	1.459	1.509	101.32	539.93	0.69	10.34	12.92	7.77	-13.44	41.95

5.5 Linear regression analysis of the data set

5.5.1 Preliminary analysis of the data set

The data set was studied before performing linear regression analysis, to evaluate the correlation of the independent variables (molecular modelling descriptors) with the dependent variables (parameters describing imide hydrolysis), and to ascertain that the data are self-consistent, *i. e.* that all of the imides have a similar mechanism of hydrolysis. Data analysis was done using Sigmastat, version 1.01 for DOS (Jandel Scientific, San Rafael, CA).

The logarithm of the rate constant describing a chemical reaction is directly proportional to the transition state free energy change of the reaction. Since the descriptors extracted from molecular modelling may be expected to be related to the energy of the structures, regression analysis was done using log k_2 as the dependent variable. For diacetamide, succinimide, and maleimide, *N*-methyl substitution increases k_2 by a factor of two (Table 5.1). For succinimide and maleimide, *N*-xylyl substitution increases k_2 by a factor of five. Structure apparently affects the second order hydrolysis rate constant in a multiplicative manner, rather than additively. Thus, correlation of descriptors of structure with the hydrolysis rate constant were made using the logarithm of k_2, so that the sum of the terms in the equations would result in multiplication of k_2 by the appropriate factor.

Kinetic analysis of two imides, BLPD E1 and BLPD TTHA, was complicated by their tertiary amine functional groups. The pK_a values of these amines are expected to be near 10, which is close to the expected pK_a of the imide functional groups, and therefore within the pH range of the kinetic studies. Since deprotonation may affect the pH dependence of imide hydrolysis, these two imides were not included in the statistical analysis.

The Pearson product moment correlation coefficient measures the relationship between two variables, and is calculated by

$$r = \frac{\Sigma(u_i - \bar{u})(a_i - \bar{a})}{\sqrt{\Sigma(u_i - \bar{u})^2 \; \Sigma(a_i - \bar{a})^2}} \qquad (5.7)$$

in which u and a are the residuals and independent variable, and $\bar{u}$ and $\bar{a}$ are their means. As r approaches ±1, the relationship between the variables strengthens. Correlations of log k_2 with the descriptors extracted from the MMX-optimized structures were weak. Residual plots of PTRCR ($r = -0.683$), PIRCR ($r = -0.590$), PICCN ($r = -0.480$), and PIRCN ($r = 0.479$), the four descriptors with the highest correlation coefficients are shown in Figure 5.39. These data indicated two outliers, 1,2,3,6-tetrahydrophthalimide and 3,4,5,6-tetrachlorophthalimide. The residuals for these imides were consistently negative, and were often larger than two standard deviations. Thus, they hydrolyze significantly more slowly than the trend among the remaining imides, and were removed from the data set, leaving 24 imides.

The descriptors extracted from the MMX-optimized structures which measure the atomic charges of the imide functional group were not well determined. Although the structures of the imides in the data set vary considerably, these descriptors adopt very few different values, suggesting imprecision, and perhaps also inaccuracy, in their calculation. The atomic charges of the carbonyl carbon atoms of the imide functional group should increase with log k_2, since higher positive charge on this atom should, in general, increase the electrostatic attraction to the negatively charged nucleophile, hydroxide ion. However, the descriptors PIZC and PTZC, which measure the charge on this atom of the imide and the

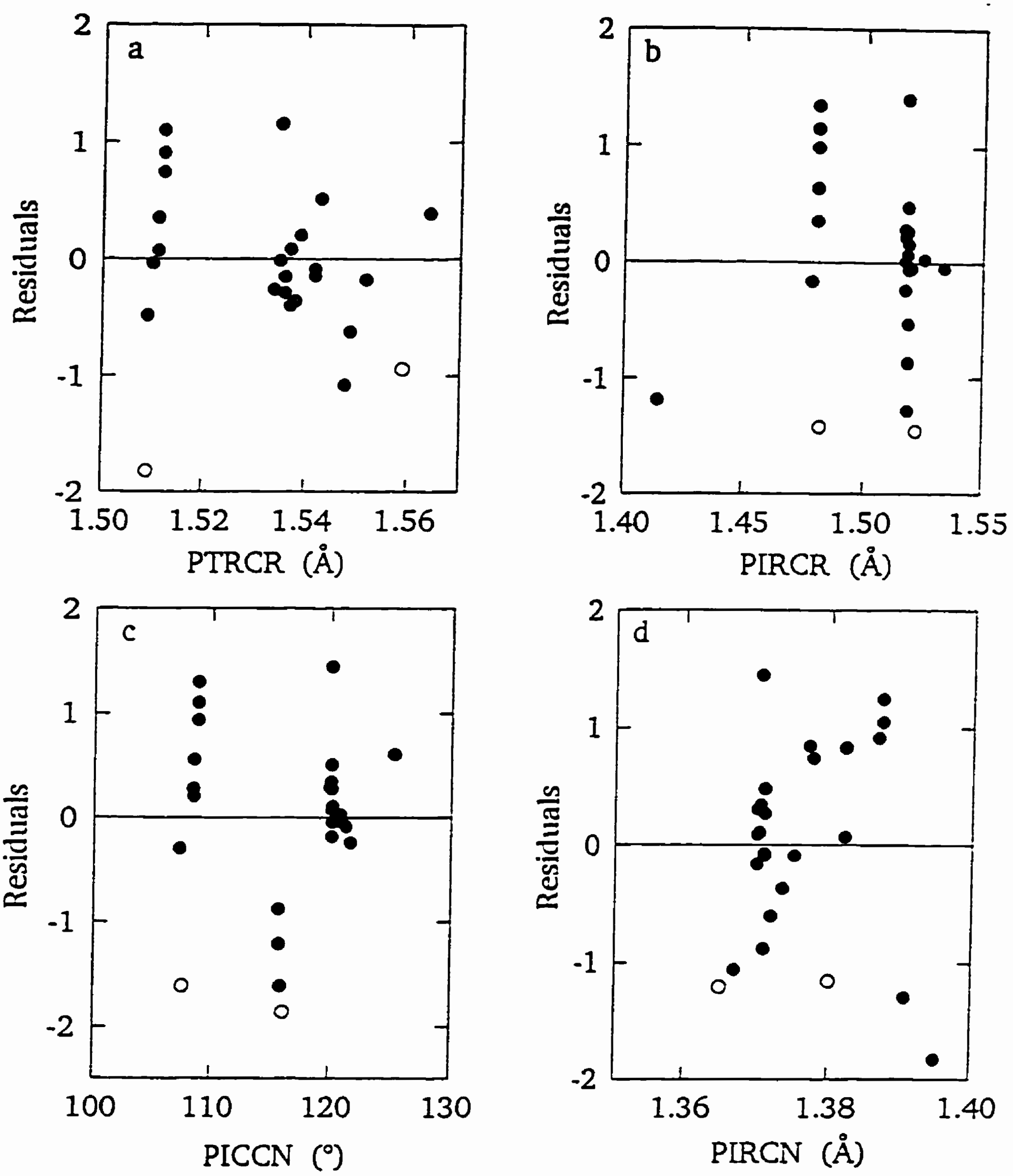

Figure 5.39. Residual (observed values - calculated values) plots for the 26 imides in the kinetic study of the dependent variable, log k_2, for the four best single descriptors from MM2-optimized modelling structures, a) PTRCR, b) PIRCR, c) PICCN, and d) PIRCN. The units of k_2 are $M^{-1}min^{-1}$. 1,2,3,6-Tetrahydrophthalimide and 3,4,5,6-tetrachlorophthalimide (O) were consistent outliers. Residuals of the other imides are represented by filled circles (●).

tetrahedral intermediate, respectively, are negatively correlated with log k_2. The high correlation coefficients of some atomic charge descriptors with log k_2 is due to the distribution of values between the saturated and unsaturated imides. The atomic charges of the maleimides, which hydrolyze faster than the rest of the data set, are significantly different from those of the non-aromatic imides. These descriptors behave simply as dummy variables which distinguish between saturated and unsaturated imides, and may provide no information regarding the electronic properties of the imides in the data set. In fact, a dummy variable, with values of one and zero for the saturated and unsaturated imides, respectively, has a Pearson product moment correlation coefficient with log k_2 of 0.792, which is similar to those determined for the MMX-derived atomic charge descriptors (Table 5.5). All descriptors from the MMX-optimized structures which measure atomic charges were excluded from further analysis.

Since electronic properties are not explicitly calculated by molecular mechanics methods, it may be that the electronic properties which determine imide hydrolysis are insufficiently described by the MMX algorithm. The set of descriptors calculated by the AM1 algorithm, which calculates molecular geometry and properties by solution of the Schrödinger equations for the molecular orbitals, and may therefore be expected to better describe electronic properties, was added to the data set.

The data set containing descriptors extracted from structures minimized by both algorithms yielded much stronger correlations with the dependent variable, log k_2. Despite the prior residual analysis using only the MMX-derived descriptors, analysis of the descriptors with high coefficients of correlation, for which the four best, I15-16 ($r = 0.814$), PTRCR (r

Table 5.5. Pearson product moment correlation coefficients for molecular modelling descriptors and dependent variables, log k_2 and pK_a.

Descriptor	Complete Data Set[a] (log k_2)	Saturated Imides[b] (log k_2)	Maleimides[c] (log k_2)	Bisdioxo-piperazines[d] (log k_2)	Non-*N*-Substituted Imides[e] (pK_a)
IZO	0.383	-0.324	0.968	0.500	-0.460
IZC	0.633	0.184	0.962	0.222	-0.051
IZN	0.298	-0.239	0.852	0.045	-0.338
IZR	-0.571	0.302	-0.805	0.688	-0.110
IRCO	-0.477	0.624	-0.941	-0.474	0.398
IRCN	0.637	-0.680	0.903	0.039	0.038
IRCR	-0.358	-0.118	-0.974	-0.251	-0.611
ITOCNC	-0.227	0.162	-0.270	0.298	0.182
IPLAN	-0.154	0.162	0.935	0.170	0.235
ICCN	-0.514	0.817	0.755	-0.045	0.152
IRING	-0.343	0.805	0.557	-0.297	0.164
IHOMO	0.483	0.342	0.892	-0.216	-0.643
ILUMO	-0.798	-0.005	-0.807	-0.132	0.314
IDPM	-0.250	0.481	0.540	0.122	-0.121
IBIN	0.063	-0.479	-0.761	0.733	0.636
IHF	0.533	-0.122	0.952	0.510	0.361
IELEC	0.122	-0.486	-0.835	0.649	0.647
ICORE	-0.119	0.492	0.826	-0.635	-0.643
IATOM	0.138	-0.413	-0.887	0.719	0.676
ITOT	0.135	-0.418	-0.883	0.721	0.675
IZO2	-0.415	0.345	-0.968	-0.497	0.481
IZN2	-0.288	0.224	-0.838	-0.045	0.329
IRCO2	-0.476	0.624	-0.941	-0.474	0.399
IRCN2	0.638	-0.679	0.904	0.039	0.037
IRCR2	-0.357	-0.119	-0.974	-0.251	-0.612
ITOC2	-0.177	0.092	-0.500	0.283	0.260
ICCN2	-0.509	0.815	0.755	-0.045	0.154
IRING2	-0.335	0.774	0.557	-0.297	0.198
IHOMO2	-0.472	-0.350	-0.890	0.225	0.644

ILUMO2	0.817	-0.208	0.804	-0.058	-0.077
I4+5	0.636	-0.347	0.967	0.354	-0.296
I5+6	0.587	-0.183	0.869	0.217	-0.434
I6+7	-0.521	0.176	-0.059	0.387	-0.212
I4-5	0.096	-0.300	0.963	-0.074	-0.439
I5-6	0.031	0.252	-0.832	0.220	0.145
I6-7	0.503	-0.297	0.930	-0.468	-0.098
I15-16	0.841	0.362	0.918	-0.235	-0.786
I8-9	-0.612	0.722	-0.917	-0.196	0.109
IZON	0.213	-0.228	0.968	0.530	-0.245
IZCN	0.098	-0.133	0.963	-0.275	-0.218
IZNN	0.361	-0.341	0.910	0.037	-0.742
IRCON	0.540	-0.573	0.942	0.496	-0.170
IRCNN	0.825	-0.336	0.922	-0.035	-0.260
IRCRN	-0.282	-0.137	-0.973	-0.266	-0.664
ICCNN	0.612	-0.810	-0.754	-0.086	-0.094
IHOMON	0.548	0.145	0.870	-0.113	-0.573
IZO-	0.398	-0.359	0.968	0.165	-0.381
IZC+	0.641	0.362	0.962	-0.417	-0.259
IZN-	0.301	-0.260	0.852	0.152	-0.313
IRCOL	-0.479	0.661	-0.944	-0.142	0.340
IRCNL	0.638	-0.641	0.907	0.075	0.101
IRCRL	-0.374	-0.098	-0.978	-0.287	-0.552
TZO-	0.409	-0.193	0.908	-0.171	-0.474
TZO	0.460	-0.103	0.963	0.016	-0.374
TZ=O	0.453	-0.244	0.956	0.120	-0.604
TZC	0.512	-0.250	0.712	0.250	0.020
TZN	0.349	-0.132	0.894	0.213	-0.004
TZR	-0.581	0.329	-0.927	0.046	-0.740
TRCO	-0.484	0.200	-0.970	-0.312	0.469
TRCO-	-0.372	0.392	-0.908	0.199	0.449
TRCN	0.606	-0.390	0.955	-0.134	-0.059
TRCR	-0.545	-0.112	-0.946	0.035	-0.514
TRING	-0.340	0.815	0.547	0.178	0.140
TCCN	-0.523	0.836	-0.773	0.316	0.121

THOMO	-0.114	-0.190	-0.426	-0.611	0.784
TLUMO	-0.163	-0.451	-0.949	0.886	0.803
TDPM	-0.187	0.352	0.656	-0.712	-0.600
TBIN	0.064	-0.471	-0.763	0.753	0.636
THF	0.472	-0.114	0.911	0.469	0.422
TELEC	0.120	-0.479	-0.835	0.623	0.647
TCORE	-0.117	0.485	0.827	-0.608	-0.642
TATOM	0.125	-0.432	-0.898	0.719	0.676
TRCO2	-0.484	0.201	-0.970	-0.312	0.470
TRCO-2	-0.372	0.392	-0.908	0.199	0.449
TRCN2	0.609	-0.388	0.955	-0.135	-0.060
TRCR2	-0.408	-0.068	-0.946	0.502	-0.137
TCCN2	-0.516	0.836	-0.772	0.316	0.121
T4+7	0.493	-0.245	0.863	-0.015	-0.346
T4-7	0.168	-0.088	0.962	-0.278	-0.424
T5+7	0.564	-0.210	0.907	0.159	-0.276
T5-7	0.052	0.054	0.010	-0.111	-0.329
T7+8	0.477	-0.203	0.859	0.263	0.013
T7-8	0.037	-0.086	-0.930	0.083	0.017
T8+9	-0.608	0.353	-0.926	0.194	-0.358
T8-9	0.555	-0.304	0.925	0.190	0.421
T17-16	-0.149	-0.439	-0.927	0.889	0.762
T10-11	-0.319	-0.148	-0.401	-0.403	0.105
T10-12	-0.615	0.391	-0.959	0.003	0.180
T11-12	-0.596	0.431	-0.950	0.172	0.157
PIRCN	0.511	-0.037	0.965	0.475	0.081
PIZR	0.052	0.357	0.600	—[f]	-1.5×10^{-16}
PIRCO	-0.334	0.538	0.555	0.143	-0.010
PIZC	-0.882	-0.120	-0.780	-0.377	0.225
PIZN	-0.032	-0.389	-0.681	—[f]	-0.644
PICCN	-0.694	0.646	0.940	-0.553	0.268
PITOC	0.232	0.081	-0.229	0.441	-0.178
PIRING	-0.016	0.858	0.184	-0.314	0.010
PIRCR	-0.700	-0.198	0.573	-0.077	0.162
PIZO	0.880	0.602	0.835	0.143	-0.394

PIPLAN	-0.169	-0.223	-0.029	0.194	0.372
PISTR	-0.202	0.463	0.796	-0.309	-0.580
PIBND	0.675	-0.037	0.819	-0.180	-0.365
PITOR	0.180	0.092	0.942	0.082	-0.356
PIVDW	-0.149	0.621	0.875	-0.416	-0.538
PIDDQQ	0.218	-0.460	0.695	0.697	0.494
PIDPM	-0.301	0.182	0.323	0.059	0.041
PTZO-	0.525	0.489	--[f]	-0.141	0.174
PTZN	-0.032	-0.405	-0.486	--[f]	0.077
PTZC	-0.869	0.231	-0.834	--[f]	0.114
PTZ=O	0.661	0.518	0.959	0.135	0.579
PTZR	-0.268	0.384	-0.046	--[f]	4.4×10^{-18}
PTRCO-	0.147	0.212	0.889	0.450	0.090
PTRCOH	-0.071	0.384	0.672	0.252	0.659
PTRCN	0.429	-0.216	0.678	0.412	0.128
PTRCR	-0.864	-0.553	0.908	0.434	0.190
PTCCN	-0.499	0.734	0.920	-0.572	0.126
PTRING	-0.286	0.770	-0.843	-0.339	0.125
PTSTR	-0.242	0.397	0.797	-0.341	0.259
PTBND	0.546	0.036	0.860	-0.165	0.254
PTTOR	0.261	0.071	0.922	0.050	0.058
PTVDW	-0.162	0.609	0.924	-0.329	0.203
PTDDQQ	-0.021	-0.529	-0.437	0.194	-0.115
PTDPM	0.212	0.391	0.695	0.009	-0.239

[a] n = 23, except for the descriptors IRING, IRING2, TRING, PIRING, and PTRING, for which n = 20.

[b] n = 17, except for the descriptors IRING, IRING2, TRING, PIRING, and PTRING, for which n = 14.

[c] n = 6.

[d] n = 8.

[e] n = 14, except for the descriptors IRING, IRING2, TRING, PIRING, and PTRING, for which n = 13.

[f] There is no variation of these descriptors for the specified subsets of the data.

= -0.761), ILUMO (r = -0.750), and PIRCR (r = -0.652), are shown in Figure 5.40, revealed another outlier, BLPD G2A. The residuals for this bisdioxopiperazine were consistently positive, with a magnitude of approximately one, indicating that it hydrolyzes approximately ten times faster than the trend among the remaining imides. The k_2 values of the bisdioxopiperazines are similar, ranging from 65 to 320 $M^{-1}min^{-1}$, while the k_2 of 2800 M^{-1} min^{-1} for BLPD G2A is approximately ten times higher than this range. The descriptors from molecular modelling were unable to account for this difference in hydrolysis rate constant of this imide. Since its mechanism of hydrolysis appears to be different from that of the other imides, its k_2 may depend on different properties. Thus, it was removed from the data set, which finally consisted of three diacetamides, three succinimides, six maleimides, phthalimide, adipimide, glutarimide, and eight bisdioxopiperazines.

The individual descriptors were examined for correlation with the dependent variable, log k_2. Subsets of the data were also studied, both because they may better demonstrate the relationship between log k_2 and the descriptors, and to examine the possibility that subsets of the data skew the results. The subsets examined, in addition to the complete data set, included the 16 saturated imides, the six maleimides, and the eight bisdioxopiperazines , and are defined in Table 5.6. To predict the hydrolysis rates at physiological pH, predictions of the pK_a values of imides must also be made. Thus, the descriptors of the subset of non-N-substituted imides were examined for correlation with experimentally determined pK_a values. Pearson product moment correlation coefficients of the descriptors with log k_2 or pK_a for all five subsets of the data are listed in Table 5.5.

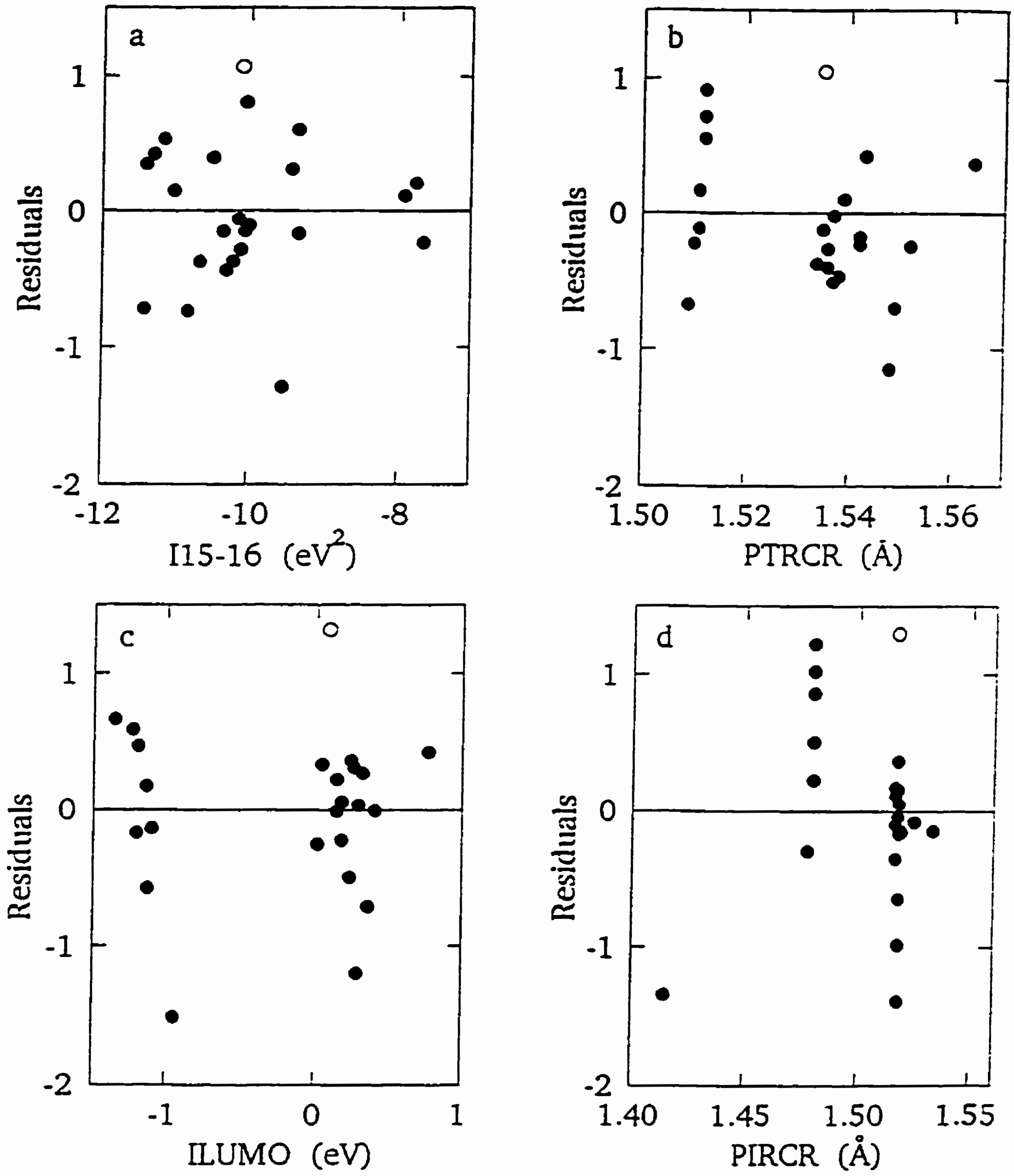

Figure 5.40. Residual (observed values - calculated values) plots for the remaining 24 imides in the kinetic study of the dependent variable, log k_2, for the four best single descriptors from AM1- and MM2-optimized modelling structures, a) I15-16, b) PTRCR, c) ILUMO, and d) PIRCR. BLPD G2A (○) was a consistent outlier. Residuals of the other imides are represented by filled circles (●).

Table 5.6. Definitions of subsets for linear regression analysis.

Imide[a]	Complete Data Set	Saturated Imides	Maleimides	Bisdioxo-piperazines	Non-*N*-Substituted Imides
diacetamide	√	√			√
N-methyl-"	√	√			
N-methylbis(trifluoro-")	√	√			
succinimide	√	√			√
N-methyl-"	√	√			
N-2,6-xylyl-"	√	√			
maleimide	√		√		√
N-methyl-"	√		√		
N-ethyl-"	√		√		
N-phenyl-"	√		√		
N-3,4-xylyl-"	√		√		
N-4-chlorophenyl-"	√		√		
phthalimide	√				√
adipimide	√	√			√
glutarimide	√	√			√
ICRF-154	√	√		√	√
ICRF-193	√	√		√	√
LYZ 17B	√	√		√	√
LYZ 19	√	√		√	√
LYZ 2	√	√		√	√
LYZ 8	√	√		√	√
LYZ 22	√	√		√	√
BLPD B2	√	√		√	√

[a] Structures are shown in Figures 5.4-5.6.

Analysis of the complete set of 23 imides revealed that the four best single descriptors of log k_2 were measurements of bond lengths and frontier molecular orbitals (Figure 5.41). ILUMO2 (r^2 = 0.667), the square of the LUMO energy of the imide, was negatively correlated with log k_2. This relationship is expected, as the nucleophile, hydroxide ion, interacts with the LUMO to form the tetrahedral hydrolysis intermediate (Figure 5.3). As the energy of this orbital decreases, the more easily the intermediate may be formed, and the faster the imide hydrolyzes. I15-16 (r^2 = 0.707), the difference between the HOMO and LUMO had a higher correlation with log k_2, which may be due to cancellation of errors in the molecular orbital energy calculations due to the subtraction of one measurement from the other. IRCNN (r^2 = 0.681) was negatively correlated with log k_2, indicating that as the imide carbon-nitrogen bond length deviates from that of diacetamide, log k_2 increases. Diacetamide may be considered a relatively unstrained system, since it is acyclic, and has minimal steric strain. Electronic or geometric influences due to structure may affect this bond length, and as it increases, the interaction of these two atoms weakens, the energy required to break the bond decreases, and the hydrolysis rate constant can be expected to increase. PTRCR (r^2 = 0.746), the C(tetrahedral)-Cα bond length of the intermediate structure (shown in Figure 5.38) had the highest correlation with log k_2. The significance of this relationship is unclear, and it may be that this descriptor reflects some other property indirectly. The differences between the values for the imide and tetrahedral intermediate structures for the binding, electronic, and core-core interaction energy terms calculated by the AM1 algorithm were also examined for correlation with log k_2. Since the values of r^2 for all three of these descriptors were less than 0.003, they were not included in the multiple linear regression analysis.

A different group of descriptors was highly correlated with log k_2 when the saturated imides were examined (Figure 5.42). All of the four best descriptors, TCCN (r^2 = 0.699),

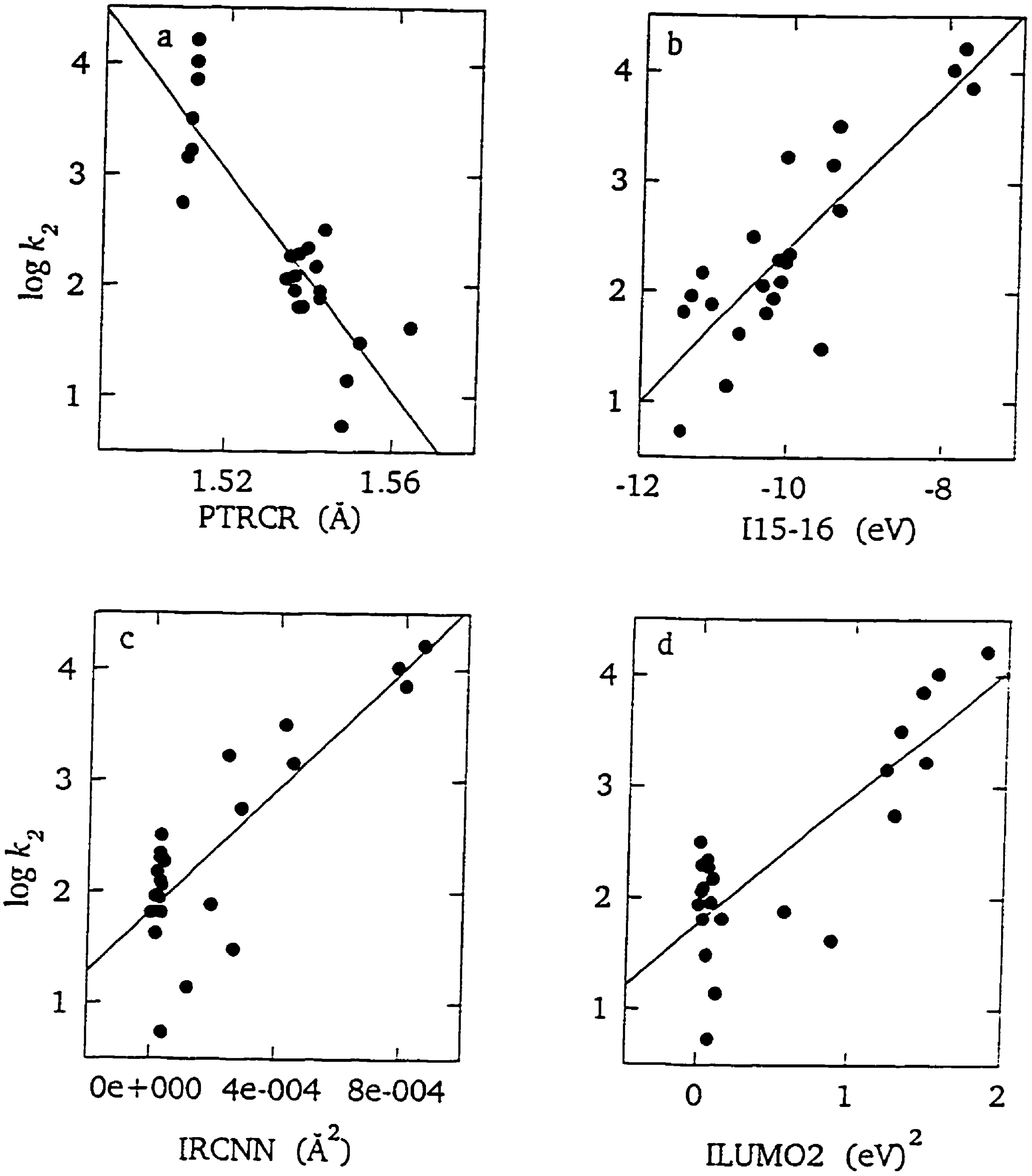

Figure 5.41. Relationship of the dependent variable, log k_2, to the four best single descriptors from the optimized modelling structures, using the complete set of 23 imides. a) PTRCR (r^2 = 0.746), b) I15-16 (r^2 = 0.707), c) IRCNN (r^2 = 0.681) and d) ILUMO2 (r^2 = 0.667).

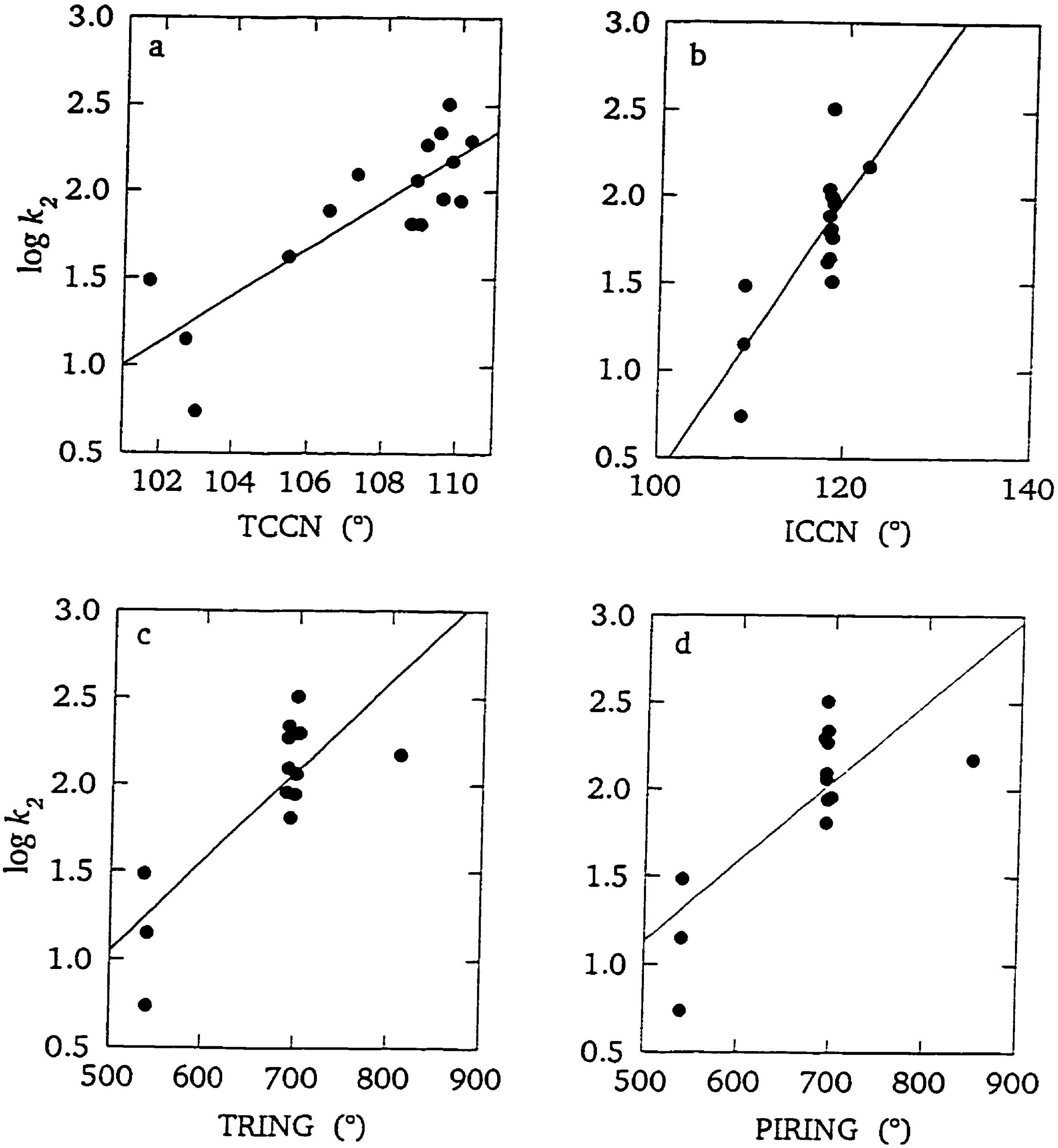

Figure 5.42. Relationship of the dependent variable, log k_2, to the four best single descriptors from the optimized modelling structures, using the set of 16 saturated imides. a) TCCN (r^2 = 0.699), b) ICCN (r^2 = 0.667), c) TRING (r^2 = 0.664) and d) PIRING (r^2 = 0.594).

ICCN (r^2 = 0.667), TRING (r^2 = 0.664), and PIRING (r^2 = 0.594), were measures of bond angles, which likely describe the ring strain of these imides. In this subset of the data, the remaining imides with five-membered rings (*i. e.* the three succinimides) hydrolyze much more slowly than the others. A dummy variable, with values of 0 and 1 for the succinimides and non-succinimides, respectively, had a coefficient of determination with log k_2 of 0.672. Thus, descriptors such as bond angles, which distinguish between five- and six-membered rings, may be expected to be highly correlated with hydrolysis rate. Since the values of r^2 for the differences between the values for the imide and tetrahedral intermediate structures for the binding, electronic, and core-core interaction energies, were below 0.04, they were not included in the multiple liniear regression analysis.

When the subset of maleimides are considered (Figure 5.43), three of the four best single descriptors of log k_2, T10-12 (r^2 = 0.921), TRCN (r^2 = 0.911), and T11-12 (r^2 = 0.902), measured C(tetrahedral)-N bond lengths of the tetrahedral intermediate. Two of these, T 10 - 12 and T 11 - 12, measured the differences between this bond length and the C(tetrahedral)-O(protonated) and the C(tetrahedral)-O(deprotonated) bond lengths, respectively. The significance of these composite parameters is unclear. Their high correlation with log k_2 may reflect correction of errors in the measurements of the C-N bond length, which is expected to be positively correlated with imide hydrolysis rate, as it is this bond which is broken during the rate-determining step. The fourth descriptor shown in Figure 5.43, IHF (r^2 = 0.905), which measured the heat of formation of the imide is also highly correlated with log k_2. Since the electron-withdrawing effects of the *N*-substituents of this series increase with molecular weight, the high correlation of heat of formation with log k_2 may be due only to its correlation, within this series of compounds, to molecular weight. As the electron-withdrawing effect of the *N*-substituent increases, the electron density of the imide functional

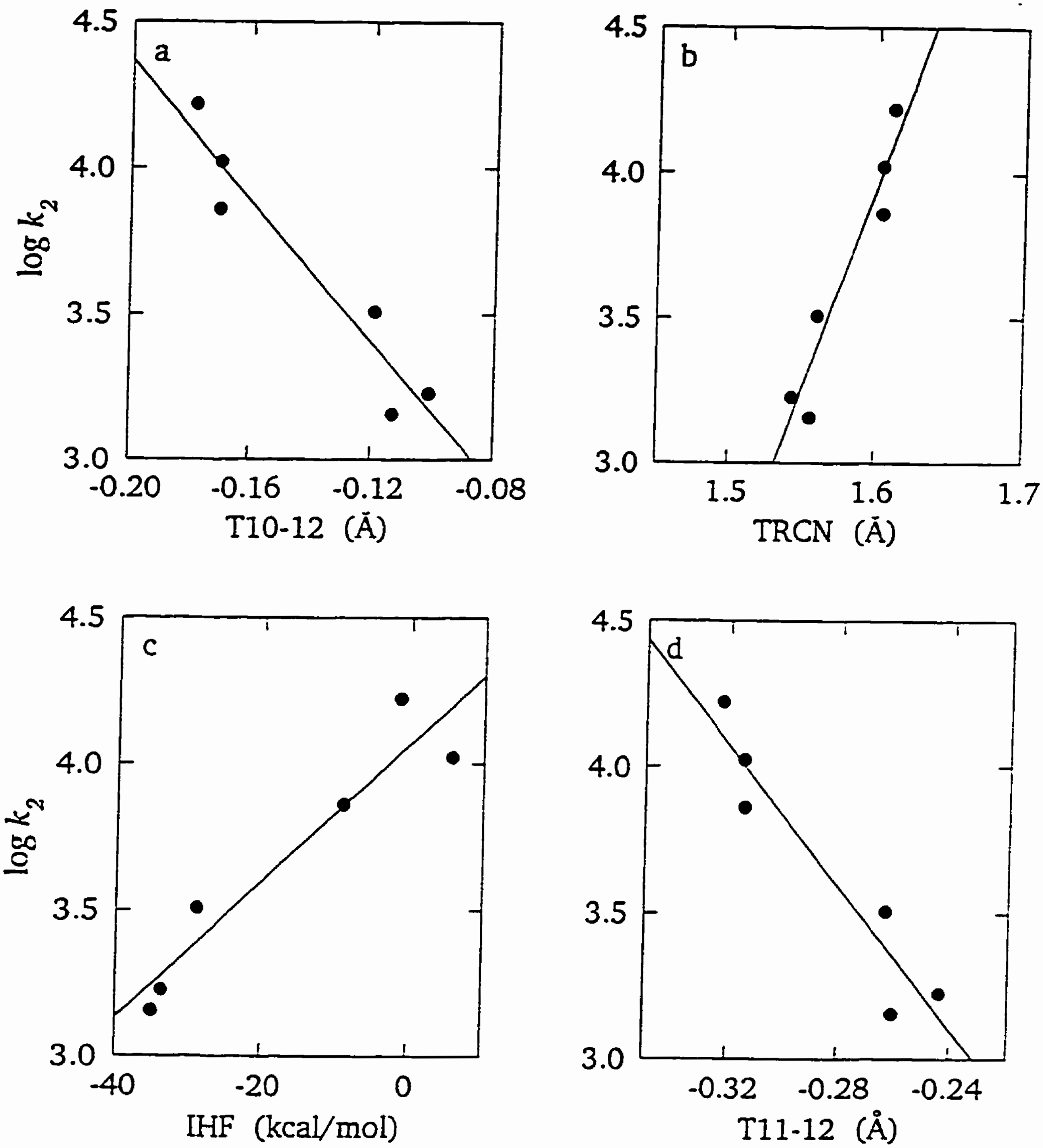

Figure 5.43. Relationship of the dependent variable, log k_2, to the four best single descriptors from the optimized modelling structures, using the set of 6 maleimides. a) T10-12 (r^2 = 0.921), b) TRCN (r^2 = 0.911), c) IHF (r^2 = 0.905) and d) T11-12 (r^2 = 0.902).

group decreases, increasing its susceptibility to nucleophilic attack by hydroxide ion.

When only the dexrazoxane analogs were examined, the best single descriptors of log k_2, T17-16 ($r^2 = 0.680$), TLUMO ($r^2 = 0.659$), TDPM ($r^2 = 0.539$), and PICCN ($r^2 = 0.451$), measured energies of the frontier molecular orbitals (Figure 5.44). TLUMO, the LUMO energy, and T17-16, the difference between the LUMO and HOMO energies, of the tetrahedral intermediate were the most highly correlated with log k_2. The relationships between log k_2 and dipole moment and the N-C(carbonyl)-Cα angle are unclear.

The pK_a of the imide functional group was highly correlated with descriptors measuring the frontier molecular orbital energies (Figure 5.45). I 15 - 16, the difference between the HOMO and LUMO energies of the imide, was correlated with IZN, the charge of the imide nitrogen atom, which may be expected to predict the strength of the N-H bond. However, atomic charges of the imide functional group were not highly correlated with pK_a.

5.5.2 Linear regression of the kinetic parameters, log k_2 and pK_a

Linear regression analysis produces an equation of the form $y = \beta_0 + \beta_1 x_1 + \beta_2 x_2 + \beta_i x_i + \cdots + \beta_\pi x_\varpi$ in which y is the dependent variable, x_i are the independent variables, and β_i are the regression coefficients. The equation predicts the value of the dependent variable based on the values of one or more independent variables. The dependent variables in this study, log k_2 and pK_a, were predicted from values of the descriptors extracted from molecular modelling structures. Data were analyzed using Sigmastat, version 1.01 for DOS (Jandel Scientific, San Rafael, CA).

Equations containing too many independent variables may be overparameterized, and may therefore not reflect a true relationship of the independent variables with the dependent variable. Of the five subsets of the data to be analyzed, three contain a sufficient number of

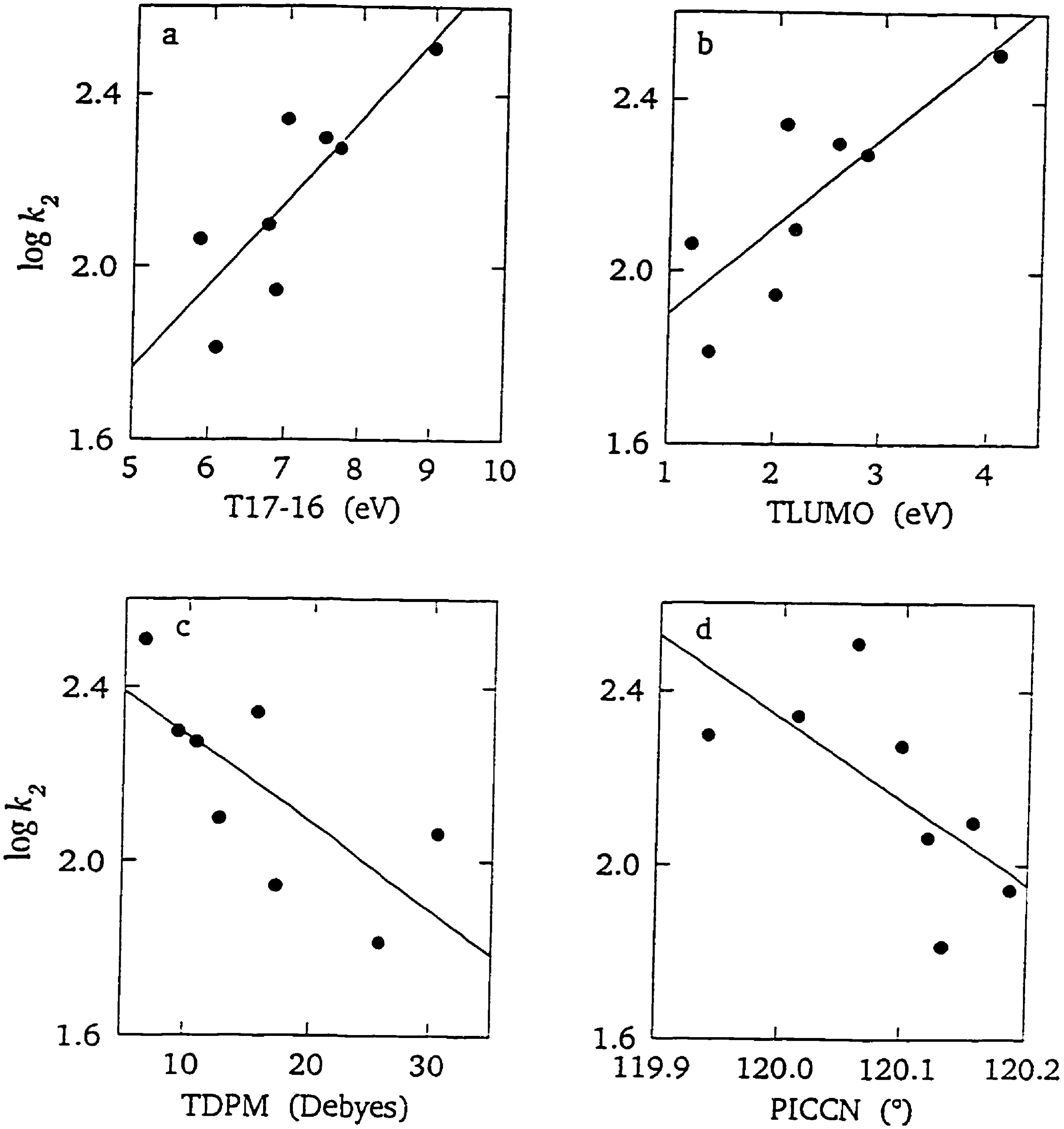

Figure 5.44. Relationship of the dependent variable, log k_2, to the four best single descriptors from the optimized modelling structures, using the set of 8 dexrazoxane analogs. a) T17-16 ($r^2 = 0.680$), b) TLUMO ($r^2 = 0.659$), c) TDPM ($r^2 = 0.539$) and d) PICCN ($r^2 = 0.451$).

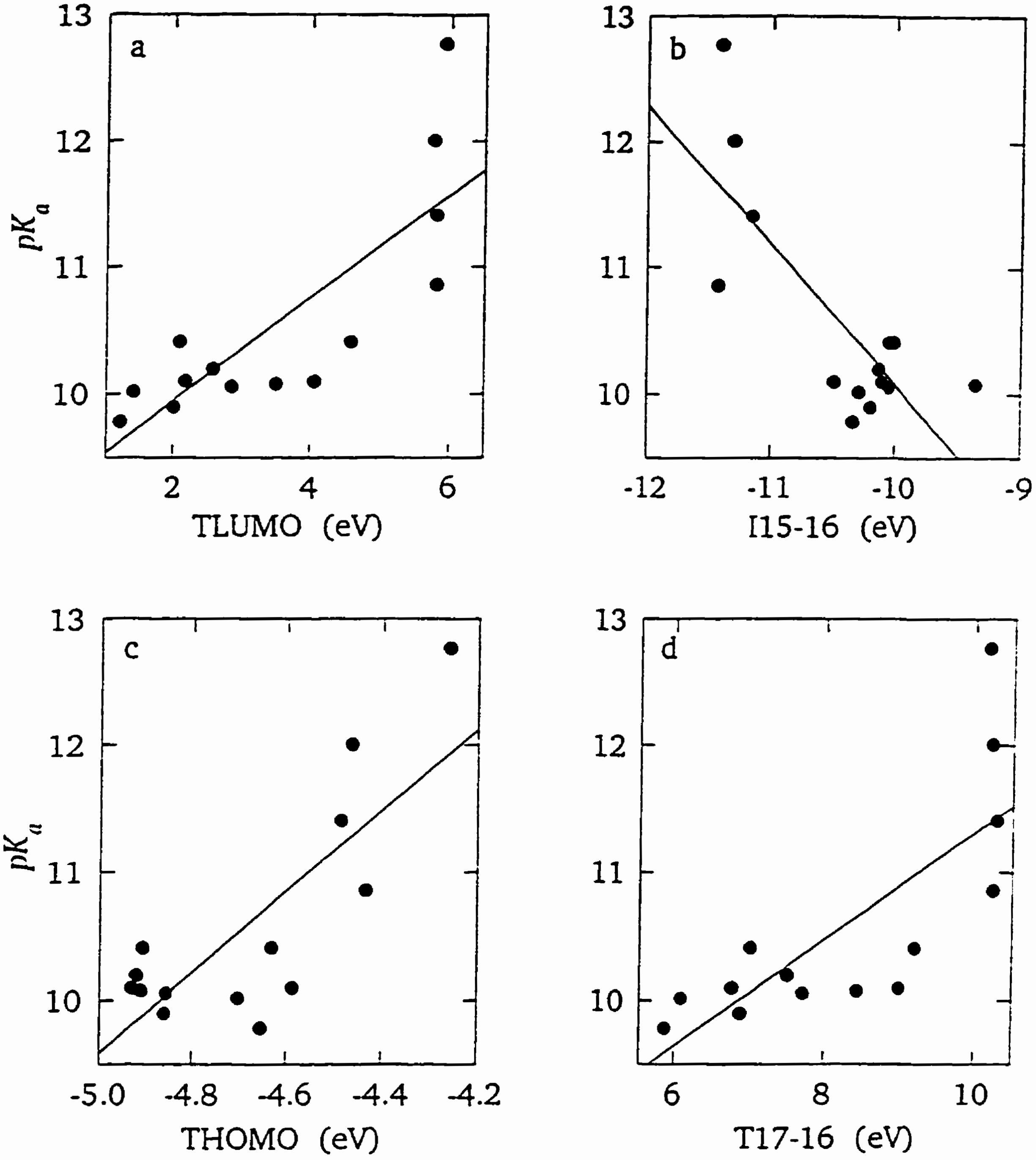

Figure 5.45. Relationship of the dependent variable, pK_a, to the four best single descriptors from the optimized modelling structures, using the set of 14 non-*N*-substituted imides. a) TLUMO ($r^2 = 0.644$), b) I15-16 ($r^2 = 0.618$), c) THOMO ($r^2 = 0.615$) and d) T17-16 ($r^2 = 0.581$).

observations to be described by a two-variable equation: the complete data set, the saturated imides, and the non-*N*-substituted imides, for which the numbers of observations are 23, 16, and 14, respectively. These were analyzed by the best subsets algorithm. Equations for the remaining two subsets, the maleimides (n = 6) and the bisdioxopiperazines (n = 8), were ranked by the absolute values of the Pearson product moment correlation coefficients, listed in Table 5.5.

In this study, there are 114 independent variables, from which two-variable regression equations are to be developed. Since there are ${}_{114}C_2 = 6441$ possible two-variable equations, an automated approach is necessary to identify the pairs of descriptors which may result in useful equations. A best subsets algorithm identifies such pairs quickly, as it does not require the examination of each pair in order to identify those which best describe the data.

The best subsets algorithm included in the Sigmastat software was used to identify the two-variable combinations which best describe the dependent variables, log k_2 and pK_a. The regression degrees of freedom can not exceed the total degrees of freedom, which is equal to the number of observations in the data set. Thus, the independent variables were submitted for analysis in small batches, such that each descriptor was submitted with every other descriptor at least once. The output consisted of the top ten pairs for each batch, and the best pairs of descriptors were ranked in decreasing order of r^2.

r^2, the coefficient of determination, measures the fraction of variability in the dependent variable which is described by the equation. As r^2 approaches one, the better the equation describes the data. r^2 was used to select the equations which best described the two dependent variables which determine imide hydrolysis rates, log k_2 and pK_a. The potential equations in the ranked series for each subset were analyzed for adherence to the assumptions of linear regression analysis.

Linear regression analysis requires the assumption that the variance of the independent variables is constant over the observed range. To evaluate the validity of this assumption, the residuals of the best equations were tested for constant variance by the Spearman rank correlation coefficient, which examines trends in the residuals with respect to the independent variable, and is calculated by Equation 5.7, in which u and a are the ranks of the residuals and independent variable, and $\bar{u}$ and $\bar{a}$ are their means. The cutoff for this test was $p = 0.05$. Linear regression analysis also requires the assumption that the data are normally distributed about the regression line. Thus, the residuals were examined for normality using the Kolmogorov-Smirnov test, the cutoff for which was set at $p = 0.05$. If the regression equation accounts for all the variance in the dependent variable, the residuals equal the random error component, and should therefore be random with respect to the dependent and independent variables. No trends among the residuals were detected for the best equations for each subset. 95% of the residuals for each regression equation should lie within two standard deviations. If this is not the case, the equation may not adequately describe the data, or may be influenced by outlying data points.

In addition to the coefficient of determination, a second measurement was made of the fit of the equations to the data. The predicted residual error sum of squares (*PRESS*) describes how well the equation predicts new data. It is calculated by removing one observation form the data set, recalculating the regression coefficients, and predicting the value of the dependent variable for the removed data point. This is repeated for each observation, and the squares of the residuals are summed. As *PRESS* decreases, the predictions made by the equations improve.

The significance of each independent variable in the regression equations was examined by calculating the *F* statistic. *F* is the ratio of the mean squares of the regression equation about the mean and the residuals about the regression equation. As the fit of the equation improves, the denominator decreases, and *F* increases. The cutoff for this test was set at 4, which corresponds to $p < 0.05$ that the independent variable was inappropriately included in the equation. For the two-variable equations, a stepwise regression was performed, in which the independent variable with the higher *F* value was entered into the equation first, followed by the second.

High correlation among the independent variables in a regression equation inflates the errors associated with the equation, since the variables do not contribute unique information for prediction of the dependent variable. Consequently, many pairs of independent variables which were selected by the best subsets regression analysis did not meet the requirements of the *F* test, and were rejected. Thus, multicollinearity was rarely observed among the equations which passed the tests of the assumptions of multiple linear regression analysis, as determined by the correlation coefficients of the two independent variables. Equations were not rejected solely on the basis of this test.

Molecular modelling data from four subsets of the data set (the complete data set, the saturated imides, the maleimides, and the dexrazoxane analogs) were regressed against log k_2. Data from the subset of non-*N*-substituted imides were regressed against pK_a. The top three equations for each subset, which passed all the above-mentioned statistical tests, are listed in Table 5.7. It can be seen that the three measures of how well the equations describe the data, r^2, *PRESS*, and the standard deviation of the residuals, provide essentially the same information; the ranks of the equations by each statistic were identical within each subset. The number of residuals exceeding two standard deviations was approximately 95%, indicating the absence of consistent outliers. The *F* tests for each variable often exceeded the cutoff of four by a large margin, indicating that each contributed significantly to the description of the dependent variable. The correlation coefficients for the two-variable equations were generally low, indicating that these variables provided unique information in the description of the dependent variable.

When the complete data set of 23 imides was considered, the best equation describing $\log k_2$ was

$$\log k_2 = 68.8736 - 43.5273(\mathrm{PTRCR}) + 0.21446(\mathrm{IHOMON}) \quad (5.8)$$

In this equation, $\log k_2$ is described in terms of PTRCR, the C(tetrahedral)-Cα bond length, measured on the MMX-optimized tetrahedral intermediate structure (Figure 5.3), and IHOMON, the HOMO (highest occupied molecular orbital) energy of the AM1-optimized imide structure. Residual analysis of Equation 5.8 (Figure 5.46) demonstrated the randomness of the residuals with respect to the dependent variable and the independent variables. Thus, the equation described most of the variability in the dependent variable, $\log k_2$, and the residuals may be assumed to represent the random error component of the measurement of $\log k_2$. The experimentally determined values of $\log k_2$ and those predicted from Equation 5.8 are shown in Figure 5.47, and are listed in Table 5.8.

Table 5.7. Best equations for each subset of the 23 imides.

Data Set	Equation[a]	n	r^2	*PRESS*	$\sigma_{residuals}$	Residuals $> 2\sigma$[b]	*F* (var1)	*F* (var2)	r[c]
Complete Data Set	$\log k_2 = 68.9-43.5(PTRCR)+0.214(IHOMON)$	23	0.833	4.27	0.371	2	62.0	10.3	-0.340
	$\log k_2 = 79.5-46.4(PTRCR)+8.96(TZO-)$	23	0.819	4.28	0.386	0	62.0	8.0	-0.216
	$\log k_2 = 26.2-44.3(PTRCR)+32.0(PIRCN)$	23	0.819	4.37	0.386	1	62.0	8.0	-0.274
Saturated	$\log k_2 = -17.0+0.181(TCCN)+10.21(I5+6)$	16	0.850	0.62	0.178	1	32.5	13.2	-0.594
	$\log k_2 = -14.4+0.150(TCCN)+0.225(IHOMON)$	16	0.830	0.79	0.190	1	32.5	10.0	-0.246
	$\log k_2 = -9.54+0.134(TCCN)+0.284(I15-16)$	16	0.823	0.88	0.194	0	32.5	9.1	0.013
Maleimides	$\log k_2 = 1.951-12.1(T10-12)$	6	0.921	0.16	0.123	0	46.4	--	--
	$\log k_2 = -18.7+14.2(TRCN)$	6	0.911	0.18	0.130	0	41.2	--	--
	$\log k_2 = 4.07+0.023(IHF)$	6	0.905	0.25	0.134	0	38.3	--	--
Bisdioxopiperazines	$\log k_2 = 0.812+0.191(T17-16)$[d]	8	0.680	0.19	0.130	0	12.7	--	--
Non-*N*-Substituted	$pK_a = 204.02-114.22(IRCR)-62.71(IZC)$	14	0.917	1.68	0.255	0	7.2	71.9	-0.734
	$pK_a = 6.18+0.0000257(IATOM)+58.9(IZO2)$	14	0.877	2.57	0.310	1	10.1	37.6	-0.089
	$pK_a = 6.16+0.0000246(ITOT)+59.0(IZO2)$	14	0.877	2.57	0.311	1	10.1	37.6	-0.102

[a] Variables are defined in Table 5.3. Variables in two-variable equations are reported in order of their entry into a stepwise regression.

[b] Number of residuals greater than two standard deviations from zero.

[c] Pearson product moment correlation coefficient for the two independent variables.

[d] Only one equation was found with a significant relationship between the independent variable and $\log k_2$ ($p \leq 0.05$).

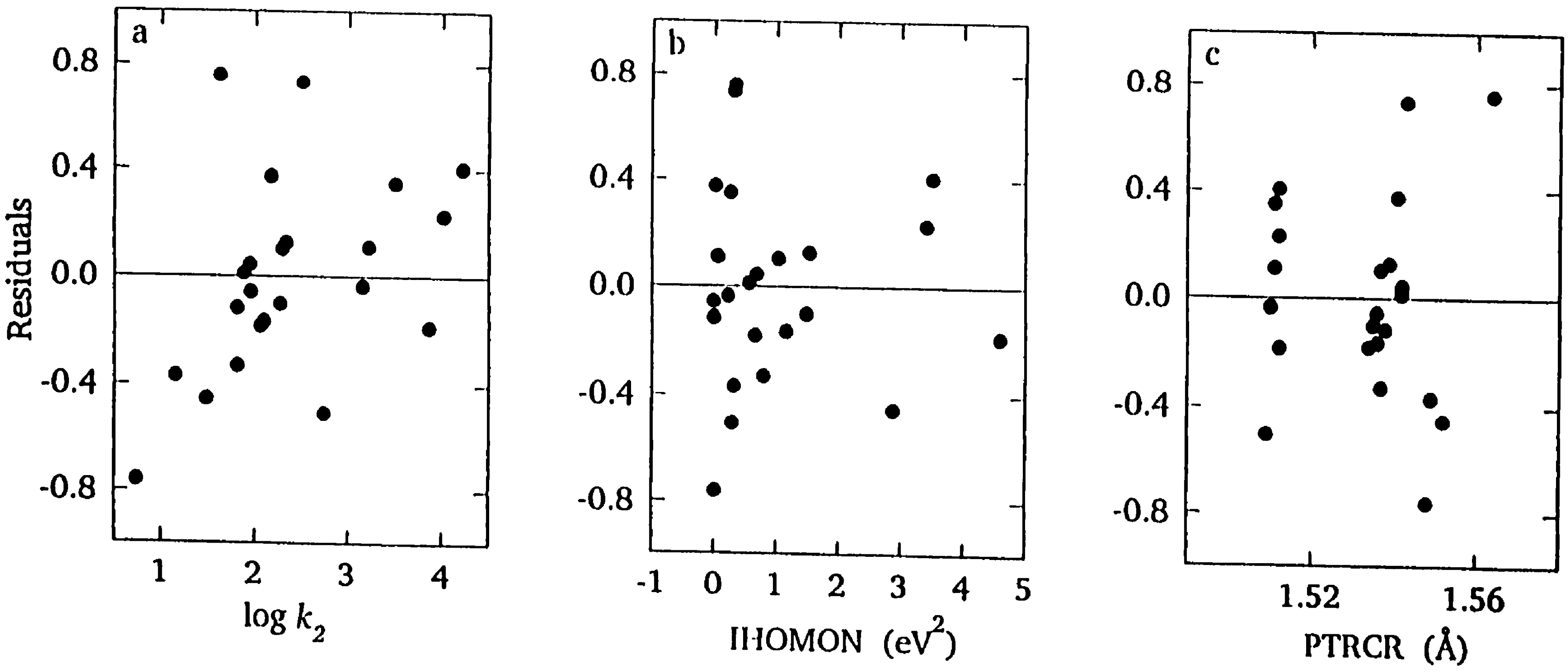

Figure 5.46. Residual analysis of Equation 5.8 for the complete set of imides. Residuals are random with respect to the dependent variable a) log k_2, and the independent variables, b) IHOMON and c) PTRCR.

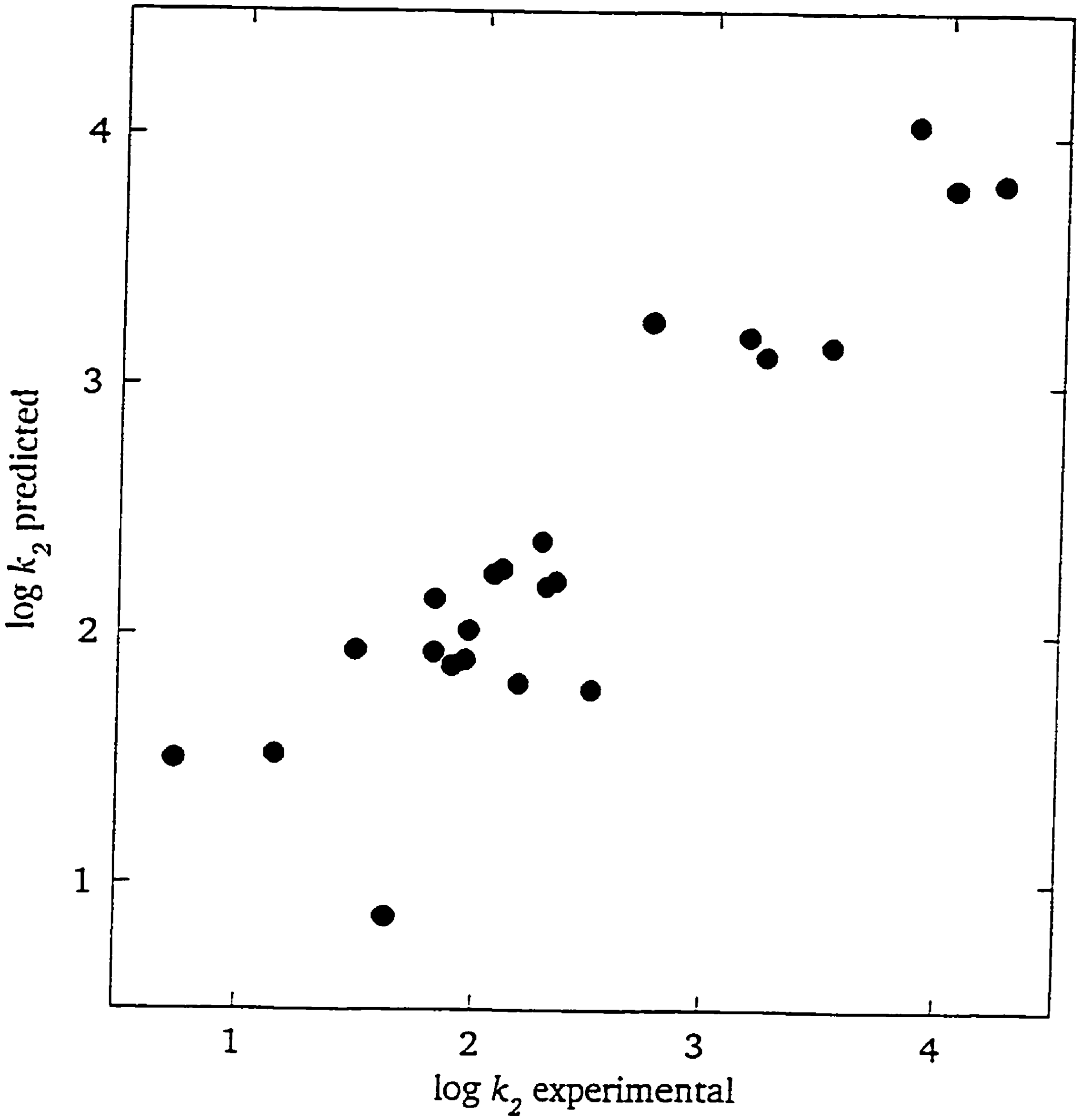

Figure 5.47. Comparison of expermental determinations of log k_2 for the complete data set with values predicted by Equation 5.8. Experimental and predicted values are listed in Tables 5.1 and 5.8, respectively.

Table 5.8. Predicted and experimental determinations of log k_2 for the set of 23 imides.

Compound	**log k_2 Equation 5.8[a] (Complete Data Set)**	**log k_2 Equation 5.9[b] (Saturated)**	**log k_2[c] (Experimental)**
diacetamide	1.929	1.962	1.813
N-methyl-"	1.875	1.763	1.889
N-methylbis(trifluoro-")	0.868	1.685	1.624
Succinimide	1.497	0.791	0.739
N-methyl-"	1.517	1.211	1.150
N-2,6-xylyl-"	1.937	1.490	1.487
maleimide	3.117	--	3.228
N-methyl-"	3.159	--	3.509
N-ethyl-"	3.194	--	3.158
N-phenyl-"	3.794	--	4.024
N-3,4-xylyl-"	3.814	--	4.221
N-4-chlorophenyl-"	4.047	--	3.862
phthalimide	3.253	--	2.748
adipimide	1.804	2.109	2.178
glutarimide	2.016	2.139	1.959
ICRF-154	2.264	1.727	2.098
ICRF-193	2.216	2.105	2.343
LYZ 17B	1.779	2.259	2.508
LYZ 19	1.900	2.131	1.945
LYZ 2	2.142	2.104	1.813
LYZ 8	2.243	2.133	2.063
LYZ 22	2.377	2.197	2.275
BLPD B2	2.193	2.376	2.299

[a] log k_2 = 68.8736 - 43.5372(PTRCR) + 0.21446(IHOMON)

[b] log k_2 = -16.975 + 0.181(TCCN) + 10.2098(I5+6)

[c] The units of k_2 are M^{-1} min^{-1}.

The descriptor, PTRCR, was very highly correlated with log k_2 (Figure 5.41a), and was included in each of the top ten equations describing log k_2. The second descriptor in these equations was chosen most frequently (six times of the ten) from the descriptors extracted from the structure of the AM1-optimized tetrahedral intermediate. For this subset of the data, it appears that the tetrahedral intermediate provided the most useful information in the prediction of log k_2.

Two single descriptors which predicted log k_2 well, I15-16 and IRCNN (Figure 5.41b&c), were not included in any two-variable equations. No second descriptor, when regressed against log k_2 with I15-16, which measures the difference between the LUMO and HOMO energies, passed the *F* test. That is, when this descriptor was included in the equation, no descriptor could account for the remaining variability in log k_2. Most of the remaining variability was likely random error, given the high correlation coefficient for I15-16 with log k_2 (Table 5.5). The descriptor, IRCNN, measured the square of the difference between the C(carbonyl)-N bond length and that of diacetamide. This descriptor was likely not included in the two-variable equation because it had a very small range of values.

When the subset of saturated imides were considered, the best equation describing log k_2 was

$$\log k_2 = -16.975 + 0.181(\mathrm{TCCN}) + 10.2098(\mathrm{I5{+}6}) \qquad (5.9)$$

In this equation, log k_2 is described in terms of TCCN, the Cα-C(tetrahedral)-N angle of the AM1-optimized tetrahedral intermediate structure (Figure 5.3), and I5+6, the sum of the charges of the nitrogen and carbonyl carbon of the imide. Residual analysis of Equation 5.9 (Figure 5.48) demonstrated the randomness of the residuals with respect to the dependent

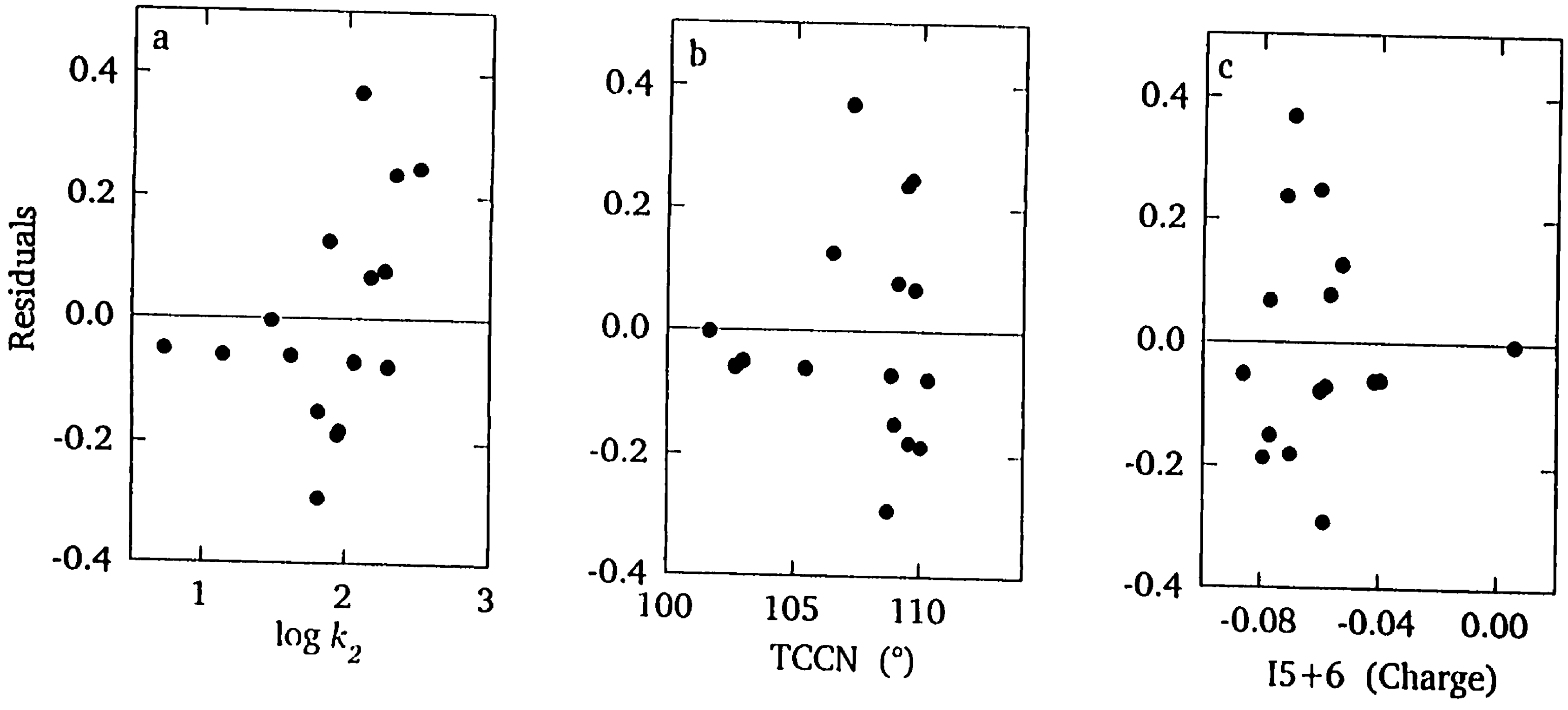

Figure 5.48. Residual analysis of Equation 5.9 for the subset of saturated imides. Residuals are random with respect to the dependent variable a) log k_2, and the independent variables, b) TCCN and c) I5+6.

variable and the independent variables. Thus, the equation described most of the variability in the dependent variable, log k_2, and the residuals may be assumed to represent the random error component of the measurement of log k_2. The experimentally determined values of log k_2 and those predicted from Equation 5.9 are shown in Figure 5.49, and are listed in Table 5.8.

The descriptor, TCCN, was the best single descriptor of log k_2 (Figure 5.42a), and was included in each of the top three equations describing log k_2 (Table 5.7). The second descriptor in these equations described electronic properties of imides, such as frontier molecular orbital energies and atomic charges.

Although descriptors which measured the sum of the angles of the imide rings were good single predictors of log k_2 (Figure 5.42), they were not included in the best equations. Since these descriptors are undefined for the diacetamides, which are acyclic, linear regression of equations which included these descriptors was performed on only 13 of the 16 saturated imides. Thus, a significant fraction of the data were lost, which may have had an adverse effect on the relationship between the descriptor and log k_2. If the remaining data were insufficient to describe imide hydrolysis, equations including these variables would not predict the dependent variable well.

When the maleimides were considered, the best equation predicting log k_2 was

$$\log k_2 = 1.951 - 12.080(\mathrm{T10\text{-}12}) \qquad (5.10)$$

In this equation, log k_2 is described in terms of the difference between the bond lengths between the tetrahedral carbon atom and the nitrogen and protonated oxygen atoms (Figure 5.3). Residual analysis of Equation 5.10 (Figure 5.50) demonstrated the randomness of the

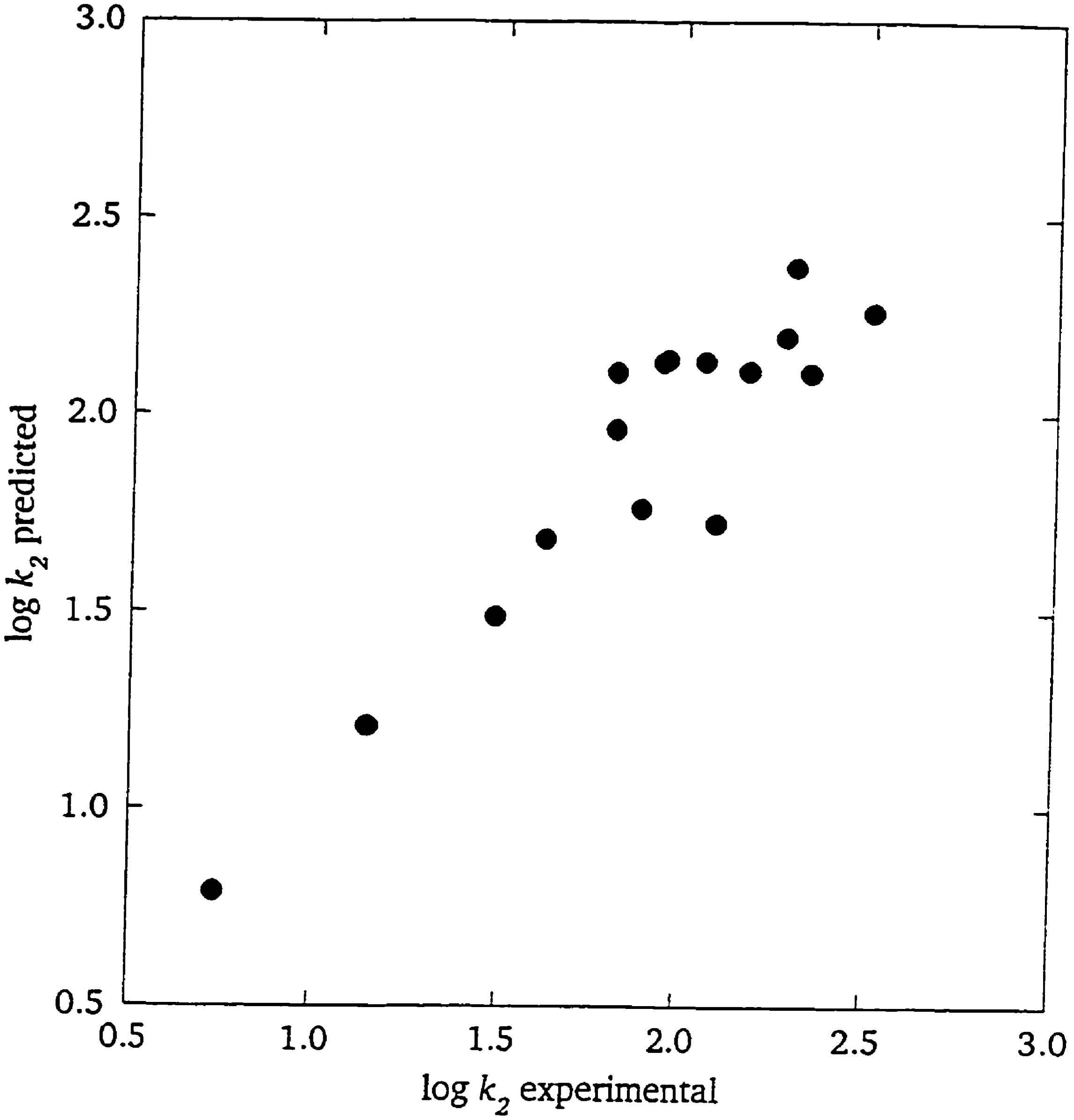

Figure 5.49. Comparison of expermental determinations of log k_2 for the subset of saturated imides with values predicted by Equation 5.9. Experimental and predicted values are listed in Tables 5.1 and 5.8, respectively.

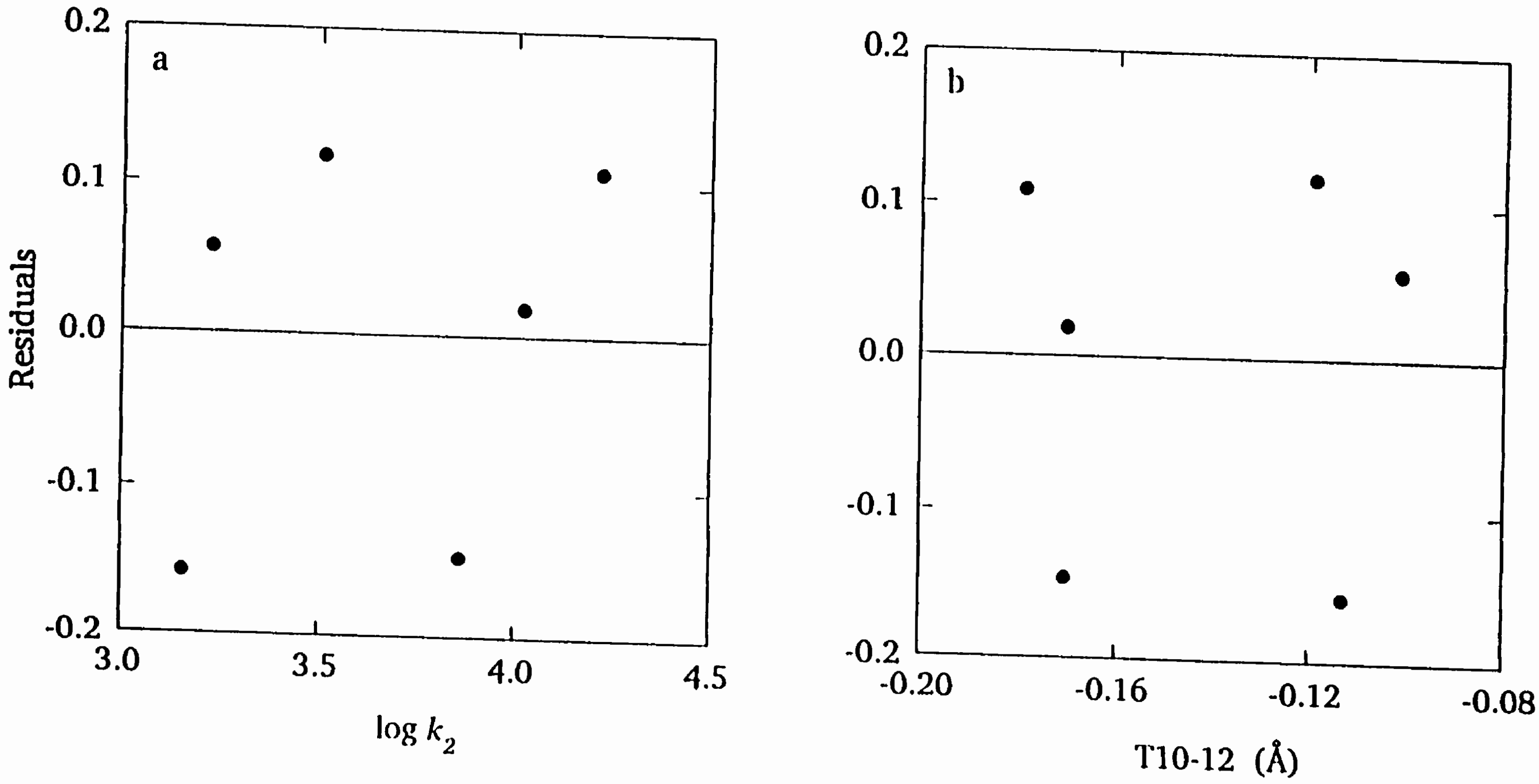

Figure 5.50. Residual analysis of Equation 5.10 for the subset of maleimides. Residuals are random with respect to the dependent variable a) log k_2, and the independent variable, b) T10-12.

residuals with respect to both the dependent and independent variables. Thus, the equation described most of the variability in the dependent variable, log k_2, and the residuals may be assumed to represent the random error component of the measurement of log k_2. The experimentally determined values of log k_2 and those predicted from Equation 5.10 are shown in Figure 5.51, and are listed in Table 5.8. Equations developed from this subset of the data precisely described the effect of *N*-substitution on the hydrolysis rate constant over a very narrow range of structure. However, since the imides for which hydrolysis rates are to be predicted are likely to be structurally different from the maleimides, these equations can not be used reliably.

When the bisdioxopiperazine subset was considered, the only equation which was significantly able to predict log k_2 was

$$\log k_2 = 0.812 + 0.191(\mathrm{T17\text{-}16}) \qquad (5.11)$$

In this equation, log k_2 is described in terms of the difference between the LUMO and HOMO of the tetrahedral intermediate (Figure 5.3). Residual analysis of Equation 5.11 (Figure 5.52) demonstrated the randomness of the residuals with respect to both the dependent and independent variables. Thus, the equation described most of the variability in the dependent variable, log k_2, and the residuals may be assumed to represent the random error component of the measurement of log k_2. The experimentally determined values of log k_2 and those predicted from Equation 5.11 are shown in Figure 5.53, and are listed in Table 5.8. No other descriptor passed the F test, indicating an unacceptable level of uncertainty in the relationship between log k_2 and any other descriptor.

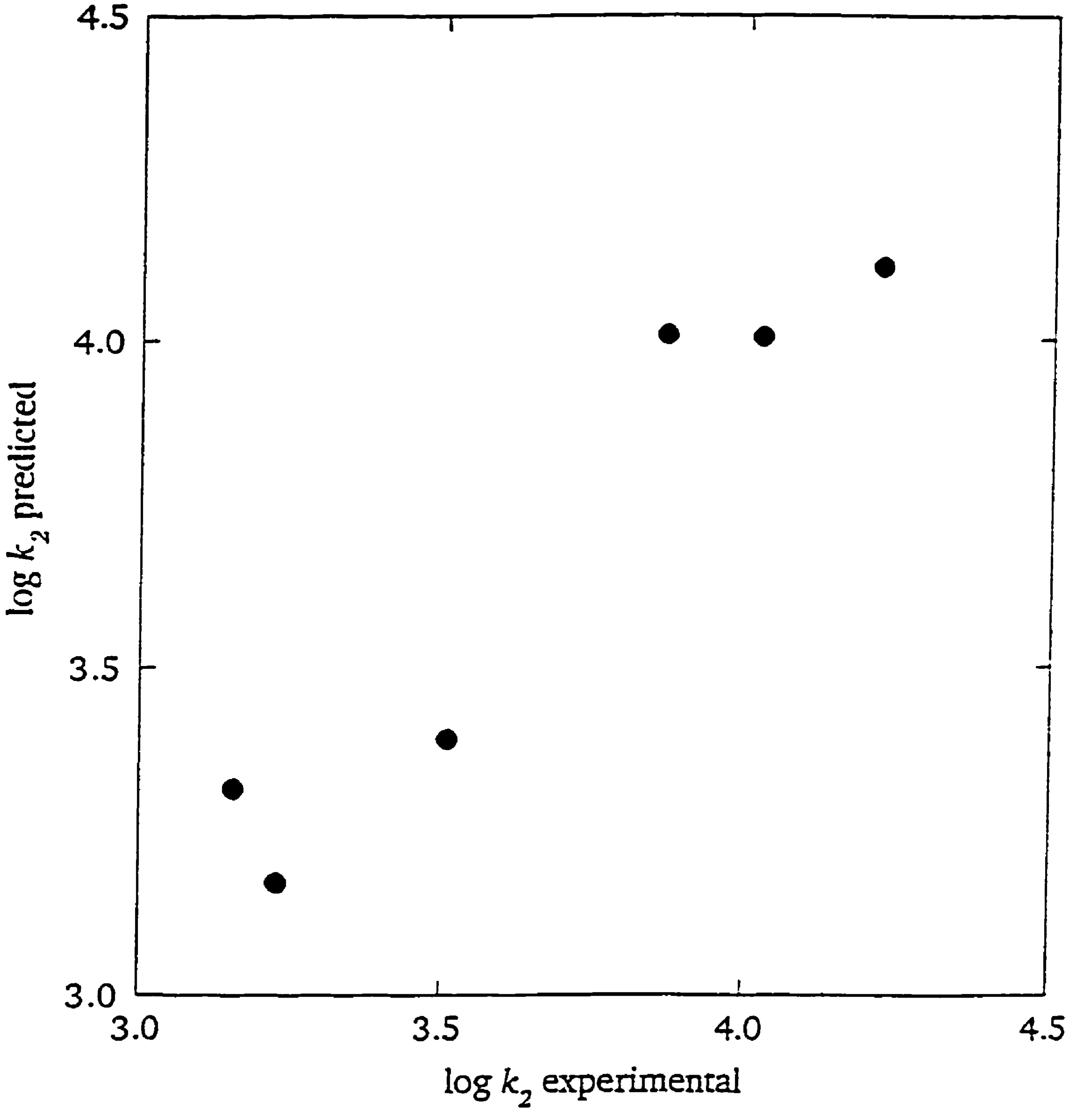

Figure 5.51. Comparison of expermental determinations of log k_2 for the subset of maleimides with values predicted by Equation 5.10. Experimental values are listed in Table 5.1.

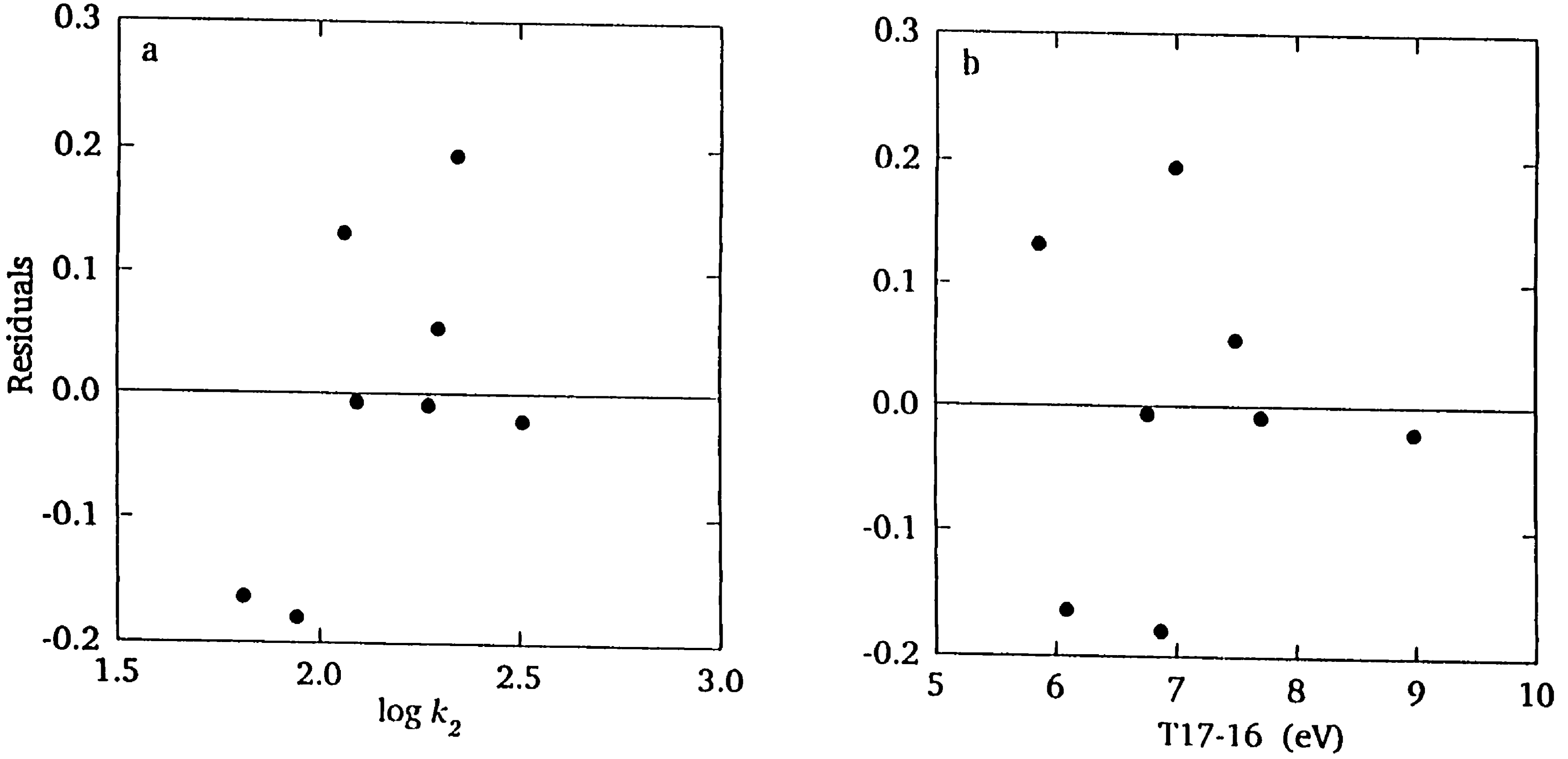

Figure 5.52. Residual analysis of Equation 5.11 for the subset of bisdioxopiperazines. Residuals are random with respect to the dependent variable a) log k_2, and the independent variable, b) T17-16.

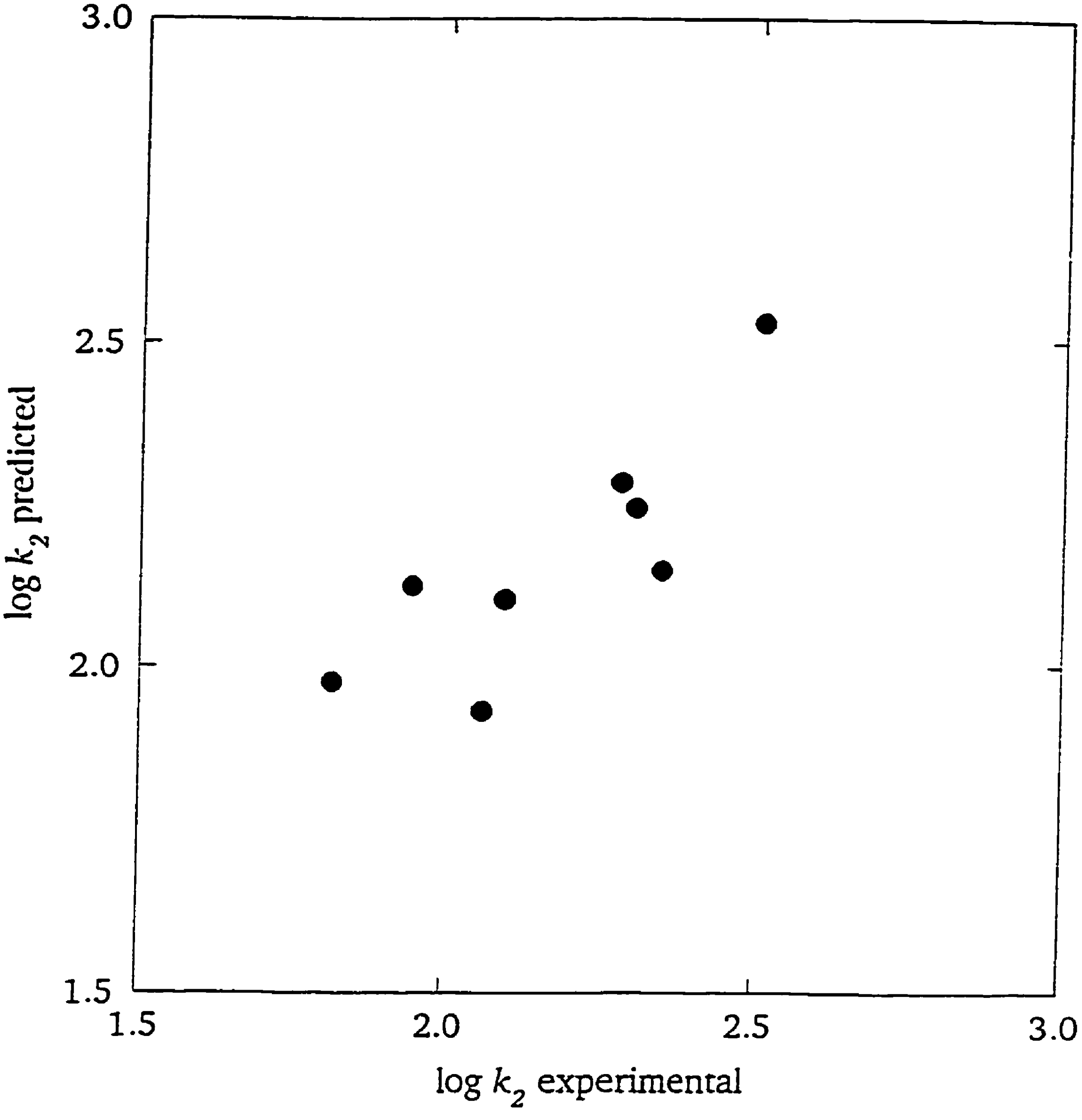

Figure 5.53. Comparison of expermental determinations of log k_2 for the subset of bisdioxopiperazines with values predicted by Equation 5.11. Experimental values are listed in Table 5.1.

As can be seen in Figure 5.44, the random error component of log k_2 for this subset of the data was higher than for the other subsets. Measurements of k_2 for the analogs of dexrazoxane fall within a narrow range. It may be that this range does not contain sufficient variability to allow accurate predictions. This may be the case, as larger subsets of the data (*i. e.* the complete data set, and the saturated imides) yielded better results. The observed imprecision in the description of the dexrazoxane analogs may not be a problem in the prediction of new analogs, since a somewhat wider range of log k_2 is desired.

When the non-*N*-substituted imides were considered, the best equation describing the kinetically determined pK_a (Table 5.1) was

$$pK_a = -62.7126 + 204.015(\text{IRCR}) - 114.215(\text{IZC}) \quad (5.12)$$

In this equation, pK_a is described in terms of the C(carbonyl)-Cα bond length and the charge of the carbonyl carbon atom, both measured on the AM1-optimized imide structure. Residual analysis of Equation 5.12 (Figure 5.54) demonstrated the randomness of the residuals with respect to the dependent variable, and the independent variables. Thus, the equation described most of the variability in the dependent variable, pK_a, and the residuals may be assumed to represent the random error component of the measurement of pK_a. The experimentally determined values of pK_a and those predicted from Equation 5.12 are shown in Figure 5.55, and are listed in Table 5.8.

The descriptors which were included in the best two-variable equations describing pK_a were completely different from the best single descriptors, which measured frontier molecular orbital energies (Figure 5.45). Neither of the descriptors in the best equation, IZC and IRCR, were included in any other equations describing pK_a. The next eight best equations in this

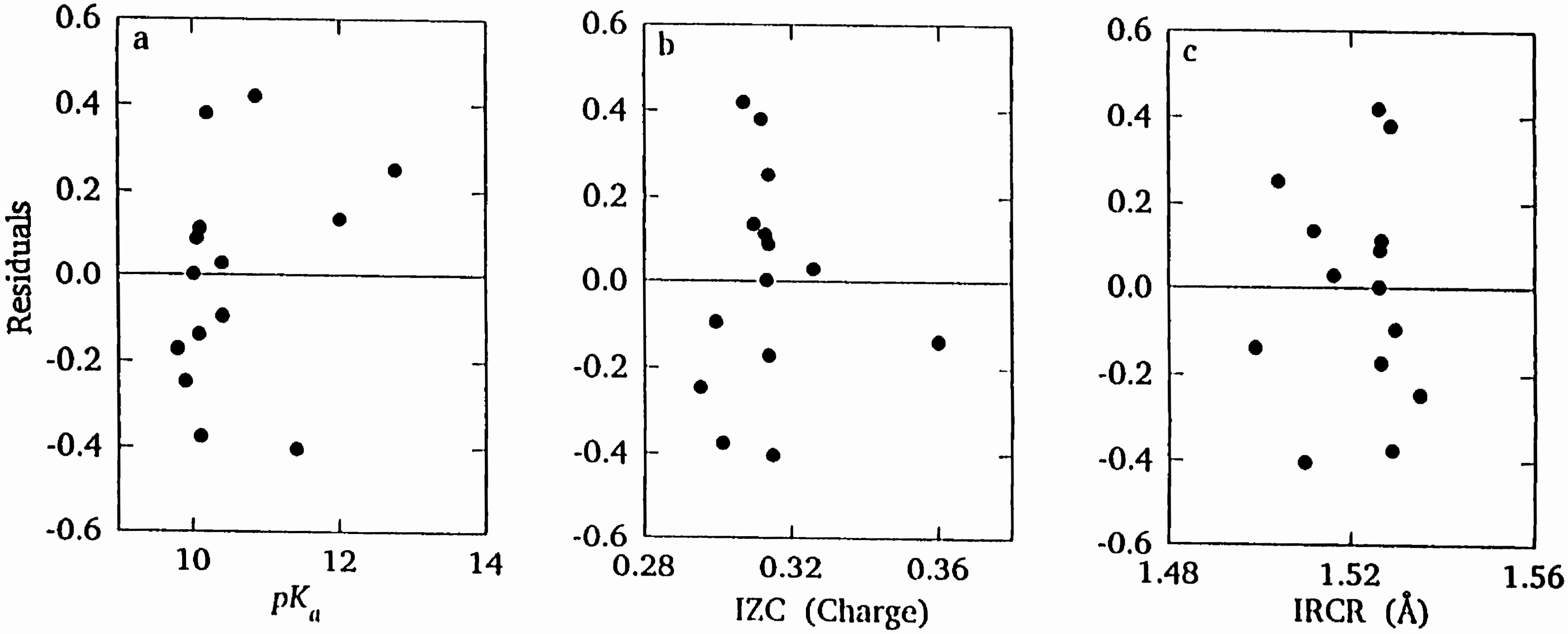

Figure 5.54. Residual analysis of Equation 5.12 for the subset of non-*N*-substituted imides. Residuals are random with respect to the dependent variable a) pK_a, and the independent variables, b) IZC and c) IRCR.

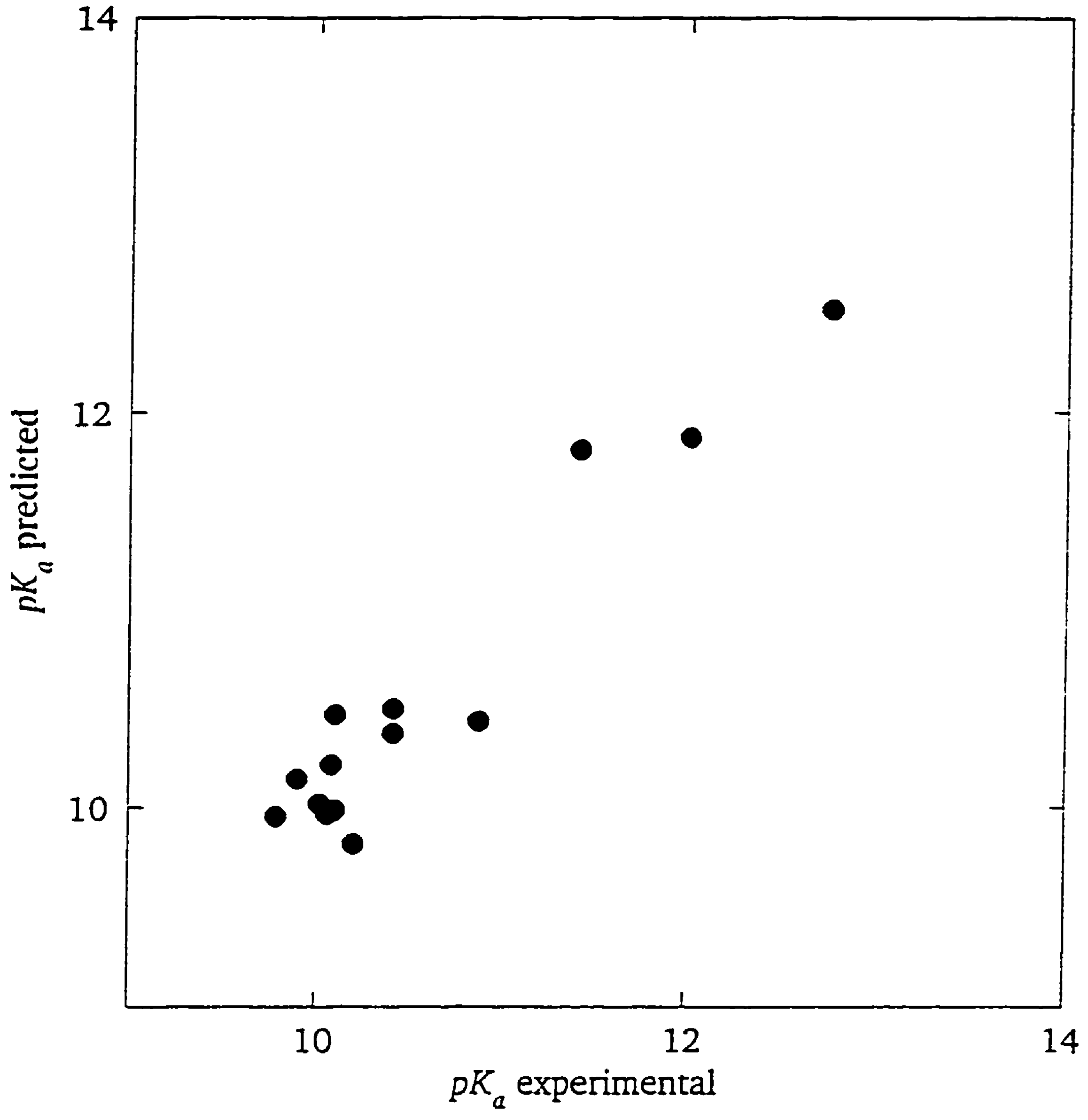

Figure 5.55. Comparison of expermental determinations of pK_a for the subset of non-*N*-substituted imides with values predicted by Equation 5.12. Experimental values are listed in Table 5.1.

series all contained IZO2, which measures the square of the atomic charge on the carbonyl oxygen atom, and a descriptor corresponding to one of the energy terms calculated by the AM1 algorithm in the determination of the total energy of the system. The latter descriptors are highly correlated with each other, indicating that they may reflect the same properties of imides. Since they generally increase in magnitude with increasing molecular weight, they may be proxy variables for any property which increases with molecular weight.

As can be seen in Figure 5.55, the range of pK_a values among the non-*N*-substituted imides was not optimal for the development of a quantitative structure-activity relationship. Only four of the fourteen imides had pK_a values significantly different from 10 (Table 5.1): diacetamide, succinimide, glutarimide, and adipimide. Thus, the equations developed were strongly weighted in favor of these four points. Since the equations are to be used to predict pK_a values of dexrazoxane analogs, which will surely fall outside this range, these equations can not be used without large extrapolations. Thus, linear regression equations will not be used to predict the pK_a values of the proposed analogs of dexrazoxane.

Equations 5.8 and 5.9 represent the most reliable relationships between the molecular modelling data and the kinetic parameters, log k_2 and pK_a. Equation 5.8 was developed using the entire data set, and therefore contains the most information. Equation 5.9 has a smaller standard deviation of residuals (Table 5.7), and is therefore capable of more precise predictions, although perhaps over a more restricted range of structure. Because Equation 5.11 was developed from a very small subset of the data, it contains only one independent variable, and therefore describes the subset relatively poorly. Thus, although it was developed from a subset of dexrazoxane analogs, it can not reliably be used to predict the hydrolysis rates of such compounds. Both Equations 5.8 and 5.9 will be used for the prediction of hydrolysis rates of dexrazoxane analogs.

5.6 Prediction of Hydrolysis Rates of New Dexrazoxane Analogs

5.6.1 Prediction of log k_2 and pK_a of three test compounds

Three imides, 3-methylglutarimide and 4-methyl-2,6-dioxopiperazine (studied at 25 °C and ionic strength of 0.5) [120], and mitindomide (studied at 25 °C) [202] (Figure 5.56), for which the kinetic parameters describing hydrolysis have been previously described, were not included in the data set. They were modelled, and the extracted parameters were used with Equations 5.8 and 5.9 to predict k_2. The predicted and experimentally determined parameters are compared in Table 5.9. In the case of mitindomide, k_2 was calculated by linear least squares regression of pseudo-first-order rate constant data to Equation 5.2 [202].

The k_2 values of 3-methylglutarimide and 4-methyl-2,6-dioxopiperazine are predicted within a factor of two to four by Equations 5.8 and 5.9 (Table 5.9), while the predicted values of k_2 for mitindomide are 120- and 1200-fold too low. Mitindomide has two imide functional groups; it was determined that the imide fused to the cyclobutyl ring hydrolyzes faster [202]. This is expected, since the cyclobutyl ring must impose strain on the imide ring to which it is attached, increasing its reactivity significantly. Kinetic data support this hypothesis. The k_2 for succinimide was 5.5 M^{-1} min^{-1}, while that of mitindomide was determined to be 5000 M^{-1} min^{-1} as described above [202], indicating the significant effect of the fused ring structure of mitindomide. However, since the predicted values of k_2 for mitindomide were far lower than the experimentally determined values, it may be that the equations are best for predicting

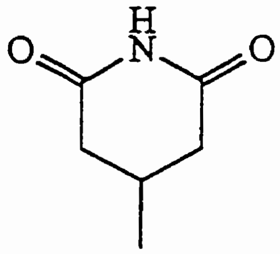

3-Methylglutarimide

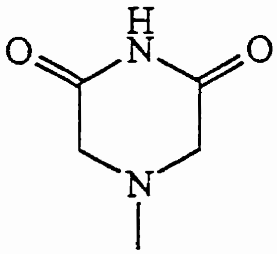

4-Methyl-2,6-dioxopiperazine

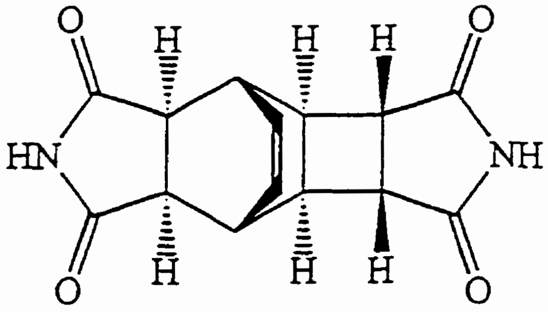

Mitindomide

Figure 5.56. Structures of the test compounds.

Table 5.9. Predicted and experimental values of log k_2 for the test compounds.

	Decriptors used to predict log k_2 using Equations 5.8 & 5.9						
Compound	**IHOMON (eV^2)**	**PTRCR (Å)**	**TCCN (°)**	**I5+6**	**log k_2 Eqn. 5.8[a]**	**log k_2 Eqn. 5.9[b]**	**log k_2 Exptl.**
3-methylglutarimide	9.18×10^{-6}	1.539	109.345	-0.070	1.885	2.102	1.602[c]
4-methyl-2,6-dioxopiperazine	0.899	1.545	109.114	-0.059	1.817	2.172	2.408[c]
mitindomide	0.668	1.547	101.912	-0.078	1.680	0.675	3.699[d]

[a] $\log k_2 = 68.9 - 43.5(\text{PTRCR}) + 0.214(\text{IHOMON})$

[b] $\log k_2 = -17.0 + 0.181(\text{TCCN}) + 10.21(\text{I5+6})$

[c] [120].

[d] Calculated from data previously reported [202] as described in the text.

hydrolysis rate constants of imides whose hydrolyses are affected mainly by electronic, rather than geometric, factors.

5.6.2 Design of lead compounds

A series of 24 lead compounds was developed for prediction of hydrolysis rates, the structures of which are shown in Figure 5.57. Analogs of dexrazoxane bearing electron-withdrawing groups (compounds I-XVIII) may be expected to have faster hydrolysis rates, as the electron density of the imide functional group may be appreciably lower. Thus, the nucleophile, hydroxide ion, should have higher affinity for these analogs. Many analogs containing fluoro groups were included in the series, as this is a small, relatively non-polar group with a strong inductive effect. Other potential advantages of this group include the variety of readily available starting materials for the synthesis of fluorine-containing dexrazoxane analogs, and the possibility of designing multiply fluorinated compounds to obtain a series of analogs which cover a wide range of hydrolysis rates. Analogs of dexrazoxane with increased ring size (compounds XXI and XXIII) were included in the series, since, in general, an increase in ring size decreases stability, perhaps resulting in faster hydrolysis rates.

Because of the importance of chelation in the putative mechanism of action of dexrazoxane, the proposed analogs must be expected to chelate metal ions. The hydrolysis products of compounds I-III, V-XIII, XV, and XVI may be expected to have similar coordination geometry to the homologous compound, EDTA. The Fe^{3+} complexes of the hydrolysis products of compounds IV and XIV were modelled using PCModel; the

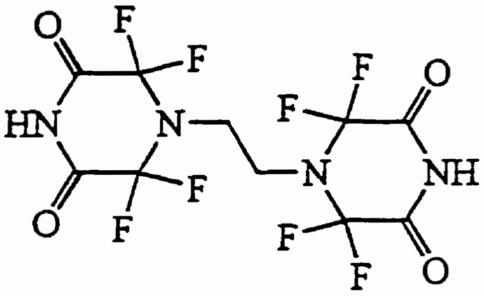

I

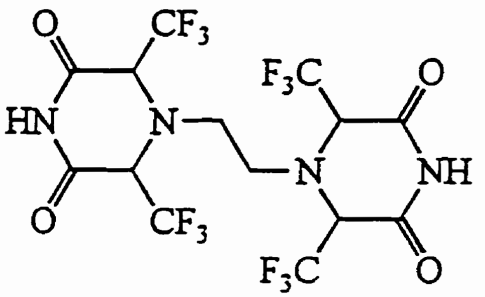

II

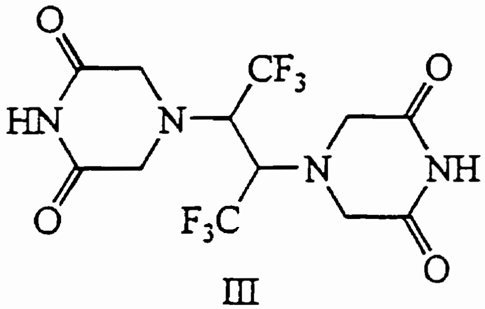

III

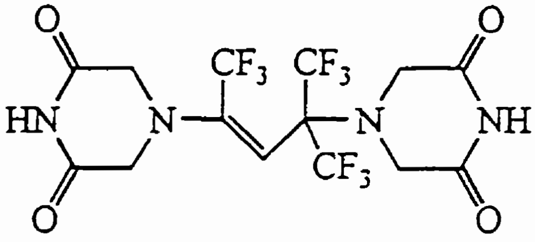

IV

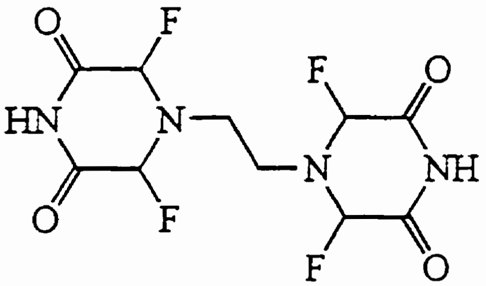

V

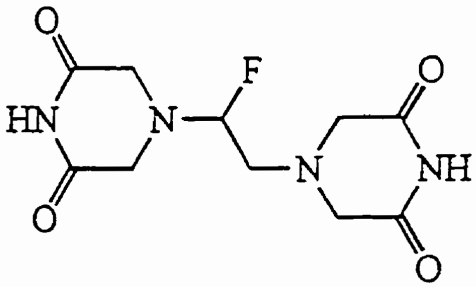

VI

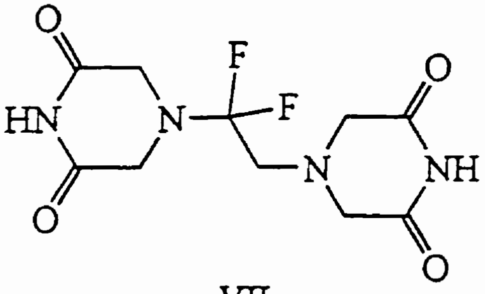

VII

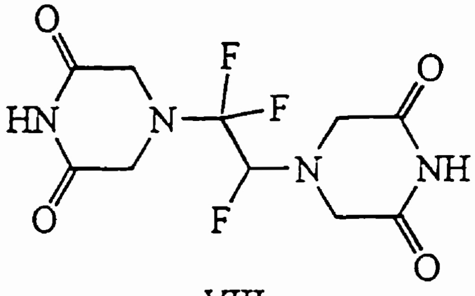

VIII

Figure 5.57. Structures of the lead compounds.

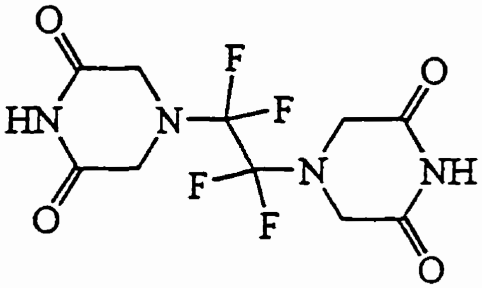
IX

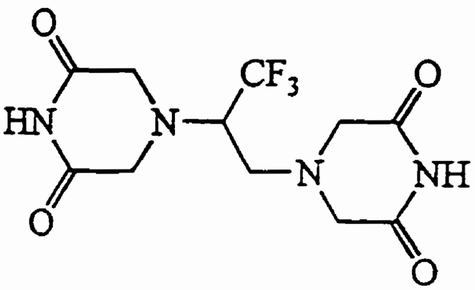
X

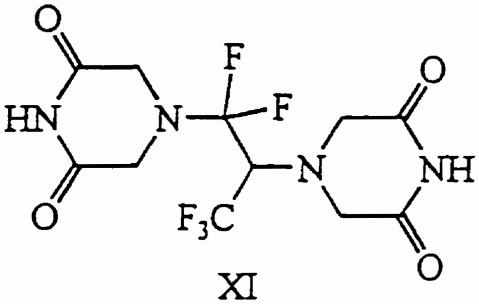
XI

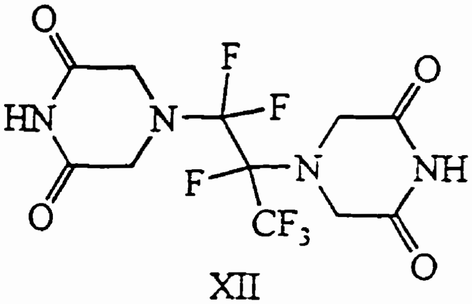
XII

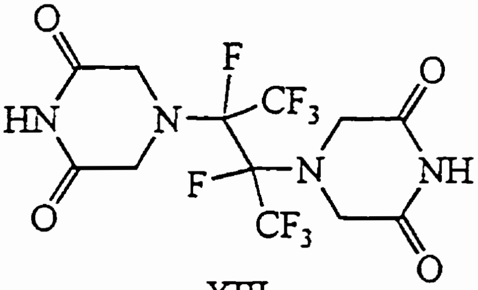
XIII

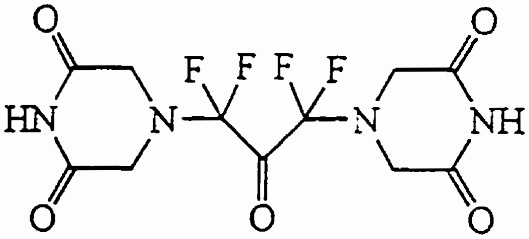
XIV

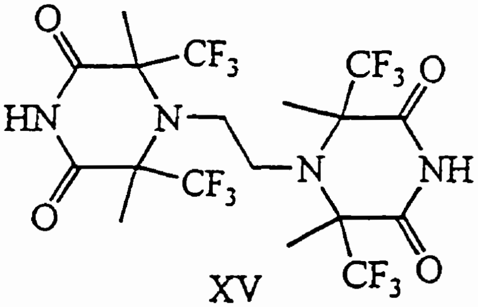
XV

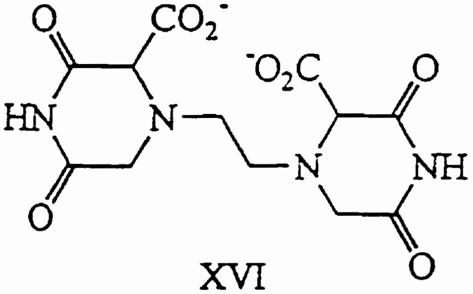
XVI

Figure 5.57 (contd). Structures of the lead compounds.

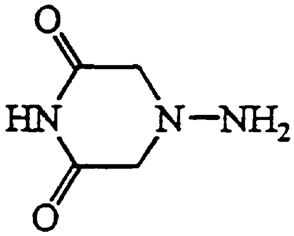

XVII

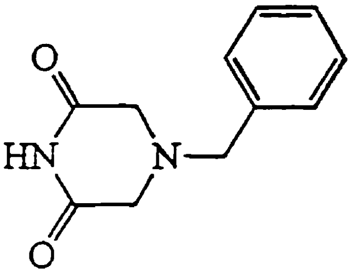

XVIII

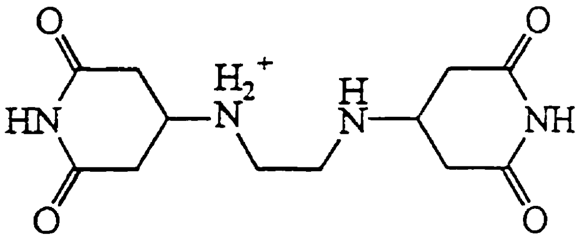

XIX

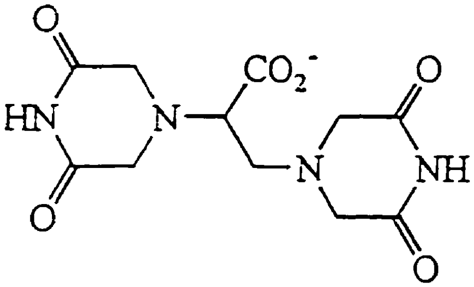

XX

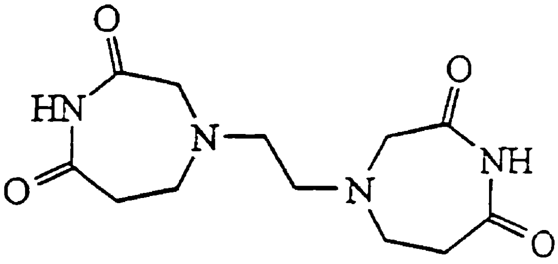

XXI

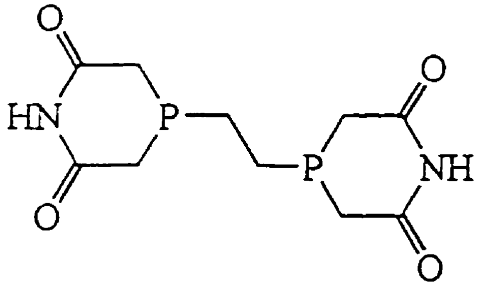

XXII

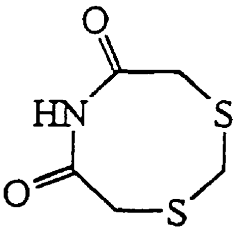

XXIII

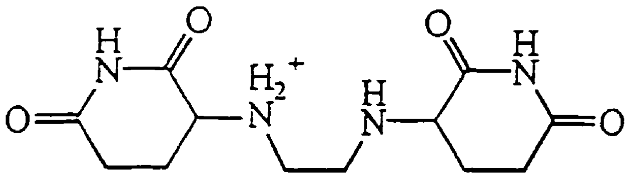

XXIV

Figure 5.57 (contd). Structures of the lead compounds.

geometries of the optimized structures permitted octahedral coordination. Compounds which were not specifically designed for increased hydrolysis rates, but whose hydrolysis products may be expected to be chelators by analogy to their respective tetracarboxylic acids (compounds XVII [203], XVIII [204], XX [205], XXI [206], XXII [207], and XXIV [208]) were included in the series. The hydrolysis product of compound XIX may also be expected to chelate, although with lower affinity than structures which are homologous to EDTA, due to the larger rings formed on metal ion coordination.

5.6.3 Prediction of pK_a values of lead compounds

Predictions of pK_a by Equation 5.12 are of questionable value, due to the limitations of the data set from which it was obtained. Thus, the pK_a values of the series of lead compounds were determined by analogy to imides in the data set, for which the pK_a values were determined in Section 5.2 (Table 5.1). The pK_a values for the compounds I-XXIV were corrected for structural differences by adding ΔpK_a values, calculated from the effects on pK_a values of carboxylic acids for a series of model compounds, corresponding to the individual functional groups (Table 5.10) [209]. Inductive electronic effects are attenuated as a function of the distance from the acidic center. Thus, for each carbon atom or -CH=CH- group between the α carbon and the functional group, the individual ΔpK_a values were multiplied by the "transmission factors" of 0.4 or 0.51, respectively [209]. The transmission factor for a nitrogen atom was assumed to be the same as for the methylene group. For example, the pK_a of compound III (Figure 5.57) was calculated as follows:

$$pK_a(\text{III}) = pK_a(\text{ICRF-154}) + (-1.70)(0.4)^2 + (-1.70)(0.4)^3 \quad (5.13)$$

$$= 10.10 - 0.272 - 0.1088 = 9.72$$

in which the first term is the pK_a of ICRF-154, the structure most similar to compound III. The second term describes the effect of the trifluoromethyl group closest to the imide functional group; because it is two atoms away from the α carbon, the transmission factor is squared. The third term describes the effect of the other trifluoromethyl group; because it is three atoms away from the α carbon, the transmission factor is cubed. The estimated pK_a values of compounds I-XXIV are listed in Table 5.11.

Table 5.10. ΔpK_a values for α-substituents of carboxylic acids.[a]

Functional Group	**Effect on pK_a**
-F	-2.08
$-CF_3$	-1.70
$-NH_2$	-0.45
$-CO_2^-$	+0.61
-phenyl	-0.44
-SR	-1.04[b]
-C(O)-R	-1.10[c]
$-PR_2$	0[d]
$-[NH_2R]^+$	-2.62[e]
$-NR_2$	-0.83[f]

[a] [209]
[b] -SR was assumed to have the same effect as $-SCH_3$.
[c] The carbonyl group was assumed to have the same effect as $-C(O)CH_3$.
[d] $-PR_2$ was assumed to have the same effect as $-NR_2$, *i. e.* since $-PR_2$ was substituted for $-NR_2$ in compound XXII, it was assumed that this change had no effect on pK_a.
[e] $-[NH_2R]^+$ was assumed to have the same effect as the average of the $-[NH(CH_3)_2]^+$ and the $-NH_3^+$ groups.
[f] $-NR_2$ was assumed to have the same effect as $-[NH(CH_3)_2]^+$, minus the difference between the $-NH_3^+$ and $-NH_2$ groups.

Table 5.11. Estimated pK_a values of the lead compounds.

Compound	Base Structure[a]	Predicted pK_a
I	ICRF-154	5.16
II	ICRF-154	8.10
III	ICRF-154	9.72
IV	ICRF-154[b]	9.48
V	ICRF-154	7.66
VI	ICRF-154	9.77
VII	ICRF-154	9.43
VIII	ICRF-154	9.30
IX	ICRF-154	9.17
X	ICRF-154	9.83
XI	ICRF-154	9.33
XII	ICRF-154	9.19
XIII	ICRF-154	9.25
XIV	ICRF-154[b,c]	9.26
XV	ICRF-154	8.10
XVI	ICRF-154	9.41
XVII	LYZ 17B	10.10
XVIII	LYZ 17B	10.22
XIX	ICRF-154[d]	9.79
XX	ICRF-154	10.16
XXI	ICRF-154[d]	10.60
XXII	ICRF-154	10.10
XXIII	Adipimide[e]	9.22
XIV	ICRF-154	7.18

[a] pK_a values for the base structures are listed in Table 5.1.

[b] The increased distance between the two dioxopiperazine rings was assumed to have no effect on the pK_a.

[c] The carbonyl group was assumed to have an effect equal to that of an acetyl group.

[d] The effect of an unprotonated tertiary amine was estimated by subtracting the difference between the effects of protonated and unprotonated amino groups from the effect of a protonated tertiary amine.

[e] The effect of the sulfur atom was assumed to be the same as that of a thiol group.

5.6.4 Prediction of hydrolysis rates of lead compounds

The values of log k_2 were predicted from the series of lead compounds, using Equations 5.8 and 5.9 (Table 5.12). Although the equations describe a relationship which is linear over the examined range of the independent variables, extrapolation beyond this range is not possible. To be sure that the predictions are valid, values of the descriptors for predictions should lie within the range of the data set. Figure 5.58 shows the ranges of both independent variables of Equation 5.8, PTRCR and IHOMON. It can be seen that measurements of IHOMON for two compounds lie outside the range of the data set, compounds XVI and XX, the only carboxylate-containing imides in the series. It is reasonable that the HOMOs of these compounds are centered around the carboxylate groups; thus, this descriptor may not describe the imide functional group at all for these compounds. The values of log k_2 predicted for these compounds were much higher than might be expected, given the weak electron-donating effect expected of the carboxylate group. The predicted log k_2 for these compounds are unlikely to be accurate. Fig 5.59 shows the ranges of both independent variables of Equation 5.9, TCCN and I5+6. The combination of values for the compound XVI is outside the two-dimensional range of values of the data set. The values of TCCN for compounds II, VI-IX, and XXII are also beyond the range of values of the data set. Since the values of log k_2 for compounds VI-IX by Equations 5.8 and 5.9 are quite different, it may be for this series of compounds, which are fluorinated on the main chain (Figure 5.57), that use of Equation 5.9 is not appropriate. Overall, the compounds for which inappropriate extrapolation is possible are those for which irregular predictions were made.

Table 5.12. Predicted values of log k_2 for dexrazoxane and the lead compounds.[a]

	Descriptors used to predict log k_2 with Equations 5.8 & 5.9							
Compound	**HHOMON** (eV)^2	**PTRCR** (Å)	**TCCN** (°)	**15+6**	**log k_2^b Eqn. 5.8**	**log k_2^b Eqn. 5.9**	**$k_{7.4}^c$ Eqn. 5.8 (h^{-1})**	**$k_{7.4}^d$ Eqn 5.9 (h^{-1})**
Dexrazoxane	1.285	1.543[e]	108.903[e]	-0.0603[f]	2.054	2.096	0.0017	0.0019
I	0.131	1.563	104.586	-0.0585	0.869	1.357	6.3×10^{-7}	2.0×10^{-6}
II	0.037	1.526	111.494	-0.0632	2.459	2.559	0.0036	0.0046
III	0.172	1.540	109.749	-0.0838	1.878	2.034	0.0011	0.0016
IV	0.009	1.536	109.627	-0.0795	2.018	2.055	0.0016	0.0017
V	0.182	1.551	105.196	-0.0810	1.402	1.238	0.00021	0.00017
VI	0.858	1.546	111.623	-0.0702	1.764	2.511	0.00087	0.0049
VII	0.495	1.544	111.745	-0.0712	1.774	2.523	0.00088	0.0050
VIII	0.542	1.544	111.419	-0.0695	1.784	2.482	0.0009	0.0045
IX	0.172	1.543	112.015	-0.0680	1.745	2.605	0.00082	0.0060
X	0.613	1.543	108.425	-0.0712	1.842	1.923	0.00010	0.0012
XI	0.229	1.549	108.685	-0.0690	1.499	1.992	0.00047	0.0015

XII	0.166	1.549	108.595	-0.0700	1.485	1.965	0.00045	0.0014
XIII	0.178	1.533	108.689	-0.0690	2.184	1.993	0.0022	0.0015
XIV	0.020	1.529	109.656	-0.0598	2.325	2.262	0.0031	0.0027
XV	0.190	1.538	107.689	-0.0492	1.969	2.014	0.0016	0.0013
XVI	63.120	1.552	110.096	-0.0405	14.857	2.538	$1.1\text{x}10^{10}$	0.0052
XVII	0.390	1.541	109.428	-0.0555	1.882	2.264	0.0011	0.0028
XVIII	1.472	1.540	109.531	-0.0590	2.157	2.247	0.0021	0.0027
XIX	1.107	1.537	107.716	-0.0702	2.210	1.804	0.0024	0.00095
XX	32.850	1.540	109.475	-0.0750	8.886	2.074	12000	0.0018
XXI	1.473	1.539	109.440	-0.0630	2.201	2.190	0.0024	0.0024
XXII	1.696	1.540	111.143	-0.0688	2.205	2.439	0.0024	0.0043
XXIII	3.037	1.546	108.023	-0.0630	2.232	1.933	0.0025	0.0013
XXIV	1.168	1.549	106.470	-0.0738	1.700	1.708	0.00083	0.00029

[a] Compare values of $k_{7.4}$ to the value of 0.00077 min^{-1} for dexrazoxane, calculated from data in Table 5.1 and Equation 5.5.

[b] The units of k_2 are M^{-1}min^{-1}.

[c] k_{obs} calculated at pH 7.4 from predicted k_2 values and Equations 5.8 and 5.5.

[d] k_{obs} calculated at pH 7.4 from predicted k_2 values and Equations 5.9 and 5.5.

[e] The tetrahedral carbon atom was modelled on the ring closest to the methyl group.

[f] The charges of all four carbonyl carbon atoms and both imide nitrogen atoms were averaged.

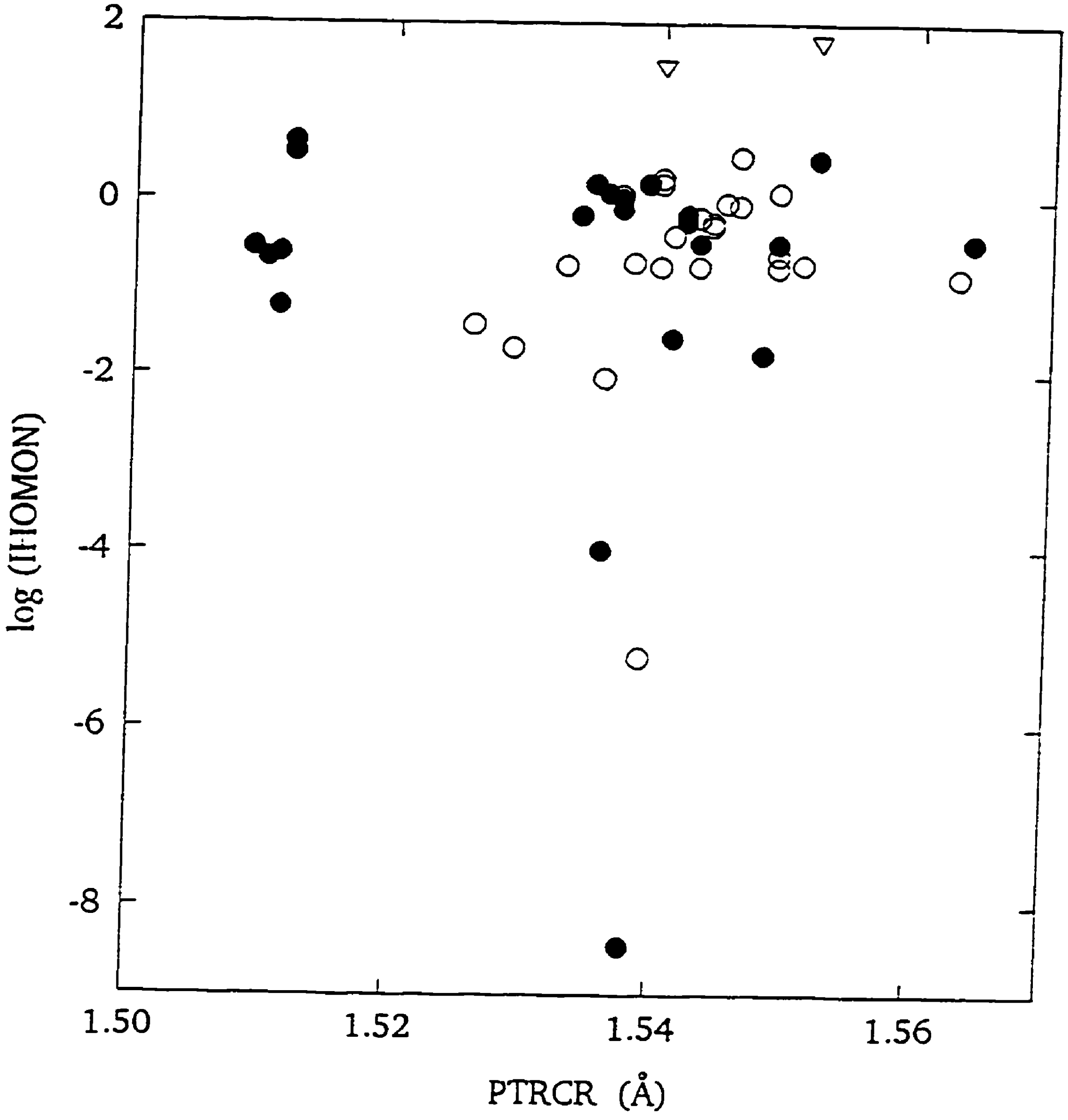

Figure 5.58. Scatter plot of the independent variables of Equation 5.8. Values for these descriptors for the imides used to generate the equation (●) and the lead compounds (○) occupy approximately the same space. IHOMON is shown on a log scale for clarity. Triangular symbols represent two outliers, compounds XVI and XX.

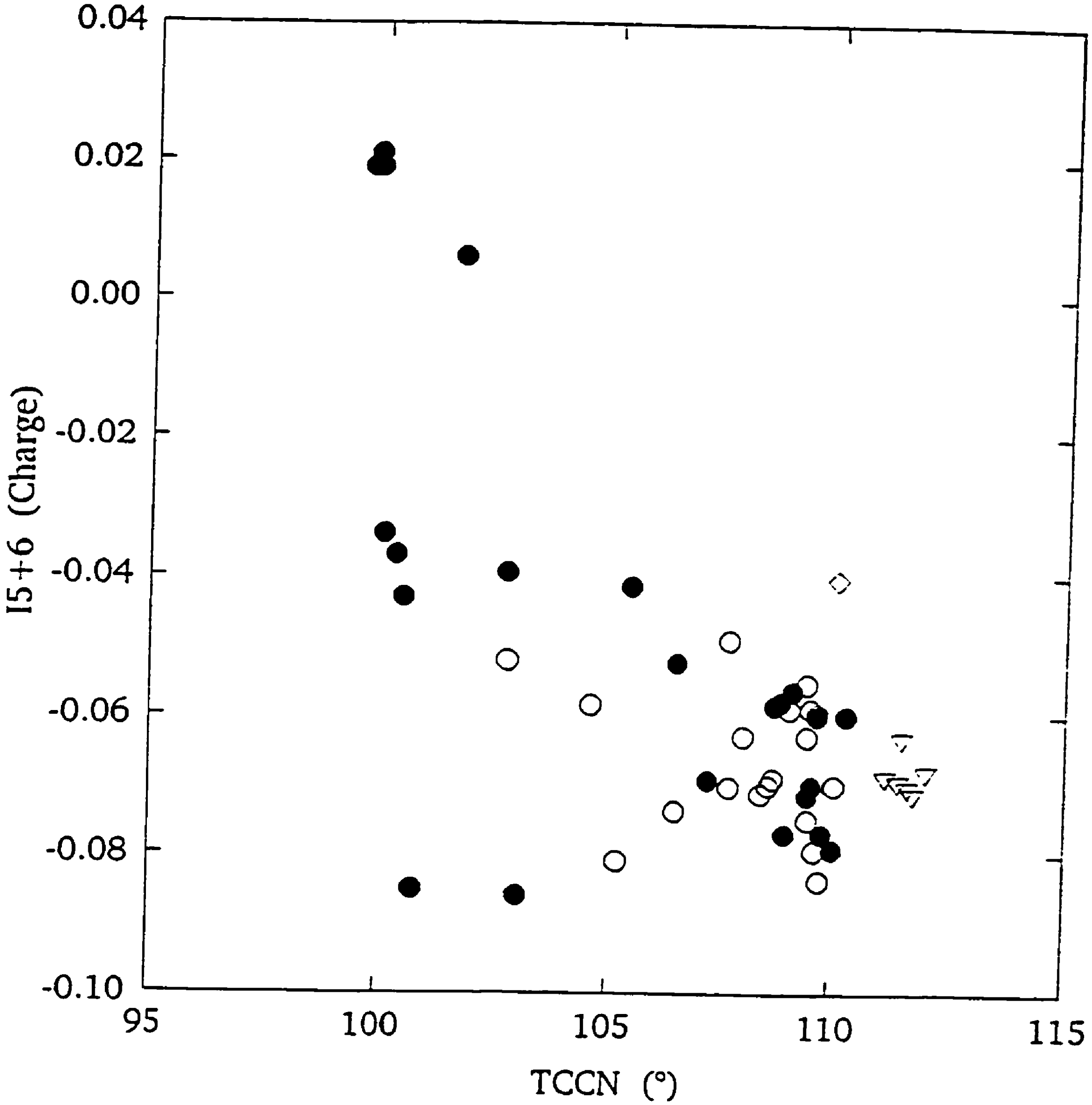

Figure 5.59. Scatter plot of the independent variables of Equation 5.9. Values for these descriptors for the imides used to generate the equation (●) and the lead compounds (○) occupy approximately the same space. Triangular symbols represent six outliers, compounds II, VI-IX, and XXII, and the diamond represents the outlier, XVI.

The predicted values of $k_{7.4}$ (k_{obs} at pH 7.4) for compounds I-XXIV, calculated from Equations 5.8, 5.9, and 5.5, are listed in Table 5.12. Since a two- to five-fold increase in the hydrolysis rate constant over that of dexrazoxane (0.00077 min^{-1} ffrom Table 5.1 and Equation 5.5) is desired, imides with values of $k_{7.4}$ within the range of 0.0015 - 0.0038 h^{-1} (based on the parameters for dexrazoxane listed in Table 5.1) may be considered target compounds. The averages of the values of log $k_{7.4}$ were used to determine whether each compound fell inside or outside the range, with the exception of compounds XVI and XX, for which the predictions from Equation 5.9 only were used, and VI-IX, for which the predictions from Equation 5.8 only were used. Compounds for which log $k_{7.4}$ was predicted to fall within this range included IV, XIII, XIV, and XVII - XXIII. Of these, the hydrolysis products of compounds XIII, XVIII, XX, XXI, and XXII may be expected to be good chelators, and are therefore the compounds in this series most likely to be more effective in preventing doxorubicin-induced cardiac damage through chelation of Fe^{3+}.

5.6.5 Evaluation of linear regression approach to the development of dexrazoxane analogs

The development of analogs using a quantitative structure-activity relationship, such as described in this study, offers the possibility of predicting not only the effect of structural alterations, but also the magnitude of such alterations. Of the ten compounds for which values of $k_{7.4}$ fell within the desired range, it could be predicted on the basis of the inductive effects of the altered functional groups that most of these compounds would hydrolyze somewhat faster than dexrazoxane. What could not be known, however, was whether the magnitude of the changes in the hydrolysis rate constant would be appropriate for their use in preventing doxorubicin cardiotoxicity.

The equations developed in this study describe the hydroxide-ion-catalyzed hydrolysis of imides. It may be that some or all of the lead compounds investigated also undergo water-catalyzed hydrolysis, as does dexrazoxane [120]. Experimental conditions, such as low solubility of the neutrally charged imides in water, high background absorbance of the buffer system in the range of wavelengths at which the neutrally charged imides absorb, and the slow rate of imide hydrolysis at pH values lower than those used in this study, prevented the investigation water-catalyzed hydrolysis. However, it is reasonable to assume that the structural variations which affect the electrophilicity of the imide functional group will have similar effects on hydroxide-ion- and water-catalyzed hydrolysis. Thus, the predicted effects of structure on k_2 may be expected to have similar effects on the water-catalyzed rate constant, k_1.

Although a number of the compounds in the lead series were problematic in that they deviated from the trends described by Equation 5.8 and 5.9, it appears that these equations may be used with care in the prediction of hydrolysis rates on imides, relative to that of dexrazoxane.

Section 6 Conclusions

The putative mechanism of action of dexrazoxane is sequestration of redox-active metal ions by **D**. The ligand competition studies described in Chapter 2 demonstrated that **B** and **C**, the one-ring open hydrolysis intermediates of dexrazoxane, displace Fe^{3+} from its complexes with anthracyclines nearly as quickly and completely as did **D**, the final hydrolysis product. This discovery of potential pharmacological activity of the intermediates means that complete hydrolysis may not be necessary for activation of dexrazoxane, and that active species may be produced much faster than **D** *in vivo*, as they are *in vitro* [128].

One element in understanding the mechanism of action of a drug is its fate in biological systems. The pharmacokinetics of dexrazoxane, including its distribution, hydrolysis, and possible metabolism will remain unknown until human pharmacokinetic studies are done which identify and quantitate dexrazoxane and each of its metabolic products. The present studies, however, provide information with which to estimate the kinetics of dexrazoxane hydrolysis *in vivo* by analogy to its kinetics *in vitro*, which have been characterized [128]. Although, in Chapters 3 and 4, many transition metal ions were shown to strongly promote the hydrolyses of **B** and **C** to **D**, the concentrations of these metal ions in biological systems are too low to significantly affect the rates of these reactions. In contrast, Ca^{2+} and Mg^{2+}, which had much weaker effects, were able to reduce the half-time for the production of **D** at pH 7.4 and 37 °C from 33 h to approximately 25 h, at concentrations similar to those in plasma. These experiments, and previous studies which characterized the catalysis of hydrolysis of dexrazoxane to **B** and **C** by dihydropyrimidine amidohydrolase [124, 125], demonstrate that hydrolysis of dexrazoxane *in vivo* may be significantly faster than *in vitro* [128].

Clinical pharmacokinetic studies have demonstrated that 40-50% of an intravenous dose of dexrazoxane is excreted unchanged [133, 135]. Since approximately half the dose is not activated, a faster-hydrolyzing analog of dexrazoxane would allow the administration of lower doses, all other factors being equal. The development of a quantitative structure-activity relationships described in Chapter 5 may allow more precise estimation of the hydrolysis rates of lead compounds than chemical intuition alone.

Section 6 Appendix: Derivations of equations used in Chapters 3 and 5

6.1 Derivation of Equation 3.4

$$K_{a1} = \frac{[Y][H^+]}{[X]} \qquad (6.1)$$

$$K_{a2} = \frac{[Z][H^+]}{[Y]} \qquad (6.2)$$

The Fe^{3+}-(C)-(H_2O) complex has two dissociable protons in the pH range studied. The equilibria among the three species, Fe^{3+}-(C)-(H_2O), Fe^{3+}-(C^-)-(H_2O), and Fe^{3+}-(C^-)-(OH^-), which are denoted as **X**, **Y**, and **Z**, respectively, are described by the following equations:The mass-balance equation for $[Im]_T$, the total concentration of the complex, is

$$[Im]_T = [X] + [Y] + [Z] \qquad (6.3)$$

Substitution of Equations 6.1 and 6.2 into Equation 6.3, and solving for [Y] yields

$$[Y] = \frac{[Im]_T K_{a1}[H^+]}{[H^+]^2 + K_{a1}[H^+] + K_{a1}K_{a2}} \qquad (6.4)$$

The rate expression for hydrolysis of the Fe^{3+}-C complex, at constant pH, is

$$Rate = k_{obs}[Im]_T \qquad (6.5)$$

From the scheme shown in Figure 3.5, this rate expression, at any pH, is

$$Rate = k_1[OH^-][X] + k_2[OH^-][Y] + k_3[Y] \qquad (6.6)$$

Rearrangement of Equation 6.2 to solve for [Y], and substitution into Equation 6.6 yields, on rearrangement

$$Rate = \frac{k_1K_w[Y]}{K_{a1}} + k_2[OH^-][Y] + k_3[Y] \qquad (6.7)$$

Substitution of Equation 6.4 into Equation 6.7 yields, on rearrangement

$$Rate = \frac{[Im]_T(k_2K_wK_{a1} + [H^+](k_1K_w + k_3K_{a1}))}{[H^+]^2 + K_{a1}[H^+] + K_{a1}K_{a2}} \qquad (6.8)$$

Because Equations 6.5 and 6.8 are identical in form,

$$k_{obs} = \frac{k_2K_wK_{a1} + [H^+](k_1K_w + k_3K_{a1})}{[H^+]^2 + K_{a1}[H^+] + K_{a1}K_{a2}} \qquad (6.9)$$

which is identical to Equation 3.4.

6.2 Derivation of Equations 3.5 and 5.6

Imides have one dissociable proton in the pH range studied. The equilibrium between the neutral and anionic species, which are denoted as **X** and **Y**, respectively, are described by the following equation:

$$K_{a2} = \frac{[Y][H^+]}{[X]} \qquad (6.10)$$

The mass-balance equation for $[Im]_T$, the total concentration of the complex, is

$$[Im]_T = [X] + [Y] \qquad (6.11)$$

Substitution of Equation 6.10 into Equation 6.11, and solving for [Y] yields

$$[Y] = \frac{[Im]_T}{1 + \dfrac{[H^+]}{K_{a2}}} \qquad (6.12)$$

From a scheme in which only species **Y** absorbs,

$$A = \epsilon[Y] \qquad (6.13)$$

in which ϵ is the difference in molar absorptivity between the reactants and the products of the reaction. Substitution of Equation 6.12 into Equation 6.13 yields

$$A = \frac{\epsilon[Im]_T}{1 + \dfrac{[H^+]}{K_{a2}}} \qquad (6.14)$$

which is identical to Equation 3.5. Multiplication of the right-hand side of Equation 6.14 by K_{a2}/K_{a2}, and addition of a constant term yields an equation of the same form as Equation 5.6:

$$A = \frac{\epsilon[Im]_T K_{a2}}{[H^+] + K_{a2}} + C \qquad (6.15)$$

The variables A, $\epsilon[Im]_T$, and K_a in Equation 6.15 correspond to Amp, Amp_{max}, and K_a, respectively, in Equation 5.6.

6.3 Derivation of Equations 3.6 and 5.5

Imides have one dissociable proton in the pH range studied. The equilibrium between the neutral and anionic species, which are denoted as **X** and **Y**, respectively, are described by the following equation:

$$K_{a1} = \frac{[Y][H^+]}{[X]} \qquad (6.16)$$

The mass-balance equation for $[Im]_T$, the total concentration of the complex, is

$$[Im]_T = [X] + [Y] \qquad (6.17)$$

Substitution of Equation 6.16 into Equation 6.17, and solving for [X] yields

$$[X] = \frac{[Im]_T}{\frac{K_{a1}}{[H^+]} + 1} \qquad (6.18)$$

From a scheme in which only species X absorbs,

$$A = \epsilon[X] \qquad (6.19)$$

in which $\Delta\epsilon$ is the difference in molar absorptivity between the reactants and the products of the reaction. Substitution of Equation 6.18 into Equation 6.19 yields

$$A = \frac{\epsilon[Im]_T}{\frac{K_{a1}}{[H^+]} + 1} \qquad (6.20)$$

Addition of a term corresponding to the absorbance when [Y] = $[\mathrm{Im}]_\mathrm{T}$ yields

$$A = \frac{\epsilon[Im]_T}{\frac{K_{a1}}{[H^+]} + 1} + A_1 \qquad (6.21)$$

which is identical to Equation 3.6. With the addition of a hydroxide ion term, the pH dependence of Equation 6.20 is the same as that in Equation 5.5:

$$A = \frac{\epsilon[Im]_T[OH^-]}{\frac{K_{a1}}{[H^+]} + 1} \qquad (6.22)$$

The variables A, $\epsilon[Im]_T$, and K_{a1} in Equation 6.22 correspond to k_{obs}, k_2, and K_a, respectively, in Equation 5.5.

Section 8 References

[1] Di Marco A., Geatani M., Scarpinato B. Adriamycin (NSC-123,127): a new antibiotic with antitumor activity. *Cancer Chemother. Rep.* **53 (part 1)** 33-37. (1969)

[2] Carter S.K. Adriamycin - a review. *J. Natl. Cancer Inst.* **55** 1265-74. (1975)

[3] Gianni L., Corden B.J., Myers C.E. The biochemical basis of anthracycline toxicity and anti-tumor activity. *Rev. Biochem. Toxicol.* **5** 1-82. (1983)

[4] Ferrans V.J. Overview of cardiac pathology in relation to anthracycline toxicity. *Cancer. Treat. Rep.* **62** 955-61. (1978)

[5] Canadian Pharmaceutical Association. Compendium of Pharmaceuticals and Specialties. 32nd ed. : Canadian Pharmaceutical Association. (1997)

[6] Halliwell B., Gutteridge J.M.C. Free Radicals in Biology and Medicine. 2nd ed. Oxford: Clarendon. (1989)

[7] Lown J.W., Sim S.K., Majumdar K.C., Chang R.Y. Strand scission of DNA by bound adriamycin and daunorubicin in the presence of reducing agents. *Biochem. Biophys. Res. Comm.* **76** 705-10. (1977)

[8] Myers C.E., Gianni L., Simone C.B., Klecker R., Greene R. Oxidative destruction of erythrocyte ghost membranes catalyzed by the doxorubicin-iron complex. *Biochemistry* **21** 1707-13. (1982)

[9] Bachur N.R., Gordon S.L., Gee M.V., Kon H. NADPH cytochrome P-450 reductase activation of quinone anticancer agents to free radicals. *Proc. Natl. Acad. Sci. USA* **76** 954-57. (1979)

[10] Pan S.S., Pedersen L., Bachur N.R. Comparative flavoprotein catalysis of anthracycline antibiotic reductive cleavage and oxygen consumption. *Mol. Pharmacol.* **19** 184-86. (1981)

[11] Butler J., Hoey B.M., Swallow A.J. Reactions of the semiquinone free radicals of antitumor agents with oxygen and iron complexes. *FEBS Lett.* **182** 95-98. (1985)

[12] Davies K.J.A., Doroshow J.H. Redox cycling of anthracyclines by cardiac mitrochondria. I. Anthracycline radical formation by NADH dehydrogenase. *J. Biol. Chem.* **261** 3060-67. (1986)

[13] Doroshow J.H., Davies K.J.A. Redox cycling of anthracyclines by cardiac mitochondria. II. Formation of superoxide anion, hydrogen peroxide and hydroxyl radical. *J. Biol. Chem.* **261** 3068-74. (1986)

[14] Gianni L., Zweier J.L., Levy A., Myers C.E. Characterization of the cycle of iron-mediated electron transfer from adriamycin to molecular oxygen. *J. Biol. Chem.* **260** 6820-26. (1985)

[15] Gutteridge J.M.C. Lipid peroxidation and possible hydroxyl radical formation stimulated by the self-reduction of a doxorubicin-iron(III) complex. *Biochem. Pharmacol.* **33** 1725-28. (1984)

[16] Beraldo H., Garnier-Suillerot A., Tosi L., Lavelle F. Iron(III)-adriamycin and iron(III)-daunorubicin complexes: Physicochmemical characteristics, interaction with DNA, and antitumour activity. *Biochemistry* **24** 284-89. (1985)

[17] Hasinoff B.B. Oxyradical production results from the Fe^{3+}-doxorubicin complex undergoing self-reduction by its α-ketol group. *Biochem. Cell. Biol.* **68** 1331-36. (1990)

[18] Malisza K.L., Hasinoff B.B. Production of hydroxyl radical by iron(III)-anthraquinone complexes through self-reduction and through reductive activation by the xanthine oxidase/hypoxanthine system. *Arch. Biochem. Biophys.* **321** 51-60. (1995)

[19] May P.M., Williams G.K., Williams D.R. Speciation studies of adriamycin, quelamycin, and their metal ion complexes. *Inorg. Chim. Acta* **46** 221-28. (1980)

[20] Eliot H., Gianni L., Myers C.E. Oxidative destruction of DNA by the adriamycin-iron complex. *Biochemistry* **23** 928-36. (1984)

[21] Beraldo H., Garnier-Suillerot A., Tosi L. Copper(II)-adriamycin complexes. A circular dichroism and resonance raman study. *Inorg. Chem.* **22** 4117-24. (1983)

[22] Herman E.H., Ferrans V.J. Reduction of chronic doxorubicin cardiotoxicity in dogs by pretreatment with (±)-1,2-bis(3,5-dioxopiperazinyl-1-yl)propane (ICRF-187). *Cancer Res.* **41** 3436-40. (1981)

[23] Herman E.H., Ferrans V.J. Timing of treatment with ICRF-187 and its effect on chronic doxorubicin cardiotoxicity. *Cancer Chemother. Pharmacol.* **32** 445-49. (1993)

[24] Herman E.H., Ferrans V.J., Jordan W., Ardalan B. Reduction of chronic daunorubicin cardiotoxicity by ICRF-187 in rabbits. *Res. Commun. Chem. Pathol. Pharmacol.* **31** 85-97. (1981)

[25] Herman E.H., Ferrans V.J. Influence of vitamin E and ICRF-187 on chronic doxorubicin cardiotoxicity in miniature swine. *Lab. Invest.* **49** 69-77. (1983)

[26] Herman E.H., El-Hage A., Ferrans V.J. Protective effect of ICRF-187 on doxorubicin-induced cardiac and renal toxicity in spontaneously hypertensive (SHR) and normotensive (WKY) rats. *Toxicol. Appl. Pharmacol.* **92** 42-53. (1988)

[27] Villani F., Galimberti M., Monti E., Cova D., Lanza E., Rozza-Dionigi A., Favalli L., Poggi P. Effect of ICRF-187 pretreatment against doxorubicin-induced delayed cardiotoxicity in the rat. *Toxicol. Appl. Pharmacol.* **102** 292-99. (1990)

[28] Demant E.J.F. Transfer of ferritin-bound iron to adriamycin. *FEBS Lett.* **176** 97-100. (1984)

[29] Fukuda Y., Herman E.H., Ferrans V.J. Effect of ICRF-187 on the pulmonary damage induced by hyperoxia in the rat. *Toxicol.* **74** 185-202. (1992)

[30] Flandina C., Sanguedolce R., Rausa L., D'Alessandro N. Ameliorative effects of ICRF-187 [(+)-1,2-bis(3,5-dioxopiperazinyl-1-yl)propane] on the cardiotoxicity induced by doxorubicin or by isoproterenol in the mouse. *Res. Commun. Chem. Pathol. Pharmacol.* **70** 259-72. (1990)

[31] Thomas C.E., Morehouse L.A., Aust S.D. Ferritin and superoxide-dependent lipid peroxidation. *J. Biol. Chem.* **260** 3275-80. (1985)

[32] Duarte-Karim M., Ruysschaert J.M., Hildebrand J. Affinity of adriamycin to phospholipids a possible explanation for cardiac mitochondrial lesions. *Biochem. Biophys. Res. Comm.* **71** 658-63. (1976)

[33] Demant E.J.F. Binding of adriamycin-Fe^{3+} to membrane phospholipids. *Eur. J. Biochem.* **142** 571-75. (1984)

[34] Comte J., Maisterrena B., Gautheron D.C. Lipid composition and protein profiles of outer and inner membranes from pig heart mitochondria. *Biochim. Biophys. Acta* **419** 271-84. (1976)

[35] Doroshow J.H., Tallent C., Schechter J.E. Ultrastructural features of adriamycin-induced skeletal and cardiac muscle toxicity. *Am. J. Pathol.* **118** 288-97. (1985)

[36] Goormaghtigh E., Chatelain P., Caspers J., Ruysschaert J.M. Evidence of a specific complex between adriamycin and negatively charged phospholipids. *Biochim. Biophys. Acta* **597** 1-14. (1980)

[37] Goormaghtigh E., Chatelain P., Caspers J., Ruysschaert J.M. Evidence of a complex between adriamycin derivatives and cardiolipin: possible role in cardiotoxicity. *Biochem. Pharmacol.* **29** 3003-10. (1980)

[38] Tritton T.R., Yee G. The anticancer agent adriamycin can be actively toxic without entering cells. *Science* **217** 248-50. (1982)

[39] Bredehorst R., Panneerselvam M., Vogel C.W. Doxorubicin enhances complement susceptibility of human melanoma cells by extracellular oxygen radical formation. *J. Biol. Chem.* **87** 2034-41. (1987)

[40] Noel G., Peterson C., Trouet A., Tulkens P. Uptake and subcellular localization of daunorubicin and adriamycin in cultured fibroblasts. *Eur. J. Cancer* **14** 363-68. (1978)

[41] Mimnaugh E.G., Gram T.E., Trush M.A. Stimulation of mouse heart and liver microsomal lipid peroxidation by anthracycline anticancer drugs: characterization and effects of reactive oxygen scavengers. *J. Pharmacol. Exp. Ther.* **226** 806-16. (1983)

[42] Sugioka K., Nakano H., Noguchi T., Tsuchiya J., Nakano M. Decomposition of unsaturated phospholipid by iron-ADP-adriamycin co-ordination complex. *Biochem. Biophys. Res. Comm.* **100** 1251-58. (1981)

[43] Demant E.J.F., Jensen P.K. Destruction of phospholipids and respiratory-chain activity in pig-heart submitochondrial particles induced by an adriamycin-iron complex. *Eur. J. Biochem.* **132** 551-56. (1983)

[44] Praet M., Pollakis G., Goormaghtigh E., Ruysschaert J.M. Damages of the mitochondrial membrane in adriamycin treated mice. *Cancer Letters* **25** 89-96. (1984)

[45] Hasinoff B.B. The iron(III)-adriamycin induced inactivation of the respiratory chain enzyme NADH cytochrome *c* reductase. *Biochem. J.* **265** 865-70. (1990)

[46] Fry M., Green D.E. Cardiolipin requirement by cytochrome oxidase and the catalytic role of phospholipid. *Biochem. Biophys. Res. Comm.* **93** 1238-46. (1980)

[47] Hasinoff B.B., Davey J.P. The iron(III)-adriamycin complex inhibits cytochrome *c* oxidase before its inactivation. *Biochem. J.* **250** 827-34. (1988)

[48] Demant E.J.F. NADH oxidation in submitochondrial particles protects respiratory chain activity against damage by adriamycin-Fe^{3+}. *Eur. J. Biochem.* **137** 113-18. (1983)

[49] Phillips D.R., Roberts G.C.K. Proton nuclear magnetic resonance study of the self-complementary hexanucleotide d(pTpA)3 and its interaction with daunomycin. *Biochemistry* **19** 4795-801. (1980)

[50] Calendi E., Di Marco A., Reggiani M., Scarpinato B., Valentini L. On physico-chemical interactions between daunomycin and nucleic acids. *Biochim. Biophys. Acta* **103** 25-49. (1965)

[51] Marafino Jr. B.J., Giri S.N., Siegel D.M. Pharmacokinetics, covalent binding and subcellular distribution of [^{3}H]doxorubicin after intravenous administration in the mouse. *J. Pharmacol. Exp. Ther.* **216** 55-61. (1981)

[52] Terasaki T., Iga T., Sugiyama Y., Hanano M. Pharmacokinetic study on the mechanism of tissue distribution of doxorubicin: interorgan and interspecies variation of tissue-to-plasma partition coefficients in rats, rabbits, and Guinea pigs. *J. Pharm. Sci.* **73** 1359-63. (1984)

[53] Page E., McCallister L.P. Quantitative electron microscopic description of heart muscle cells application to normal, hypertrophied and thyroxin-stimulated hearts. *Am. J. Cardiol.* **31** 172-81. (1973)

[54] Halliwell B., Gutteridge J.M.C. Free Radicals in Biology and Medicine. 2nd ed. Oxford: Clarendon, p. 87. (1989)

[55] Schlabach M.R., Bates G.W. The synergistic binding of anions and Fe^{3-} by transferrin. *J. Biol. Chem.* **250** 2182-88. (1975)

[56] Alderton P., Gross J., Green M.D. Role of (±)-1,2-bis(3,5-dioxopiperazinyl-1-yl)propane (ICRF-187) in modulating free radical scavenging enzymes in doxorubicin-induced cardiomyopathy. *Cancer Res.* **50** 5136-42. (1990)

[57] Thayer W.S. Adriamycin stimulated superoxide formation in submitochondrial particles. *Chem. Biol. Interact.* **19** 265-78. (1977)

[58] Doroshow J.H., Locker G.Y., Myers C.E. Enzymatic defenses of the mouse heart against reactive oxygen metabolites. *J. Clin. Invest.* **65** 128-35. (1980)

[59] Kanter M.M., Hamlin R.L., Unverferth D.V., Davis H.W., Merola A.J. Effect of exercise training on antioxidant enzymes and cardiotoxicity of doxorubicin. *J. Appl. Physiol.* **59** 1298-303. (1985)

[60] Chen X., Xue A., Morris V.C., Ferrans V.J., Herman E.H., El-Hage A., Levander O.A. Effect of selenium deficiency on the chronic toxicity of adriamycin in rats. *J. Nutr.* **116** 2453-65. (1986)

[61] Creighton A.M., inventor. Piperazine derivatives. U. K. Patent 1,234,935. (1971)

[62] Creighton A.M., Hellmann K., Whitecross S. Antitumour activity in a series of bisdiketopiperazines. *Nature* **222** 384-85. (1969)

[63] Zil'berman E.N. Products of reaction of adipic acid with ammonia. *Zhur. Obsh. Khim.* **25** 2127-32. (1955)

[64] Crockett G.C., Swanson B.J., Anderson D.R., Koch T.H. A preferred method for imide preparation. *Synth. Comm.* **11** 447-54. (1981)

[65] Klug H., Kuclinka K. German Patent 1,222,058 (1966). *Chem. Abst.* **66** 2228. (1967)

[66] Roeder G. Zur Kondensation von Harnstoffen mit Säureestern. *Chem. Ber.* **46** 2560-64. (1913)

[67] Paris G., Gaudry R., Berlinguet L. Nouvelles syntheses de l'acide glutarique, de la glutarimide et de l'acide glutamique. *Bull. Soc. Chim. Fr.* **33** 1724-28. (1955)

[68] Salmon-Legangneur F. Recherches dans la serie des diacides, α, α-disubstitués et de leurs derivés. IV.- Synthèse, proprietés physiques et chimiques des diacides, α, α-diphenyles. *Bull. Soc. Chim. Fr.* 411-18. (1956)

[69] Woodman R.J. Enhancement of antitumor effectiveness of ICRF-159 (NSC-129943) against early L1210 leukemia by combination with *cis*-diamminedichloroplatinum (NSC-119875) or daunomycin (NSC-82151). *Cancer Chemother. Rep.* **4** 45-52. (1974)

[70] Bellet R.E., Engstrom P.F., Catalano R.B., Creech R.H., Mastrangelo M.J. Phase II study of ICRF-159 in patients with metastatic colorectal carcinoma previously exposed to systemic chemotherapy. *Cancer. Treat. Rep.* **60** 1395-97. (1976)

[71] Gilbert J.M., Hellmann K., Evans M., Cassell P.G., Taylor R.H., Stoodley B., Ellis H., Wastell C. Randomized trial of oral adjuvant razoxane (ICRF-159) in resectable colorectal cancer: five-year follow-up. *Br. J. Surg.* **73** 446-50. (1986)

[72] O'Connell M.J., Begg C.B., Silverstein M.N., Glick J.H., Oken M.M. Randomized clinical trial comparing two dose regimens of ICRF-159 in refractory malignant lymphomas. *Cancer. Treat. Rep.* **64** 1355-59. (1980)

[73] Repta A.J., Baltezor M.J., Bansal P.C. Utilization of an enantiomer as a solution to a pharmaceutical problem: application to solubilization of 1,2-di(4-piperazine-2,6-dione)propane. *J. Pharm. Sci.* **65** 238-42. (1976)

[74] Creaven P.J., Allen L.M., Alford D.A. The bioavailability in man of ICRF-159 a new oral antineoplastic agent. *J. Pharm. Pharmacol.* **27** 914-18. (1975)

[75] Liesmann J., Belt R., Haas C., Hoogstraten B. Phase I evaluation of ICRF-187 (NSC-169780) in patients with advanced malignancy. *Cancer* **47** 1959-62. (1981)

[76] Hellmann K., Newton K.A., Whitmore D.N., Hanham I.W.F., Bond J.V. Preliminary clinical assessment of I.C.R.F. 159 in acute leukemia and lymphosarcoma. *Br. J. Med.* **1** 822-24. (1969)

[77] Wheeler R.H., Clauw D.J., Natale R.B., Ruddon R.W. The cytokinetic and cytotoxic effects of ICRF-159 and ICRF-187 *in vitro* and in human bone marrow *in vivo*. *Invest. New Drugs* **1** 283-95. (1983)

[78] Creighton A.M., Birnie G.D. The effect of bisdioxopiperazines on the synthesis of deoxyribonucleic acid, ribonucleic acid and protein in growing mouse-embryo fibroblasts. *Biochem. J.* **114** 58P. (1969)

[79] Hellmann K., Field E.O. Effect of ICRF 159 on the mammalian cell cycle: Significance for its use in cancer chemotherapy. *J. Natl. Cancer Inst.* **44** 539-43. (1970)

[80] Taylor I.W., Bleehen N.M. Razoxane-induced polyploidy. *Br. J. Cancer* **38** 143-47. (1978)

[81] Traganos F., Darzynkiewicz Z., Melamed M.R. Effects of the l isomer (+)-1,2-bis(3,5-dioxopiperazine-1-yl)propane on cell survival and cell cycle progression of cultured mammalian cells. *Cancer Res.* **41** 4566-76. (1981)

[82] Gorbsky G.J. Cell cycle progression and chromosome segregation in mammalian cells cultured in the presence of the topoisomerase II inhibitors ICRF-187 [(+)-1,2-bis(3,5-

dioxopiperazinyl-1-yl)propane; ADR-529] and ICRF-159 (razoxane). *Cancer Res.* **54** 1042-48. (1994)

[83] Tanabe K., Ikegami Y., Ishida R., Andoh T. Inhibition of topoisomerase II by antitumor agents bis(2,6-dioxopiperazine) derivatives. *Cancer Res.* **51** 4903-08. (1991)

[84] Ishida R., Miki T., Narita T., Yui R., Sato M., Utsumi K.R., Tanabe K., Andoh T. Inhibition of intracellular topoisomerase II by antitumor bis(2,6-dioxopiperazine) derivatives: mode of cell growth inhibition distinct from that of cleavable complex-forming type inhibitors. *Cancer Res.* **51** 4909-16. (1991)

[85] Hasinoff B.B., Kuschak T.I., Yalowich J.C., Creighton A.M. A QSAR study comparing the cytotoxicity and DNA topoisomerase II inhibitory effects of bisdioxopiperazine analogs of ICRF-187 (dexrazoxane). *Biochem. Pharmacol.* **50** 953-58. (1995)

[86] Ishida R., Sato M., Narita T., Utsumi K.R., Nishimoto T., Morita T., Nagata H., Andoh T. Inhibition of DNA topoisomerase II by ICRF-193 induces polyploidization by uncoupling chromosome dynamics from other cell cycle events. *J. Cell Biol.* **126** 1341-51. (1994)

[87] Perkins W.E., Schroeder R.L., Carrano R.A., Imondi A.R. Effect of ICRF-187 on doxorubicin-induced myocardial effects in the mouse and guinea pig. *Br. J. Cancer* **46** 662-67. (1982)

[88] Speyer J.L., Green M.D., Zeleniuch-Jacquotte A., Wernz J.C., Rey M., Sanger J., Kramer E., Ferrans V., Hochster H., Meyers M., Blum R.H., Feit F., Attubato M., Burrows W., Muggia F.M. ICRF-187 permits longer treatment with doxorubicin in women with breast cancer. *J. Clin. Oncol.* **10** 117-27. (1992)

[89] Wexler L.H., Andrich M.P., Venzon D., Berg S.L., Weaver-McClure L., Chen C.C., Dilsizian V., Avila N., Jarosinski P., Balis F.M., Poplack D.G., Horowitz M.E. Randomized trial of the cardioprotective agent ICRF-187 in pediatric sarcoma patients treated with doxorubicin. *J. Clin. Oncol.* **14** 362-72. (1996)

[90] Herman E.H., El-Hage A.N., Ferrans V.J., Witiak D.T. Reduction by ICRF-187 of acute daunorubicin toxicity in syrian golden hamsters. *Res. Commun. Chem. Pathol. Pharmacol.* **40** 217-31. (1983)

[91] Myers C., McGuire W., Liss R., Ifrim I., Grotzinger K., Young R. Adriamycin: the role of lipid peroxidation in cardiac toxicity and tumor response. *Science* **197** 165-67. (1977)

[92] Mimnaugh E.G., Siddik Z.H., Drew R., Sikic B.I., Gram T.E. The effects of α-tocopherol on the toxicity, disposition, and metabolism of adriamycin in mice. *Toxicol. Appl. Pharmacol.* **49** 119-26. (1979)

[93] Herman E., Ardalan B., Bier C., Waravdekar V., Krop S. Reduction of daunorubicin lethality and myocardial cellular alterations by pretreatment with ICRF-187 in Syrian golden hamsters. *Cancer. Treat. Rep.* **63** 89-92. (1979)

[94] Herman E.H., Ferrans V.J. Pretreatment with ICRF-187 provides long lasting protection against chronic daunorubicin cardiotoxicity in rabbits. *Cancer Chemother. Pharmacol.* **16** 102-06. (1986)

[95] Yeung T.K., Jaenke R.S., Wilding D., Creighton A.M., Hopewell J.W. The protective activity of ICRF-187 against doxorubicin-induced cardiotoxicity in the rat. *Cancer Chemother. Pharmacol.* **30** 58-64. (1992)

[96] Swain S.M., Whaley F.S., Gerber M.C., Ewer M.S., Bianchine J.R., Gams R.A. Delayed administration of dexrazoxane provides cardioprotection for patients with advanced breast cancer treated with doxorubicin-containing therapy. *J. Clin. Oncol.* **15** 1333-40. (1997)

[97] Lenaz L., Page J.A. Cardiotoxicity of adriamycin and related anthracyclines. *Cancer Treat. Rev.* **3** 111-20. (1976)

[98] Steinherz L.J., Steinherz P.G., Tan C.T.C., Heller G., Murphy M.L. Cardiac toxicity 4 to 20 years after completing anthracycline therapy. *JAMA* **266** 1672-77. (1991)

[99] Hasinoff B.B., Kala S.V. The removal of metal ions from transferrin, ferritin and ceruloplasmin by the cardioprotective agent ICRF-187 ((+)-1,2-bis(3,5-dioxopiperazinyl-1-yl)propane) and its hydrolysis product ADR-925. *Agents Actions* **39** 72-81. (1993)

[100] Hochster H., Liebes L., Wadler S., Oratz R., Wernz J.C., Meyers M., Green M., Blum R.H., Speyer J.L. Pharmacokinetics of the cardioprotector ADR-529 (ICRF-187) in escalating doses combined with fixed-dose doxorubicin. *J. Natl. Cancer Inst.* **84** 1725-30. (1992)

[101] Hasinoff B.B. The interaction of the cardioprotective agent ICRF-187 ((+)-1,2-bis(3,5-dioxopiperazinyl-1-yl)propane), its hydrolysis product ICRF-198, and other chelating agents with the Fe(III) and Cu(II) complexes of adriamycin. *Agents Actions* **26** 378-85. (1989)

[102] Wang G., Finch M.D., Trevan D., Hellmann K. Reduction of daunomycin toxicity by razoxane. *Br. J. Cancer* **43** 871-77. (1981)

[103] Baldwin J.R., Uhrig B.A., Imondi A.R., Narang P.K. Disposition of cardioprotective agent ADR-529 in rats. *Pharm. Res.* **5 (Suppl. 10)** S-186. (1988)

[104] Narang P.K., Baldwin J.R., Benjamin E.J., Bianchine J.R. ADR-529: disposition of a cardioprotective agent in mice. *Pharm. Res.* **5 (Suppl. 10)** S-189. (1988)

[105] Baldwin J.R., Lewis R.C., Phillips B.A., Overmyer S.K., Hatfield N.Z., Narang P.K. Dose-independent pharmacokinetics of the cardioprotective agent dexrazoxane in dogs. *Biopharm. Drug Dispos.* **17** 541-50. (1996)

[106] Dawson K.M. Studies on the stability and cellular distribution of dioxopiperazines in cultured BHK-21S cells. *Biochem. Pharmacol.* **24** 2249-53. (1975)

[107] Thomas C., Vile G.F., Winterbourn C.C. The hydrolysis product of ICRF-187 promotes iron-catalysed hydroxyl radical production via the Fenton reaction. *Biochem. Pharmacol.* **45** 1967-72. (1993)

[108] Decorti G., Bartoli Klugman F., Mallardi F., Klugman S., Benussi B., Grill V., Baldini L. Effects of ICRF 159 on adriamycin-induced cardiomyopathy in rats. *Cancer Letters* **19** 77-83. (1983)

[109] Vile G.F., Winterbourn C.C. *dl*-N,N'-dicarboxamidomethyl-N,N'-dicarboxymethyl-1,2-diaminopropane (ICRF-198) and *d*-1,2-bis(3,5-dioxopiperazine-1-yl)propane (ICRF-187) inhibition of Fe^{3+} reduction, lipid peroxidation, and CaATPase inactivation in heart microsomes exposed to adriamycin. *Cancer Res.* **50** 2307-10. (1990)

[110] Gianni L., Vigano L., Lanzi C., Niggeler M., Malatesta V. Role of daunosamine and hydroxyacetyl side chain in reaction with iron and lipid peroxidation by anthracyclines. *J. Natl. Cancer Inst.* **80** 1104-11. (1988)

[111] Rajagopalan S., Politi P.M., Sinha B.K., Myers C.E. Adriamycin-induced free radical formation in the perfused rat heart: implications for cardiotoxicity. *Cancer Res.* **48** 4766-69. (1988)

[112] Voest E.E., van Acker S.A.B.E., van der Vijgh W.J.F., van Asbeck B.S., Bast A. Comparison of different iron chelators as protective agents against acute doxorubicin-induced cardiotoxicity. *J. Mol. Cell Cardiol.* **26** 1179-85. (1994)

[113] Herman E.H., Ferrans V.J., Myers C.E., Van Vleet J.F. Comparison of the effectiveness of (±)-1,2-Bis(3,5-dioxopiperazinyl-1-yl)propane (ICRF-187) and *N*-acetylcysteine in preventing chronic doxorubicin cardiotoxicity in beagles. *Cancer Res.* **45** 276-81. (1985)

[114] Herman E.H., Ferrans V.J. Amelioration of chronic anthracycline cardiotoxicity by ICRF-187 and other compounds. *Cancer Treat. Rev.* **14** 225-29. (1987)

[115] Huang Z.-X., May P.M., Quinlan K.M., Williams D.R., Creighton A.M. Metal binding by pharmaceuticals. Part 2. Interactions of Ca(II), Cu(II), Fe(II), Mg(II), Mn(II) and Zn(II) with the intracellular hydrolysis products of the antitumor agent ICRF-159 and its inactive homologue ICRF-192. *Agents Actions* **12** 536-42. (1982)

[116] Hasinoff B.B. The iron(III) and copper(II) complexes of adriamycin promote the hydrolysis of the cardioprotective agent ICRF-187 ((+)-1,2-bis(3,5-dioxopiperazinyl-1-yl)propane). *Agents Actions* **29** 374-81. (1990)

[117] Hasinoff B.B. The hydrolysis-activation of the doxorubicin cardioprotective agent ICRF-187 ((+)-1,2-bis(3,5-dioxopiperazinyl-1-yl)propane). *Drug Metab. Dispos.* **18** 344-49. (1990)

[118] Bender M.L. Oxygen exchange as evidence for the existence of an intermediate in ester hydrolysis. *J. Am. Chem. Soc.* **73** 1626-29. (1951)

[119] Khan M.N., Khan A.A. Kinetics and mechanism of base-catalyzed hydrolysis of phthalimide. *J. Chem. Soc. Perkin II* 796-98. (1979)

[120] Sisco J.M. The physicochemical, analytical and pharmacokinetic properties of the antineoplastic agent, ICRF-187 [Dissertation]. University of Kansas, Lawrence, Kansas, 254 p. (1989)

[121] Barradas R.G., Fletcher S., Porter J.D. The hydrolysis of maleimide in alkaline solution. *Bull. Soc. Chim. Fr.* **54** 1400-04. (1976)

[122] Euler H.V., Olander A. Uber die hydrolytische Spaltung des Succinimids. *Z. Physikal. Chem.* **137** 393-98. (1928)

[123] Yakatan G.J., Fan T. Kinetics of hydrolysis of succinimides. *Drug Dev. Ind. Pharm.* **3** 315-38. (1977)

[124] Hasinoff B.B. Enzymatic ring-opening reactions of the chiral cardioprotective agent (+)(*S*)-ICRF-187 and its (-)(*R*)-enantiomer ICRF-186 by dihydropyrimidine amidohydrolase. *Drug Metab. Dispos.* **21** 883-88. (1993)

[125] Hasinoff B.B., Reinders F.X., Clark V. The enzymatic hydrolysis-activation of the adriamycin cardioprotective agent (+)-1,2-bis(3,5-dioxopiperazinyl-1-yl)propane. *Drug Metab. Dispos.* **19** 74-80. (1991)

[126] Mhatre R.M., Tew K.D., van Hennik M.B., Waravdekar V.S., Schein P.S. Absorption, distribution and pharmacokinetics of ICRF-187 in dogs. *Proc. Am. Assoc. Cancer Res.* **24** 290. (1983)

[127] Herman E.H., El-Hage A.N., Creighton A.M., Witiak D.T., Ferrans V.J. Comparison of the protective effect of ICRF-187 and structurally related analogues against acute daunorubicin toxicity in syrian golden hamsters. *Res. Commun. Chem. Pathol. Pharmacol.* **48** 39-55. (1985)

[128] Hasinoff B.B. An HPLC and spectrophotometric study of the hydrolysis of ICRF-187 (dexrazoxane, (+)-1,2-bis(3,5-dioxopiperazinyl-1-yl)propane) and its one-ring opened intermediates. *Int. J. Pharm.* **107** 67-76. (1994)

[129] Aoyama R. G. The metabolism of razoxane and dexrazoxane in the Sprague-Dawley rat [Dissertation]. University of Manitoba, Winnipeg, Manitoba, 183 p. (1998)

[130] McPherson E., Archila R., Schein P.S., Tew K.D., Mhatre R.M. Preclinical pharmacokinetics, disposition and metabolism of ICRF-187. *Proc. Am. Assoc. Cancer Res.* **26** 362. (1984)

[131] Field E.O., Mauro F., Hellmann K. Blood clearance of ICRF 159 (NSC-129943). *Cancer Chemother. Rep.* **55** 527-30. (1971)

[132] Sadée W., Staroscik J., Finn C., Cohen J. Determination of (±)-1,2-bis(3,5-dioxopiperazinyl)propane plasma levels in rats, rabbits, and humans by glc and mass fragmentography. *J. Pharm. Sci.* **64** 998-1001. (1975)

[133] Von Hoff D.D., Soares N., Gormley P., Poplack D.G. Pharmacokinetics of ICRF-187 in the cerebrospinal fluid of subhuman primates. *Cancer. Treat. Rep.* **64** 734-36. (1980)

[134] Holcenberg J.S., Tutsch K.D., Earhart R.H., Ungerleider R.S., Kamen B.A., Pratt C.B., Gribble T.J., Glaubiger D.L. Phase I study of ICRF-187 in pediatric cancer patients and comparison of its pharmacokinetics in children and adults. *Cancer. Treat. Rep.* **70** 703-09. (1986)

[135] Jakobsen P., Sorensen B., Bastholt L., Mirza M.R., Gjedde S.B., Mouridsen H.T., Rose C. The pharmacokinetics of high-dose epirubicin and of the cardioprotector

ADR 529 given together with cyclophosphamide, 5-fluorouracil, and tamoxifen in metastatic breast-cancer patients. *Cancer Chemother. Pharmacol.* **35** 45-52. (1994)

[136] Earhart R.H., Tutsch K.D., Koeller J.M., Rodriguez R., Robins H.I., Vogel C.L., Davis H.L., Tormey D.C. Pharmacokinetics of (+)-1,2-di(3,5-dioxopiperazin-1-yl)propane intravenous infusions in adult cancer patients. *Cancer Res.* **42** 5255-61. (1982)

[137] Vogel C.L., Gorowski E., Davila E., Eisenberger M., Kosinski J., Agarwal R.P., Savaraj N. Phase I clinical trial and pharmacokinetics of weekly ICRF-187 (NSC 169780) infusion in patients with solid tumors. *Invest. New Drugs* **5** 187-98. (1987)

[138] Rosing H., van Gijn R., ten Bokkel Huinink W.W., Beijnen J.H. High performance liquid chromatographic analysis of the cardioprotective agent dexrazoxane in human plasma and urine. *J. Liq. Chrom. & Rel. Technol.* **20** 583-601. (1997)

[139] Mhatre R.M., Rahman A., Raschid S., Schein P.S. Pharmacokinetic and tissue distribution of ICRF-187 in mice. *Proc. Am. Assoc. Cancer Res.* **23** 212. (1982)

[140] Legha S.S., Wang Y.M., Mackay B., Ewer M., Hortobagyi G.N., Benjamin R.S., Ali M.K. Clinical and pharmacologic investigation of the effects of α-tocopherol on adriamycin cardiotoxicity. *Ann. N.Y. Acad. Sci.* **393** 411-18. (1982)

[141] Breed J., Zimmerman A., Dormans J., Pinedo H. Failure of the antioxidant vitamin E to protect against adriamycin-induced cardiotoxicity in the rabbit. *Cancer Res.* **40** 2003-38. (1980)

[142] Siveski-Iliskovic N., Kaul N., Singal P.K. Probucol promotes endogenous antioxidants and provides protection against adriamycin-induced cardiomyopathy in rats. *Circulation* **89** 2829-35. (1994)

[143] Iliskovic N., Singal P.K. Lipid lowering: an important factor in preventing adriamycin-induced heart failure. *Am. J. Pathol.* **150** 727-34. (1997)

[144] Voest E.E., van Acker A.B.E., van Vijgh W.J.F., van Asbeck B.S., Bast A. Comparison of different iron chelators as protective agents against acute doxorubicin-induced cardiotoxicity. *J. Mol. Cell Cardiol.* **26** 1179-85. (1994)

[145] Al-Harbi M.M., Al-Gharably N.M., Al-Shabanah O.A., Al-Bekairi A.M., Osman A.M.M., Tawfik H.N. Prevention of doxorubicin-induced myocardial and haematological toxicities in rats by the iron chelator desferrioxamine. *Cancer Chemother. Pharmacol.* **31** 200-04. (1992)

[146] Halliwell B., Gutteridge J.M.C. Free Radicals in Biology and Medicine. 2nd ed. Oxford: Clarendon, pp. 489-492. (1989)

[147] Burke T.G., Pritos C.A., Sartorelli A.C., Tritton T.R. The structural basis for anthracycline antibiotic stimulation of oxygen consumption by HL-60 cells and mitochondria. *Cancer Biochem. Biophys.* **9** 245-55. (1987)

[148] Burke T.G., Lee T.D., van-Balgooy J., Doroshow J.H. Characterization of the aqueous decomposition products of (+)1,2-bis(3,5-dioxopiperazinyl-1-yl)-propane (ICRF-187) by liquid chromatographic and mass spectral analysis. *J. Pharm. Sci.* **80** 338-40. (1991)

[149] Hasinoff B.B. Pharmacodynamics of the hydrolysis-activation of the cardioprotective agent (+)-1,2-bis(3,5-dioxopiperazinyl-1-yl)propane. *J. Pharm. Sci.* **83** 64-67. (1994)

[150] Burkert U., Allinger N.L. Molecular Mechanics. ACS Monograph 177. Washington: American Chemical Society. (1982)

[151] Vandegaer J., Chaberek S., Frost A.E. Iron chelates of diethylenetriaminepentaacetic acid. *J. Inorg. Nucl. Chem.* **11** 210-21. (1989)

[152] Nolan K.B., Murphy T., Hermanns R.D., Rahoo H. Chelating agents as antitumour drugs: Formation of chelating agents from the antitumour pro-drug razoxane. *Inorg. Chim. Acta* **168** 283-88. (1990)

[153] Daeid N.N., Nolan K.B., Ryan L.P. Copper(II) complexes of hydrolysis products of the anticancer bis(3,5-dioxopiperazin-1-yl)alkanes. Displacement of co-ordinated carboxylate ligands by deprotonated amide groups in basic solution. *J. Chem. Soc. Dalton Trans.* 2301-04. (1991)

[154] Graf E., Mahoney J.R., Bryant R.G., Eaton J.W. Iron-catalyzed hydroxyl radical formation. Stringent requirement for free iron coordination site. *J. Biol. Chem.* **259** 3620-24. (1984)

[155] Prout C.K., Sanderson D.S., Couldwell M.C. *N,N'*-methylethylenebis(*N*-methylcarbamylglycinato)copper(II) dihydrate and *N,N'*-ethylethylenebis(*N*-methylcarbamylglycinato)copper(II) dihydrate. *Cryst. Struct. Comm.* **8** 181-88. (1979)

[156] Lind M.D., Hamor M.J., Hamor T.A., Hoard J.L. Stereochemistry of ethylenediaminetetraacetato complexes. II. The structure of crystalline Rb[Fe(OH$_2$)Y.H$_2$O]. III. The structure of crystalline Li[Fe(OH$_2$Y.2H$_2$O]. *Inorg.*

Chem. **3** 34-43. (1964)

[157] Malisza K.L., Hasinoff B.B. Hydroxyl radical production by the iron complex of the hydrolysis product of the antioxidant cardioprotective agent ICRF-187 (dexrazoxane). *Redox Rep.* **2** 69-73. (1996)

[158] Hasinoff B.B., Venkataram S., Singh M., Kuschak T.I. Metabolism of the cardioprotective agents dexrazoxane (ICRF-187) and levrazoxane (ICRF-186) by the isolated hepatocyte. *Xenobiotica* **24** 977-87. (1994)

[159] Buss J.L., Hasinoff B.B. The one-ring open hydrolysis product intermediates of the cardioprotective agent ICRF-187 (dexrazoxane) displace iron from iron-anthracycline complexes. *Agents Actions* **40** 86-95. (1993)

[160] Fife T.H., Przystas T.J. Divalent metal ion catalysis in amide hydrolysis. The hydrolysis of *N*-acylimidazoles. *J. Am. Chem. Soc.* **108** 4631-36. (1986)

[161] Sayre L.M., Reddy K.V., Jacobson A.R., Tang W. Metal ion catalysis of amide hydrolysis. Very large rate enhancements by copper(II) in the hydrolysis of simple ligand-functionalized tertiary amides. *Inorg. Chem.* **31** 935-37. (1992)

[162] Groves J.T., Olson J.R. Models of zinc-containing proteases. Rapid amide hydrolysis by an unusually acidic Zn^{2+}-OH_2 complex. *Inorg. Chem.* **24** 2715-17. (1985)

[163] Berg O.G., von Hippel P.H. Diffusion-controlled macromolecular interactions. *Ann. Rev. Biophys. Biophys. Chem.* **14** 131-60. (1985)

[164] Buss J.L., Hasinoff B.B. Ferrous ion strongly promotes the ring opening of the hydrolysis intermediates of the antioxidant doxorubicin cardioprotective agent ICRF-187 (dexrazoxane). *Arch. Biochem. Biophys.* **317** 121-27. (1995)

[165] Hasinoff B.B. NADPH-cytochrome-P450 reductase promotes hydroxyl radical production by the iron complex of ADR-925, the hydrolysis product of ICRF-187 (dexrazoxane). *Free Rad. Res.* **22** 319-25. (1995)

[166] Houghton R.P., Williams E. Synthesis of bis(imides) and bis(half amides) of *NN'*-ethylenebis(iminodiacetic acid). *J. Chem. Soc. Perkin Trans. I* 2693-96. (1982)

[167] Angus P.M., Jackson W.G. Synthesis and reactivity of the pentaamminecobalt(III) linkage isomers of succinimide. *Inorg. Chem.* **30** 4806-13. (1991)

[168] Sobol M.M., Amiet R.G., Green M.D. In vitro evidence for direct complexation of ADR-529/ICRF-187 [(+)-1,2-bis-(3,5-dioxo-piperazin-1-yl)propane] onto an existing ferric-anthracycline complex. *Mol. Pharmacol.* **41** 8-17. (1992)

[169] Nolan K.B., Ryan L.P., Gonzalez E.B. Synthesis and hydrolysis of an ester of the 'one ring open' hydrolysis product of the anticancer drug 1,2-bis(3,5-dioxopiperazine-1-yl)propane, 'razoxane'. *Inorg. Chim. Acta* **215** 55-60. (1994)

[170] Bertini I., Gray H.B., Lippard S.J., Valentine J.S. Bioinorganic Chemistry. Mill Valley, CA: University Science Books. (1994)

[171] Fraústo da Silva J.J.R., Williams J.J.R. The biological chemistry of the elements the inorganic chemistry of life. Oxford, England: Clarendon Press. (1991)

[172] Magneson G.R., Puvathingal J.M., Ray W.J. The concentrations of free Mg^{2+} and free Zn^{2+} in equine blood plasma. *J. Biol. Chem.* **262** 11140-48. (1987)

[173] Hargreaves M.K., Pritchard J.G., Dave H.R. Cyclic carboxylic monoimides. *Chem. Rev.* **70** 439-68. (1970)

[174] Edward J.T., Terry K.A. The hydrolysis of amides and related compounds. Part IV.* Diacetylamine and succinimide in aqueous alkali. *J. Chem. Soc.* 3527-31. (1957)

[175] Tirouflet J., Le Trouit E. Cinétique de l'hydrolyse des phthalimides en milieu tampon (dosage polarographique). *C. R. Acad. Sci.* **240** 1053-55. (1955)

[176] Matsui S., Aida H. Hydrolysis of some *N*-alkylmaleimides. *J. Chem. Soc. Perkin II* 1277-80. (1978)

[177] Machida M., Machida M.I., Kanaoka Y. Hydrolysis of *N*-substituted maleimides: stability of fluorescence thiol reagents in aqueous media. *Chem. Pharm. Bull.* **25** 2739-43. (1977)

[178] Dickey F.H., Fickett W., Lucas H.J. Stereoisomeric 2,3-butanediamines, 3-amino-2-butanols and 2,3-dimethylethyleneimines; stereochemistry of the opening and closing of the imine ring. *J. Am. Chem. Soc.* **74** 944-51. (1952)

[179] Fenton R.R., Vagg R.S. Chiral metal complexes. 25*. Cobalt (III) complexes of some linear mesomeric tetramine ligands. *Inorg. Chim. Acta* **128** 219-29. (1987)

[180] Dwyer F.P., Garvan F.L. The preparation of 1,2-propylenediaminetatraacetic acid and its resolution through the cobalt complex. *J. Am. Chem. Soc.* **81** 2955-57. (1959)

[181] Jeffery W.A. Bisdioxopiperazines and related prodrugs: Physico-chemical and antitumour properties [Dissertation]. Council for National Academic Awards, London. (1987)

[182] Barradas R.G., Fletcher S., Porter J.D. The hydrolysis of maleimide in alkaline solution. *Bull. Soc. Chim. Fr.* **54** 1400-04. (1975)

[183] Walton H.F., Schilt A.A. The ionization constant and rate of hydrolysis of succinimide. *J. Am. Chem. Soc.* **74** 4995-96. (1952)

[184] Wood J.K. The acidic constants of some ureides and uric acid derivatives. *J. Chem. Soc.* **89** 1831-39. (1906)

[185] Schwarzenbach G., Lutz K. Aciditatsmessungen an mesomeren Säuren and Basen. Einige Aussagen über die Resonanzenergie. *Helv. Chim. Acta* **23** 1162-90. (1940)

[186] Matias P.M., Jeffrey G.A., Ruble J.R. Structures of the *E,Z* (*cis-trans*) isomer of diacetamide and the 1:1 complex with acetamide at 123 K. Ab-initio molecular orbital calculations on the *Z,Z* (*trans-trans*), *E,Z* (*cis-trans*) and *E,E* (*cis-cis*) isomers of diacetamide. *Acta Cryst. B* **44** 516-22. (1988)

[187] Hall H.K. Jr., Brandt M.K., Mason R.M. Hydrolysis rates and mechanisms of cyclic monomers. *J. Am. Chem. Soc.* **80** 6420-27. (1958)

[188] Brown H.C., Brewster J.H., Shechter H. An interpretation of the chemical behavior of five- and six-membered ring compounds. *J. Am. Chem. Soc.* **76** 467-74. (1954)

[189] Herman E.H., Zhang J., Hasinoff B.B., Chadwick D.P., Clark Jr. J.R., Ferrans V.J. Comparison of the protective effects against chronic doxorubicin cardiotoxicity and the rates of iron (III) displacement reactions of ICRF-187 and other bisdiketopiperazines. *Cancer Chemother. Pharmacol.* **40** 400-08. (1997)

[190] Charton M. Electrical effect substituent constants for correlation analysis. *Prog. Phys. Org. Chem.* **13** 119-251. (1981)

[191] Bender M.L. Mechanisms of catalysis of nucleophilic reactions of carboxylic acid derivatives. *Chem. Rev.* **60** 53-113. (1960)

[192] Khan M.N., Khan A.A. Kinetics and mechanism of hydrolysis of succinimide under highly alkaline medium. *J. Org. Chem.* **40** 1793-94. (1975)

[193] Rochon F.D., Kong P.C., Melanson R. Hydrolysis and dimerization of nitrile to diacetamide and crystal structures of chloro(2,2,2,2',2',2'-hexachlorodiacetamido)-

(dimethyl sulfoxide)platinum(II) and *cis*-aquadichloro(dimethyl sulfoxide)platinum(II). *Inorg. Chem.* **29** 2708-12. (1990)

[194] Mason R. The magnetic anisotropy and electron distribution in succinimide. *Acta Cryst. B* **14** 720-24. (1961)

[195] McPhalen C.A., James M.N.G. Structure of *N*-ethylmaleimide, $C_6H_7NO_2$. *Acta Crystallogr. C* **39** 1441-45. (1983)

[196] Ng S.W. Structure of 1H-isoindole-1,3(2H)-dione (phthalimide). *Acta Crystallogr. C* **48** 1695-98. (1992)

[197] Kirfel A. 1,2,3,6-Tetrahydrophthalimide. *Acta Cryst. B* **32** 1556-57. (1976)

[198] Petersen C.S. The crystal structure of glutarimide. *Acta Chem. Scand.* **25** 379-89. (1971)

[199] Camerman N., Hempel A., Camerman A. Bimolane: Structure determination indicates anticancer activity is attributable to ICRF-154. *Science* **225** 1165-66. (1984)

[200] Pranata J. *Ab initio* study of the base-catalyzed hydrolysis of methyl formate. *J. Phys. Chem.* **98** 1180-84. (1994)

[201] Frau J., Donoso J., Munoz F., Blanco F.G. Theoretical calculations of β-lactam antibiotics. III. AM1, MNDO, and MINDO/3 calculations of hydrolysis of β-lactam compound (azetidin-2-one ring). *J. Comp. Chem.* **13** 681-92. (1992)

[202] Vishnuvajjala B.R., Cradock J.C. Tricyclo[4.2.2.$0^{2,5}$]dec-9-ene-3,4,7,8-tetracarboxylic acid diimide: formulation and stability studies. *J. Pharm. Sci.* **75** 301-03. (1986)

[203] Tichane R.M., Bennett W.E. Coordination compounds of metal ions with derivatives and analogs of ammoniadiacetic acid. *J. Am. Chem. Soc.* **79** 1293-96. (1957)

[204] Shtacher G. Potentiometric determination of stability constants of metal complexes with certain amino dicarboxylic acids. *J. Inorg. Nucl. Chem.* **28** 845-61. (1966)

[205] Kozlov Y.M., Babich V.A. Synthesis and complexing properties of complexons, derivatives of diamino acids. II. *D,L*-1,2diaminopropionic-*N,N,N',N'*-tetraacetic acid. Potentiometric and spectrophotometric study of complexing with copper. *Zhur. Obsh. Khim.* **51** 1115-19. (1981)

[206] Chaberek Jr. S., Martell A.E. Stability of metal chelates. IV. *N,N'*-ethylenediaminediacetic acid and *N,N'*-ethylenediaminediacetic-*N,N'*-dipropionic acid. *J. Am. Chem. Soc.* **74** 6228-31. (1952)

[207] Podlahova J., Podlaha J. The stability constants of ethylenediphosphinetetraacetate complexes. *Coll. Czech. Chem. Commun.* **47** 1078-85. (1982)

[208] Majer J., Springer V., Kopecka B. Nove komplexany (VIII) Kyselina etylendiamin-*N,N'*-dijantarova a spektrofotometricke studium jej komplexonov s tazkymi kovmi. *Chemicke Zvesti* **20** 414-22. (1966)

[209] Perrin D.D., Dempsey B., Serjeant E.P. *pKa* prediction for organic acids and bases. Cambridge: University Printing House. (1981)

IMAGE EVALUATION
TEST TARGET (QA-3)

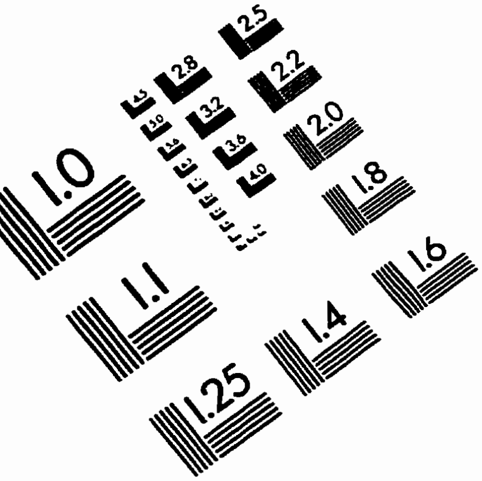

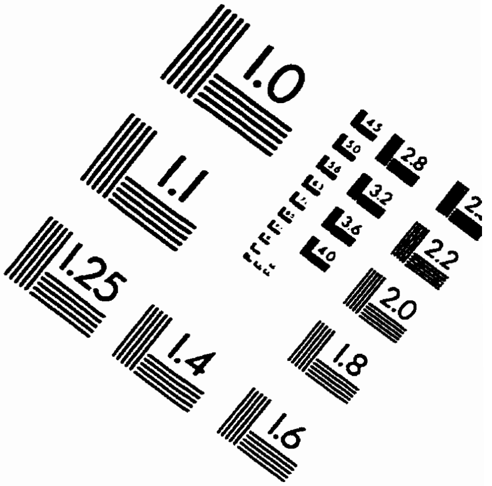

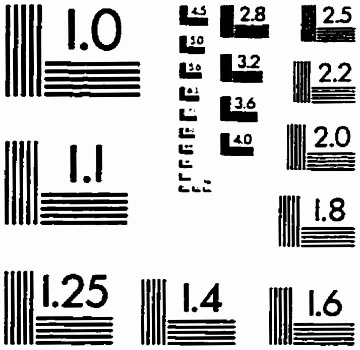

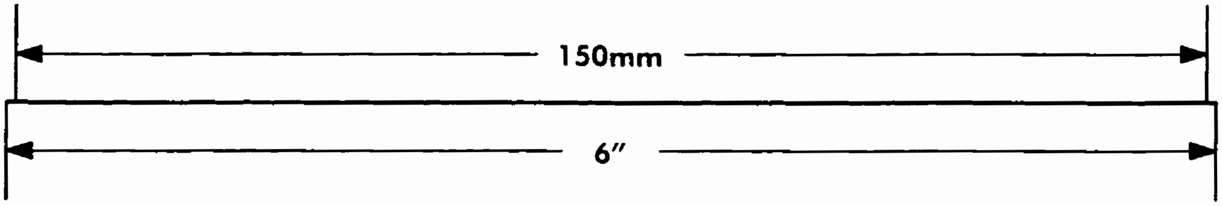

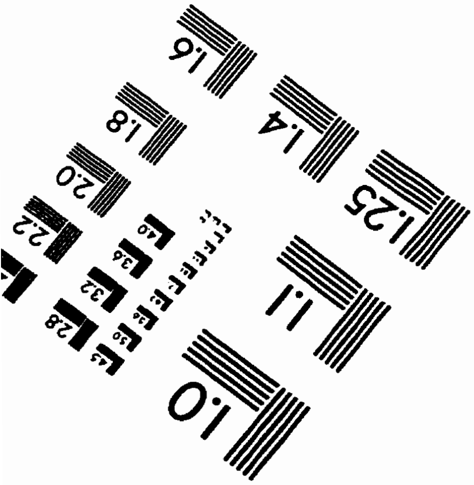

APPLIED IMAGE . Inc
1653 East Main Street
Rochester, NY 14609 USA
Phone: 716/482-0300
Fax: 716/288-5989